UNIVERSITÉ DE LORRAINE | BIBLIOTHÈQUES UNIVERSITAIRES

AVERTISSEMENT

Ce document est le fruit d'un long travail approuvé par le jury de soutenance et mis à disposition de l'ensemble de la communauté universitaire élargie.

Il est soumis à la propriété intellectuelle de l'auteur. Ceci implique une obligation de citation et de référencement lors de l'utilisation de ce document.

D'autre part, toute contrefaçon, plagiat, reproduction illicite encourt une poursuite pénale.

Contact bibliothèque : ddoc-theses-contact@univ-lorraine.fr
(Cette adresse ne permet pas de contacter les auteurs)

LIENS

Code de la Propriété Intellectuelle. articles L 122. 4
Code de la Propriété Intellectuelle. articles L 335.2- L 335.10
http://www.cfcopies.com/V2/leg/leg_droi.php
http://www.culture.gouv.fr/culture/infos-pratiques/droits/protection.htm

Sciences et Ingénieries des Molécules, des Produits, des Procédés et de l'Énergie (SIMPPÉ)

École Nationale Supérieure des Industries Chimiques (ENSIC)

Zhejiang Sci-Tech University

Thèse

Pour l'obtention du titre de

Docteur de l'Université de Lorraine

Mention : Génie des Procédés, des Produits et des Molécules

Sujet: Dynamics in dip coating with complex fluids and its rheometric application

Par

Heng-Kuan ZHANG

Présentée et soutenue publiquement le 30 Octobre 2025

Membres du Jury :

Ms. Bo-Na LU	University professor	Rapporteur
Mr. Jean-Baptiste SALMON	Research director	Rapporteur
Ms. Xiao-Hong HAN	University professor	Examiner, President
Ms. Cecile LEMAITRE	Lecturer	Thesis supervisor
Mr. Xian-Ming ZHANG	University professor	Co-supervisor
Mr. Guo-Hua HU	University professor	Guest member

Laboratoire Réactions et Génie des Procédés
UMR 7274

Acknowledgements

I always thought six years would feel like an eternity, yet here I am, already standing at the threshold of graduation. Looking back to the summer of 2019, it was Professor Zhang Xian-Ming who, with his pedagogical wisdom and exemplary guidance, opened the door to scientific research for me. I extend my sincere gratitude to Professor Zhang for his meticulous academic guidance and profound personal support over these past six years. You not only steered the direction of my research but also gave me the freedom to explore; you often reminded me that a Ph.D. is not just about research training but also a personal journey, to become a responsible individual. These words remain deeply engraved in my heart. Whenever I encountered obstacles in my research, you never rushed me, allowing me the space to reflect; and when challenges exceeded my abilities, you were always there to offer insights and guide me toward diverse solutions. Thank you once again for your guidance and companionship throughout this journey; without you, none of the stories that followed would have been possible.

When I first joined the research group, I was still a novice. I was fortunate to receive the dedicated time and effort of Dr. Yin Ya-Ran, who patiently taught me how to analyze scientific problems and the techniques for writing, submitting, and revising research papers. For this, I am deeply grateful. I also extend my thanks to my seniors and peers in the research group: Chen Meng-Di, Pan Xu-Qi, Xin Si-Cheng, Lai Xiao-Qing, Wan Su-Ying, Zhao Meng-Xiao, Zhang Ze-Min, Huang Zheng, Wang Xiao-Xiao, Zhu Meng, Zong Chen-Yang, as well as my roommate Li Yong, for their support in both research and daily life. I thank my old friend Zheng Ming-Fu. Though we often held different perspectives, we always respected each other; we maintained our individuality while progressing together. I dedicate the phrase “harmony in diversity” to our friendship.

Later, thanks to Professor Zhang Xian-Ming’s recommendation, I had the privilege of being guided by Professor Hu Guo-Hua of the Université de Lorraine in France. Professor Hu’s critical scientific spirit and rigorous academic attitude have deeply inspired me and remain ideals I strive to emulate. During my study abroad in France in 2024, Professor Hu further introduced me to Dr. Cecile

Lemaitre. I am immensely grateful for the careful guidance and support of my French supervisors, Dr. Cecile and Professor Hu, during my stay. Professor Hu frequently checked on my research progress, helping me clarify issues and plan next steps; Dr. Cecile meticulously reviewed everything from formula derivations to code logic and provided enthusiastic support in research, conferences, and daily life. I also extend my thanks to my friends: Wang Pan, Fei Ying-Jie, Zeng Shuo, Li Li-Wei, Hao Fu-Lan, Wen Meng-Xi, Yuan Cong, Mohammad, Adilson, and Yanis, for making my study abroad experience enriching and vibrant.

I extend my heartfelt gratitude to my parents. You are my strongest pillar of support, and your understanding and encouragement have been the foundation that allowed me to fully dedicate myself to my research and ultimately complete my studies.

I also wish to express my sincere thanks and apologies to my girlfriend, Ms. Zhou Ning-Xia. Looking back on my years of study, we had little time together, yet your support was always unwavering. Thank you for your silent companionship and steadfast support along the way; your understanding and dedication are invaluable to me.

This research was supported by the National Natural Science Foundation of China (No. 51973196) and the China Scholarship Council (No. 202308330424), for which I am deeply thankful.

Reflecting on these six years of research, I realize I was merely following in the footsteps of my mentors, guided by curiosity, on a journey of exploration. I dedicate this work to all my mentors, friends, and peers who have cared for and supported me along the way.

Résumé

Le dépôt par immersion, en tant que technique efficace pour déposer un liquide sur un substrat solide, est facile à mettre à l'échelle et très flexible. Cette technologie est largement utilisée dans un large éventail d'applications, de l'industrie à la fabrication. Il est important de prédire et de contrôler l'épaisseur du film liquide qui régit les performances mécaniques et fonctionnelles du revêtement final durci. Cette thèse se concentre sur la modélisation de l'épaisseur du film, basée sur l'hydrodynamique et le comportement de dépôt des fluides newtoniens et viscoplastiques dans les procédés de dépôt par immersion. De plus, une nouvelle méthode rhéométrique pour mesurer les paramètres de Herschel-Bulkley des fluides viscoplastiques est développée. La thèse comprend quatre tâches principales, organisées comme suit:

Évolution spatio-temporelle de l'épaisseur du film lors du dépôt par immersion de fluides newtoniens: Nous étudions le profil d'épaisseur de couche des fluides newtoniens pendant le dépôt par immersion avec retrait vertical dans le régime visco-gravitaire. Les études antérieures se sont principalement concentrées sur le profil d'épaisseur de l'extrémité du film, mais les modèles existants ne parviennent pas à prédire avec précision cette partie. Le présent travail démontre que la couche s'amincit le long de la direction de retrait et présente une auto-similarité sous une mise à l'échelle adimensionnelle. En prenant complètement en compte les caractéristiques du profil d'épaisseur, nous proposons un modèle capable de prédire l'ensemble du profil de couche, validé sur une large gamme de nombres de Reynolds.

Dépôt de film de fluides newtoniens sur un cylindre partiellement mouillant lors du dépôt par immersion: Nous étudions le mouillage et le dépôt de fluides newtoniens sur un cylindre partiellement mouillant pendant le dépôt par immersion à l'aide de la simulation numérique directe et de la théorie de la lubrification. Les résultats révèlent que le nombre capillaire et le rayon du cylindre modifient qualitativement la morphologie interfaciale au-delà de la simple affectation de l'épaisseur du film. Pour des rayons > 2.3, quatre scénarios interfaciaux successifs émergent avec l'augmentation du nombre

capillaire: (I) un ménisque stationnaire, (II) la coexistence d'un film épais et d'une dépression stationnaire, (III) la coexistence d'un film épais et d'un film classique de Landau-Levich (LL), et (IV) un film monotone. Pour des rayons < 2.3, le scénario (II) disparaît. La diminution supplémentaire du rayon déclenche l'apparition d'un film ondulé. L'état ondulé du film LL dépend à la fois du nombre capillaire et du rayon, tandis que le film épais devient ondulé seulement en dessous d'un rayon critique (= 0.255). La théorie de la lubrification prédit avec succès les profils de film et les transitions de scénario (à l'exclusion des films ondulés). La combinaison de la théorie de la lubrification avec la théorie de l'instabilité absolue-convective donne des critères pour évaluer les états ondulés du film.

Hydrodynamique des fluides viscoplastiques lors du dépôt par immersion: Nous étudions le dépôt par immersion sur plaque avec des fluides viscoplastiques sous un nombre de Bingham inférieur à 1 en utilisant la simulation numérique directe, en nous concentrant sur la façon dont la contrainte d'écoulement et la viscosité dépendante du cisaillement affectent à la fois l'hydrodynamique à l'intérieur du récipient et l'épaisseur du film. Les limites écoulées/non écoulées, les profils de vitesse et les distributions de contrainte de cisaillement sont déterminés théoriquement. Notre analyse capture les caractéristiques clés du drainage dans la région du ménisque. Lorsque les effets de tension de surface sur la formation du film sont négligeables, nous développons un modèle d'épaisseur de film semi-empirique incorporant les effets de drainage, qui montre une excellente capacité prédictive.

Hydrodynamique et caractérisation rhéologique lors du processus de pénétration d'une plaque à fente dans des fluides viscoplastiques: Le phénomène inherent de glissement pariétal dans les fluides viscoplastiques complique à la fois l'analyse de l'écoulement et la caractérisation rhéologique. Cette étude investigate la pénétration d'une plaque à fente dans des fluides viscoplastiques à travers des approches combinées expérimentales, de dynamique des fluides numérique (CFD) et analytiques. Nous examinons la force de pénétration et la dynamique de l'écoulement à l'intérieur du récipient, en corrélant la contrainte de cisaillement à diverses vitesses de pénétration avec un modèle pseudo-Herschel-Bulkley pour déterminer la contrainte d'écoulement. L'indice d'écoulement et le facteur de

consistance sont dérivés de notre modèle d'écoulement analytique. La méthode de pénétration est rigoureusement validée en comparant les courbes d'écoulement résultantes avec les mesures sur disques parallèles et les données de la littérature, démontrant un excellent accord. Notre approche fournit de nouvelles perspectives sur les effets de glissement pariétal tout en offrant une alternative pratique pour la caractérisation rhéologique.

Abstract

Dip coating, as an efficient technique to deposit liquid on a solid substrate, is easy to scale up and highly flexible. This technology is extensively used in a wide range of applications, spanning from industry to manufacturing. It is important to predict and control the thickness of the liquid film which governs the mechanical and functional performance of the final cured coating. This thesis focuses on the modelling of the film thickness, based on the hydrodynamics and deposition behaviour of Newtonian and viscoplastic fluids in dip coating processes. Additionally, a new rheometric method for measuring the Herschel-Bulkley parameters of the viscoplastic fluids is developed. The thesis comprises four principal tasks, organized as follows:

Spatial-temporal evolution of film thickness upon dip coating of Newtonian fluids: We investigate the layer thickness profile of Newtonian fluids during dip coating with vertical withdrawal in the visco-gravity regime. Previous studies have primarily focused on the thickness profile of the film tip, yet existing models fail to accurately predict this part. The present work demonstrates that the layer thins along the withdrawal direction and exhibits self-similarity under dimensionless scaling. By comprehensively accounting for the thickness profile characteristics, we propose a model capable of predicting the entire layer profile, validated across a broad range of Reynolds numbers.

Film deposition of Newtonian fluids on a partially wetting cylinder upon dip coating: We study the wetting and deposition of Newtonian fluids on a partially wetting cylinder during dip coating using direct numerical simulation and lubrication theory. Results reveal that both the capillary number and cylinder radius qualitatively alter interfacial morphology beyond just affecting film thickness. For radii > 2.3, four successive interfacial scenarios emerge with increasing capillary number: (I) a stationary meniscus, (II) coexistence of a thick film and a stationary dimple, (III) coexistence of a thick film and a classical Landau-Levich (LL) film, and (IV) a monotonic film. For radii < 2.3, scenario (II) disappears. The further decrease in radius triggers the appearance of wavy film. The waving state of LL film depends on both capillary number and the radius, while the thick film becomes wavy only

below a critical radius (= 0.255). Lubrication theory successfully predicts film profiles and scenario transitions (excluding wavy films). Combining lubrication theory with absolute-convective instability theory yields criteria for assessing film waving states.

Hydrodynamics of viscoplastic fluids upon dip coating: We investigate plate dip coating with viscoplastic fluids under Bingham number below 1 using direct numerical simulation, focusing on how yield stress and shear-dependent viscosity affect both hydrodynamics inside the container and film thickness. The yielded/unyielded boundaries, velocity profiles, and shear stress distributions are theoretically determined. Our analysis captures key drainage characteristics in the meniscus region. When surface tension effects on film formation are negligible, we develop a semi-empirical film thickness model incorporating drainage effects, which shows excellent predictive capability.

Hydrodynamics and rheological characterization upon the immersion process of a slotted plate into viscoplastic fluids: The inherent wall slip phenomenon in viscoplastic fluids complicates both flow analysis and rheological characterization. This study investigates the immersion of a slotted plate into viscoplastic fluids through combined experimental, computational fluid dynamics (CFD), and analytical approaches. We examine the immersion force and flow dynamics inside the container, correlating the shear stress at various immersion velocities with a pseudo-Herschel-Bulkley model to determine the yield stress. The flow index and consistency factor are derived from our analytical flow model. The immersion method is rigorously validated by comparing the resulting flow curves with both parallel disk measurements and literature data, demonstrating excellent agreement. Our approach provides new insights into wall slip effects while offering a practical alternative for rheological characterization.

Contents

Acknowledgements I

Résumé III

Abstract VI

Contents VIII

Résumé étendu en français XIII

I. Introduction XIII

II. Formulation du problème et objectifs de recherche XIV

III. Contenu de la recherche et résultats clés de la thèse XVIII

IV. Conclusions XXIII

Reference XXIV

1 Introduction 1

1.1 Research background 1

1.2 Research significance 2

1.3 Research objectives 3

Reference 6

2 Literature review and state of the art 7

2.1 Research method 7

2.1.1 Experimental techniques 7

2.1.1.1 Dip coating device 7

2.1.1.2 Film thickness measurement technique 9

2.1.2 Computational fluid dynamics 11

2.2 Dip coating of Newtonian fluids 13

2.3 Key factors affecting dip coating 16

2.3.1 Substrate characteristics 16

2.3.1.1 Substrate geometry 16
2.3.1.2 Wetting properties 18
2.3.2 Rheological properties of liquid 20
2.3.2.1 Shear-thinning fluid 20
2.3.2.2 Viscoplastic fluid 25
2.4 Problem formulation 29
Reference 30
3 Methodology 36
3.1 CFD simulation 37
3.1.1 Governing equations 37
3.1.2 Numerical schemes 39
3.2 Material and experiment in work 1 40
3.2.1 Experimental fluid 40
3.2.2 Dip coating experiment 41
3.3 Material and experiment in work 4 42
3.3.1 Materials 42
3.3.2 Parallel disk method 44
3.3.3 Immersion device platform 46
3.3.4 Immersion procedure 47
Reference 48
4 Spatial-temporal evolution of a Newtonian liquid layer on a fully wetting plate during dip coating 50
4.1 Introduction 50
4.2 Simulation settings 53
4.2.1 Boundary and initial conditions 53

4.2.2 Mesh independence 54
4.3 Results and discussions 56
4.3.1 Validity of the simulation 56
4.3.2 Factors controlling the layer formation 58
4.3.3 Characteristics of the layer thickness profile 59
4.3.4 Modelling of the transient layer thickness profile 60
4.3.4.1 Modelling of the unsteady part 63
4.3.4.2 Modelling of the steady part 66
4.3.4.3 Modelling of the entire layer 70
4.3.5 Validity of the model 70
4.4 Conclusion 74
Reference 75
5 Film deposition of Newtonian fluids on a partially wetting cylinder upon dip coating 77
5.1 Introduction 77
5.2 Method 79
5.2.1 Simulation settings 79
5.2.2 Lubrication theory 81
5.3 Overview of the interfacial morphology 83
5.4 Stationary meniscus before wetting 86
5.5 Film deposition after wetting 91
5.5.1 Scenario II 91
5.5.2 Scenario III 96
5.5.3 Scenario IV 103
5.5.4 Wavy films: WTFL, WTWL and FTWL 105
5.6 Conclusion 111

Reference 113

6 Hydrodynamics of viscoplastic fluids upon dip coating of a fully wetting plate 114

6.1 Introduction 114

6.2 Numerical settings 116

6.2.1 Fluid properties 116

6.2.2 Computational domain and meshing 117

6.3 Results and discussions 119

6.3.1 Model validation 119

6.3.2 Flow regime 121

6.3.3 Shear stress and velocity profiles 123

6.3.4 Film thickness 128

6.4 Conclusion 134

Reference 135

7 Hydrodynamics and rheological characterization upon the immersion process of a slotted plate into viscoplastic fluids 137

7.1 Introduction 137

7.2 Force and flow characteristics 141

7.2.1 Regime identification 141

7.2.1.1 Regime I 142

7.2.1.2 Regime II 144

7.2.1.3 Regime III 147

7.2.1.4 Regime IV 148

7.2.2 Flow characteristics 149

7.3 Rheological measurement by immersion method 152

7.3.1 Determination of shear stress 152

7.3.1.1 Impact of geometric parameter 152
7.3.1.2 Impact of immersion velocity 154
7.3.2 Measuring rheological parameters 155
7.3.2.1 Yield stress 155
7.3.2.2 Consistency factor and flow index 157
7.3.3 Validation of immersion method 158
7.3.3.1 Comparison of flow curves obtained from different methods 158
7.3.3.2 Comparison of analytical and simulated velocity profiles 160
7.3.4 Applicability of immersion method 163
7.4 Conclusion 164
Reference 164
8 Summary and perspectives 167
8.1 Summary 167
8.2 Perspectives 168
Appendix A 170
A.1 Accuracy and reproducibility of the dip coating experiment 170
A.2 Additional three-dimensional simulation 171
A.3 Evaluation of the extent of edge bead phenomenon 175
Appendix B 177
Nomenclature 179
Greek letters 181
Dimensionless numbers 182
Publications 185

Résumé étendu en français

I. Introduction

Le revêtement est une technique de génie de surface qui consiste à déposer une couche de matériau sur des substrats afin d'améliorer leurs caractéristiques de performance ou de prolonger leur durée de vie. Comme présenté dans les synthèses de Ruschak (1985)[1] et Weinstein *et al.* (2004)[2], les procédés de revêtement peuvent être classés en deux catégories: le revêtement pré-dosé et le revêtement auto-dosé. Dans le revêtement pré-dosé, l'épaisseur de la couche déposée est directement déterminée par le débit imposé. Les techniques de revêtement pré-dosé, telles que le revêtement par fente[3] et le revêtement par écoulement gravitaire[4], nécessitent un système d'alimentation contrôlé et une distribution latérale précise du liquide. En revanche, dans le revêtement auto-dosé, l'épaisseur de la couche est déterminée simultanément par les propriétés du liquide, la vitesse du substrat et la géométrie de l'équipement. La revêtement par immersion-retrait, une méthode classique de revêtement auto-dosé, se distingue par son extensibilité et sa grande flexibilité, ce qui explique son adoption généralisée dans les contextes industriels. Par exemple, elle est utilisée pour déposer un film antireflet sur des cristaux générateurs d'ondes[5], un film conducteur sur des fibres[6,7], et des cellules solaires organiques de grande surface[8]. La revêtement par immersion-retrait est suffisamment flexible pour revêtir différents substrats (plaque ou cylindre[7,9]; substrat solide, mou ou même poreux[10-12]; substrat plat ou courbe[8,13]) avec des fluides aux propriétés rhéologiques variées (fluides newtoniens[11,14,15], fluides viscoplastiques[16,17] et suspensions[18-21]).

Le procédé de revêtement par immersion-retrait comprend deux étapes techniques: l'immersion du substrat dans le liquide, puis son retrait. (1) Immersion: Le substrat est immergé dans la solution de revêtement à une vitesse constante, éventuellement suivie d'un temps de pause prédéterminé pour assurer un mouillage complet du substrat. (2) Retrait: Une couche de liquide est entraînée et déposée sur le substrat lors de son retrait du bain. La vitesse de retrait est généralement constante pour obtenir des films uniformes. Les performances mécaniques et fonctionnelles du film final après séchage

dépendent largement de l'épaisseur du film liquide. La relation fondamentale entre l'épaisseur du film et les propriétés du revêtement solide souligne l'importance capitale de la prédiction et du contrôle précis de l'épaisseur du film. La distribution de l'épaisseur du film est principalement déterminée par le comportement hydrodynamique lors du processus de retrait. Ce comportement hydrodynamique résulte de l'interaction complexe des forces visqueuses, gravitationnelles, capillaires et même inertielles. Ces forces gouvernantes sont principalement déterminées par trois facteurs clés: les propriétés du liquide de revêtement, les propriétés du substrat et la vitesse de retrait.

Face à des conditions opératoires complexes telles qu'un nombre capillaire élevé, un mouillage partiel ou des fluides non newtoniens, l'efficacité prédictive des théories dynamiques existantes de la revêtement par immersion-retrait diminue significativement. L'écart entre la théorie et la pratique indique que la compréhension actuelle des mécanismes dynamiques intrinsèques de la revêtement par immersion-retrait présente des lacunes qui nécessitent d'être clarifiées. L'objectif principal de cette thèse est de développer un modèle reliant l'épaisseur du film aux propriétés du liquide, aux caractéristiques du substrat et à la vitesse de retrait, en se basant sur l'hydrodynamique et les mécanismes de formation du film. Étant donné que différents systèmes liquide-substrat et différentes vitesses de retrait présentent des mécanismes de formation de film distincts, des études différenciées sont nécessaires pour divers scénarios afin de développer des modèles d'épaisseur individuels. Cette recherche suit une approche progressive allant des scénarios fondamentaux aux scénarios complexes. Pour le substrat, nous considérons d'abord une plaque à mouillage complet avant d'étendre l'étude à un cylindre à mouillage partiel. En parallèle, nous passons d'un liquide newtonien à un liquide viscoplastique. De plus, nous proposons une nouvelle méthode rhéométrique pour caractériser les fluides viscoplastiques, basée sur le processus d'immersion de la plaque.

II. Formulation du problème et objectifs de recherche

Comme le montre la Figure II.1, ce mémoire adopte la mécanique des fluides numérique (CFD) comme méthodologie centrale, en l'articulant avec la validation expérimentale et l'analyse théorique,

afin de révéler et de quantifier systématiquement les forces dominantes et leurs mécanismes de couplage lors du procédé de revêtement par immersion-retrait sous différentes conditions physiques. La démarche de recherche suit une progression théorique allant des systèmes fondamentaux aux systèmes complexes, dont la logique interne se traduit par une extension graduelle des conditions aux limites et des lois de comportement dans les équations gouvernantes.

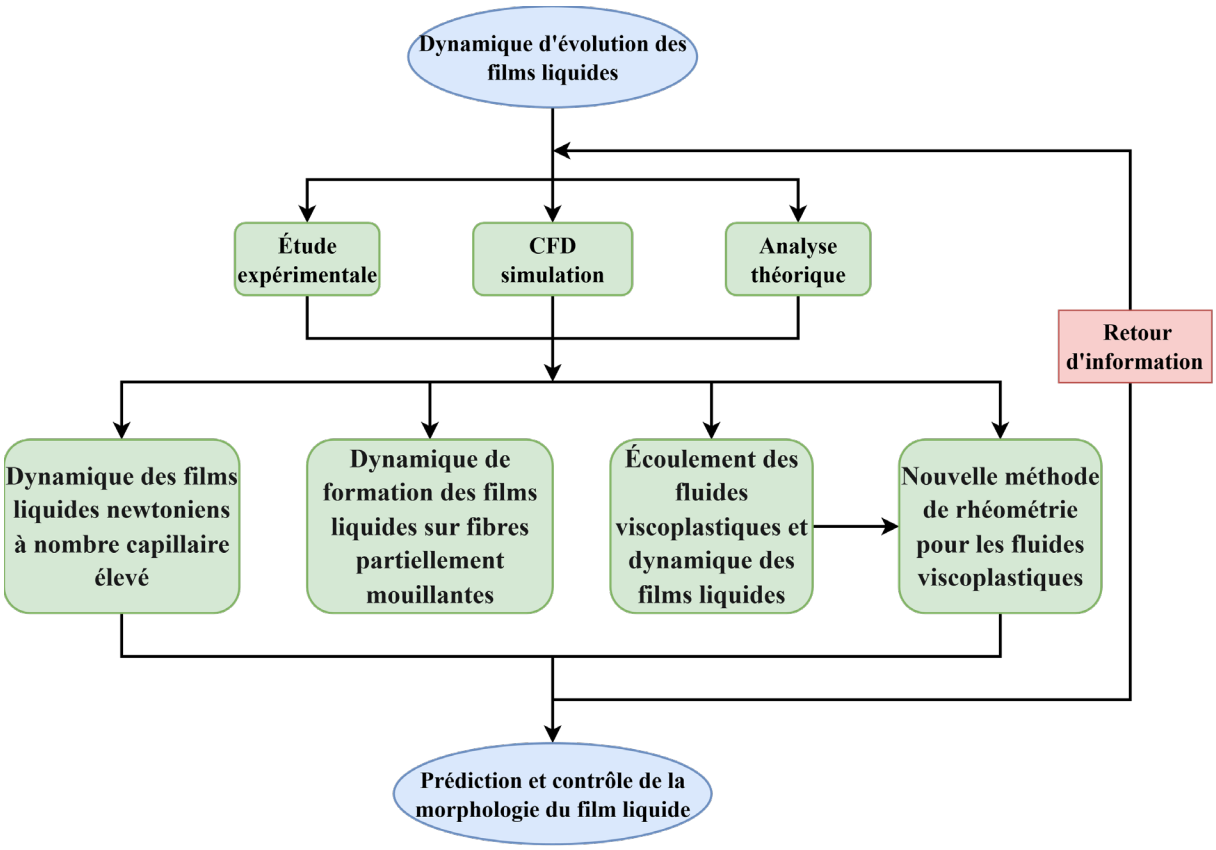

Figure II.1 Schéma du plan de recherche et de la démarche scientifique

Comme illustré dans la Figure II.1, le point de départ de cette recherche est la résolution de la problématique dynamique liée à la compétition entre les forces visqueuses et gravitationnelles sous un nombre capillaire élevé. Lors du retrait d'une plaque parfaitement mouillante, à un nombre capillaire suffisamment grand, les forces capillaires deviennent négligeables et le procédé est dominé par la compétition entre les forces visqueuses et gravitationnelles en régime instationnaire. La théorie classique de Landau-Levich devient alors inapplicable. La première contribution de cette thèse est de

construire un nouveau modèle dynamique, s'affranchissant de la condition traditionnelle de raccordement au niveau du ménisque, afin de décrire complètement l'évolution spatio-temporelle du film liquide sous le régime dominé par les forces visqueuses et gravitationnelles, établissant ainsi les bases théoriques de la dynamique dans le régime des hauts nombres capillaires.

Après avoir élucidé le rôle du système fondamental de forces visqueuses-gravitationnelles, le champ de l'étude s'étend naturellement à des systèmes à frontières complexes où les forces capillaires ne peuvent être négligées. Lorsque le substrat présente une mouillabilité partielle et une courbure finie, la dynamique se complexifie considérablement suite à l'introduction de deux nouveaux facteurs: d'une part, la singularité de contrainte induite par le mouvement de la ligne de contact triphase gaz-liquide-solide, et d'autre part, le champ de pression capillaire radiale additionnel dû à la courbure de la fibre. Cette étude résoudra la singularité en introduisant un modèle de glissement de Navier, dérivera la forme complète de l'équation de lubrification axisymétrique, et révélera pour la première fois de façon systématique la dynamique de formation du film liquide sous l'action combinée des pressions capillaires axiales et radiales, des forces visqueuses, de la gravité et de la ligne de contact mobile.

Cependant, les études susmentionnées sont toutes applicables aux fluides newtoniens (relation linéaire entre la contrainte et le taux de cisaillement) et ne considèrent que l'écoulement visqueux. Pour se rapprocher des fluides industriels réels, l'approfondissement théorique nécessite une généralisation de la loi de comportement afin de prendre en compte les fluides viscoplastiques, caractérisés par une contrainte seuil. Le comportement dynamique de ces fluides est gouverné par cette contrainte seuil, paramètre intrinsèque qui introduit un seuil de contrainte dans les équations gouvernantes, conduisant à une partition spatiale de l'écoulement en zones cisaillées (cédées) et rigides (non cédées). Cela transforme le problème dynamique, passant d'un transport continu de quantité de mouvement à un problème couplé d'évolution de l'interface de yielding, d'écoulement visqueux dans les zones cédées et de mouvement de corps rigide dans les zones non cédées. Cette recherche révèlera comment la contrainte seuil remodèle la structure de l'écoulement, comment elle détermine

conjointement avec les forces visqueuses et gravitationnelles le volume de fluide entraîné, et établira finalement une théorie dynamique de la formation du film prenant en compte le couplage entre l'écoulement plastique et visqueux.

L'étude approfondie de la dynamique de formation des films de fluides viscoplastiques met en lumière une contradiction technique fondamentale: la précision des modèles théoriques dépend fortement de la saisie précise des paramètres rhéologiques, tels que la contrainte seuil, tandis que les mesures rhéométriques rotationnelles conventionnelles sont entachées d'erreurs significatives dues à l'effet de glissement pariétal. Pour répondre à cette difficulté de caractérisation rhéologique, la dernière partie des travaux de recherche vise à développer une nouvelle méthode de rhéométrie basée sur l'inversion de la dynamique d'immersion. Son principe est le suivant: en établissant une interface sans glissement, la contrainte à cette interface est directement reliée à la vitesse d'immersion du substrat; la résolution du problème inverse permet d'extraire les paramètres de la loi de comportement à partir de la réponse dynamique, évitant ainsi les inexactitudes de mesure induites par le glissement pariétal. Contrairement aux méthodes d'immersion traditionnelles qui se limitent souvent à la détermination de la contrainte seuil, la méthode d'immersion proposée ici permet la détermination simultanée de multiples paramètres rhéologiques.

En résumé, ce mémoire a pour fil conducteur principal de révéler et de modéliser les forces dominantes et l'évolution de l'écoulement lors du procédé de revêtement par immersion-retrait. Il explore un spectre dynamique complet, allant de l'équilibre d'un système de forces unique à la compétition de systèmes multiples, jusqu'à l'introduction d'un nouveau système de forces (contrainte seuil) via la loi de comportement, suivant une logique interne de progression naturelle des mécanismes physiques. Enfin, face au défi de la caractérisation des fluides viscoplastiques, il établit une méthode et un principe de mesure innovants basés sur la dynamique d'immersion. Cette recherche systématique approfondit couche par couche la compréhension de la dynamique du revêtement par immersion-retrait, et construit une boucle complète allant de la théorie à l'application. Elle fournit une base théorique

solide pour le contrôle précis de la fabrication des revêtements, et ouvre de nouvelles perspectives pour l'extension des applications de la technique d'immersion-retrait dans le domaine de la rhéométrie.

III. Contenu de la recherche et résultats clés de la thèse

1. Revêtement par immersion-retrait de fluides newtoniens à haut nombre capillaire

Ce chapitre a combiné de manière intégrée la simulation CFD, des expériences de revêtement par immersion-retrait et l'analyse théorique pour étudier la dynamique du revêtement par immersion-retrait des fluides newtoniens à haut nombre capillaire. Des modèles théoriques pertinents ont été développés, et leur précision ainsi que leur domaine de validité ont été déterminés. Les principales conclusions sont les suivantes:

(1) Le film liquide global est contrôlé par les forces visqueuses et gravitationnelles. La force visqueuse est la force motrice du procédé d'immersion-retrait, entraînant un épaississement du film, tandis que la force gravitationnelle s'y oppose, provoquant un amincissement du film le long de la direction de retrait. Les caractéristiques dynamiques varient selon les régions du film. Dans la région du ménisque, l'écoulement au sein du film est bidimensionnel et l'épaisseur du film tend progressivement vers une épaisseur asymptotique. En revanche, dans la zone du film proprement dite, l'écoulement présente des caractéristiques unidimensionnelles marquées, avec une évolution temporelle et une hétérogénéité spatiale prononcées.

(2) À l'échelle adimensionnelle, le film liquide présente une auto-similarité. Pour un même temps adimensionnel, les profils de film obtenus sous différentes conditions (vitesse de retrait, viscosité du fluide, densité du fluide) se superposent.

(3) Une nouvelle stratégie de modélisation ‘‘modélisation partitionnée, recomposition globale’’ de la distribution du film a été proposée. Un modèle composite capable de décrire avec précision le profil complet du film, depuis la région du ménisque jusqu'au front du film liquide, a été construit, surmontant ainsi les limitations des modèles uniques. Ce modèle est hautement fiable pour un temps adimensionnel supérieur à 16 et un nombre de Reynolds compris entre 0 et 1.1.

(4) Pour de faibles angles de retrait, les caractéristiques d'écoulement unidimensionnel dans la région instationnaire sont plus prononcées, ce qui valide que l'approche actuelle de ''modélisation partitionnée, recomposition globale'' peut être directement étendue aux procédés d'immersion-retrait avec différents angles de retrait. Cela démontre que cette étude ne résout pas seulement un problème spécifique, mais propose également un cadre théorique général et extensible.

2. Revêtement par immersion-retrait sur fibre partiellement mouillante avec un fluide newtonien

Ce chapitre intègre la simulation numérique CFD et l'analyse théorique de la lubrification pour étudier systématiquement la dynamique de mouillage et de formation du film liquide lors du procédé de revêtement par immersion-retrait d'un fluide newtonien sur une fibre partiellement mouillante. Ce travail représente une extension de la théorie fondamentale vers des conditions de mouillage complexes et des géométries de substrat complexes. Les résultats de l'étude constituent un complément et un approfondissement importants de la théorie fondamentale sous des conditions aux limites plus complexes. Il est à nouveau souligné que le modèle théorique présenté ici est dérivé des équations de Navier-Stokes via l'approximation de lubrification, et sa validité n'est pas limitée à la plage de rayons utilisée dans les simulations numériques actuelles. La théorie reste également applicable pour des rayons de fibre plus petits. Les principales conclusions de cette recherche peuvent être résumées en trois points:

(1) L'étude révèle l'influence de la courbure de la fibre sur les conditions critiques de transition de mouillage, dépassant ainsi les limitations de la théorie des plaques. La recherche montre que le rayon de la fibre $\bar{r}_0$ affecte non seulement quantitativement l'épaisseur du film liquide, mais modifie aussi qualitativement l'évolution morphologique de l'interface gaz-liquide. Lorsque $\bar{r}_0 > 2.3$, l'interface passe successivement par quatre étapes distinctes avec l'augmentation du nombre capillaire *Ca*. En revanche, lorsque $\bar{r}_0 < 2{,}3$, le système saute l'étape de ''coexistence d'un film épais et d'une dépression'' et passe directement d'un ménisque statique à une structure de film composée d'un film

épais, d'une crête capillaire et d'un film de Landau-Levich (LL). La découverte de ce phénomène de saut met en évidence le rôle clé de la courbure dans la dynamique de formation du film liquide.

(2) L'étude clarifie systématiquement l'évolution de deux nombres capillaires critiques en fonction de la courbure dans les systèmes fibreux et révèle le mécanisme de bifurcation sous-jacent. Les nombres capillaires critiques $Ca_{c,1}$ (transition de mouillage) et $Ca_{c,2}$ (transition de la dépression au film LL) présentent des tendances opposées en fonction du rayon de la fibre $\bar{r}_0$: $Ca_{c,1}$ diminue avec l'augmentation de $\bar{r}_0$, indiquant qu'une courbure plus importante facilite le mouillage initial; $Ca_{c,2}$ augmente avec $\bar{r}_0$, suggérant qu'une courbure plus importante rend la formation d'un film LL stable plus difficile. En reliant ces deux transitions, via la théorie de la lubrification, respectivement à des bifurcations pli (saddle-node) de la solution du ménisque statique et de la solution de dépression, l'étude fournit un cadre théorique solide pour comprendre la nature physique de ces transitions.

(3) L'étude identifie et clarifie le phénomène d'ondulation du film liquide induit par la courbure, et présente son diagramme de phase d'existence. Pour la première fois, il a été observé qu'à de petits rayons de fibre, le film épais et le film LL développent des ondulations indépendamment, avec des mécanismes et des plages de stabilité distincts: l'ondulation du film épais est contrôlée uniquement par le rayon $\bar{r}_0$, avec une valeur critique bien définie ($\bar{r}_0$ = 0.255) en dessous de laquelle l'ondulation est inévitable; l'ondulation du film LL est régulée conjointement par Ca et $\bar{r}_0$, présentant un comportement plus complexe. Ce travail établit systématiquement son état (plat ou ondulé) dans différents intervalles de paramètres et définit les frontières entre stabilité et instabilité.

3. Revêtement par immersion-retrait de fluides viscoplastiques

Ce chapitre utilise la simulation numérique CFD pour étudier l'écoulement lors du revêtement par immersion-retrait de fluides viscoplastiques. À travers l'analyse coordonnée de la distribution des régimes d'écoulement, des profils de vitesse, de la contrainte et de l'épaisseur du film, il révèle la dynamique de l'écoulement et de la formation du film pour ces fluides. Les principales conclusions sont les suivantes:

(1) Dans le réservoir, le fluide se divise en trois zones distinctes le long de la direction allant de la plaque vers la paroi du réservoir: une zone cédée interne, une zone rigide (non cédée) et une zone cédée externe. Dans la zone cédée interne, la vitesse du fluide décroît en s'éloignant de la plaque, atteignant une vitesse descendante maximale u_d à l'interface entre la zone cédée interne et la zone rigide. La zone rigide se déplace vers le bas comme un solide à la vitesse constante u_d. Dans la zone cédée externe, la vitesse du fluide commence à la valeur négative u_d et augmente progressivement pour atteindre zéro à la paroi du réservoir.

(2) L'épaisseur du film est corrélée positivement avec la contrainte dans la zone cédée interne. L'augmentation de la vitesse de retrait, de la contrainte seuil et de l'indice de consistance accroît la contrainte et son gradient dans la zone cédée interne, conduisant à une épaisseur de film plus importante. L'influence de l'indice d'écoulement dépend de l'amplitude du taux de cisaillement: à faible vitesse de retrait (taux de cisaillement inférieur à 1 s^{-1}), un indice d'écoulement plus élevé entraîne une contrainte dans la zone cédée interne et une épaisseur de film plus faibles; à haute vitesse de retrait (taux de cisaillement supérieur à 1 s^{-1}), l'influence de l'indice d'écoulement s'inverse.

(3) Une partie du fluide entraîné par le substrat près de la région du ménisquerefluer vers le réservoir sous l'effet du drainage gravitationnel, tandis que la partie restante participe à la formation du film. Bien que ce drainage n'affecte pas la structure de l'écoulement pleinement développé dans le réservoir, il réduit significativement l'épaisseur du film final.

(4) En se basant sur l'hypothèse d'un écoulement unidimensionnel, un modèle théorique complet pour la distribution de l'écoulement a été développé. Sur cette base, un modèle théorique de prédiction de l'épaisseur du film, prenant en compte l'effet de drainage gravitationnel, a été établi. La validation montre que le modèle proposé dans cette étude offre une précision supérieure aux modèles d'épaisseur de film existants, fournissant ainsi un outil fiable pour l'optimisation des procédés concernés.

4. Nouvelle méthode de rhéométrie par immersion dynamique

Ce chapitre se concentre sur le développement d'une nouvelle méthode de rhéométrie pour les fluides viscoplastiques, inspirée par le modèle théorique d'écoulement dans le réservoir présenté dans les chapitres précédents. Cette méthode innovante est basée sur la dynamique d'immersion. Les principales conclusions sont les suivantes:

(1) L'étude a révélé les caractéristiques d'écoulement clés lors du processus d'immersion d'une plaque rainurée, jetant les bases théoriques de la nouvelle méthode. L'analyse de l'influence des paramètres a montré qu'un rapport hauteur de rainure sur épaisseur de plaque inférieur à 2 supprime efficacement la génération d'écoulements secondaires. Le fluide à l'intérieur des rainures reste stationnaire par rapport à la plaque, tandis qu'un cisaillement significatif se produit à l'interface avec le fluide du réservoir. L'effet du glissement pariétal sur cet écoulement est négligeable, confirmant ainsi la faisabilité de mesurer la rhéologie en cisaillement pur.

(2) Une nouvelle méthode de rhéométrie basée sur l'immersion d'une plaque rainurée a été proposée, contournant efficacement les interférences dues au glissement pariétal. Contrairement aux méthodes d'immersion traditionnelles limitées à la détermination de la contrainte seuil, l'innovation majeure de cette méthode réside dans sa capacité à déterminer simultanément plusieurs paramètres rhéologiques. L'utilisation de l'interface fluide-fluide permet une mesure directe de la contrainte de cisaillement sans perturbation par le glissement pariétal, surmontant ainsi les biais de mesure inhérents aux méthodes conventionnelles. Un modèle complet d'inversion des paramètres rhéologiques a été construit, établissant une méthodologie pour extraire simultanément la contrainte seuil, l'indice de consistance et l'indice d'écoulement à partir des données d'immersion.

(3) La validité et la polyvalence de la méthode proposée ont été vérifiées par des comparaisons avec plusieurs techniques. Les résultats de la comparaison avec la méthode conventionnelle des plaques parallèles ont confirmé la précision de la nouvelle approche pour mesurer la contrainte seuil, l'indice de consistance et l'indice d'écoulement. Son application étendue à une plaque rugueuse non rainurée a démontré que la méthode est également applicable à une structure sans rainures, les valeurs

d'indice de consistance et d'indice d'écoulement obtenues étant en bon accord avec les données de la littérature. La cohérence entre les simulations numériques et le modèle analytique du champ d'écoulement renforce davantage la fiabilité du modèle théorique sous-jacent.

IV. Conclusions

Cette recherche explore systématiquement la dynamique des fluides lors du procédé de revêtement par immersion-retrait, en combinant modélisation numérique, investigations expérimentales et développement théorique. Elle révèle les mécanismes fondamentaux gouvernant le comportement des fluides newtoniens et viscoplastiques sur différents substrats (plaque plane ou fibre), et a permis de développer une série de modèles théoriques aux excellentes capacités prédictives ainsi que des méthodes innovantes de caractérisation rhéologique.

Dans l'étude des systèmes de fluides newtoniens, ce travail a établi un cadre théorique pour la distribution de l'épaisseur du film, allant de la plaque plane à la fibre. Pour la plaque parfaitement mouillante, le mécanisme de compétition entre les forces visqueuses et gravitationnelles a été clarifié, et une loi d'auto-similarité des profils de film a été découverte. Un modèle composite décrivant l'évolution spatio-temporelle du film liquide a été construit et validé sur une large plage de paramètres. Pour la fibre partiellement mouillante, l'étude a systématiquement mis en lumière le rôle régulateur du rayon de la fibre et du nombre capillaire sur la morphologie de l'interface gaz-liquide, produisant un diagramme de phase complet des morphologies interfaciales. Les conditions déclenchant les ondulations du film épais et du film de Landau-Levich ont été délimitées théoriquement, approfondissant ainsi la compréhension de la dynamique de formation des films liquides sur surfaces courbes.

Dans l'étude des systèmes de fluides viscoplastiques, cette recherche a dépassé les limitations des théories traditionnelles de formation de film et des méthodes de rhéométrie conventionnelles. Lors du retrait d'une plaque, ce travail a révélé la structure d'écoulement en trois-zones dans le réservoir, élucidé le lien complexe entre les paramètres rhéologiques et l'épaisseur du film, et a établi un modèle

de prédiction d'épaisseur de haute précision prenant en compte le drainage gravitationnel. Plus innovant encore, une nouvelle méthode de rhéométrie basée sur le processus d'immersion d'une plaque rainurée a été proposée. Cette méthode permet d'éliminer les interférences dues au glissement pariétal et réalise une détermination précise et simultanée de l'ensemble des paramètres rhéologiques pour les fluides de type Herschel-Bulkley, offrant ainsi un nouveau paradigme pour la caractérisation des fluides complexes.

Par cette investigation approfondie et multi-systèmes, cette thèse apporte des avancées significatives dans la compréhension fondamentale de la dynamique du revêtement par immersion-retrait. Elle a permis de construire des modèles théoriques plus précis et plus universels, et a développé une technique de rhéométrie innovante et applicable. Ces résultats enrichissent systématiquement le cadre théorique du domaine et possèdent des implications importantes pour les applications industrielles, notamment dans les domaines des revêtements de matériaux et de la caractérisation des fluides.

Reference

1. Ruschak KJ. Coating Flows. *Annu. Rev. Fluid Mech.* 1985;17(1):65-89.
2. Weinstein SJ. Coating Flows. *Annu. Rev. Fluid Mech.* 2004;36(1):29-53.
3. Pan W, Chen Z, Chen X, Wang F, Dai G. Slot die coating window for a uniform fuel cell ink dispersion. *AIChE J.* 2022;68(8):e17719.
4. Tjiptowidjojo K, Park J, Mauger SA, Ulsh M, Schunk PR. Process model for multilayer slide coating of polymer electrolyte membrane fuel cells. *J. Coat. Technol. Res.* 2021;19(1):73-81.
5. Uchida H, Kawauchi T, Otake G, Koyama C, Takeya K, Tripathi SR. Optical thin film coated organic nonlinear crystal for efficient terahertz wave generation. *Sci. Rep.* 2022;12(1):15082.
6. Tang Y, Guo B, Cruz MA, et al. Colorful Conductive Threads for Wearable Electronics: Transparent Cu–Ag Nanonets. *Adv. Sci.* 2022;9(24):2201111.
7. Bi L, Perry W, Wang R, et al. MXene Functionalized Kevlar Yarn via Automated, Continuous Dip Coating. *Adv. Funct. Mater.* 2023;34(14):2312434.
8. Wang J, Zheng Z, Ke Y, et al. Fluid Control of Dip Coating for Efficient Large-Area Organic Solar Cells. *Adv. Mater.* 2025;37(10):2417160.
9. Ceratti DR, Louis B, Paquez X, Faustini M, Grosso D. A New Dip Coating Method to Obtain Large-Surface Coatings with a Minimum of Solution. *Adv. Mater.* Sep 9 2015;27(34):4958-4962.
10. Bertin V, Snoeijer JH, Raphaël E, Salez T. Enhanced dip coating on a soft substrate. *Phys. Rev. Fluids.* 2022;7(10):L102002.
11. Michels JJ, Zhang K, Wucher P, Beaujuge PM, Pisula W, Marszalek T. Predictive modelling of structure formation in semiconductor films produced by meniscus-guided coating. *Nat. Mater.* 2020;20(1):68-75.

12. Sathyanath R, Aarthi A, Kalpathy SK. Features of colloidal silica deposits dip coated onto porous alumina membranes from aqueous suspensions. *Colloid Interface Sci. Commun.* 2021;45:100526.

13. Catalini G, García NA, Vega DA, Nikoubashman A. Simulations of Thin Polymer Films on Flat and Curved Substrates. *Macromolecules.* 2024;57(8):2530-2538.

14. Landau L, Levich B. Dragging of a liquid by a moving plate. *Acta Physicochim. URSS.* 1942;17(2):42-54.

15. Sathyanath R, Aarthi A, Kalpathy SK. Liquid film entrainment during dip coating on a saturated porous substrate. *Chem. Eng. Sci.* 2020;218:115552.

16. Smit WJ, Kusina C, Joanny JF, Colin A. Stress field inside the bath determines dip coating with yield-stress fluids in cylindrical geometry. *Phys. Rev. Lett.* Oct 4 2019;123(14):148002.

17. Smit WJ, Kusina C, Colin A, Joanny J-F. Withdrawal and dip coating of an object from a yield-stress reservoir. *Phys. Rev. Fluids.* 2021;6(6):063302.

18. Liu X, Danglad-Flores J, Eickelmann S, et al. Controlled-Alignment Patterns of Dipeptide Micro- and Nanofibers. *ACS Nano.* 2022;16(7):10372-10382.

19. Jeong D-H, Xing L, Lee MKH, Vani N, Sauret A. Deposition and alignment of fiber suspensions by dip coating. *J. Colloid Interface Sci.* 2023;650:407-415.

20. Gans A, Dressaire E, Colnet B, Saingier G, Bazant MZ, Sauret A. Dip-coating of suspensions. *Soft Matter.* Jan 2 2019;15(2):252-261.

21. Jeong D-H, Lee MKH, Thiévenaz V, Bazant MZ, Sauret A. Dip coating of bidisperse particulate suspensions. *J. Fluid Mech.* 2022;936:A36.

1 Introduction

1.1 Research background

Coating is a surface engineering technique that involves depositing a coating layer onto substrates to enhance their performance characteristics or prolong their service life. As reviewed by Ruschak (1985)[1] and Weinstein *et al.* (2004)[2], coating could be classified as pre-metered coating and self-metered coating. In pre-metered coating, the thickness of the coated layer is directly determined by the imposed flow rate. Pre-metered coating, including slot coating[3] and slide coating[4], requires controlled liquid delivery system and precise lateral distribution of the liquid. In self-metered coating, however, the thickness of the coated layer is determined simultaneously by the liquid properties, substrate velocity, and the geometry of the equipment. Dip coating, as a classical self-metered coating method, has emerged as particularly noteworthy due to its superior scalability and high flexibility, leading to widespread adoption in industrial contexts. For example, it has been used for performing the anti-reflecting film onto wave-generating crystal[5], the conductive film onto fibres[6,7], and the large-area organic solar cells[8]. Dip coating is sufficiently flexible to coat different substrates (plate or cylinder,[7,9] solid, soft or even porous substrate,[10-12] flat or curved substrate[8,13]) with fluids of various rheological properties (Newtonian fluids,[11,14,15] viscoplastic fluids[16,17] and suspensions[18-21]).

The dip coating process consists of two technical stages: the immersion of a substrate into a liquid and then its withdrawal from the liquid. (1) Immersion: The substrate is immersed into the coating solution at a constant velocity, possibly followed by a predetermined dwell time to completely wet the substrate. (2) Withdrawal: A layer of coating liquid is entrained by and deposited on the substrate by withdrawing the substrate from the liquid. The withdrawal velocity is typically constant to yield uniform films. However, some studies[22] have demonstrated that dip coating in acceleration mode enables the fabrication of films with controlled thickness gradients, thereby achieving functionality gradients. The liquid film is then cured into a solid coating by heat treatment.

1.2 Research significance

As illustrated in Figure 1.1, the thickness of the liquid film governs the mechanical and functional performance of the final cured film. Excessive thickness induces internal stress, leading to delamination or cracking; while insufficient thickness fails to provide adequate reinforcement. For optical coatings, thickness dictates light interference effects, directly influencing transmittance, reflectance, and chromaticity. An archetypal example is the anti-reflection film, which thickness should be controlled to one-quarter of the incident light wavelength to achieve optimal anti-reflective performance.

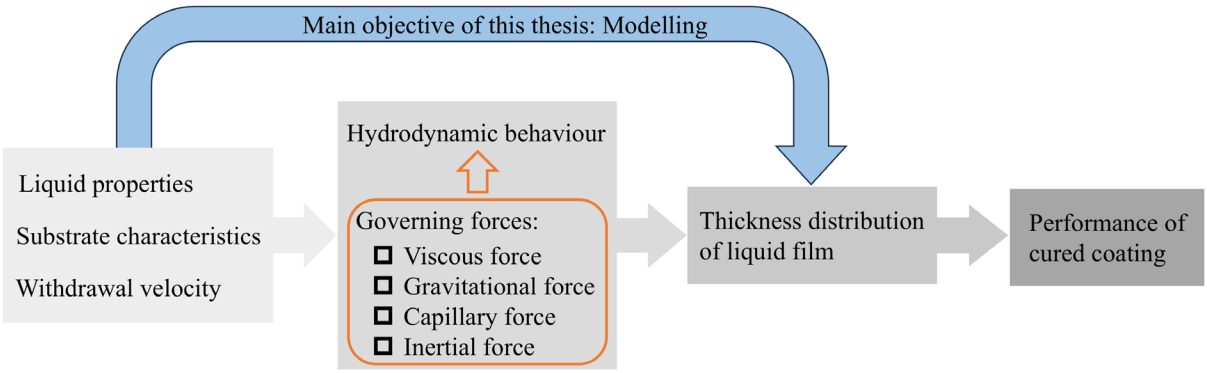

Figure 1.1. Schematic of the key factors influencing the thickness distribution of liquid film which directly determines the performance of the final cured coating.

The fundamental relationship between the film thickness and properties of the solid coating underlines the paramount importance of precise film thickness prediction and control. The thickness distribution of the film is predominantly determined by the hydrodynamic behaviour during the withdrawal process. The hydrodynamic behaviour arises from the intricate interplay of viscous, gravitational, capillary, and even inertial forces. These governing forces are primarily determined by three key factors:

(1) Coating liquid properties

The diverse spectrum of coating liquids exhibits complex rheological behaviours, ranging from pure Newtonian to viscoplastic behaviours, each requiring specific constitutive equation for accurate characterization.

(2) Substrate Characteristics

Geometric configuration: Laplace pressure varies significantly with surface curvature profiles. For instance, planar substrates exhibit unidirectional curvature along the withdrawal direction, while cylindrical geometries demonstrate bi-directional curvature (axial and radial) and thus bi-directional capillary pressure.

Surface wettability: The wettability of the substrate surface alters the liquid-air contact angle, thereby affecting the liquid film thickness. On partially wetting surfaces, the three-phase contact line may slide relative to the substrate, resulting in more complex liquid film morphology.

(3) Withdrawal velocity

The withdrawal velocity not only quantitatively alters the film thickness but also shifts the governing forces. Inertial effects may become non-negligible at high withdrawal velocity, introducing strong nonlinearity into the momentum conservation equation that significantly complicates their resolution.

1.3 Research objectives

As shown in Figure 1.1, the main objective of this thesis is to develop the model linking the film thickness to the liquid properties, substrate characteristics and withdrawal velocity, according to the hydrodynamics and film formation mechanisms. Since different liquid-substrate systems and withdrawal velocities exhibit distinct film formation mechanisms, differentiated studies are required for various scenarios to develop individual thickness models. This research follows a progressive approach from fundamental to complex scenarios. For the substrate, we first consider a completely wetting plate before extending the study to partially wetting cylinder. In parallel, we progress from a

Newtonian to a viscoplastic liquid. Additionally, we propose a new rheometric method to characterize viscoplastic fluids, based on the plate immersion process.

The thesis comprises eight chapters, organized as follows:

Chapter 1 Introduction

It provides the research background, significance, objectives, and overall framework.

Chapter 2 Literature review and state of the art

This chapter reviews the research methods through three main approaches: experiments, direct numerical simulations, and theoretical studies. It summarizes the research on the dynamics in dip coating processes of complex fluids, clearly identifying the current shortcomings in film formation theories. Furthermore, it discusses new applications of dip coating, with particular focus on analysing the problems encountered in rheometric application.

Chapter 3 Methodology of direct numerical simulation

The Volume of Fluid (VOF) method implemented in ANSYS Fluent is used as the principal method to simulate directly the dip coating process. This chapter specifies the governing equations and the numerical schemes including the discretization schemes and convergence criteria.

Chapter 4 Spatial-temporal evolution of a Newtonian liquid layer on a fully wetting plate during dip coating

Through parametric studies, this chapter elucidates key factors controlling the film formation of Newtonian fluids on completely wetting plate at high capillary number. The investigation reveals the characteristics of the spatial-temporal evolution of film thickness and establishes a predictive model for thickness distribution. Model validation confirms its quantitative accuracy as well as the upper limit of the withdrawal velocity.

Chapter 5 Film deposition of Newtonian fluids on a partially wetting cylinder upon dip coating

In this chapter, we investigate the wetting and deposition of a Newtonian liquid on a partially wetting cylinder in dip coating through direct numerical simulation and lubrication theory. We demonstrate the complete transition of liquid-air interfacial morphology in the presence of a moving contact line. The different interfacial morphologies and the critical conditions between different scenarios are analysed theoretically and compared with direct numerical simulations.

Chapter 6 Hydrodynamics of viscoplastic fluids upon dip coating of a fully wetting plate

By direct numerical simulation, the hydrodynamics of viscoplastic fluids upon dip coating is investigated. We systematically analyse the effect of yield stress, flow index, and consistency factor on both the flow (i.e., distribution of flow regime, velocity, and stress) in the container and the film thickness. Building upon these analyses, we develop theoretical models to predict the flow in the container and the film thickness. The model validity is rigorously verified through comprehensive comparisons with direct numerical simulation.

Chapter 7 Hydrodynamics and rheological characterization upon the immersion process of a slotted plate into viscoplastic fluids

We develop a novel rheometric method for viscoplastic fluids based on the plate immersion process. A new rheometric platform is constructed with specially designed slotted plates for this innovative approach. The forces and flow characteristics during the entire immersion process are thoroughly analysed to provide theoretical foundations for the methodology. The robustness of this new method is validated through comparisons with literature and conventional measurement techniques.

Chapter 8 Summary and perspectives

This chapter synthesizes the principal conclusions of the thesis and proposes potential directions for further research.

Reference

1. Ruschak KJ. Coating Flows. *Annu. Rev. Fluid Mech.* 1985;17(1):65-89.
2. Weinstein SJ. Coating Flows. *Annu. Rev. Fluid Mech.* 2004;36(1):29-53.
3. Pan W, Chen Z, Chen X, Wang F, Dai G. Slot die coating window for a uniform fuel cell ink dispersion. *AIChE J.* 2022;68(8):e17719.
4. Tjiptowidjojo K, Park J, Mauger SA, Ulsh M, Schunk PR. Process model for multilayer slide coating of polymer electrolyte membrane fuel cells. *J. Coat. Technol. Res.* 2021;19(1):73-81.
5. Uchida H, Kawauchi T, Otake G, Koyama C, Takeya K, Tripathi SR. Optical thin film coated organic nonlinear crystal for efficient terahertz wave generation. *Sci. Rep.* 2022;12(1):15082.
6. Tang Y, Guo B, Cruz MA, et al. Colorful Conductive Threads for Wearable Electronics: Transparent Cu–Ag Nanonets. *Adv. Sci.* 2022;9(24):2201111.
7. Bi L, Perry W, Wang R, et al. MXene Functionalized Kevlar Yarn via Automated, Continuous Dip Coating. *Adv. Funct. Mater.* 2023;34(14):2312434.
8. Wang J, Zheng Z, Ke Y, et al. Fluid Control of Dip Coating for Efficient Large-Area Organic Solar Cells. *Adv. Mater.* 2025;37(10):2417160.
9. Ceratti DR, Louis B, Paquez X, Faustini M, Grosso D. A New Dip Coating Method to Obtain Large-Surface Coatings with a Minimum of Solution. *Adv. Mater.* Sep 9 2015;27(34):4958-4962.
10. Bertin V, Snoeijer JH, Raphaël E, Salez T. Enhanced dip coating on a soft substrate. *Phys. Rev. Fluids.* 2022;7(10):L102002.
11. Michels JJ, Zhang K, Wucher P, Beaujuge PM, Pisula W, Marszalek T. Predictive modelling of structure formation in semiconductor films produced by meniscus-guided coating. *Nat. Mater.* 2020;20(1):68-75.
12. Sathyanath R, Aarthi A, Kalpathy SK. Features of colloidal silica deposits dip coated onto porous alumina membranes from aqueous suspensions. *Colloid Interface Sci. Commun.* 2021;45:100526.
13. Catalini G, García NA, Vega DA, Nikoubashman A. Simulations of Thin Polymer Films on Flat and Curved Substrates. *Macromolecules.* 2024;57(8):2530-2538.
14. Landau L, Levich B. Dragging of a liquid by a moving plate. *Acta Physicochim. URSS.* 1942;17(2):42-54.
15. Sathyanath R, Aarthi A, Kalpathy SK. Liquid film entrainment during dip coating on a saturated porous substrate. *Chem. Eng. Sci.* 2020;218:115552.
16. Smit WJ, Kusina C, Joanny JF, Colin A. Stress field inside the bath determines dip coating with yield-stress fluids in cylindrical geometry. *Phys. Rev. Lett.* Oct 4 2019;123(14):148002.
17. Smit WJ, Kusina C, Colin A, Joanny J-F. Withdrawal and dip coating of an object from a yield-stress reservoir. *Phys. Rev. Fluids.* 2021;6(6):063302.
18. Liu X, Danglad-Flores J, Eickelmann S, et al. Controlled-Alignment Patterns of Dipeptide Micro- and Nanofibers. *ACS Nano.* 2022;16(7):10372-10382.
19. Jeong D-H, Xing L, Lee MKH, Vani N, Sauret A. Deposition and alignment of fiber suspensions by dip coating. *J. Colloid Interface Sci.* 2023;650:407-415.
20. Gans A, Dressaire E, Colnet B, Saingier G, Bazant MZ, Sauret A. Dip-coating of suspensions. *Soft Matter.* Jan 2 2019;15(2):252-261.
21. Jeong D-H, Lee MKH, Thiévenaz V, Bazant MZ, Sauret A. Dip coating of bidisperse particulate suspensions. *J. Fluid Mech.* 2022;936:A36.
22. Faustini M, Ceratti DR, Louis B, et al. Engineering functionality gradients by dip coating process in acceleration mode. *ACS Appl. Mater. Interfaces.* Oct 8 2014;6(19):17102-17110.

2 Literature review and state of the art

2.1 Research method

In this chapter, we present a synthetic view of the research methods on dip coating from three different perspectives: experimental techniques, direct numerical simulation, and theoretical analysis.

2.1.1 Experimental techniques

2.1.1.1 Dip coating device

Two main types of dip coating devices exist in experimental investigations: the intermittent type and the continuous type. The intermittent device is suitable for rigid substrates, while the continuous one is generally used for soft substrates. The immersion and withdrawal processes of intermittent device are carried out sequentially in separate steps. As illustrated in Figure 2.1, the intermittent devices may be further subclassified into two types: a substrate-moving type[1] and container-moving type[2]. In the substrate-moving type, the container remains stationary while the substrate is vertically displaced by a stepper motor. Conversely, in the container-moving type, the relative displacement between the substrate and the solution is realized by controlling the motion of the container. This latter type minimizes substrate perturbations that could affect the thickness of the coating film.[2,3] However, it faces challenges in large-scale industrial applications due to the difficulty in precisely controlling the motion of large and heavy containers.

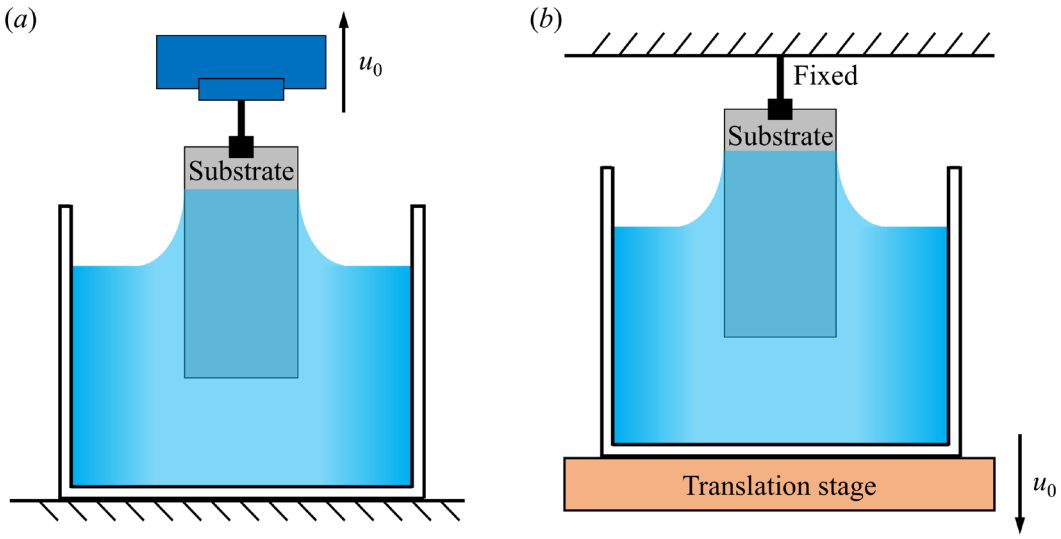

Figure 2.1. Schematic of substrate-moving type (*a*) and container-moving type (*b*) dip coating devices.

According to the authors' best knowledge, the continuous type devices cover linear dip coating device[4-6] and cyclic dip coating device[7,8] (see Figure 2.2). In this type device, the immersion and withdrawal processes are carried out simultaneously. The linear dip coating device, as shown in Figure 2.2 (*a*), consists of several rollers: the driving roller, the immersion roller, the guide roller, and the unwinding roller. The substrate is motioned unidirectionally from the unwinding roller to the driving roller. Figure 2.2(*a*) is a schematic diagram showing only one immersion roller. In practice, the number of immersion rollers can be increased to extend the immersion time (residence time) of the substrate in the liquid. In addition, Van Rossum (1958)[7] and numerous subsequent researchers[8-10] developed a cyclic dip coating device (cf. Figure 2.2*b*) employing a two-roller configuration. Either roller can function as the driving roller in the system. With its straightforward design and convenient substrate-swapping capability, this last device is predominantly used in laboratory research but finds limited application in industrial-scale manufacturing.

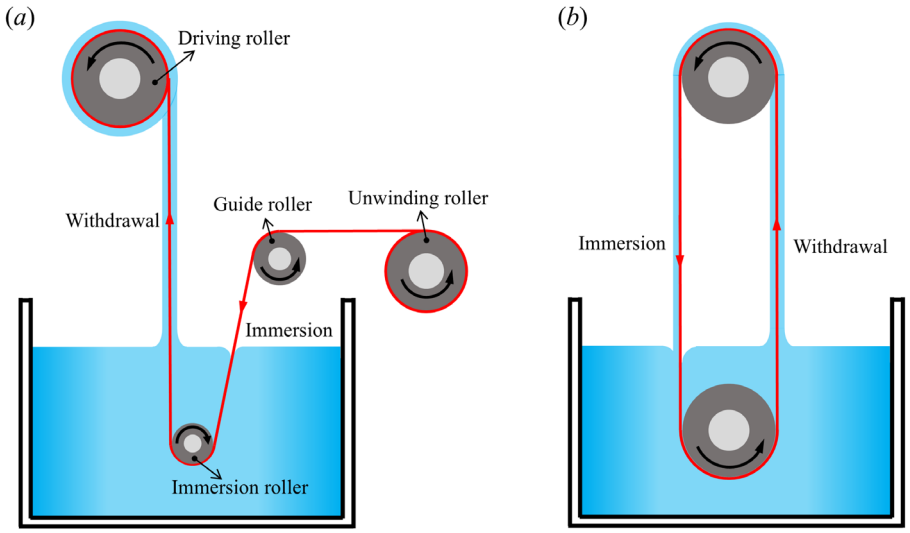

Figure 2.2. Schematic of linear (*a*) and cyclic (*b*) dip coating devices.

2.1.1.2 Film thickness measurement technique

A synthetic view of film thickness measurement techniques was previously provided by Rio *et al.* (2017).[11] We critically revisit their views and give additional perspectives in this chapter. The techniques are summarized in Table 2.1.

Table 2.1 Experimental techniques used to measure the film thickness.

Film thickness	Techniques	Plate	Fiber
Average	Gravimetric method	2,7,12-19	1,20-25
	Volumetric variation		26,27
Local	Micrometrw screw gauge	7-9,28	
	Capacitance	10,29,30	
	Multi-wavelength light	31-33	
Profile	Monochromatic light	34	
	Optical distortion	31,35	
	Photographic method	7,34,36-39	1

Probably as the simplest and most ancient method to measure the film thickness h, the gravimetric method has been used for non-volatile liquids in many studies.[1,2,7,12-22,24,25,40] This method determines the film thickness through gravimetric analysis, either by measuring the absolute weight[1,2,13,17-19,21,22,24,25,40] of the film or by quantifying the mass variation of the coating liquid in the container[7,12,14-16,20]. The gravimetric method exhibits two inherent limitations. First, this method yields an average film thickness, necessitating prior verification of thickness uniformity. Specifically, when measuring liquid film mass at varying immersion depths, a linear proportionality between mass and depth confirms adequate uniformity for gravimetric application; deviation from this relationship invalidates the method.[1] Second, the method proves unsuitable for intermittent type dip device with highly viscous liquid, where irreproducible rupture of liquid occurs at the lower edge of the substrate and the determination of the weight of film is very uncertain.[7] Carroll *et al.* (1973)[26] and Quéré *et al.* (1989)[27] developed a modified gravimetric method to measure the film thickness on fiber surfaces. More

precisely, the film thickness was derived by monitoring volumetric variation of the liquid in the container.

The local film thickness could be measured by different methods. In pioneering studies, the micrometre screw gauge with a needle attached was used to measure the local film thickness. The key to this technique is the determination of the point of contact between the needle and the film, which is generally determined visual observation[7-9,28]. For conductive liquid, the screw could be connected to a galvanometer. Once the needle contacts the surface of the conductive film, the circuit forms a closed loop and the galvanometer produces a reading.[8] Finally, the film thickness is exactly the difference between the initial needle-substrate distance and the displacement of the needle. However, the contact of the screw with the liquid may affect the film thickness. Some studies have used the capacitance method to achieve contactless measurement of film thickness.[10,29,30] The film thickness is measured by two non-contact capacitive probes located on both sides of the substrate. The probes measure the air gap on both sides of the substrate, from which the film thickness can be easily calculated. In addition to the advantages of contactless measurement, the capacitance method eliminates errors due to the possible small lateral movements of the substrate.[10] The other non-contact method is multi-wavelength light spectrometry.[31-33] The film thickness was determined by spectroscopic analysis of multi-wavelength light interference patterns reflected from the film surface (see details in ref. [31]).

In some situations, we attempt to capture the profile of the film thickness. One of the feasible techniques is to use a laser beam for monochromatic light interferometry.[34] The monochromatic light is split by a beamsplitter into two beams: one directed toward the film, and the other toward a reference mirror. The light reflected from the film and the light returned from the reference mirror recombine at the beamsplitter, generating an interference pattern consisting of the bright and fringes. The film thickness is precisely calculated by fitting the interference pattern to a theoretical model. More precisely, the fringes are counted starting from the tip of film downwards. In the regions where the film thickness is greater than one-quarter of the wavelength, the film thickness can be determined by

the following equation: $h = (\chi_1 \lambda_w/4)(\chi_2^2 - \sin^2 \theta_i)^{-1/2}$, where χ_1 is the number of fringes, λ_w is the wavelength of the light incident on the film, $\chi_2$is the refractive index of the liquid, and θ_i is the incident angle of the light on the film.. For regions where the film thickness is less than one-quarter of the wavelength (usually the head region of the film), the intensity of the reflected light is converted to the film thickness using an air-liquid-solid three-layer optical model. Before using monochromatic light interferometry, we must pre-estimate whether the film thickness exceeds one-quarter of wavelength, in order to choose the correct method of calculating the film thickness. To circumvent fringe counting and film thickness pre-estimation, Snoeijer *et al.* (2006, 2008)[31,35] developed an optical distortion method. A wire aligned parallel to the substrate is positioned between the film and the camera, enabling simultaneous capture of both the wire and its reflection at the film surface. The distribution of the film is subsequently derived through optical geometric analysis on the deformation of the reflection of the wire. A more direct method is the photographic method.[7,34,36-39] One could use objects of known dimensions (say, the thickness of the plate or the radius of the cylinder) as reference to measure the distribution of film thickness along the substrate from the photos.[39]

2.1.2 Computational fluid dynamics

Computational fluid dynamics methodologies can be systematically categorized into three distinct approaches: macroscopic, mesoscopic, and microscopic approaches. The macroscopic framework is established upon the Navier-Stokes equations under the continuum assumption, while the mesoscopic approach is founded on kinetic theory-based statistical mechanics, and the microscopic method employs molecular dynamics theory. This chapter focuses on giving a synthetic view of different macroscopic methods, and is not intended to be comprehensive. It should be explicitly noted that the scope of this work does not encompass mesoscale approaches such as the Lattice Boltzmann Method nor microscopic approaches including molecular dynamics simulations. The macroscopic approach can be further subdivided into interface tracking method and interface capture method:

1. Interface tracking method

The interface tracking method, which includes the boundary-fitted mesh method and the arbitrary Lagrangian-Eulerian method, traces the phase interface through the mesh boundary, which is a discontinuous interface with no thickness. As the phase interface deforms, the mesh undergoes deformation or reconstruction, leading to additional computational overhead. This approach struggles to handle topological changes such as droplet breakup or coalescence.

(1) Boundary-fitted mesh method

This method employs a computational mesh that dynamically deforms to precisely align with the evolving fluid interface, maintaining explicit interface representation through mesh node coordinates. This approach offers high interface resolution and accurate surface tension calculation through direct boundary condition application, making it particularly efficient for steady-state problems with smooth interface deformation.

(2) Arbitrary Lagrangian-Eulerian (ALE) method

The Arbitrary Lagrangian-Eulerian (ALE) method represents a hybrid computational approach that combines Lagrangian and Eulerian frameworks. This method requires the introduction of a reference domain and the establishment of mapping relationships between physical and spatial domains. Within the Arbitrary Lagrangian-Eulerian (ALE) framework, the computational mesh exhibits unique kinematic characteristics: the mesh does not remain fixed in the laboratory reference frame like in traditional Eulerian methods, nor does it strictly adhere to the Lagrangian approach where meshes are bound to fluid material points. Instead, it enables autonomous and controllable motion within the computational domain. By precisely governing the mesh motion, this method achieves highly accurate tracking of interfaces while effectively preventing mesh distortion caused by large deformations during computation.

2. Interface capturing method

This Interface capturing method allows the mixing of different phases at the interface which is treated as a region with a very small thickness. The distribution of the phases and the location of the

interface are determined by an interface function. The mesh remains unchanged throughout the calculation and does not deform with the interface motion. There are three widely used interface capturing methods:

(1) Volume of Fluid method

The Volume of Fluid method adopts the volume fraction to distinguish different phases and the interface between phases. This method solves a phase advection equation to capture interface evolution and utilizes geometric reconstruction techniques to determine interface orientation. The VOF method offers several significant advantages, including strict mass conservation and robust handling of complex topological changes.

(2) Level set method

The Level set (LS) method uses the signed distance function to implicitly represent the different phases and their interface. The interface is advanced by solving a transport equation for this function, with periodic reinitialization required to maintain a unit gradient magnitude across the computational domain.

(3) Phase field method

The Phase field method uses phase field variable (typically varying between -1 and +1 for distinct phases) to describe the different phases and the interface. This method solves the Cahn-Hilliard equation which describes the advection and diffusion of the variable to determine its distribution and accordingly capture the position of the interface.

2.2 Dip coating of Newtonian fluids

Landau and Levich[41] (LL) conducted groundbreaking research on the dip coating process where a plate is withdrawn at a velocity u_0 from a Newtonian fluid with a density ρ_L, a viscosity η_L and a surface tension σ. They subdivided the film into three sub-regions: (1) a region of constant film thickness, (2) the dynamic meniscus region, and (3) the static meniscus region (Figure 2.3). In the

constant-thickness film region, the curvature of the liquid-air interface is vanishing, thus the capillary force is negligible and the flow is controlled by viscous and gravitational forces. In the static meniscus, the flow is neglected and only capillary and gravitational forces are considered. The dynamic meniscus is the transition region between the constant-thickness film and the static meniscus regions, where the flow is affected by viscous, gravitational and capillary forces. Such a division of the regions allowed Landau and Levich to elucidate quantitatively the relationship between the constant film thickness h_0, the capillary length l_c (defined as $l_c = \sigma/(\rho_L g)$) and the capillary number Ca (defined as $\eta_L u_0/\sigma$):

$$h_0 = 0.946 l_c Ca^{2/3}. \tag{2.1}$$

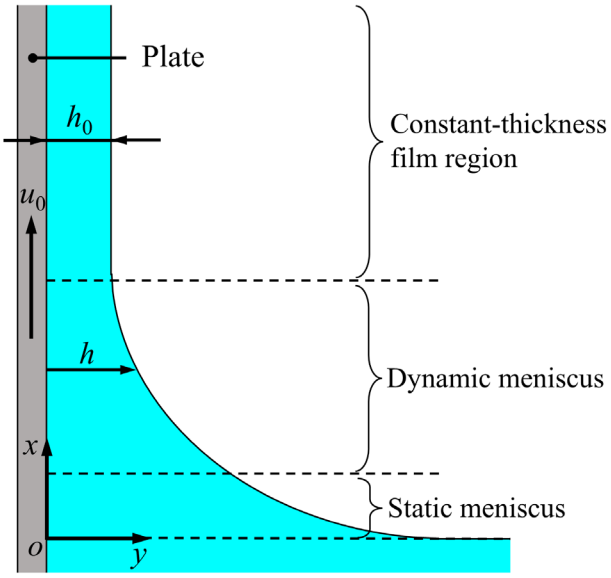

Figure 2.3. Schematic of the different liquid film regions in dip coating according to Landau and Levich. (1) constant-thickness film region, (2) dynamic meniscus, and (3) static meniscus.

It is noteworthy that the LL theory (2.1) has been shown by many studies to be only valid for $Ca < 0.01$ (visco-capillary regime), since this model does not consider the effect of gravitational force.[3,10,42] For $Ca > 0.01$, the effect of gravitational force becomes significant (visco-capillary-gravity regime), so that the LL theory predicts a thicker film than in the experiments. Many researchers extended the LL theory by including the effect of gravitational force in their theories using different

methods.[10,43,44] Among these, Wilson (1982)[44] proposed a concise model through a matched expansion method:

$$h_0 = 0.946 l_c Ca^{2/3} - 0.107 l_c Ca. \quad (2.2)$$

This model (2.2) predicts well the film thickness for $Ca < 0.4$.[45]

The further increase in Ca ($Ca > 1$, visco-gravity) leads the gravitational force to overcome the capillary force, so that the film thickness is determined by the equilibrium between the viscous and gravitational forces, that is $\eta_L u_0/h_0 \sim \rho_L g h_0$ with g the gravitational acceleration. Therefore, the film thickness is obtained as:

$$h_0 \sim l_c Ca^{1/2}, \text{ or equivalently } h_0 = A_S l_c Ca^{1/2}, \quad (2.3)$$

where parameter A_S is a scaling factor. Derjaguin (1943)[46] and Peralta *et al.* (2014)[47,48], assumed the flow in the film to be one-dimensional and derived theoretically the film thickness as $h_0 = l_c Ca^{1/2}$ (i.e., $A_S = 1$). Tuck (1983)[49] also obtained a theoretical A_S of 1 by the mean of perturbation. However, these models actually represent the upper limit of film thickness, which is often over-predicted.[45,50] Different studies have presented various values of A_S. Benilov *et al.* (2008) determined A_S as 0.7 by finite element simulation,[50] while the finite volume simulation of Filali *et al.* (2013) gave a scaling factor A_S of 0.66.[51] In terms of theoretical analysis, the theories of Kheshgi *et al.* (1992)[52] and Baikov *et al.* (2019)[42] yielded scaling factors of 0.61 and 0.79, respectively. In terms of experimental investigation, A_S ranges from 0.56 to 0.82.[10,53] To be concluded, the reported scaling factors range from 0.56 to 1 (summarized in Table 2.2). For accurate film thickness prediction under different operating conditions and fluid properties, the appropriate theory must be carefully selected among visco-capillary regime, visco-capillary-gravity regime, and visco-gravity regime.

Table 2.2 Various values of scaling factor A in literature by different methods.

Method	Literature	Value of A_S
Theoretical analysis	[52]	0.61
	[42]	0.79

	[46-49]	1
Direct numerical simulation	[45]	0.64
	[51]	0.66
	[50]	0.7
Experimental investigation	[53]	0.56
	[28]	0.67
	[10]	0.82

2.3 Key factors affecting dip coating

The properties of the substrate and the liquid significantly influence the dip coating process, and will be the focus of the following discussion. Other phenomena such as Marangoni effects induced by surfactants[12,22,24,54-62] or by temperature gradient along the substrate[63], evaporation effects[64,65], and confinement effects[52,66], will not be addressed here, as detailed studies can be found in the literature.

2.3.1 Substrate characteristics

2.3.1.1 Substrate geometry

Section 2.2 describes the dip coating of a plate, however curved substrates are often involved in industry. Cylinders, as a typical and commonly used curved substrate, have been extensively studied. For dip coating of cylinders, the liquid-air interface has two principal curvatures in the withdrawal direction and the radial direction, and is thus subject to capillary pressures in both directions. There are three different scenarios: (1) small cylinder radius r_0 ($r_0/l_c \ll 1$), (2) large cylinder radius ($r_0/l_c \gg 1$), and (3) the cylinder radius and capillary length are comparable ($r_0/l_c \sim 1$). For small cylinder radius ($r_0/l_c \ll 1$), the curvature of the liquid-air interface in the withdrawal direction (which is approximated as $1/l_c$) is negligible comparing to that in the radial direction. Derjaguin 1963[67] treated the radial curvature as $1/r_0$ and modified the Landau and Levich theory[41] to apply it to cylindrical dip coating:

$$h_0 = 1.34 r_0 Ca^{2/3}. \tag{2.4}$$

This theory shows that the film thickness, for small cylinder radius, is independent of the capillary length and affected instead by the capillary number and cylinder radius. Due to the simplification of

the radial curvature, the experimental comparison by Zhang *et al.* (2022)[1] shows that the theory (2.4) is invalid when $Ca > 0.02$ even for small cylinder radius. White and Tallmadge (1966)[20] improved the radial curvature expression from $1/r_0$ to $1/(r_0+h_0)$, modifying equation (2.4) into the following form:

$$h_0 = \frac{1.33 r_0 Ca^{2/3}}{1\text{-}1.33 r_0 Ca^{2/3}}. \tag{2.5}$$

De Ryck and Quéré (1996) evidenced that this expression (2.5) provided a good prediction of film thickness for $Ca < 0.64$.[25]

For large cylinder radius ($r_0/l_c \gg 1$), the radial curvature is negligible and thus the cylinder reduces to plate. The dip coating in this situation is governed by the mechanism discussed in section 2.2.

If the ratio of the cylinder radius to the capillary length approaches 1 ($r_0/l_c \sim 1$), the curvatures in withdrawal and radial directions become comparable, and the film thickness is determined jointly by Ca, l_c and r_0. White and Tallmadge (1966)[20] derived an analytical model of film thickness by matching approach for this case. This model was verified for all radii tested and for a range of capillary numbers, showing significant deviations for $Ca > 0.03$. Later, White and Tallmadge (1967)[43] incorporated a gravity correction into their previous model, and the revised model holds for $Ca < 0.3$ and all radii tested. Wilson (1988)[68] argued that the theory of White and Tallmadge (1967)[43] contained both errors and unnecessary complexity and hence proposed a more concise analytical model. Wilson's model did not demonstrate superior agreement with experimental results, yet it offers distinct advantages in terms of mathematical rigor and practical applicability. Recently, Zhang *et al.* (2022) developed a lubrication equation maintaining the full nonlinear capillary pressure term. The numerical solution of their lubrication theory was verified to apply for all Ca up to 1.

2.3.1.2 Wetting properties

The studies referred before in sections 2.2 and 2.3.1.1 assumed the plate was completely wetted by the liquid and there was thus no three-phase contact line. In some natural phenomena and

experiments[69,70] however, the surface is partially wetted by the liquid. Owing to the existence of contact line, the surface can only be wetted when the capillary number Ca is beyond the critical value $Ca_{c,1}$.[71,72] Below this critical capillary number $Ca_{c,1}$, the liquid-air interface is raised by the plate and evolves into a stationary meniscus, there is thus no film deposited on the plate. It has been a big challenge to solve theoretically the dynamics of the contact line, due to the stress singularities on this line.[73-75] An effective theoretical approach is to introduce the Navier slip model to eliminate the singularities.[76] Within the framework of lubrication theory allowing for slipping, Eggers (2004, 2005)[77,78] and Chan *et al*. (2011, 2012)[79,80] obtained the analytical expression describing how the vertical height y_{cl} of the contact line and the apparent contact angle θ_{ap} evolves with the capillary number:

$$\frac{y_{cl}}{l_c} = \sqrt{2\left(1-\sin\theta_{ap}\right)}, \tag{2.6}$$

$$\frac{\theta_{ap}}{\theta_e} = -\frac{2^{2/3}(3Ca)^{1/3}Ai'(s_1)}{Ai(s_1)}, \tag{2.7}$$

where θ_e is the equilibrium contact angle and Ai is the Airy function[81]. The value of s_1 is determined by matching the inner and outer solutions of a nonlinear equation.[79,80] Furthermore, they suggested that the wetting transition occurs at $\theta_{ap} = 0$. Accordingly, the critical height $y_{cl,c}$ of contact line and the critical capillary number $Ca_{c,1}$ are respectively:

$$y_{cl,c} = \sqrt{2}l_c, \tag{2.8}$$

$$Ca_{c,1} = \frac{\theta_e^3}{9}\left[\ln\left(\frac{\left(3Ca_{c,1}\right)^{1/3}\theta_e}{2^{5/6}\times 3\pi Ai_{\max}^2\lambda}\right)\right]^{-1}, \tag{2.9}$$

where $Ai_{\max} = 0.53565$ is the maximum of the Airy function and λ is the Navier slip length[76].

In fact, as demonstrated by Snoeijer *et al*. (2007), the critical capillary number is associated with the saddle-node bifurcation of the stable and unstable meniscus solutions.[82] The solution revealed by Eggers (2004, 2005)[77,78] and Chan *et al*. (2011)[79] is only the stable branch of the complete family of

solutions. The unstable solution exhibits a series of bifurcations, with the capillary number oscillating around a capillary number Ca^* ($< Ca_{c,1}$).

After the wetting transition ($Ca > Ca_{c,1}$), the morphology of the entrained film is rather complicated due to the contact line motion. On the one hand, the contact line adjacent to the margins of the plate is inclined and stationary. Accordingly, only the central part of the plate is wetted and the margins keep dry.[35,83,84] On the other hand, the structure of the film evolves with the capillary number. As shown by the experiments of Snoeijer *et al*. (2006, 2008), a thick film exists at the region below the contact line, which thickness h_T deviates from the LL theory ($h_T \propto Ca^{2/3}$) and scales instead as $h_T \propto \Delta Ca_{cl}^{1/2}$ where ΔCa_{cl} is the withdrawal velocity relatively to the contact line.[31,35] The thick film either connects to the container through a dimple[31] or connects to the LL film through a travelling capillary ridge,[35] depending on the capillary number. Based on the lubrication theory and the diffuse-interface simulation, Gao *et al.* (2016) obtained a complete scenario of the wetting and film deposition.[85] Specifically, as the capillary number increases, there are four successive scenarios: (I) for $Ca < Ca_{c,1}$, a stationary meniscus, (II) for $Ca_{c,1} < Ca < Ca_{c,2}$, a thick film connected to the liquid container through a stationary dimple, (III) for $Ca_{c,2} < Ca < Ca_{c,3}$, a thick film connected to the LL film through a travelling capillary ridge and (IV) for $Ca > Ca_{c,3}$, a monotonic film. Interestingly, their numerical solution demonstrated that the existence of the critical capillary number $Ca_{c,2}$ between scenarios II and III was also due to a saddle-node bifurcation of stable and unstable solutions.

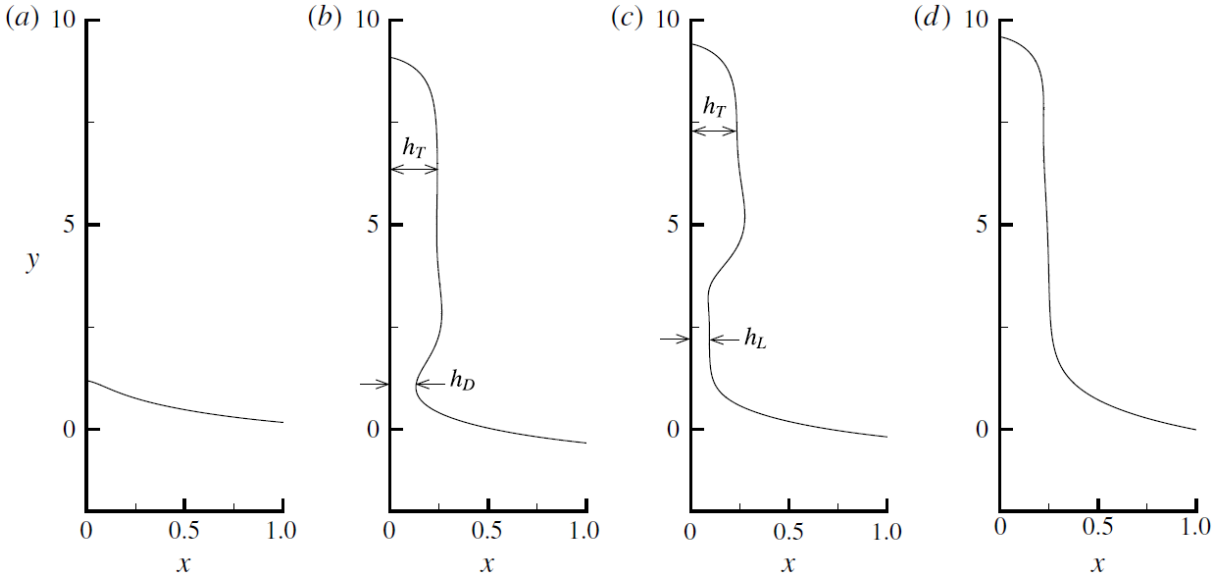

Figure 2.4. Interfacial morphologies in dimensionless scale for typical values of *Ca*. (*a*) Scenario I: *Ca* = 0.024, a stationary meniscus. (*b*) Scenario II: *Ca* = 0.028, a thick film connected to the liquid container through a stationary dimple. (*c*) Scenario III: *Ca* = 0.035, a thick film connected to the LL film through a travelling capillary ridge. (*d*) Scenario IV: *Ca* = 0.17, a film with monotonic thickness. The film solutions in (*b-d*) are snapshots at t = 1100, 603 and 63, respectively. The lengths are scaled by l_c and the time is scaled by $\eta_L l_c/\sigma$. Source: The figure is extracted from reference[85].

2.3.2 Rheological properties of liquid

The rheological properties of liquid directly affect the stress and accordingly the dynamics of dip coating. We have reviewed past studies on Newtonian fluids in sections 2.2 and 2.3.1. In the industry, however, some liquids may exhibit various non-Newtonian behaviours, including shear-thinning[86], viscoplastic[87], and viscoelastic[88]. In this thesis, we have not considered the effect of fluid elasticity, so that we focus next on the dip coating of shear thinning and viscoplastic fluids. However, some articles on dip coating of viscoelastic fluid can be found in the literature[40,76,89-91].

2.3.2.1 Shear-thinning fluid

Shear thinning is usually caused by disruption of the internal structure of the fluid. Taking polymer melts and concentrated solutions as examples, their internal structure is disordered with entangled polymer chains. At low shear rates, the rate of disentanglement roughly equals the rate of

entanglement, maintaining a dynamic equilibrium in the number of entanglement junctions, and thus the viscosity remains constant. This region is defined as the first Newtonian plateau, and the viscosity as the shear rate approaches zero is termed the zero-shear viscosity (η_0) (see Figure 2.5). As the shear rate increases, shear-induced disentanglement becomes more pronounced, breaking the balance between entanglement and disentanglement. Consequently, the number of entanglement junctions within the polymer gradually decreases, leading to a viscosity that declines with increasing shear rate. In this region, viscosity and shear rate exhibit a power-law relationship, it is hence often referred to as the power-law region. When the shear rate reaches a critical value, the entanglements between polymer chains are almost entirely disrupted, and the chains become highly aligned. At this point, the relative motion between polymer chains becomes much easier, and the viscosity stabilizes at a constant minimum value. This region is called the second Newtonian plateau, and the corresponding viscosity is defined as the infinite-shear viscosity (η_∞).

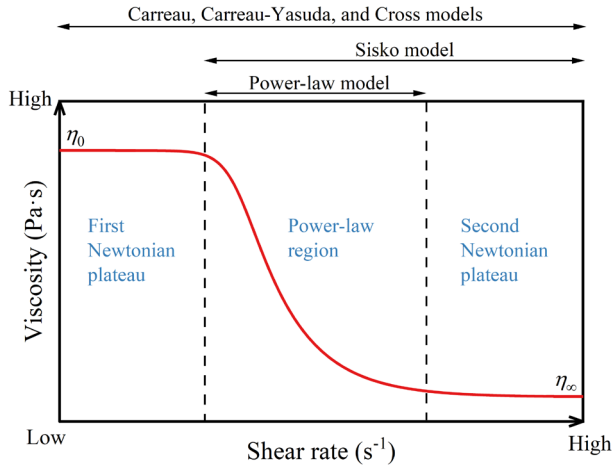

Figure 2.5. Shear-rate dependence of viscosity in polymer melts and concentrated solutions.

As summarized in Table 2.3, the models commonly used to describe shear-thinning fluid can be broadly categorized into three types:

(1) Shear stress ($\boldsymbol{\tau}$) *vs.* shear rate ($\dot{\boldsymbol{\gamma}}$) type: power-law model[92];

(2) Viscosity (η) *vs.* shear rate ($\dot{\boldsymbol{\gamma}}$) type: Carreau model[93], Carreau-Yasuda model[93,94], Cross model[95], and Sisko model[96];

(3) Viscosity (η) *vs.* shear stress ($\boldsymbol{\tau}$) type: Ellis model[97].

The shear rate in two-dimensional flow is calculated by the following equation:

$$\dot{\boldsymbol{\gamma}} = \begin{pmatrix} 2\dfrac{\partial u}{\partial x} & \dfrac{\partial u}{\partial y}+\dfrac{\partial v}{\partial x} \\ \dfrac{\partial u}{\partial y}+\dfrac{\partial v}{\partial x} & 2\dfrac{\partial v}{\partial y} \end{pmatrix}. \tag{2.10}$$

The different models possess distinct characteristics and are applicable within specific shear rate ranges. As shown in Table 2.3 and Figure 2.5, the power-law model has a simple form as a two-parameter model but exhibits no viscosity plateau at either the low or high shears. The Sisko model, as a three-parameter model, features a viscosity plateau solely at the high shear (infinite-shear viscosity). The Carreau and Cross models are four-parameter models with viscosity plateaus at both the low and high shears. The Carreau-Yasuda model as a five-parameter model exhibits also viscosity plateaus at both ends. Contrary to typical three-parameter models, the Ellis model successfully predicts viscosity plateaus at both low and high shear rates.[98] In summary, models with fewer (resp. more) parameters are easier (resp. more difficult) to use and have narrower (resp. wider) applicable ranges.

Table 2.3 Some flow models of shear-thinning fluid.

Types	Models	Equations
Shear stress *vs.* shear rate	Power-law	$\boldsymbol{\tau} = K\lvert\dot{\boldsymbol{\gamma}}\rvert^{n-1}\dot{\boldsymbol{\gamma}}$
Viscosity *vs.* shear rate	Carreau	$\dfrac{\eta-\eta_\infty}{\eta_0-\eta_\infty} = [1+(\lambda_C\lvert\dot{\boldsymbol{\gamma}}\rvert)^2]^{\frac{n-1}{2}}$
	Carreau-Yasuda	$\dfrac{\eta-\eta_\infty}{\eta_0-\eta_\infty} = [1+(\lambda_{CY}\lvert\dot{\boldsymbol{\gamma}}\rvert)^s]^{\frac{n-1}{s}}$
	Cross	$\dfrac{\eta-\eta_\infty}{\eta_0-\eta_\infty} = [1+(\lambda_{CY}\lvert\dot{\boldsymbol{\gamma}}\rvert)^n]^{-1}$
	Sisko	$\eta = \eta_\infty + K\lvert\dot{\boldsymbol{\gamma}}\rvert^{n-1}$

Viscosity *vs.* shear stress	Ellis	$\frac{\eta}{\eta_0} = \left(1+\frac{\lvert\tau\rvert}{\tau_{1/2}}\right)^{n-1}$

K and n are the consistency factor and flow index, respectively; λ_C and λ_{CY} are the relaxation times in Carreau and Carreau-Yasuda models, respectively, which are the inverses of the critical shear rates above which shear-thinning begins; s is the transition sharpness parameter adjusting the curvature between Newtonian plateau and shear-thinning region; $\tau_{1/2}$ is the shear stress at a viscosity of $\eta_0/2$.

Different flow models vary in their ability to describe shear-thinning fluids, leading to different predictions of film thickness when different models are employed. As the simplest model of shear-thinning fluid, the power-law model has been widely adopted in dip coating studies. Gutfinger and Tallmadge (1965)[8], by using the matching method, developed two analytical expressions of film thickness of power-law fluid for small and large capillary numbers, respectively:

$$h_0 = A_S(n) l_c Ca^{2/3} \text{ for small } Ca, \tag{2.11}$$

$$h_0 = l_c Ca^{1/2} \text{ for large } Ca, \tag{2.12}$$

where $A_S(n)$ is a function of flow index n. At first glance equations (2.11) and (2.12) are very similar to models (2.1) and (2.3) for Newtonian fluids. However, it is noteworthy that the capillary number Ca for power-law fluid is defined as:

$$Ca = \frac{K u_0^n h_0^{1-n}}{\sigma}. \tag{2.13}$$

If $n = 1$ and $K = \eta_L$, the capillary number (2.13) for power-law fluid reduces to the one for Newtonian fluid, i.e., $Ca = \eta_L u_0/\sigma$. Correspondingly, equations (2.11) and (2.12) reduce to (2.1) and (2.3). Many studies[8,99,100] show that equations (2.11) and (2.12) always overestimate the film thickness and the disagreement becomes larger for lower flow indices n. There are two possible reasons suggested to explain differences between their theory and experiment. One is that the power-law model is unable to describe the fluid behaviour at low shear and the other is that inaccurate values of the curvature coefficient in dynamic meniscus is used in modelling. On the one hand, Tallmadge (1966)[101]

established a withdrawal theory based on Ellis model which is valid at low shear. This theory was experimentally verified by Hildebrand and Tallmadge (1968)[102]. On the other hand, Tallmadge (1969)[99] investigated the curvature coefficient in dynamic meniscus and developed a variable-curvature-coefficient theory based on the power-law model. In addition, there are many other theories including Groenveld's zero gravity theory[100] and Tallmadge's empirical 'patch' theory[103]. Various theoretical models show significant divergence in their predictions of film thickness, with notable inconsistencies between different models.[104,105] Hewson *et al*. (2009)[106] treated the dip coating problem as a boundary value problem and established a new film thickness model which numerical solution agrees well with the experimental film thickness.

Spiers *et al.* (1975)[104] developed a theory involving a differential equation for a power-law fluid and an Ellis fluid. The theory based on the Ellis model predicts the film thickness more accurately than the theory based on the power-law model, but the former still overestimates the film thickness. Javidi *et al*. (2016)[98] modelled the film thickness by using the matching method for different flow models. The Ellis-model-based theory predicts the film thickness very well but the power-law-model-based one always gives an overprediction. However, the film thickness models of Baikov *et al.* (1986)[107] established by using power-law model and Ellis model nearly yield indistinguishable numerical solutions. According to the authors' understanding, the theory based on the Ellis model should be more accurate than that based on the power-law model, as the Ellis model incorporates a low shear parameter that better describes the rheological behaviour of shear-thinning fluid. However, some approximations or assumptions made during the modelling process may also affect the final model's accuracy.

Although numerous studies have investigated dip coating of shear-thinning fluid, research employing the Carreau or Carreau-Yasuda models remains relatively scarce. Javidi *et al*. (2015)[108] and Zhang *et al*. (2016)[30] investigated the dip coating of a Carreau-Yasuda fluid, with particular focus on the film thickness and the flow field under different sets of conditions. Afanasiev *et al*. (2007)[97], through lubrication analysis, derived a film thickness model based on Carreau and Carreau-Yasuda

models at small capillary number. Peralta *et al*. (2017)[109] derived the analytical model for Carreau and Carreau-Yasuda fluids at large capillary number where the surface tension could be neglected.

2.3.2.2 Viscoplastic fluid

The intricate rheology of viscoplastic fluid and its impact on film formation mechanisms remain a key challenge. This study specifically examines simple viscoplastic fluid without time-dependent effects (thixotropy[110] or rheopexy[111]). These fluids exhibit three defining characteristics: Below a critical shear stress (static yield stress), they maintain solid-like behaviour with intact internal structures; When shear stress exceeds this threshold, structural breakdown initiates flow; upon stress reduction below the dynamic yield stress (equal to static yield stress), solid-like properties recover; both yield stresses remain history-independent. Typical examples include foams[112], gels[113,114], suspensions[115], and emulsions[116]. Notably, colloidal suspensions are excluded due to their complex rheology involving colloidal interactions[117] and Brownian motion[118]. The rheological behaviour of simple viscoplastic fluid can be described by various generalized Newtonian constitutive models including the Casson[119,120], Bingham[121] and Herschel-Bulkley[122,123] models. Among these, the Herschel-Bulkley model is more realistic and provides a better description on the nonlinear viscous behaviour of the viscoplastic fluids in the liquid regime, by the shear rate-dependent viscosity term in this model.[87] The Herschel-Bulkley model can be expressed by the following equation:

$$\begin{cases} \boldsymbol{\tau} = \left(\dfrac{\tau_c}{|\dot{\boldsymbol{\gamma}}|} + K|\dot{\boldsymbol{\gamma}}|^{n-1}\right)\dot{\boldsymbol{\gamma}} & \text{for } |\boldsymbol{\tau}| > \tau_c \text{ (liquid regime)} \\ |\dot{\boldsymbol{\gamma}}| = 0 & \text{for } |\boldsymbol{\tau}| \le \tau_c \text{ (solid regime)} \end{cases}, \tag{2.14}$$

where τ_c represents the yield stress. The three-dimensional tensor formulation of the Herschel-Bulkley model can be derived from equation (2.14) using the Von Mises yielding criterion[124,125]. If the flow index n tends to 1, the consistency factor K equals the plastic viscosity η_p and the Herschel-Bulkley model reduces to the Bingham model:

$$\begin{cases} \boldsymbol{\tau} = \left(\dfrac{\tau_c}{|\dot{\gamma}|} + \eta_p\right)\dot{\gamma} & \text{for } |\boldsymbol{\tau}| > \tau_c \text{ (liquid regime)} \\ |\dot{\gamma}| = 0 & \text{for } |\boldsymbol{\tau}| \leq \tau_c \text{ (solid regime)} \end{cases}. \tag{2.15}$$

To the best of the author's knowledge, research on dip coating of viscoplastic fluids has diverged into two distinct strategies. The first strategy focuses on the liquid film itself, establishing film thickness models based on the thickness distribution of the film and the flow characteristics in the film. This approach typically involves analysing the balance between viscous, gravitational, capillary and yield stress effects to predict film thickness. Spiers *et al*. (1975)[104] derived an approximate theory of the film thickness by the matching method for the Bingham fluid. Their theory indicates that the presence of a yield stress increases the film thickness. Also employing the matching method, Shul'man and Baikov (1985)[126] obtained the analytical expressions of film thickness for a Bingham fluid. Peev *et al*. (1988)[126] compared the results of both studies mentioned just before to experiments, demonstrating that while both theories provided comparable predictions of film thickness at low *Ca*, the Shul'man and Baikov (1985) theory[126] exhibited superior predictive accuracy, particularly at high *Ca*. Recently, Baikov and Chorny (2019)[42] carried out a more rigorous theoretical study on dip coating of Bingham fluid and derived the lubrication theory applicable to a Bingham fluid. By solving numerically the resulting lubrication equations, film thicknesses under different conditions are obtained. Their theory shows three different film formation regimes depending on the value of capillary number *Ca* defined as $Ca = \eta_p u_0/\sigma$: (1) At high capillary number ($Ca > 2$), the film thickness does not depend on yield stress and surface tension, but depends on withdrawal velocity, plastic viscosity, and gravity; (2) At moderate capillary number ($Ca_y < Ca < 2$, where the value of Ca_y depends on the ratio of yield stress to surface tension), withdrawal velocity, yield stress, plastic viscosity, surface tension, and gravity all significantly influence film thickness; (3) At low capillary number ($Ca < Ca_y$), the film thickness is plastic viscosity- and withdrawal velocity-independent, but is instead determined by yield stress, surface tension, and gravity.

Peralta *et al*. (2014)[47] theoretically studied the dip coating of generalized Newtonian fluids, encompassing the Bingham and Herschel-Bulkley fluids. Their analysis yielded the analytical solutions for several key parameters like the film thickness profile and the velocity profile within the film. This theory was validated against experimentally measured average film thickness, demonstrating good agreement with a deviation within 15%.[48] It should be noted, however, that this theoretical framework remains strictly applicable only to cases where surface tension effects are negligible.

Numerous experimental studies[14,15,127] and numerical simulations[30,51,128,129] have consistently demonstrated that during dip coating processes, yielding is confined to a distinct fluid layer adjacent to the substrate (Figure 2.6*a*). This yielded region maintains a nearly uniform thickness along the substrate surface, while the remaining fluid outside this layer persists in an unyielded state. The volume of the fluid entrained by the substrate is insufficient to feed the film as would be required by the static meniscus. Correspondingly, the film thickness is governed by the flow inside the container rather than inside the meniscus. Some studies[29,30,39] have even observed the depression of the meniscus, and confirm that the flow inside the container plays a role in the film formation. This inherent constraint gave rise to the secondary modelling strategy, that is to model the film thickness based on the flow dynamics inside the container. Maillard *et al*. (2014)[14] observed in their coating experiment that the film thickness mainly varies with the yield stress, but is only slightly dependent of the withdrawal velocity. More importantly, they noticed that the film thickness scaled proportionally with the thickness of the yielded region, where the latter can be determined through the balance between viscous dissipation and gravitational forces. This observation allowed them to derive a general empirical expression for the film thickness.

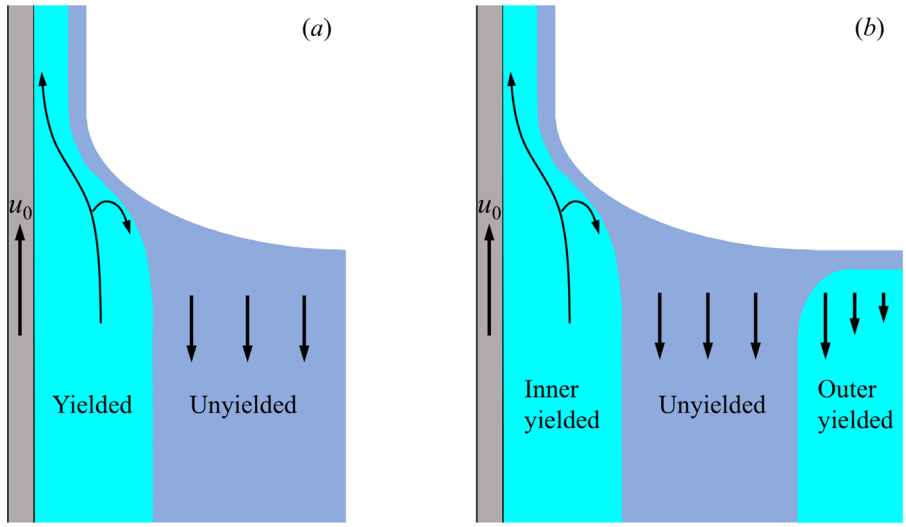

Figure 2.6. Schematic of the flow regime during dip coating of viscoplastic fluid proposed by Maillard (*a*) and Smit (*b*). The light blue region and dark blue region correspond to the yielded region and unyielded region, respectively.

Maillard *et al.* (2016)[16] studied further the flow inside the container and modelled the velocity. According to the mass conservation, they proposed a model of film thickness:

$$h_0 = \frac{Q_{up}\text{-}Q_{drain}}{u_0}, \tag{2.16}$$

where Q_{up} and Q_{drain} represent the flow rates entrained up by the plate and that due to the gravitational drainage per width of plate, respectively. However, since their analysis exclusively considers flow within the inner yielded region, the proposed model (2.16) inherently requires experimental determination of certain parameters. Recently, Smit *et al.* (2019)[127] identified three distinct flow regimes within the container: an inner yielded region, an intermediate unyielded region, and an outer yielded region (see Figure 2.6*b*). Through comprehensive modelling of these interacting regions, they successfully developed a fully theoretical film thickness model that requires no empirical parameters. However, this pioneering work had two limitations: it neither accounts for gravitational drainage effects nor validates its applicability for plate coating configurations.

2.4 Problem formulation

The dynamics of the dip coating process (including the evolution of film thickness, the distribution of the flow in the film and in the container, and the forces on the substrate) is difficult to obtain directly through experiments. Computational fluid dynamics serves as a robust tool for accurately simulating these processes and visualizing critical hydrodynamic features. Through the above literature review, we identified the following (but not limited to) pressing problems in the field of dip coating, and differentiated our research to address them:

1. For the dip coating of fully wetting plate with Newtonian fluid at high capillarity number, the asymptotic film thicknesses reported in different studies vary considerably. Existing studies report significant discrepancies in asymptotic film thickness predictions for planar substrates under high *Ca* conditions. More importantly, the film thickness distribution is extremely nonuniform, so that the study of the entire film distribution is more meaningful than focusing only on the asymptotic film thickness. Current theories, limited to tip region of the film, exhibit poor agreement with experimental film thickness distribution. Through direct numerical simulations, we capture complete film dynamics, enabling development of an accurate global thickness distribution model.

2. For the dip coating of partially wetting plate with Newtonian fluid, the existing studies systematically investigated the contact line dynamics before wetting and the film morphology after wetting over a wide range of capillary number, by using phase-field simulation and lubrication theory. For cylindrical geometry, it is clear from the existing studies on the fully wetting case that the cylinder radius affects the film thickness and even changes the film morphology. However, for Newtonian fluids coated on partially wetting cylinder, existing work solely addresses the situation before the wetting transition occurs. With reference to existing studies, the lubrication theory in the axisymmetric system is deduced here and combined with VOF simulation to study the wetting and film deposition for a wide range of radii and capillary numbers.

3. For the dip coating of a fully wetting plate in a viscoplastic fluid, the existing film thickness models incorporate a significant number of empirical parameters due to insufficient understanding of the flow characteristics in the container. Although a fully theoretical model describing both the flow field and film thickness has been developed for cylindrical geometry, it cannot be directly applied to flat plate withdrawal due to its neglect of gravitational drainage effects which play a critical role in the latter configuration. We aim to directly simulate the dip coating of a fully wetting plate in viscoplastic fluid using the Volume of Fluid (VOF) method, visualize the flow field, and parametrically investigate the influence of yield stress, consistency factor, flow index, and withdrawal speed on the flow field and resulting film thickness. Based on the revealed hydrodynamic characteristics, we attempt to develop a theoretical model for flow field distribution and film thickness suitable for flat plate geometry.

4. Wall slip effects severely compromise conventional rheometric measurements for viscoplastic fluids. Although dip-coating-based methods have been proposed to measure yield stress by circumventing wall slip, they cannot determine other key parameters like consistency factor and flow index. It is important to develop a new method based on the dip coating process that can be used to measure other parameters besides the yield stress. By analysing the force on the plate and the flow in the container during immersion (the first stage of dip coating) of the slotted plate, we develop a new rheometric method for viscoplastic fluid.

Reference

1. Zhang Z, Salamatin A, Peng F, Kornev KG. Dip coating of cylinders with Newtonian fluids. *J. Colloid Interface Sci.* Feb 2022;607(Pt 1):502-513.

2. Jeong D-H, Lee MKH, Thiévenaz V, Bazant MZ, Sauret A. Dip coating of bidisperse particulate suspensions. *J. Fluid Mech.* 2022;936:A36.

3. Maleki M, Reyssat M, Restagno F, Quere D, Clanet C. Landau-Levich menisci. *J. Colloid Interface Sci.* Feb 1 2011;354(1):359-363.

4. Evertz A, Schrein D, Olsen E, Hoffmann G-A, Overmeyer L. Dip coating of thin polymer optical fibers. *Opt. Fiber Technol.* 2021;66:102638.

5. Harrisankar N, Levecque P, van Steen E. An automated coating process to produce TiO2-coated optical fibre for photocatalytic reactor systems. *Chem. Eng. Process.* 2021;166:108479.

6. Bi L, Perry W, Wang R, et al. MXene Functionalized Kevlar Yarn via Automated, Continuous Dip Coating. *Adv. Funct. Mater.* 2023;34(14):2312434.

7. Van Rossum JJ. Viscous lifting and drainage of liquids. *Appl. Sc. Res. Sect. A volume* 1958;7:121-144.

8. Gutfinger C, Tallmadge JA. Films of non-Newtonian fluids adhering to flat plates. *AIChE J.* 1965;11(3):403-413.

9. Soroka AJ, Tallmadge JA. A test of the inertial theory for plate withdrawal. *AIChE J.* 1971;17(2):505-508.

10. Spiers RP, Subbaraman CV, Wilkinson WL. Free coating of a Newtonian liquid onto a vertical surface. *Chem. Eng. Sci.* 1974;29(2):389-396.

11. Rio E, Boulogne F. Withdrawing a solid from a bath: How much liquid is coated? *Adv. Colloid Interface Sci.* Sep 2017;247:100-114.

12. Krechetnikov R, Homsy GM. Experimental study of substrate roughness and surfactant effects on the Landau-Levich law. *Phys. Fluids.* 2005;17(10):102108.

13. Ouriemi M, Homsy GM. Experimental study of the effect of surface-absorbed hydrophobic particles on the Landau-Levich law. *Phys. Fluids.* 2013;25(8):082111.

14. Maillard M, Boujlel J, Coussot P. Solid-solid transition in Landau-Levich flow with soft-jammed systems. *Phys. Rev. Lett.* Feb 14 2014;112(6):068304.

15. Maillard M, Boujlel J, Coussot P. Flow characteristics around a plate withdrawn from a bath of yield stress fluid. *J Non-Newton Fluid.* 2015;220:33-43.

16. Maillard M, Bleyer J, Andrieux AL, Boujlel J, Coussot P. Dip-coating of yield stress fluids. *Phys. Fluids.* 2016;28(5):31-49.

17. Gans A, Dressaire E, Colnet B, Saingier G, Bazant MZ, Sauret A. Dip-coating of suspensions. *Soft Matter.* Jan 2 2019;15(2):252-261.

18. Sathyanath R, Aarthi A, Kalpathy SK. Liquid film entrainment during dip coating on a saturated porous substrate. *Chem. Eng. Sci.* 2020;218:115552.

19. Liu X, Danglad-Flores J, Eickelmann S, et al. Controlled-Alignment Patterns of Dipeptide Micro- and Nanofibers. *ACS Nano.* 2022;16(7):10372-10382.

20. White DA, Tallmadge JA. A theory of withdrawal of cylinders from liquid baths. *AIChE J.* 1966;12(2):333-339.

21. Ou Ramdane O, Quéré D. Thickening Factor in Marangoni Coating. *Langmuir.* 1997;13(11):2911-2916.

22. Quéré D, Ryck Ad, Ramdane OO. Liquid coating from a surfactant solution. *Europhys. Lett.* 1997;37(4):305-310.

23. De Ryck A, Quere D. Gravity and Inertia Effects in Plate Coating. *J. Colloid Interface Sci.* Jul 15 1998;203(2):278-285.

24. Shen AQ, Gleason B, McKinley GH, Stone HA. Fiber coating with surfactant solutions. *Phys. Fluids.* 2002;14(11):4055-4068.

25. De Ryck A, Quéré D. Inertial coating of a fibre. *J. Fluid Mech.* 1996;311:219-237.

26. Carroll BJ, Lucassen J. Capillarity-controlled entrainment of liquid by a thin cylindrical filament moving through an interface. *Chem. Eng. Sci.* 1973;28(1):23-30.

27. Quéré D, Meglio JMd, Brochard-Wyart F. Making van der Waals Films on Fibers. *Europhys. Lett.* 1989;10(4):335-340.

28. Kizito JP, Kamotani Y, Ostrach S. Experimental free coating flows at high capillary and Reynolds number. *Exp. Fluids.* 1999;27(3):235-243.

29. Chen MM, Zhang XM, Ma JP, Chen SC, Chen WX, Feng LF. Experimental study on film thickness and the problem of free surface film flow in dip coating. *Asia-Pac. J. Chem. Eng.* 2016;11(5):695-704.

30. Zhang X-M, Chen M-M, Ma J-P, Chen W-X, Feng L-F. Numerical simulation and experimental validation of liquid-film-flow characteristics in dip coating for non-Newtonian fluids. *Polym. Eng. Sci.* 2016;56(9):1070-1078.

31. Snoeijer JH, Ziegler J, Andreotti B, Fermigier M, Eggers J. Thick films of viscous fluid coating a plate withdrawn from a liquid reservoir. *Phys. Rev. Lett.* Jun 20 2008;100(24):244502.

32. Scheid B, Delacotte J, Dollet B, et al. The role of surface rheology in liquid film formation. *Europhys. Lett.* 2010;90(2):24002.

33. Seiwert J, Clanet C, QuÉRÉ D. Coating of a textured solid. *J. Fluid Mech.* 2011;669:55-63.

34. Qu D, Ramé E, Garoff S. Dip-coated films of volatile liquids. *Phys. Fluids.* 2002;14(3):1154-1165.

35. Snoeijer JH, Delon G, Fermigier M, Andreotti B. Avoided critical behavior in dynamically forced wetting. *Phys. Rev. Lett.* May 5 2006;96(17):174504.

36. Maleki M, Reyssat E, Quere D, Golestanian R. On the Landau-Levich transition. *Langmuir.* Sep 25 2007;23(20):10116-10122.

37. Delon G, Fermigier M, Snoeijer JH, Andreotti B. Relaxation of a dewetting contact line. Part 2. Experiments. *J. Fluid Mech.* 2008;604:55-75.

38. Kajiya T, Brunet P, Royon L, Daerr A, Receveur M, Limat L. A liquid contact line receding on a soft gel surface: dip-coating geometry investigation. *Soft Matter.* Nov 28 2014;10(44):8888-8895.

39. Trottet B MM, Keddie J. Mastering the coating thickness obtained using liquids with a yield-stress. *Chem. Eng. Trans.* 2017;57:1897-1902.

40. De Ryck A, Quéré D. Fluid Coating from a Polymer Solution. *Langmuir.* 1998;14(7):1911-1914.

41. Landau L, Levich B. Dragging of a liquid by a moving plate. *Acta Physicochim. URSS.* 1942;17(2):42-54.

42. Baikov VI, Chorny AD. Withdrawing a Bingham viscoplastic fluid. *J. Rheol.* 2019;63(6):927-938.

43. White DA, Tallmadge JA. A gravity corrected theory for cylinder withdrawal. *AIChE J.* 1967;13(4):745-750.

44. Wilson SDR. The drag-out problem in film coating theory. *J. Eng. Math.* 1982;16(3):209-221.

45. Jin B, Acrivos A, Münch A. The drag-out problem in film coating. *Phys. Fluids.* 2005;17(10):103603.

46. Derjaguin B. On the thickness of the liquid film adhering to the walls of a vessel after emptying. *Acta Physicochim. URSS.* 1943;20:349-352.

47. Peralta JM, Meza BE, Zorrilla SE. Mathematical modeling of a dip-coating process using a generalized Newtonian fluid.1. model development. *Ind. Eng. Chem. Res.* 2014;53(15):6521-6532.

48. Peralta JM, Meza BE, Zorrilla SE. Mathematical modeling of a dip-coating process using a generalized Newtonian fluid. 2. model validation and sensitivity analysis. *Ind. Eng. Chem. Res.* 2014;53(15):6533-6543.

49. Tuck EO. Continuous coating with gravity and jet stripping. *Phys. Fluids.* 1983;26(9):2352.

50. Benilov ES, Zubkov VS. On the drag-out problem in liquid film theory. *J. Fluid Mech.* 2008;617:283-299.

51. Filali A, Khezzar L, Mitsoulis E. Some experiences with the numerical simulation of Newtonian and Bingham fluids in dip coating. *Comput. Fluids.* 2013;82:110-121.

52. Kheshgi HS, Kistler SF, Scriven LE. Rising and falling film flows: Viewed from a first-order approximation. *Chem. Eng. Sci.* 1992;47(3):683-694.

53. Groenveld P. High capillary number withdrawal from viscous Newtonian liquids by flat plates. *Chem. Eng. Sci.* 1970;25(1):33-40.

54. Park C-W. Effects of insoluble surfactants on dip coating. *J. Colloid Interface Sci.* 1991;146(2):382-394.

55. Krechetnikov R, Homsy GM. Surfactant effects in the Landau–Levich problem. *J. Fluid Mech.* 2006;559.

56. Tiwari N, Davis JM. Theoretical analysis of the effect of insoluble surfactant on the dip coating of chemically micropatterned surfaces. *Phys. Fluids.* 2006;18(2):022102.

57. Daripa P, Paşa G. The thickening effect of interfacial surfactant in the drag-out coating problem. *J. Stat. Mech.:Theory Exp.* 2009;2009(07):L07002.

58. Campana DM, Ubal S, Giavedoni MD, Saita FA. Numerical prediction of the film thickening due to surfactants in the Landau–Levich problem. *Phys. Fluids.* 2010;22(3):032103.

59. Krechetnikov R. On application of lubrication approximations to nonunidirectional coating flows with clean and surfactant interfaces. *Phys. Fluids.* 2010;22(9):092102.

60. Campana DM, Ubal S, Giavedoni MD, Saita FA. A deeper insight into the dip coating process in the presence of insoluble surfactants: A numerical analysis. *Phys. Fluids.* May 2011;23(5):052102.

61. Delacotte J, Montel L, Restagno F, et al. Plate coating: influence of concentrated surfactants on the film thickness. *Langmuir.* Feb 28 2012;28(8):3821-3830.

62. Campana DM, Ubal S, Giavedoni MD, Saita FA. Influence of Surfactants on Dip Coating of Fibers: Numerical Analysis. *Ind. Eng. Chem. Res.* 2016;55(19):5770-5779.

63. Münch A, Evans PL. Marangoni-driven liquid films rising out of a meniscus onto a nearly-horizontal substrate. *Phys. D.* 2005;209(1-4):164-177.

64. Berteloot G, Daerr A, Lequeux F, Limat L. Dip coating with colloids and evaporation. *Chem. Eng. Process.* 2013;68:69-73.

65. Dey M, Doumenc F, Guerrier B. Numerical simulation of dip-coating in the evaporative regime. *Eur. Phys. J. E.* Feb 2016;39(2):1-9.

66. Kim O, Nam J. Confinement effects in dip coating. *J. Fluid Mech.* 2017;827:1-30.

67. Derjaguin BV. Theory of the deposition of a viscous liquid on to a fibre or wire being withdrawn from the liquid. *Prikl. Mekh. Tekh. Phys.* . 1963;3:71-78.

68. Wilson SDR. Coating flow on to rods and wires. *AIChE J.* 1988;34(10):1732-1735.

69. de Gennes P-G, Brochard-Wyart F, Quéré D. *Capillarity and Wetting Phenomena*2004.

70. Huppert HE. Flow and instability of a viscous current down a slope. *Nature.* 1982;300(5891):427-429.

71. Cox RG. The dynamics of the spreading of liquids on a solid surface. Part 1. Viscous flow. *J. Fluid Mech.* 1986;168:169-194.

72. Voinov OV. Hydrodynamics of wetting. *Fluid Dyn.* 1976;11(5):714-721.

73. Huh C, Scriven LE. Hydrodynamic model of steady movement of a solid/liquid/fluid contact line. *J. Colloid Interface Sci.* 1971;35(1):85-101.

74. Dussan V EB, Davis SH. On the motion of a fluid-fluid interface along a solid surface. *J. Fluid Mech.* 1974;65(1):71-95.

75. Sui Y, Ding H, Spelt PDM. Numerical Simulations of Flows with Moving Contact Lines. *Annu. Rev. Fluid Mech.* 2014;46(1):97-119.

76. Kansal M, Bertin V, Datt C, Eggers J, Snoeijer JH. Viscoelastic wetting: Cox–Voinov theory with normal stress effects. *J. Fluid Mech.* 2024;985:A17.

77. Eggers J. Hydrodynamic theory of forced dewetting. *Phys. Rev. Lett.* Aug 27 2004;93(9):094502.

78. Eggers J. Existence of receding and advancing contact lines. *Phys. Fluids.* 2005;17(8):082106.

79. Shing Chan T, Gueudré T, Snoeijer JH. Maximum speed of dewetting on a fiber. *Phys. Fluids.* 2011;23(11):112103.

80. Chan TS, Snoeijer JH, Eggers J. Theory of the forced wetting transition. *Phys. Fluids.* 2012;24(7):072104.

81. Florentin JJ, Abramowitz M, Stegun IA. Handbook of Mathematical Functions. *The American Mathematical Monthly.* 1966;73(10).

82. Snoeijer JH, Andreotti B, Delon G, Fermigier M. Relaxation of a dewetting contact line. Part 1. A full-scale hydrodynamic calculation. *J. Fluid Mech.* 2007;579:63-83.
83. Blake TD, Ruschak KJ. A maximum speed of wetting. *Nature.* 1979;282(5738):489-491.
84. Petrov JG, Sedev RV. On the existence of a maximum speed of wetting. *Colloids Surf.* 1985;13:313-322.
85. Gao P, Li L, Feng JJ, Ding H, Lu X-Y. Film deposition and transition on a partially wetting plate in dip coating. *J. Fluid Mech.* 2016;791:358-383.
86. Hutchinson AJ, Worster MG. Fracturing behaviour of a shear-thinning fluid in a lubricated Hele-Shaw cell. *J. Fluid Mech.* 2025;1003:A6.
87. Balmforth NJ, Frigaard IA, Ovarlez G. Yielding to stress: recent developments in viscoplastic fluid mechanics. *Annu. Rev. Fluid Mech.* 2014;46(1):121-146.
88. Lee AG, Shaqfeh ESG, Khomami B. Viscoelastic effects on interfacial dynamics in air–liquid displacement under gravity stabilization. *J. Fluid Mech.* 2005;531:59-83.
89. Abedijaberi A, Bhatara G, Shaqfeh ESG, Khomami B. A computational study of the influence of viscoelasticity on the interfacial dynamics of dip coating flow. *J Non-Newton Fluid.* Jul 2011;166(12-13):614-627.
90. Yamamoto T, Nojima N, Mori N. Numerical Analysis of Flow Behavior in Meniscus Region of Viscoelastic Dip Coating Flows. *J. Text. Eng.* 2005;51(2):21-28.
91. Ashmore J, Shen AQ, Kavehpour HP, Stone HA, McKinley GH. Coating flows of non-Newtonian fluids: weakly and strongly elastic limits. *J Eng Math.* 2007;60(1):17-41.
92. Ostwald W. Ueber die Geschwindigkeitsfunktion der Viskosität disperser Systeme. I. *Kolloid-Z.* 1925;36(2):99-117.
93. Carreau PJ. Rheological Equations from Molecular Network Theories. *Trans. Soc. Rheol.* 1972;16(1):99-127.
94. Yasuda K. *Investigation of the Analogies Between Viscometric and Linear Viscoelastic Properties of Polystyrene Fluids*. Boston: Dept. of Chemical Engineering, Massachusetts Institute of Technology; 1979.
95. Cross MM. Rheology of non-Newtonian fluids: A new flow equation for pseudoplastic systems. *J. Colloid Sci.* 1965;20(5):417-437.
96. Sisko AW. The Flow of Lubricating Greases. *Ind. Eng. Chem.* 1958;50(12):1789-1792.
97. Afanasiev K, Munch A, Wagner B. Landau-Levich problem for non-Newtonian liquids. *Phys. Rev. E.* Sep 2007;76(3):036307.
98. Javidi M, Pope MA, Hrymak AN. Investigation on dip coating process by mathematical modeling of non-Newtonian fluid coating on cylindrical substrate. *Phys. Fluids.* 2016;28(6):063105.
99. Tallmadge JA. A variable-coefficient plate withdrawal theory for power law fluids. *Chem. Eng. Sci.* 1969;24(3):471-480.
100. Groenveld P. Withdrawal of power law fluid films. *Chem. Eng. Sci.* 1970;25(10):1579-1585.
101. Tallmadge JA. A withdrawal theory for ellis model fluids. *AIChE J.* 1966;12(5):1011-1014.
102. Hildebrand RE, Tallmadge JA. A test of the withdrawal theory for ellis fluids. *Can. J. Chem. Eng.* 1968;46(6):394-397.
103. Tallmadge JA. Withdrawal of flat plates from power law fluids. *AIChE J.* 1970;16(6):925-930.
104. Spiers RP, Subbaraman CV, Wilkinson WL. Free coating of non-newtonian liquids onto a vertical surface. *Chem. Eng. Sci.* 1975;30(4):379-395.
105. Tekić MN, Popadić VO. Free coating of pseudoplastic liquids onto a vertical surface. *Chem. Eng. Sci.* 1983;38(2):285-288.
106. Hewson RW, Kapur N, Gaskell PH. A model for film-forming with Newtonian and shear-thinning fluids. *J Non-Newton Fluid.* 2009;162(1-3):21-28.
107. Baikov VI, Shul'man ZP, éngel'gardt K. Coating of a non-Newtonian fluid onto a moving surface. *Journal of Applied Mechanics and Technical Physics.* 1986;26(4):496-502.

108. Javidi M, Hrymak AN. Numerical simulation of the dip-coating process with wall effects on the coating film thickness. *J. Coat. Technol. Res.* 2015;12(5):843-853.
109. Peralta JM, Meza BE, Zorrilla SE. Analytical solutions for the free-draining flow of a Carreau-Yasuda fluid on a vertical plate. *Chem. Eng. Sci.* 2017;168:391-402.
110. Larson RG, Wei Y. A review of thixotropy and its rheological modeling. *J. Rheol.* 2019;63(3):477-501.
111. Amat Yusof FA, Yamaki M, Kawai M, Okajima MK, Kaneko T, Mitsumata T. Rheopectic Behavior for Aqueous Solutions of Megamolecular Polysaccharide Sacran. *Biomolecules.* Jan 17 2020;10(1):155.
112. Weaire D. The rheology of foam. *Curr. Opin. Colloid Interface Sci.* 2008;13(3):171-176.
113. Coussot P, Tocquer L, Lanos C, Ovarlez G. Macroscopic vs. local rheology of yield stress fluids. *J Non-Newton Fluid.* 2009;158(1-3):85-90.
114. Medina-Bañuelos EF, Marín-Santibáñez BM, Pérez-González J, Malik M, Kalyon DM. Tangential annular (Couette) flow of a viscoplastic microgel with wall slip. *J. Rheol.* 2017;61(5):1007-1022.
115. Coussot P. *Rheometry of pastes, suspensions, and granular materials (Applications in industry and environment)*: Wiley; 2005.
116. Derkach SR. Rheology of emulsions. *Adv. Colloid Interface Sci.* Oct 30 2009;151(1-2):1-23.
117. Liang Y, Hilal N, Langston P, Starov V. Interaction forces between colloidal particles in liquid: theory and experiment. *Adv. Colloid Interface Sci.* Oct 31 2007;134-135:151-166.
118. Tapia-Ignacio C, Moctezuma RE, Donado F, Weeks ER. Brownian motion of ellipsoidal particles on a granular magnetic bath. *Phys. Rev. E.* Aug 2020;102(2-1):022902.
119. Hanks RW. Couette viscometry of Casson fluids. *J. Rheol.* 1983;27(1):1-6.
120. Hayat T, Asad S, Alsaedi A. Flow of Casson fluid with nanoparticles. *Appl. Math. Mech.* 2016;37(4):459-470.
121. Rahmani H, Taghavi SM. Poiseuille flow of a Bingham fluid in a channel with a superhydrophobic groovy wall. *J. Fluid Mech.* 2022;948:A34.
122. Herschel WH, Bulkley R. Konsistenzmessungen von gummi-benzollösungen. *Kolloid-Z.* 1926;39(4):291-300.
123. Wang Y, Ewoldt RH. New insights on carbon black suspension rheology—anisotropic thixotropy and antithixotropy. *J. Rheol.* 2022;66(5):937-953.
124. Barsanescu PD, Comanici AM. von Mises hypothesis revised. *Acta Mechanica.* 2016;228(2):433-446.
125. vonMises R. Mechanik der festen Körper im plastisch deformablen Zustand. *Nachrichten von der Königlichen Gesellschaft der Wissenschaften zu Göettingen, Mathematisch-physikalische Klasse.* 1913(1913):582-592.
126. Shul'man EP, Baikov VI. Entrainment of a viscoplastic fluid by a moving surface. *J. Eng. Phys.* 1978;34(3):344-349.
127. Smit WJ, Kusina C, Joanny JF, Colin A. Stress field inside the bath determines dip coating with yield-stress fluids in cylindrical geometry. *Phys. Rev. Lett.* Oct 4 2019;123(14):148002.
128. Hurez P, Tanguy PA. Finite element analysis of dip coating with bingham fluids. *Polym. Eng. Sci.* 1990;30(18):1125-1132.
129. Bleyer J, Maillard M, de Buhan P, Coussot P. Efficient numerical computations of yield stress fluid flows using second-order cone programming. *Comput. Method. Appl. M.* 2015;283:599-614.

3 Methodology

As illustrated in Figure 3.1, computational fluid dynamics (CFD) simulation serves as the primary methodology in the fundamental investigations (Work 1, Work 2, and Work 3), whereas immersion experiments are central to the applied research of Work 4.

Work 1, investigating the dip coating of a completely wetting plate with Newtonian fluids, relied on CFD simulation to study the flow in the film and the thickness distribution, the results of which were validated against dip coating experiments.

Work 2, examining the dip coating of a partially wetting cylinder with Newtonian fluids, applied CFD simulation to capture all possible film morphologies under varying capillary numbers and cylinder radii. In parallel, a lubrication theory for the axisymmetric system was derived; the comparison between simulation and theory provided mutual validation

Work 3, dealing with the dip coating of a completely wetting plate with viscoplastic fluids, utilized CFD simulation to investigate the flow field and film thickness, with its validation achieved through benchmarking against existing experimental thickness from literature.

Work 4, centred on the immersion of a slotted plate into viscoplastic fluids, proposed a novel rheometric method. The research was therefore primarily experimental, employing CFD simulation as a verification tool for the method's underlying theoretical principle.

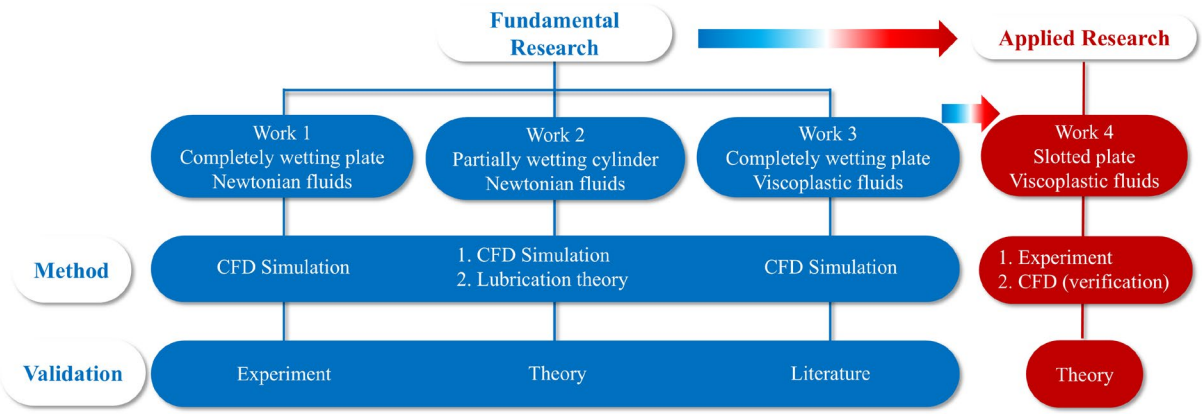

Figure 3.1. Schematic diagram of methods used in different works and their validation.

3.1 CFD simulation

Given the distinct fluid-substrate combinations examined across chapters, the computational domain configurations and meshing strategies are uniquely tailored to each case. These specific implementations will be discussed within their respective chapters to maintain contextual relevance. All simulations nevertheless adhere to the unified numerical framework presented here, which specifies the common discretization schemes and convergence criteria. All numerical algorithms maintained consistent implementations with Chapter 3, unless otherwise specified in subsequent sections.

3.1.1 Governing equations

The liquid phase and air phase are both assumed incompressible, the flow is thus governed by the following continuum and momentum conservation equations:

$$\nabla \cdot \mathbf{v} = 0, \tag{3.1}$$

$$\bar{\rho}\frac{\partial \mathbf{v}}{\partial t} + \bar{\rho}\nabla \cdot (\mathbf{vv}) = -\nabla p + \nabla \cdot [\bar{\eta}(\nabla \mathbf{v} + \nabla \mathbf{v}^{\mathrm{T}})] + \bar{\rho} g - \mathbf{F}_{\mathbf{vol}}, \tag{3.2}$$

where $\mathbf{v}$ and t represent the velocity tensor and the flow time, respectively, p is the pressure relative to atmospheric pressure, and $\mathbf{F}_{\mathbf{vol}}$ refers to the volume surface tension. $\bar{\rho}$ and $\bar{\eta}$ are the volume-fraction-averaged density and the volume-fraction-averaged viscosity, respectively. The volume of fluid (VOF) algorithm[1] was utilized to solve equations (3.1) and (3.2). The volume fractions of each phase are computed based on the volume fraction continuity equations:

$$\frac{\mathrm{d}\alpha_L}{\mathrm{d}t} = \frac{\partial \alpha_L}{\partial t} + \mathbf{v} \cdot \nabla \alpha_L = 0, \tag{3.3}$$

$$\alpha_L + \alpha_A = 1. \tag{3.4}$$

where α_L refers to the volume fraction of liquid phase and α_A refers to the volume fraction of air phase. The mesh cells with $\alpha_L = 1$ and $\alpha_L = 0$ are occupied by the liquid phase and air phase, respectively; the mesh cells with $0 < \alpha_L < 1$ contain the liquid-air interface. We defined the interface

location at α_L = 0.5 throughout the thesis. The density $\bar{\rho}$ and viscosity $\bar{\eta}$ are calculated by the following equations:

$$\bar{\rho} = \rho_L \alpha_L + \rho_A \alpha_A, \tag{3.5}$$

$$\bar{\eta} = \eta_L \alpha_L + \eta_A \alpha_A. \tag{3.6}$$

where ρ_A and η_A represent the density and viscosity of air phase, respectively. The force $\mathbf{F_{vol}}$ is modelled by the continuum surface force (CSF) model[2] which treats surface tension as a continuous effect across the liquid-air interface:

$$\mathbf{F_{vol}} = \sigma \frac{2\bar{\rho} k \nabla \alpha_L}{(\rho_L + \rho_A)}. \tag{3.7}$$

The curvature of the liquid-air interface, *k*, is computed using the following equation:

$$k = -(\nabla \cdot \hat{\mathbf{n}}) = \frac{1}{|\mathbf{n}|}\left[\left(\frac{\mathbf{n}}{|\mathbf{n}|} \cdot \nabla\right)|\mathbf{n}| - (\nabla \cdot \mathbf{n})\right], \tag{3.8}$$

where $\hat{\mathbf{n}}$ and $\mathbf{n}$ represent the unit normal and normal to the liquid-air interface, respectively.

For Newtonian fluids, the viscosity η_L is independent of the shear rate, while for viscoplastic fluid, the archetypal characteristics of this fluid is its yield stress, below which the fluid behaves like a solid (solid regime) and beyond which it flows like a liquid (liquid regime). Since the Herschel-Bulkley model (2.14) is discontinuous at the yield stress point, it does not allow calculating the viscosity in a solid state. This issue was solved by Tanner *et al.* (1983) who introduced a bi-viscosity model in order to be able to calculate the apparent viscosity at the shear rate below the critical values $\dot{\gamma}_c$.[3] The critical shear rate marks the transition from solid-like (unyielded) to liquid-like (yielded) behaviour. The viscosity is shear-dependent and given by the bi-viscous model:

$$\eta_L = \begin{cases} \dfrac{\tau_c}{\dot{\gamma}} + K\dot{\gamma}^{n-1} & \text{for } \dot{\gamma} > \dot{\gamma}_c \text{ (liquid regime)} \\ \tau_c \dfrac{2 - \dot{\gamma}/\dot{\gamma}_c}{\dot{\gamma}_c} + K\dot{\gamma}_c^{n-1}\left[(2-n) + (n-1)\dfrac{\dot{\gamma}}{\dot{\gamma}_c}\right] & \text{for } \dot{\gamma} \le \dot{\gamma}_c \text{ (solid regime)} \end{cases}, \tag{3.9}$$

In two-dimensional simulations, the shear rate magnitude $\dot{\gamma}$ is calculated by the following equation:

$$\dot{\gamma} = |\dot{\boldsymbol{\gamma}}| = \left[2\left(\frac{\partial u}{\partial x}\right)^2 + 2\left(\frac{\partial v}{\partial y}\right)^2 + \left(\frac{\partial u}{\partial y} + \frac{\partial v}{\partial x}\right)^2\right]^{1/2} = \left[4\left(\frac{\partial u}{\partial x}\right)^2 + \left(\frac{\partial u}{\partial y} + \frac{\partial v}{\partial x}\right)^2\right]^{1/2}. \quad (3.10)$$

At the critical shear rate $\dot{\gamma}_c$, the shear stress should be close to the yield stress, i.e., $\tau_c + K\dot{\gamma}_c^n \approx \tau_c$. A vanishing $\dot{\gamma}_c$ is hence required and set to 10^{-5} s^{-1} in the simulations.

3.1.2 Numerical schemes

Equations (3.1-3.10) were solved with the Finite Volume Method (FVM) in ANSYS Fluent. The Volume of Fluid (VOF) model with the implicit body force treatment was used to capture the liquid-air interface. The volume fraction discretization was realized by a geo-reconstruction scheme (a piecewise-linear interface approach) which was widely used in literature.[4] The cutoff of the volume fraction was 1×10^{-6}. The Pressure Staggering Option (PRESTO)[5] was employed for the pressure discretization, and the second-order upwind scheme was adopted for discretizing the momentum equations. The gradient discretization was performed by the Green-Gauss node-based gradient method. The pressure-velocity coupling was addressed using distinct algorithms tailored to specific fluid rheology:

For Newtonian fluids (Chapters 4-5), the Pressure-Implicit with Splitting of Operators (PISO) algorithm[6] was employed to accurately capture transient interface dynamics, particularly beneficial for high capillary number ($Ca > 0.1$) conditions.

In contrast, the Semi-Implicit Method for Pressure-Linked Equations (SIMPLE) algorithm[7] was selected for viscoplastic fluids in Chapter 6 due to its superior convergence stability when handling yield stress discontinuities. However, our subsequent investigation in Chapter 7 demonstrates that the PISO algorithm is also a viable and effective approach for simulating viscoplastic flows, successfully capturing their transient behaviour and thereby expanding its scope of application.

The maximum Courant number Cr_{max} is used to evaluate the rationalization of temporal resolution, which is defined by:

$$Cr_{\max} = \frac{u_0 \Delta t}{\Delta x_{\min}} \tag{3.11}$$

where Δt is the time step size and $\Delta x_{\min}$ is the minimum mesh cell size. $Cr_{\max}$ is less than 0.3 in our simulations, which is small enough to avoid the appearance of unphysical wiggles.[8] In all simulations, the time step size is below 10^{-3} s.

3.2 Material and experiment in work 1

3.2.1 Experimental fluid

Three silicone oils (designated by S1, S2, and S3) are used as coating liquids. Their densities (ρ_L) are almost the same (975±2 kg·m^{-3}) and their surface tensions (σ) are also close (21.5±0.2 mN·m^{-1}). Their viscosities are measured with a rotational rheometer (Physica MCR 301, Anton Paar) equipped with a 50 mm cone-and-plate geometry (cone angle: 0.0522 rad; gap: 0.341 mm), as a function of the shear rate at 25℃. Although the silicone oils appear to be slightly shear-thinning, the obtained viscosities are all independent of the shear rate in the shear rate range less than 10 s^{-1} (grey area in Figure 3.2). In the dip coating experiment, the maximum shear rate for the part of the layer we model is inferior to 10 s^{-1}. Therefore, the silicone oils can be treated as Newtonian fluids in the dip coating experiment and simulation. The measured viscosity values at shear rates lower than 10 s^{-1} are equal to 10, 74 and 118 Pa·s for S1, S2 and S3, respectively.

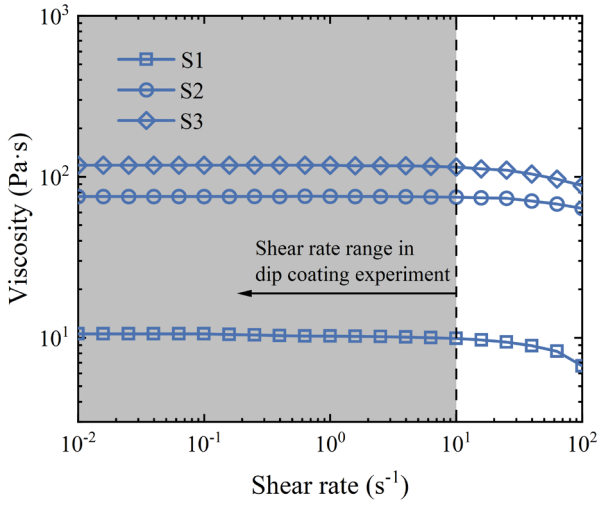

Figure 3.2. Viscosity as a function of the shear rate for three silicone oils (S1, S2 and S3) at 25℃.

3.2.2 Dip coating experiment

Figure 3.3 depicts the coating apparatus developed to validate the simulation and the layer thickness profile model. It is made of a cylindrical container with a diameter equal to its height, 100 mm, and a stainless-steel plate (height: 100 mm; width: 50 mm; thickness: 1 mm) connected to a rotational rheometer (Physica MCR 301, Anton Paar). This rheometer controls the immersion and withdrawal of the plate with a velocity resolution of 1×10^{-3} mm·s^{-1}. Dip coating experiments are carried out at 25°C. The container is filled with silicone oil. The plate is partially immersed in the oil, at an initial depth of 80 mm and is maintained at that position for 5 min so as to be completely wet by the silicone oil.[9] It is then withdrawn vertically from the silicone oil at a constant velocity u_0. The withdrawal velocity is imposed in the range of $2 < u_0 < 8$ mm·s^{-1}. Accordingly, the capillary number ranges from 0.94 to 43.94, which is well beyond the Landau-Levich regime ($Ca < 10^{-2}$). The Bond number Bo ($Bo = \rho_L g r_c^2/\sigma$ with r_c the radius of the container) is 278, indicating that the gravitational force dominates the surface tension. Our previous study[10] also revealed that the surface tension was negligible compared to viscous and gravitational forces under the above conditions. In addition, the inertial force is negligible in the experiment since the Reynolds number Re ($Re = \rho_L u_0 l/\eta_L$ with $l = \sqrt{\eta_L u_0/(\rho_L g)}$ the characteristic length) is significantly less than 1: $8.2\times10^{-5} < Re < 2.3\times10^{-3}$.

The evolution of the layer shape is captured by a camera which takes pictures at 50 frames per second, and focuses on a rectangular zone of dimension 44.8×80.0 mm (448×800 pixels). The pixel size is 0.1×0.1 mm. Each pixel is automatically labelled by the software in the form of (y_p, x_p). During the film thickness measurement, the coordinate origin is set at the intersection between the plate surface and the initial liquid surface, with the x-axis directed along the withdrawal direction and the y-axis perpendicularly to the plate. The pixel at the origin is denoted by (y_{p0}, x_{p0}), and the pixel of the point at the liquid-gas interface is denoted by (y_{p1}, x_{p1}). Therefore, the physical position (h, x) of this point is calculated as $h = 0.1(y_{p1} - y_{p0})$ and $x = 0.1(x_{p1} - x_{p0})$. Both the accuracy and repeatability of the dip

coating experiments are excellent and the edge bead phenomenon (film thickening at the edges of the plate) can be neglected under the condition of this experiment (see Appendix A).

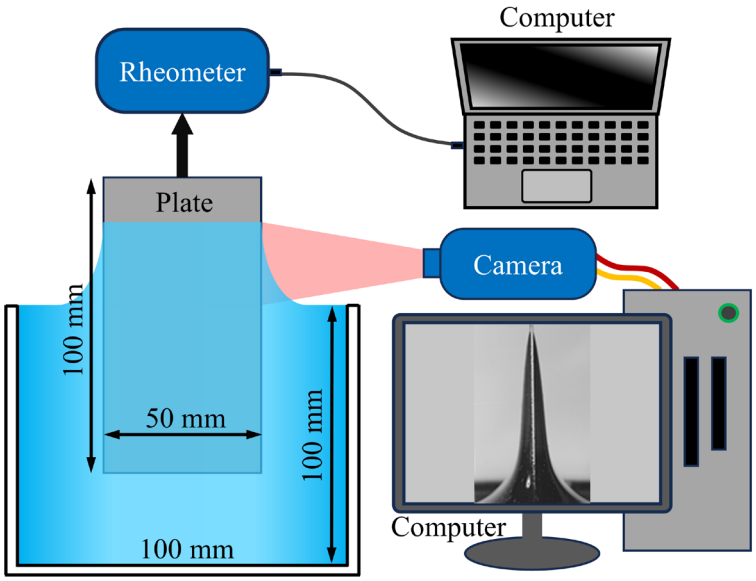

Figure 3.3. Schematic of the experimental apparatus.

3.3 Material and experiment in work 4

3.3.1 Materials

Carbopol gels are known to be viscoplastic, without thixotropic effects.[11-14] These properties suggest that Carbopol gels are well suited for our experiments. The required amount of Carbopol 940 powders (Macklin) was introduced into distilled water while stirring continuously at 600 rpm. After adding all the powder, the solution was stirred for 2 hours to ensure complete dispersion; and then left for 24 hours to make sure that the particles were fully swollen and dissolved. The pH of the solution was elevated via neutralization with an aqueous solution of 35 wt% sodium hydroxide (Aladdin). The pH of the Carbopol solution was measured for each addition of 5 drops of sodium hydroxide solution until a pH = 7 was reached. During the neutralization, the solution was stirred manually at about 30-60 rpm to accelerate the homogeneous dispersion. The addition of sodium hydroxide increased the size of the swollen Carbopol particles, which in turn increased the shear viscosity and yield stress of the resulting Carbopol gels.[15] The gentle stir during neutralization can ensure that the prepared solution was a simple viscoplastic fluid exhibiting no thixotropy. If intensive stirring were applied, the polymers

would break definitely into smaller parts, which would increases the number of polymers in the system that creates depletion forces between the larger polymers, resulting in thixotropy.[16] Two different concentrations of Carbopol gels (0.25 wt% and 0.40 wt%) were prepared, with densities ρ_L of 1014 and 1035 kg·m^{-3}, respectively.

A large number of studies[11,13,17,18] have shown that the rheological behaviour of simple viscoplastic fluids in steady simple shear can be described very well by the Herschel-Bulkley model (2.14). In addition to the Herschel-Bulkley model, Boujlel and Coussot (2012)[19] proposed a pseudo-Herschel-Bulkley model in their study about the non-slotted plate penetrating the Carbopol gels. We present it together with the scalar form of the Herschel-Bulkley model:

$$\begin{aligned} \text{Herschel-Bulkley model: } \tau &= \tau_c + K\dot{\gamma}^n \text{ for } \tau \geq \tau_c \\ \text{Pseudo-Herschel-Bulkley model: } \tau &= \tau_c + Au_0^B \text{ for } \tau \geq \tau_c \end{aligned} \tag{3.12}$$

where A and B will be designated as the pre-factor (in Pa·s^B·m^{-B}) and exponent (-), respectively. While the pseudo-Herschel-Bulkley model is not a constitutive equation of viscoplastic fluids, it gives an apparent relationship between the shear stress and immersion velocity. The pseudo-Herschel-Bulkley model follows the same trend as the Herschel-Bulkley model in terms of the variation of shear stress with the independent variables (immersion velocity and shear rate, respectively), and the yield stress is equal to the shear stress at vanishing immersion velocity and shear rate. In some scenarios, including the immersion process, it is much easier to obtain the velocity of a moving subject than the shear rate. Compared to the Herschel-Bulkley model, the advantage of pseudo-Herschel-Bulkley model is the capability to obtain the yield stress under the condition of under-determined shear rate. However, the pseudo-Herschel-Bulkley model is innately unable to be used to obtain the consistency factor K and flow index n. In addition, the applicability of the pseudo-Herschel-Bulkley model in other geometries, such as cone-and-plate and concentric cylinders, remains to be examined.

3.3.2 Parallel disk method

Rheological tests were carried out on an MCR 301 rotational rheometer (Anton Paar) with two parallel circle disks at 25 °C. The Carbopol gels were first placed on the lower disk and the upper disk was lowered to the measurement gap. Excess gels were removed from the periphery. The shear rate sweep tests were performed to characterize the rheological behaviour of each gel at a steady shear flow. Specifically, the shear rate was increased logarithmically from 10^{-3} to 10^{2} s^{-1} and decreased logarithmically in time from 10^{2} to 10^{-3} s^{-1}. The increasing sweep can bring the gels to a controlled state independent of the previous history more quickly than the method in which a pre-shear is applied, and allowing the gels to rest for some time.[20] The data in the decreasing sweep were recorded at 5 points per decade, which were considered as describing the behaviours of the gels at steady state.[20,21]

Wall slip, which always leads to an underestimation of the shear stress, can be proved by comparing the variation of the shear stress with the shear rate at different measurement gaps. Theoretically, in the absence of wall slip, the measured shear stress should be independent on the gap. However, for the slipping fluids, the wall slip is more pronounced for smaller gaps at low shear rates, that is, the smaller the gap, the lower the measured shear stress.[22,23] To evaluate wall slip effect, tests were performed at three different gaps (i.e., 1.0, 1.5, and 2.0 mm) and the corresponding data plotted as shear stress versus shear rate are shown in Figure 3.4. At high shear rates, the shear stresses are well above the yield stress, the gels are fully yielding in a bulk flow. The wall slip is negligible with respect to the deformation and the flow of the fully yielding gels. Therefore, the shear stresses at different gaps are well superimposed. However, the measured flow curve shows a kink when the shear stress is relatively low, and the shear rate does not tend to zero at the yield stress. Moreover, the shear stresses measured with different gaps are different for the same shear rates. Specifically, the shear stress is greatest for a gap of 2.0 mm, followed by 1.5 mm, and the smallest is 1.0 mm. Between the yield stress and the kink, there is a transition regime where wall slip dominates the overall rheological behaviour and yielding makes only a small contribution. At very low shear rates, the shear stresses are less than

the yield stress, and the gels slip like a solid between the two disks in a full slip regime. Interestingly, the flow curves in this regime exhibit an apparent yield stress also known as the slip yield stress, which is interpreted as the lowest stress above which steady slip motion is possible.[24] The slip yield stress should not be confused with the bulk yield stress. To be concluded, the rheological tests show that wall slip has a strong effect on the test and further illustrate that the results are only reliable in the bulk flow regime. The parameters of the Herschel-Bulkley model were determined for various Carbopol gels by fitting the model with the data in the bulk flow regime, and the parameters are summarized in Table 3.1.

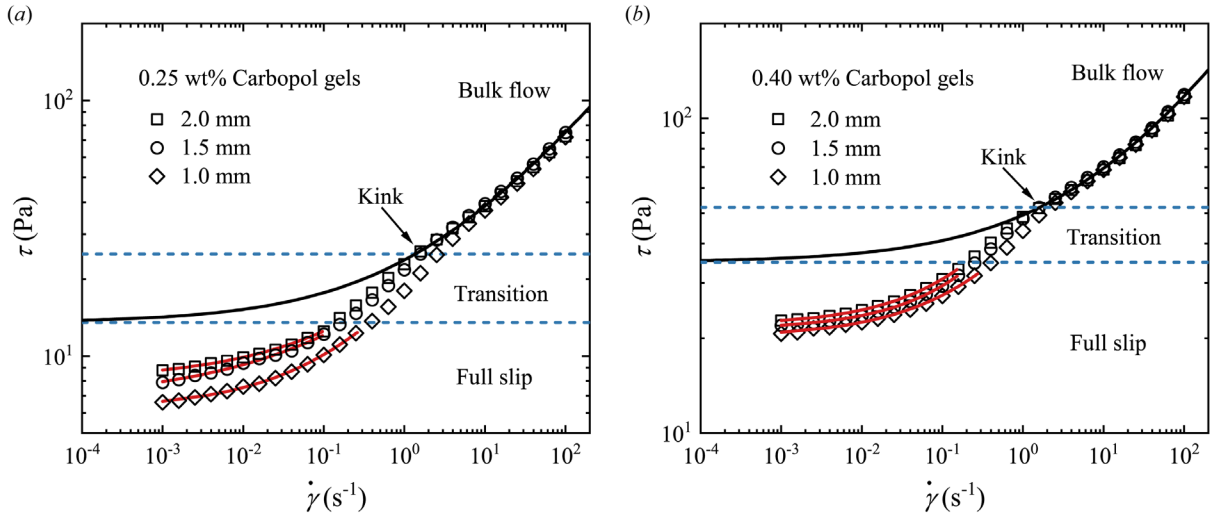

Figure 3.4. Steady-state flow curves of Carbopol gels obtained from an increasing-decreasing shear rate sweep test by the parallel disk method. The black continuous lines and red continuous lines correspond to the Herschel-Bulkley model in the bulk flow regime (see parameters in Table 3.1) and the full slip regime, respectively. (*a*) 0.25 wt% Carbopol gels; (*b*) 0.40 wt% Carbopol gels.

Table 3.1 Parameters of the Herschel-Bulkley model for Carbopol gels at 25 °C

Materials	τ_c (Pa)	K (Pa·s^n)	n
0.25 wt% Carbopol	14.84	9.83	0.39
0.40 wt% Carbopol	34.90	14.39	0.38

3.3.3 Immersion device platform

The immersion device consists of a slotted plate connected to the MCR 301 rheometer via a shaft, as depicted in Figure 3.5(*a*). All the immersion tests were conducted in a 60 mm long and 100 mm deep container. The distance between the plate and the container wall, *W*, is 40 mm. The velocity control accuracy and force measurement resolution of the rheometer are 1×10^{-3} mm·s^{-1} and 1×10^{-5} N, respectively. As displayed in Figure 3.5(*b*, *c*), the plates utilized in the immersion test are 150 mm in length (*L*), 50 mm in width (W_p), 1 mm in thickness (*E*), 45 mm in slot width (W_s), and in various slot heights (*S*), slot pitches (*P*) and slot numbers (*N*). The geometric parameters of the different slotted plates are more detailed in Table 3.1.

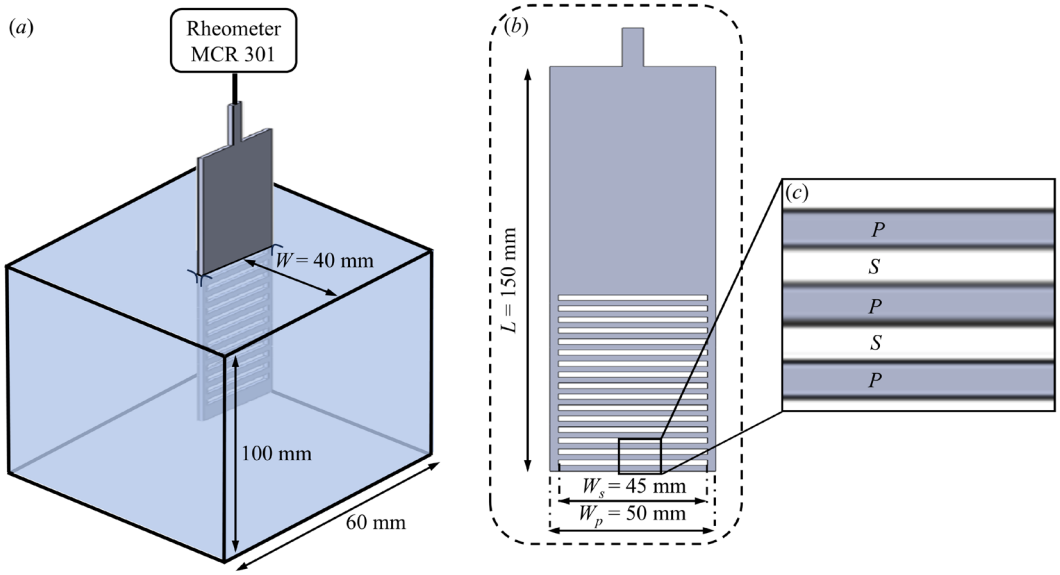

Figure 3.5. Immersion device platform: (*a*) slotted plate connected to the MCR 301 rheometer via a shaft, (*b*) schematic of the slotted plate, and (*c*) a zoomed-in view of the slotted plate.

Table 3.1 Geometric parameters of the slotted plates used in the immersion test

Plate identification	Slot pitch *P* (mm)	Slot height *S* (mm)	Slot number *N* (-)	Unchanged geometric parameters
P1S2N17	1	2	17	Plate length *L* (mm) = 150
P2S2N17	2	2	17	Plate width W_p (mm) = 50

P2S2N14	2	2	14	Plate thickness E (mm) = 1 Slot width W_s (mm) = 45
P2S2N11	2	2	11	
P2S3N14	2	3	14	
P2S4N11	2	4	11	

3.3.4 Immersion procedure

The immersion tests were performed at 25 ℃. The gels were slowly poured into the container until the container was filled, with great care not to incorporate any air bubbles. The surface of the gels was smoothed with a spatula after the gels were sightly stirred. The plate was pre-coated with gels to exhaust the air in slots to prevent the formation of air bubbles during the immersion which affects the accuracy and repeatability of the test. The gels on the plate surface were removed by the spatula but the gels in the slots were retained, also with great care not to entrain any bubbles. The gels were allowed to rest for some time before the immersion to ensure residual stress relaxation.[19,25] Before the immersion test, the rheometer was calibrated to give a zero reading force. That is to say, that the weight of the plate and pre-coated gels in slots were subtracted. The plate was then lowered by the rheometer at a constant velocity, u_0, and the force, F, exerted on the plate was recorded as a function of the immersion depth, x, i.e., the distance between the plate tip and the initial horizontal gel surface. It is specified in Chapter 7 that the upward force is positive.

Reference

1. Hirt CW, Nichols BD. Volume of fluid (VOF) method for the dynamics of free boundaries. *J. Comput. Phys.* 1981;39(1):201-225.
2. Brackbill JU, Kothe DB, Zemach C. A continuum method for modeling surface tension. *J. Comput. Phys.* 1992;100(2):335-354.
3. Tanner R, Milthorpe J. Numerical simulation of the flow of fluids with yield stress. *Numer Meth Lami Turb Flow Seattle.* 1983:680-690.
4. Xie H, Hu J, Dai G. Numerical simulation on flow behavior of twin-liquid films over a vertical plate with an open window. *AIChE J.* 2018;64(4):1458-1468.
5. Patankar SV. *Numerical Heat Transfer and Fluid Flow*. Boca Raton: CRC Press; 1980.
6. Issa RI. Solution of the implicitly discretised fluid flow equations by operator-splitting. *J. Comput. Phys.* 1986;62(1):40-65.

7. Patankar SV, Spalding DB. A calculation procedure for heat, mass and momentum transfer in three-dimensional parabolic flows. *Int. J. Heat Mass Transfer.* 1972;15(10):1787-1806.

8. Filali A, Khezzar L, Mitsoulis E. Some experiences with the numerical simulation of Newtonian and Bingham fluids in dip coating. *Comput. Fluids.* 2013;82:110-121.

9. Chen MM, Zhang XM, Ma JP, Chen SC, Chen WX, Feng LF. Experimental study on film thickness and the problem of free surface film flow in dip coating. *Asia-Pac. J. Chem. Eng.* 2016;11(5):695-704.

10. Zhang H-K, Yin Y-R, Hu G-H, Zhang X-M. Temporal evolution of demarcations between the unsteady and steady regions and between the film and meniscus during dip coating with vertical withdrawal of Newtonian fluids. *Chem. Eng. Sci.* 2024;293:120052.

11. Coussot P. Yield stress fluid flows: a review of experimental data. *J Non-Newton Fluid.* 2014;211:31-49.

12. Coussot P, Tocquer L, Lanos C, Ovarlez G. Macroscopic vs. local rheology of yield stress fluids. *J Non-Newton Fluid.* 2009;158(1-3):85-90.

13. Aktas S, Kalyon DM, Marín-Santibáñez BM, Pérez-González J. Shear viscosity and wall slip behavior of a viscoplastic hydrogel. *J. Rheol.* 2014;58(2):513-535.

14. Ortega-Avila JF, Pérez-González J, Marín-Santibáñez BM, et al. Axial annular flow of a viscoplastic microgel with wall slip. *J. Rheol.* 2016;60(3):503-515.

15. Medina-Bañuelos EF, Marín-Santibáñez BM, Pérez-González J, Malik M, Kalyon DM. Tangential annular (Couette) flow of a viscoplastic microgel with wall slip. *J. Rheol.* 2017;61(5):1007-1022.

16. Dinkgreve M, Fazilati M, Denn MM, Bonn D. Carbopol: From a simple to a thixotropic yield stress fluid. *J. Rheol.* 2018;62(3):773-780.

17. Beaulne M, Mitsoulis E. Creeping motion of a sphere in tubes filled with Herschel-Bulkley fluids. *J Non-Newton Fluid.* 1997;72(1):55-71.

18. Geffrault A, Bessaies-Bey H, Roussel N, Coussot P. Extensional gravity-rheometry (EGR) for yield stress fluids. *J. Rheol.* 2021;65(5):887-901.

19. Boujlel J, Coussot P. Measuring yield stress: a new, practical, and precise technique derived from detailed penetrometry analysis. *Rheol. Acta.* 2012;51(10):867-882.

20. Coussot P. *Rheometry of pastes, suspensions, and granular materials (Applications in industry and environment)*: Wiley; 2005.

21. Ovarlez G, Cohen-Addad S, Krishan K, Goyon J, Coussot P. On the existence of a simple yield stress fluid behavior. *J Non-Newton Fluid.* 2013;193:68-79.

22. Zhu L, Sun N, Papadopoulos K, De Kee D. A slotted plate device for measuring static yield stress. *J. Rheol.* 2001;45(5):1105-1122.

23. Barnes HA. A review of the slip (wall depletion) of polymer solutions, emulsions and particle suspensions in viscometers: its cause, character, and cure. *J Non-Newton Fluid.* 1995;56(3):221-251.

24. Cloitre M, Bonnecaze RT. A review on wall slip in high solid dispersions. *Rheol. Acta.* 2017;56(3):283-305.

25. Zhang X-M, Chen M-M, Ma J-P, Chen W-X, Feng L-F. Numerical simulation and experimental validation of liquid-film-flow characteristics in dip coating for non-Newtonian fluids. *Polym. Eng. Sci.* 2016;56(9):1070-1078.

4 Spatial-temporal evolution of a Newtonian liquid layer on a fully wetting plate during dip coating

This chapter addresses the layer thickness profile of Newtonian fluids upon dip coating with vertical withdrawal in the visco-gravity regime. The past studies have been focusing on the thickness profile of the layer tip. However, the previous models have been unable to accurately predict this part, due to assuming that the film thickness only approaches its asymptotic value near the horizontal liquid surface. This assumption is inconsistent with the fact that the film thickness approaches to an asymptotic thickness at a location significantly higher above the horizontal liquid surface. The present work shows that the layer thins along the withdrawal direction in the visco-gravity regime and is self-similar at dimensionless scales. By fully considering the characteristics of the thickness profile, a model is proposed to predict the thickness of the entire layer. The validity range of the model is investigated for different Reynolds number values, showing that this model agrees well with experimental and simulated results over a wide range of Reynolds numbers.

4.1 Introduction

During the dip coating of fully wetting plate with Newtonian fluid, three types of withdrawal regimes may appear for different values of capillary number, namely the visco-capillary regime, the transition regime, and the visco-gravity regime.[1] Figure 4.1(*b*) shows that the layer in the visco-capillary regime is uniform everywhere but at the thinned part (layer's tip) and the meniscus. This uniform part occupies the largest zone of the layer. Therefore, the uniform film thickness is the most important parameter for dip coating in this regime. It is controlled by the viscous and capillary forces, and can be characterized as a function of the capillary number Ca ($Ca = \eta_L u_0/\sigma$), where η_L is the liquid viscosity, u_0 is the withdrawal velocity and σ is the surface tension.[2] Experiments[3] prove that this regime holds for $Ca < 10^{-2}$. In the transition regime ($10^{-2} < Ca < 1$), the effect of gravity is enhanced and the uniform film thickness is controlled by the viscous, gravity, and capillary forces.

Many authors studied in detail this regime by using different methods, getting slightly different predictions for the uniform film thickness.[4-7]

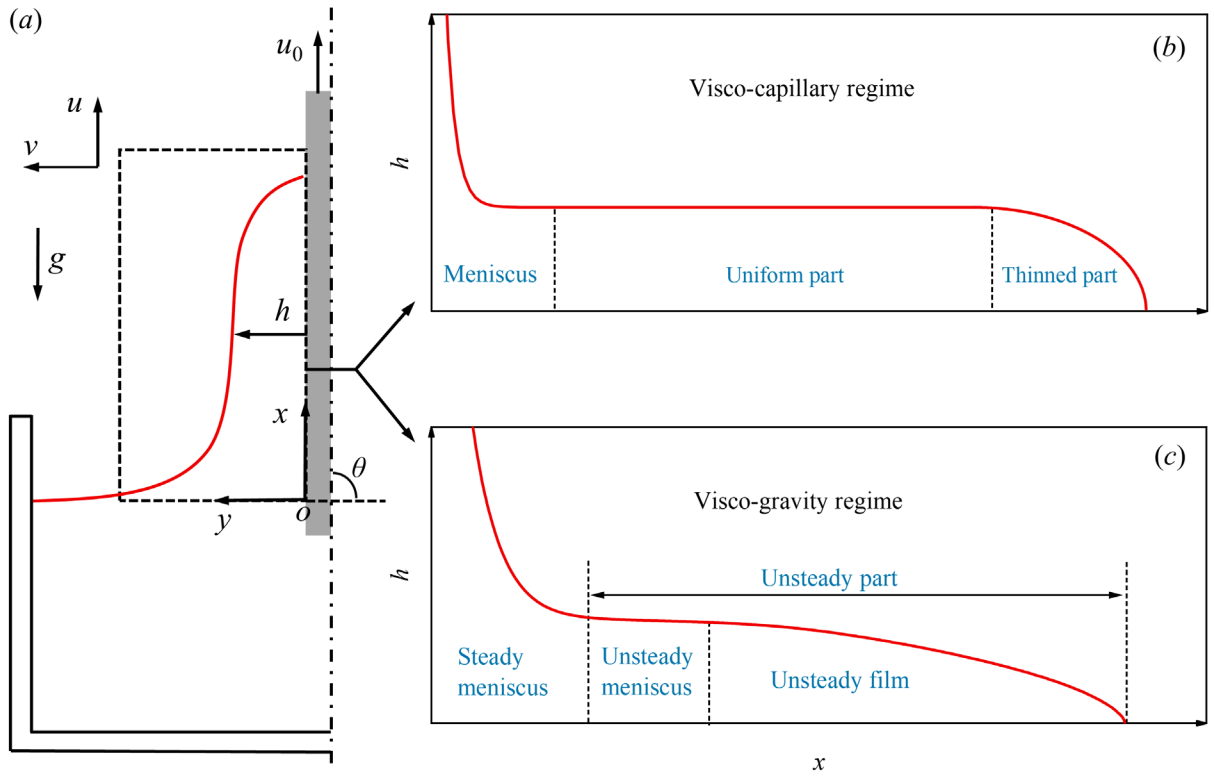

Figure 4.1. Liquid layer being entrained and deposited on a plate being withdrawn from a liquid container. (*a*) Schematic view of the withdrawal process where the region of interest is marked by a black dashed rectangle, which is then rotated; (*b*) layer thickness profile (thickness h versus height x) in the visco-capillary regime; (*c*) layer thickness profile in the visco-gravity regime.

In the visco-gravity regime ($Ca > 1$), the layer thickness is determined by the balance between the viscous force and gravity.[8] The layer after a long withdrawal time consists of a steady meniscus and an unsteady film which local thickness decreases with time, connecting through an unsteady meniscus,[9] as depicted in Figure 4.1(*c*). In the subsequent discussion and modelling, we refer to the unsteady film and the unsteady meniscus collectively as a single part: the unsteady part. The thickness of the liquid film region near the horizontal liquid surface approaches infinitely close to a certain thickness over time, yet never actually reaches or exceeds it. This thickness is referred to as the

asymptotic film thickness. Under the effect of gravity, the entire layer thins along the withdrawal direction. Moreover, the length of the unsteady part progresses fast with the withdrawal, occupying the most portion of the layer.

The dip coating of industrial polymer melts and solutions is generally conducted in the visco-gravity regime due to the high viscosities of the involved liquids (from tens to hundreds Pa·s). Additionally, in this regime, the layer (which thickness reduces along the withdrawal direction) has the potential to serve as a natural template for the preparation of films with gradient thickness and functionality. Therefore, modelling the layer thickness in viscos-gravity regime is of both scientifically and industrially significant. Derjaguin's model suggests that the thickness profile of the unsteady part is a parabola.[8] This model was subsequently adopted and developed by many other authors.[10-12] However, their models present two important unsolved issues. Firstly, the models focus on the thickness profile far away from the meniscus and thus cannot describe the other parts. Secondly, even far away from the meniscus, the models predict a thicker layer than in the experiments and simulations, due to several simplifications. The analytical modelling of the entire layer is exceedingly challenging due to the intricate spatial-temporal dynamics of the thickness and substantial flow variations between the different parts of the layer.[9] It is suggested to model the distinct parts of the layer separately and combine the models to derive a composite model for the entire layer. The existing composite model can fairly well calculate the entire layer's thickness profile for the dip coating with a withdrawal angle θ (cf. Figure 4.1 for the definition of withdrawal angle) smaller than 35°.[13] But, when the withdrawal angle is larger than 35°, in particular at 90° (vertical withdrawal), this composite model is invalid. To conclude, for the dip coating with vertical withdrawal which is a widely used dip coating mode, a robust model predicting the thickness profile of entire layer is still missing.

This chapter aims to model the thickness profile of the entire layer upon vertical dip coating in the visco-gravity regime, based on the transient layer formation mechanism. Section 4.2 introduces the specific settings of the performed numerical simulations. After validating the simulation in section

4.3.1, the factors controlling the layer formation are determined in section 4.3.2. In section 4.3.3, the characteristics of the layer thickness profile over a long withdrawal time are discussed. The unsteady part and steady meniscus are separately modelled and then combined into a composite model of the entire layer in section 4.3.4. Finally, in section 4.3.5, the results of the model are compared to the experimental and simulated results.

4.2 Simulation settings

4.2.1 Boundary and initial conditions

Figure 4.2 depicts the computational domain with the boundary conditions and initial conditions used for the numerical simulation. Note that the figure is rotated of 90°, so that gravity is directed horizontally towards the left side of the picture. The size of the computational domain varies with the withdrawal velocities and liquid properties, more specifically, scaling with l ($l = \sqrt{\eta_L u_0/(\rho_L g)}$). The boundary *AB* (length: 150*l*) is the plate moving along the *x* direction at a constant velocity u_0. The gravity direction is opposite to the withdrawal direction. On the outlets *BC* (length: 10*l*), *CD* (length: 90*l*), and *DE* (length: 40*l*), the pressure is imposed as the standard atmospheric pressure. The boundaries *EF* (length: 60*l*) and *FA* (length: 50*l*) are set as static walls. The numerical simulations impose the no-slip boundary conditions on the plate surface and at the static walls. The initial depth of the liquid (the distance between the initial liquid surface and the bottom *FA*) is 50*l*, which is large enough to ensure that the container bottom does not impact the shape of the coated layer during dip coating. The liquid depth varies typically of 0.9*l* during the simulations. In addition, the large liquid depth and large wall-plate distance allow a difference of less than 2.5% between the initial and final liquid surface levels without influence on the flow and the layer thickness profile. It is crucial to note that no contact angle boundary condition was applied at the moving plate or container walls. The liquid phase was introduced solely through a rectangular patch in the initial condition. Therefore, the 90-degree contact angle apparent in the results arises purely from this initial geometry and is not an explicitly defined model parameter.

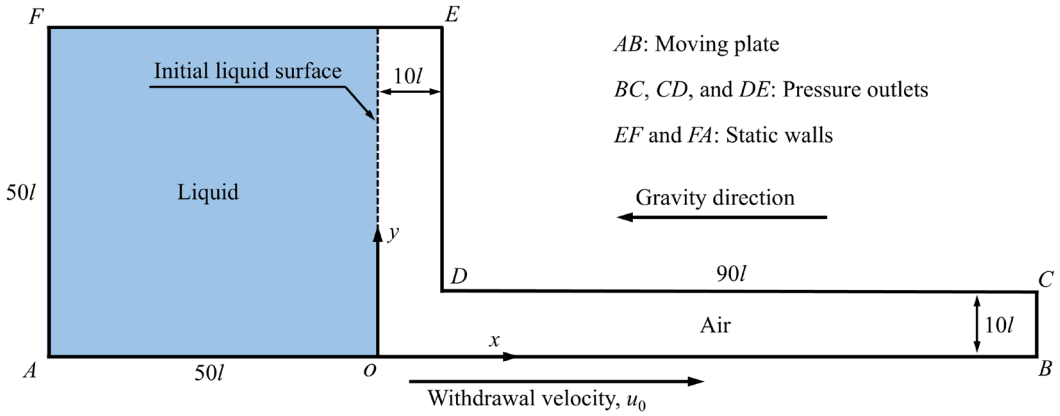

Figure 4.2. Schematic of the computational domain used for the numerical simulation with the boundary and initial conditions.

4.2.2 Mesh independence

Figure 4.3 shows the computational domain and the mesh cell size of each edge. The domain is spatially discretized with quadrilateral mesh cells. The extreme refinement of the mesh makes it difficult to display clearly the cell distribution, thus only the mesh cells near the plate and the initial liquid surface are zoomed in and the mesh cell size of each edge is clarified. The mesh cell size of edge $A'B'$ and the parallel edges $D'D$ and $E'E$ is $2l/n_m$, where n_m is the number of mesh cells per length of l. Note that l is not the length of the edge but the characteristic length defined by $l = \sqrt{\eta_L u_0/(\rho_L g)}$. The mesh cell size of edges $B'B$ and $F'A$ and their parallel edges DC, and $D'A'$, DB' and CB are l/n_m. The mesh cell size in the region (the rectangle $FF'D'E'$) far from the liquid-air interface is larger than other regions, in order to reduce the mesh cell numbers and the computational cost. Specifically, the edge $A'A$ is discretized into $20n$ non-uniform segments, with the mesh cell size increasing from $2l/n_m$ to $5l/n_m$ from point A' to point A. The parallel edges $D'F'$ and $E'F$ are discretized with the same method. The edge $F'F$ is discretized into $10n$ non-uniform segments, which size increases from l/n_m to $15l/n_m$ from point F' to point F, and their parallel edges $D'E'$ and DE are discretized in the same manner. Gradual variation in mesh cell size helps avoid slow convergence, large interpolation errors and even non-physical results caused by the large difference of size between adjacent mesh cells.

Although different edges have different mesh cell sizes, n_m is constant for a given mesh. Varying n_m enables the adjustment of overall mesh resolution. The layer thickness profiles for three different mesh cell sizes are compared (η_L = 1 Pa·s, u_0 = 1.86 mm·s^{-1}): n_m = 20, 40, and 60. When n_m increases from 20 to 60, the discrepancies on the layer profile gradually decrease and the profiles generated with n_m = 40 and n_m = 60 superimpose well with each other (Figure 4.4). The mesh with n_m = 40 is thus adopted for subsequent simulations to maintain a good balance between the accuracy and the computational cost.

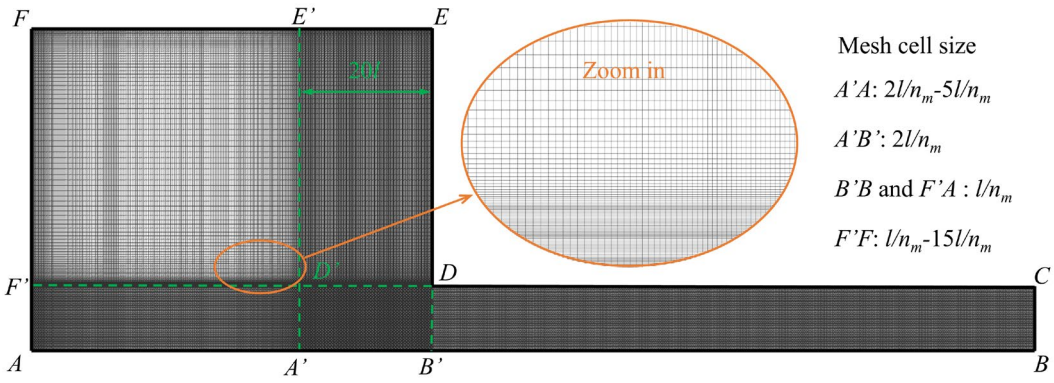

Figure 4.3. Computational domain and mesh cell size of each edge. The circle is a zoom of the mesh to show the variation of the mesh cell size.

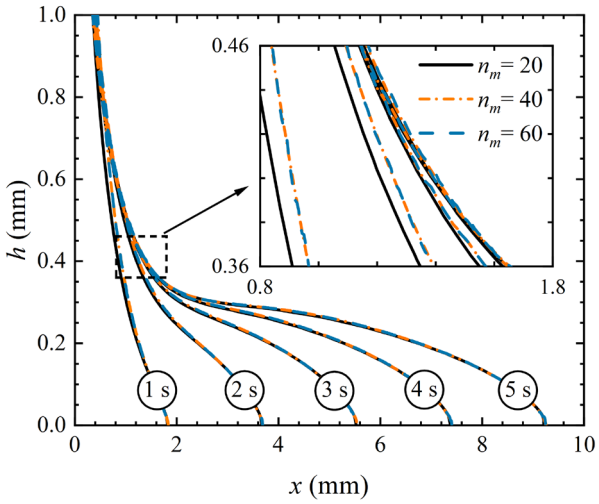

Figure 4.4. Simulated layer profiles for three different mesh refinements (n_m = 20, 40, and 60). Viscosity η_L = 1 Pa·s; withdrawal velocity u_0 = 1.86 mm·s^{-1}; withdrawal time t = 1-5 s. The curves in the dashed rectangular domain are enlarged to show the differences.

4.3 Results and discussions

4.3.1 Validity of the simulation

Figure 4.5(*a*-*c*) compare the layer thickness profile between the experiment and simulation at a withdrawal velocity of 2 mm·s^{-1}, a viscosity of 74 Pa·s, and a withdrawal time of 34.5 s. They agree well with each other, validating the simulation. Moreover, the simulation confirms that the velocity distribution in the meniscus is quite different from that in the film. To further analyse the flow in the film, velocity profiles (Figure 4.5*d*), derivatives of u (Figure 4.5*e*), and derivatives of v (Figure 4.5*f*) are compared on the lines $y = 0.2l$, $y = 0.5l$ and $y = l$. In the region far above the liquid surface, the velocity component u dominates, while the component v is vanishing, indicating that the flow is one-dimensional. However, in the region close to the liquid surface, both u and v are finite, showing in a two-dimensional flow. We further analysed the distribution of velocity derivatives in the meniscus region. In general, the magnitudes of velocity derivatives display the following characteristics: $\partial u/\partial y > \partial u/\partial x$; $\partial u/\partial x \approx \partial v/\partial y$; $\partial v/\partial y > \partial v/\partial x$.

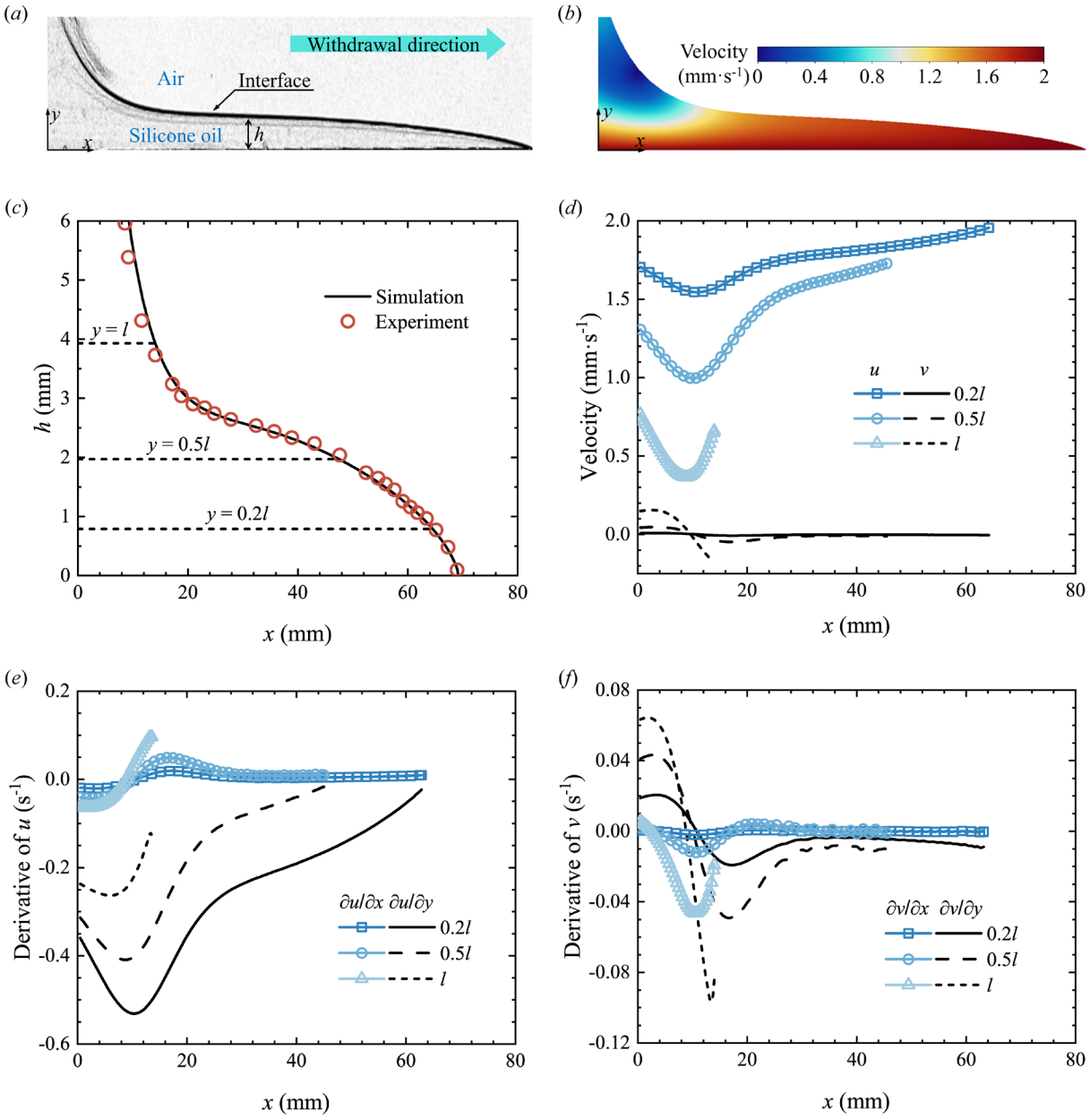

Figure 4.5. Validation of the simulations. Viscosity = 74 Pa·s; withdrawal velocity = 2 mm·s^{-1}; withdrawal time = 34.5 s. (*a*) Image obtained by binarization from photograph taken by the camera; the black curve indicates the interface between silicone oil and air; (*b*) contours of velocity magnitude in the liquid phase obtained from the simulation; (*c*) comparison of the layer thickness profile obtained from the experiment (circle symbol) and the simulation (solid curve); (*d*) velocity distributions, (*e*) derivatives of u and (*f*) derivatives of v on lines $y = 0.2l$, $y = 0.5l$ and $y = l$.

4.3.2 Factors controlling the layer formation

Many studies suggest that the viscous force increases the asymptotic thickness of the layer while gravity opposes it. However, their influence on the layer thickness profile remains unrevealed. Figure 4.6(*a*-*c*) compare the layer thickness profiles for different viscosities, withdrawal velocities and densities. The results show that the larger the viscous force, the larger the entire layer thickness; while gravity has the opposite effect to the viscous force.

To further investigate the effect of viscous force and gravity on the layer thickness profile and its gradient, three dimensionless variables are defined: $\bar{t} = u_0 t/l$ the dimensionless time, $\bar{h} = h/l$ the dimensionless layer thickness and $\bar{x} = x/l$ the dimensionless height, where $l = \sqrt{\eta_L u_0/(\rho_L g)}$. Figure 4.6(*d*) shows that the dimensionless layer thickness profiles of different viscosities, withdrawal velocities and densities nearly superimpose when the dimensionless times are the same. This phenomenon implies that the dimensionless layer thickness profile is a function of $\bar{x}$ and $\bar{t}$, i.e., $\bar{h} = f(\bar{x}, \bar{t})$, which is very valuable for modelling the layer thickness profile following.

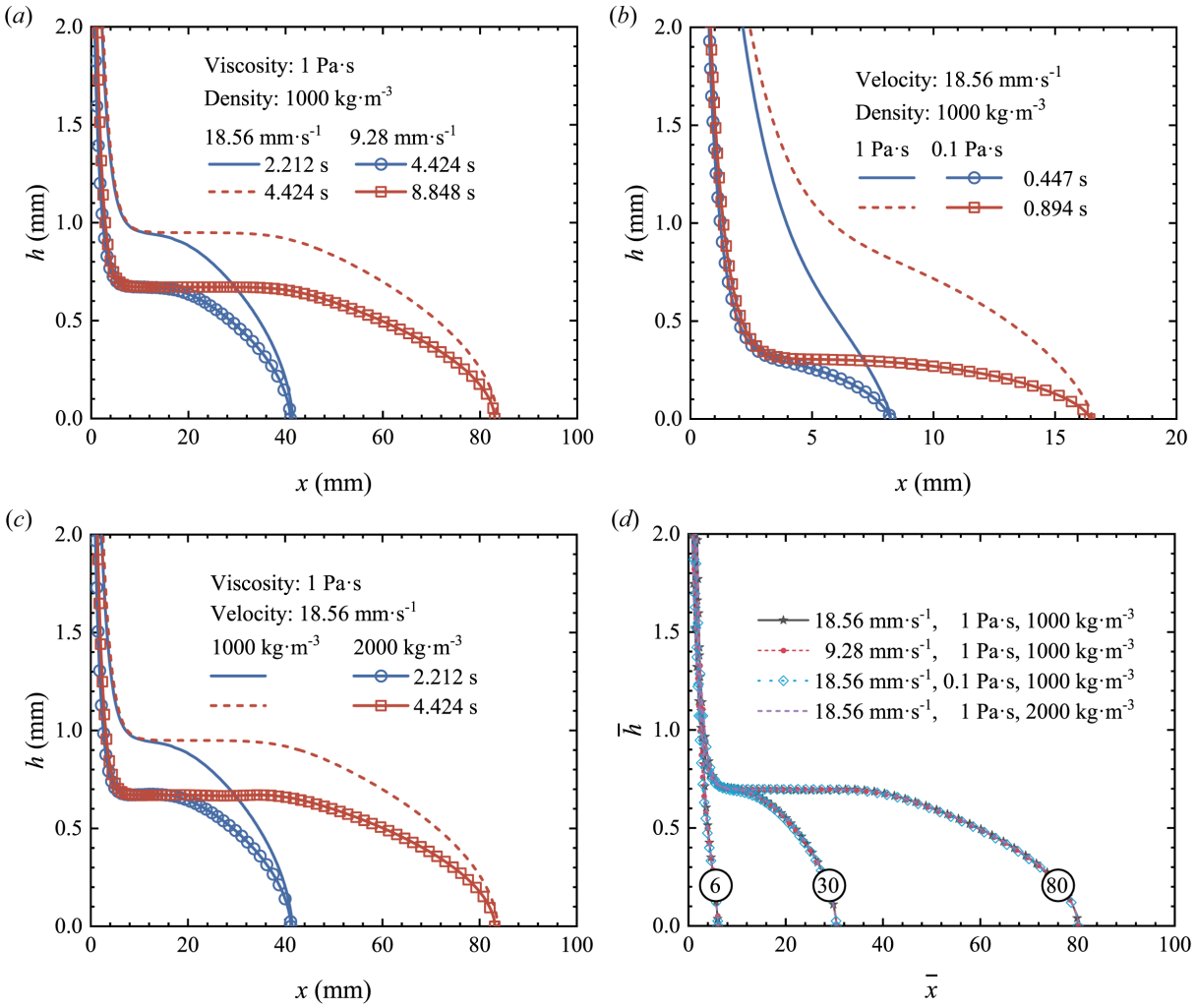

Figure 4.6. Temporal evolution of layer thickness profiles for different withdrawal velocities (*a*), liquid viscosities (*b*) and liquid densities (*c*); (*d*) temporal evolution of dimensionless layer thickness profiles for different withdrawal velocities, liquid viscosities, and liquid densities. The curves in Figure 4.6(*d*) are labelled with the corresponding dimensionless time $\bar{t}$ = 6, 30 and 80.

4.3.3 Characteristics of the layer thickness profile

Figure 4.7A and B depict the dimensionless layer thickness $\bar{h}$ profiles at different times $\bar{t}$. It is worth noting that the simulation can capture in the computational domain the entire layer for $\bar{t} < 100$, and only a portion of the layer for $\bar{t} > 100$. Figure 4.7(*a*) shows that the entire layer thins along the withdrawal direction for short withdrawal times (say $\bar{t}$ = 31). After a long withdrawal time (say $\bar{t}$ = 93), the thickness of the layer near the horizontal liquid surface approaches an asymptotic thickness

$\bar{h}_0$, but remains unsteady and non-uniform. The asymptotic thickness obtained by this simulation agrees well with that obtained by Benilov and Zubkov's simulation[13] (blue circle in Figure 4.7*a*), which further validates the simulation. As demonstrated in Figure 4.7(*b*), the layer thins along the withdrawal direction in an unsteady manner. The thinning part progresses with the withdrawal time, occupying a larger portion of the layer.

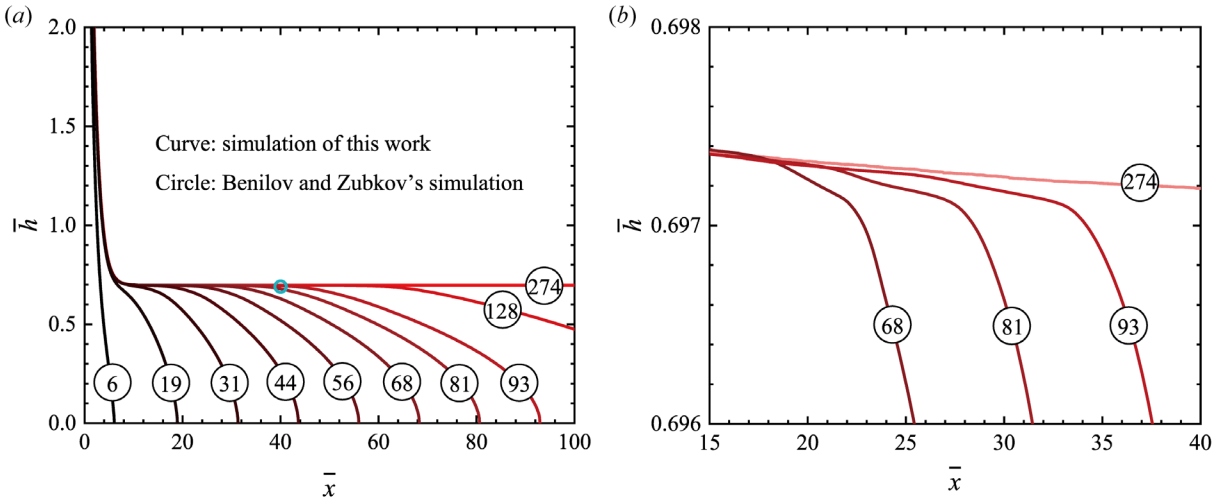

Figure 4.7. Temporal evolution of dimensionless thickness $\bar{h}$ profile with the dimensionless time $\bar{t}$ obtained from the simulation result. All the curves are labelled with the corresponding dimensionless time $\bar{t}$. (*a*) Entire layer; (*b*) Zoomed-in view in the range of $15 < \bar{x} < 40$ and $0.696 < \bar{h} < 0.698$. Viscosity η_L = 1 Pa·s; withdrawal velocity u_0 = 1.86 mm·s^{-1}; density ρ_L = 1000 kg·m^{-3}.

4.3.4 Modelling of the transient layer thickness profile

Our previous experiments and simulations show that after a period of withdrawal, the coating layer consists of an unsteady part and a steady meniscus. Moreover, the spatial-temporal evolutions of the two parts are dramatically different. Therefore, it is unlikely to directly develop a model for the entire layer. The modelling strategy of Benilov and Zubkov is adopted here.[13] The thickness profile models of the unsteady part and the steady meniscus are first established separately and then combined into a composite model for the entire layer. Prior to the modelling, we need to construct a theoretical

framework to describe the flow of the entire layer. The flow during the coating process is considered two-dimensional and is governed by the following equations:

$$\frac{\partial u}{\partial x}+\frac{\partial v}{\partial y}=0, \tag{4.1}$$

$$\frac{\partial u}{\partial t}+u\frac{\partial u}{\partial x}+v\frac{\partial u}{\partial y}=-g+\frac{1}{\rho_L}\left(-\frac{\partial p}{\partial x}+\frac{\partial \tau_{xx}}{\partial x}+\frac{\partial \tau_{xy}}{\partial y}\right), \tag{4.2}$$

$$\frac{\partial v}{\partial t}+u\frac{\partial v}{\partial x}+v\frac{\partial v}{\partial y}=\frac{1}{\rho_L}\left(-\frac{\partial p}{\partial y}+\frac{\partial \tau_{yx}}{\partial x}+\frac{\partial \tau_{yy}}{\partial y}\right). \tag{4.3}$$

The fluid behaviour can be described by the constitutive equation $\tau_{ij}=\eta_L e_{ij}$, where τ_{ij} is the deviatoric stress tensor and the strain rate tensor reads $e_{ij}=(\partial u_i/\partial x_j)+(\partial u_j/\partial x_i)$. Thus, the stress components can be expressed as

$$\tau_{xx}=2\eta_L\frac{\partial u}{\partial x}, \tag{4.4}$$

$$\tau_{yy}=2\eta_L\frac{\partial v}{\partial y}, \tag{4.5}$$

$$\tau_{xy}=\eta_L\left(\frac{\partial u}{\partial y}+\frac{\partial v}{\partial x}\right)=\tau_{yx}. \tag{4.6}$$

The no-slip and impermeable conditions on the plate yield

$$u=u_0 \text{ and } v=0 \text{ at } y=0. \tag{4.7}$$

The stress continuity at the liquid-air interface requires that

$$\mathbf{S}\cdot\mathbf{n}=0 \text{ at } y=h, \tag{4.8}$$

where

$$\mathbf{S}=\begin{pmatrix} 2\eta_L\frac{\partial u}{\partial x}-p & \eta_L\left(\frac{\partial u}{\partial y}+\frac{\partial v}{\partial x}\right) \\ \eta_L\left(\frac{\partial u}{\partial y}+\frac{\partial v}{\partial x}\right) & 2\eta_L\frac{\partial v}{\partial y}-p \end{pmatrix} \text{ and } \mathbf{n}=\begin{pmatrix}\frac{\partial h}{\partial x}\\ -1\end{pmatrix} \tag{4.9}$$

are the stress tensor at the liquid-gas interface and the normal to the interface, respectively.

The kinematic condition at the interface can be written in a form reflecting mass conservation:

$$\frac{\partial h}{\partial t}+\frac{\partial q}{\partial x}=0, \tag{4.10}$$

where $q=\int_0^h u\mathrm{d}y$ refers to the volumetric flow rate.

Equations (4.1-4.10) are then expressed in a dimensionless form. The dimensionless layer thickness profiles for different withdrawal velocities, liquid viscosities, and liquid densities collapse onto a single curve at the same dimensionless time (cf. Figure 4.6*d*), showing the rationality of the choice of characteristic length (l) and characteristic velocity (u_0). Therefore, all variables can be rescaled to introduce the following dimensionless variables:

$$\bar{x}=\frac{x}{l},\bar{y}=\frac{y}{l},\bar{u}=\frac{u}{u_0},\bar{v}=\frac{v}{u_0},\bar{h}=\frac{h}{l},\bar{t}=\frac{tu_0}{l},\bar{p}=\frac{p}{\rho_L gl}. \tag{4.11}$$

Substituting the dimensionless variables into equations (4.1-4.10) yields equations (4.12-4.18):

$$\frac{\partial \bar{u}}{\partial \bar{x}}+\frac{\partial \bar{v}}{\partial \bar{y}}=0, \tag{4.12}$$

$$\left(\frac{\partial \bar{u}}{\partial \bar{t}}+\bar{u}\frac{\partial \bar{u}}{\partial \bar{x}}+\bar{v}\frac{\partial \bar{u}}{\partial \bar{y}}\right)Re=-1-\frac{\partial \bar{p}}{\partial \bar{x}}+\frac{\partial^2 \bar{u}}{\partial \bar{x}^2}+\frac{\partial^2 \bar{u}}{\partial \bar{y}^2}, \tag{4.13}$$

$$\left(\frac{\partial \bar{v}}{\partial \bar{t}}+\bar{u}\frac{\partial \bar{v}}{\partial \bar{x}}+\bar{v}\frac{\partial \bar{v}}{\partial \bar{y}}\right)Re=-\frac{\partial \bar{p}}{\partial \bar{y}}+\frac{\partial^2 \bar{v}}{\partial \bar{x}^2}+\frac{\partial^2 \bar{v}}{\partial \bar{y}^2}, \tag{4.14}$$

$$\bar{u}=1 \text{ and } \bar{v}=0 \text{ at } \bar{y}=0, \tag{4.15}$$

$$\left(2\frac{\partial \bar{u}}{\partial \bar{x}}-\bar{p}\right)\frac{\partial \bar{h}}{\partial \bar{x}}-\left(\frac{\partial \bar{u}}{\partial \bar{y}}+\frac{\partial \bar{v}}{\partial \bar{x}}\right)=0 \text{ at } \bar{y}=\bar{h}, \tag{4.16}$$

$$\left(\frac{\partial \bar{u}}{\partial \bar{y}}+\frac{\partial \bar{v}}{\partial \bar{x}}\right)\frac{\partial \bar{h}}{\partial \bar{x}}-\left(2\frac{\partial \bar{v}}{\partial \bar{y}}-\bar{p}\right)=0 \text{ at } \bar{y}=\bar{h}, \tag{4.17}$$

$$\frac{\partial \bar{h}}{\partial \bar{t}}+\frac{\partial \bar{q}}{\partial \bar{x}}=0. \tag{4.18}$$

The effect of inertial force on layer thickness profile is neglected in this work, so that equations (4.13) and (4.14) can be simplified as:

$$0 = -1 - \frac{\partial \overline{p}}{\partial \overline{x}} + \frac{\partial^2 \overline{u}}{\partial \overline{x}^2} + \frac{\partial^2 \overline{u}}{\partial \overline{y}^2}, \tag{4.19}$$

$$0 = -\frac{\partial \overline{p}}{\partial \overline{y}} + \frac{\partial^2 \overline{v}}{\partial \overline{x}^2} + \frac{\partial^2 \overline{v}}{\partial \overline{y}^2}. \tag{4.20}$$

The entire layer thickness profile can be described by equations (4.12) and (4.15-4.20), while the insurmountable difficulty indeed exists in directly obtaining the analytical solution. As mentioned above, the models of the unsteady part and the steady meniscus are developed separately.

4.3.4.1 Modelling of the unsteady part

The flow of the unsteady part is pseudo-one-dimensional, thus the only non-vanishing components of velocity and its derivative are $\overline{u}$ and $\partial\overline{u}/\partial\overline{y}$, respectively. Therefore, equations (4.19) and (4.20) are simplified as:

$$0 = -1 - \frac{\partial \overline{p}}{\partial \overline{x}} + \frac{\partial^2 \overline{u}}{\partial \overline{y}^2}, \tag{4.21}$$

$$0 = \frac{\partial \overline{p}}{\partial \overline{y}}, \tag{4.22}$$

with the following boundary conditions:

$$\frac{\partial \overline{u}}{\partial \overline{y}} = 0 \text{ at } \overline{y} = \overline{h}, \tag{4.23}$$

$$\overline{p} = 0 \text{ at } \overline{y} = \overline{h}. \tag{4.24}$$

Combining equations (4.22) and (4.24) leads to $\overline{p}$ equals 0 everywhere. Therefore, equation (4.21) is further simplified as:

$$0 = -1 + \frac{\partial^2 \overline{u}}{\partial \overline{y}^2}. \tag{4.25}$$

Integrating equation (4.25) with respect to y with the boundary conditions (4.15) and (4.23), the velocity profile is derived as $\overline{u} = 1 - \overline{h}\overline{y} + \overline{y}^2/2$. Furthermore, integrating the velocity profile with

respect to $\bar{y}$ from 0 to $\bar{h}$ yields the flow rate: $\bar{q} = \bar{h} - \bar{h}^3/3$. Substituting the flow rate into equation (4.18) yields the differential equation describing the dynamics of the film thickness:

$$\frac{\partial \bar{h}}{\partial \bar{t}} + \frac{\partial}{\partial \bar{x}}\left(\bar{h} - \frac{\bar{h}^3}{3}\right) = 0. \tag{4.26}$$

The general solution of equation (4.26) has an implicit form:[14]

$$\left(\bar{h}^2 - 1\right)\bar{t} + \bar{x} + F(\bar{h}) = 0. \tag{4.27}$$

The term $F(\bar{h})$ is usually considered to be zero in the literature, in order to fulfil the following boundary condition:[8,11,15]

$$\bar{h} = 0 \text{ for } \bar{x} = \bar{t} \text{ and } \bar{t} > 0, \tag{4.28}$$

$$\bar{h} = +\infty \text{ for } \bar{x} < 0 \text{ and } \bar{t} = 0. \tag{4.29}$$

Therefore, the dimensionless film thickness profile is expressed as following:

$$\bar{h} = \left(1 - \frac{\bar{x}}{\bar{t}}\right)^{0.5}. \tag{4.30}$$

Figure 4.8 shows that the film thickness profile calculated by using equation (4.30) is much larger than the simulated one. In addition, equation (4.30) indicates that the dimensionless asymptotic thickness at $\bar{x} \to 0$ is 1, which is much larger than the simulated one $\bar{h}_0 = 0.698$.

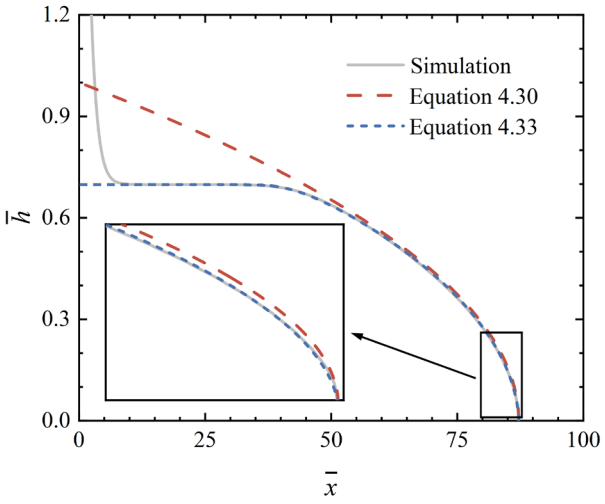

Figure 4.8. Comparison of thickness profiles in dimensionless scale obtained from direct numerical simulation (solid grey curve) with the one calculated from equation (4.30) (red dashed curve) and the one calculated from equation (4.33) (blue dotted curve). The curves in the rectangular domain are zoomed in to show the difference. Viscosity η_L: 1 Pa·s; withdrawal velocity u_0: 9.28 mm·s^{-1}; density ρ_L: 1000 kg·m^{-3}, time t: 9 s.

We suggest that this discrepancy is attributed to the incorrect expression of term $F(\bar{h})$. To constrain the term $F(\bar{h})$, an additional boundary condition is proposed:

$$\bar{h} \to \bar{h}_0 \text{ for } 0 \ll \bar{x} \ll \bar{t}, \tag{4.31}$$

where the value of the asymptotic thickness $\bar{h}_0$ is determined as 0.689.

Equation (4.31) constrains the thickness to tend to the asymptotic thickness ($\bar{h}_0 = 0.698$) for $0 \ll \bar{x} \ll \bar{t}$, after a long withdrawal time. With the above two boundary conditions (4.28) and (4.31), the expression of term $F(\bar{h})$ can be determined. We find that the film thickness profiles can fulfil both boundary conditions by considering term $F(\bar{h})$ as the following expression:

$$F(\bar{h}) = \bar{t}\bar{h}^2\left(\frac{1}{\bar{h}_0^2}-1\right)-a\frac{\bar{h}^2}{\bar{h}_0^2}-2\ln\left(1-\frac{\bar{h}}{\bar{h}_0}\right). \tag{4.32}$$

Therefore, substituting equation (4.32) to equation (4.27) yields the implicit model of the dimensionless film thickness profile:

$$\bar{x} = \bar{t}\left(1-\frac{\bar{h}^2}{\bar{h}_0^2}\right)+a\frac{\bar{h}^2}{\bar{h}_0^2}+2\ln\left(1-\frac{\bar{h}}{\bar{h}_0}\right). \tag{4.33}$$

The free parameter a can be adjusted to allow equation (4.33) to fulfil boundary condition (4.31). Figure 4.8 shows that the present model (4.33) describes well the film thickness profile. The value of a is determined by fitting equation (4.33) with the dimensionless film thickness profiles obtained from simulations. This fitting leads to different values of a at different dimensionless times $\bar{t}$. Figure 4.9

indicates that the relation between a and $\bar{t}$ can be fairly well fitted by equation 4.34 with the adjusted R^2 of 0.99:

$$a = 0.53\bar{t}+2.53. \tag{4.34}$$

Equation (4.34) will be used to calculate the value of a. The film thickness profile can be calculated by the combination of equations (4.33) and (4.34).

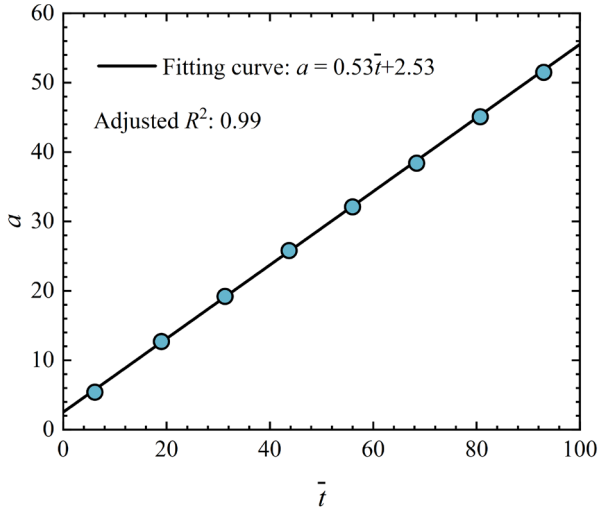

Figure 4.9. Variation of a with the dimensionless time $\bar{t}$. The symbols represent the values of a obtained by fitting equation (4.33) with the dimensionless film thickness profiles obtained from simulations. The curve is fitted by the linear function: $a = 0.53\bar{t}+2.53$. Viscosity η_L: 1 Pa·s; withdrawal velocity u_0: 9.28 mm·s^{-1}; density ρ_L: 1000 kg·m^{-3}.

4.3.4.2 Modelling of the steady part

The flow in the meniscus is two-dimensional. Considering $\partial\bar{v}/\partial\bar{y} \gg \partial\bar{v}/\partial\bar{x}$ and omitting $\partial^2\bar{u}/\partial\bar{x}^2$, equations (4.19) and (4.20) are further simplified as:

$$0 = -1-\frac{\partial\bar{p}}{\partial\bar{x}}+\frac{\partial^2\bar{u}}{\partial\bar{y}^2}, \tag{4.35}$$

$$0 = -\frac{\partial\bar{p}}{\partial\bar{y}}+\frac{\partial^2\bar{v}}{\partial\bar{y}^2}. \tag{4.36}$$

Considering $\partial\bar{v}/\partial\bar{y} \gg \partial\bar{v}/\partial\bar{x}$ in equation (4.16) yields:

$$\left.\frac{\partial \bar{u}}{\partial \bar{y}}\right|_{\bar{y}=\bar{h}} = \left(2\left.\frac{\partial \bar{u}}{\partial \bar{x}}\right|_{\bar{y}=\bar{h}} - \bar{p}|_{\bar{y}=\bar{h}}\right)\frac{\partial \bar{h}}{\partial \bar{x}}. \tag{4.37}$$

Integrating equation (4.36) with respect to $\bar{y}$ from $\bar{y}$ to $\bar{h}$, and using mass conservation, yields the pressure profile:

$$\bar{p} = \bar{p}|_{\bar{y}=\bar{h}} + \left.\frac{\partial \bar{u}}{\partial \bar{x}}\right|_{\bar{y}=\bar{h}} - \frac{\partial \bar{u}}{\partial \bar{x}}. \tag{4.38}$$

By substituting equation (4.38) into equation (4.35), we obtain:

$$\frac{\partial^2 \bar{u}}{\partial \bar{y}^2} = 1 + \left.\frac{\partial \bar{p}}{\partial \bar{x}}\right|_{\bar{y}=\bar{h}} + \left.\frac{\partial^2 \bar{u}}{\partial \bar{x}^2}\right|_{\bar{y}=\bar{h}}. \tag{4.39}$$

Integrating equation (4.39) with respect to $\bar{y}$, considering the boundary conditions (4.37) and (4.15), we obtain the velocity profile:

$$\bar{u} = 1 - \left(1 + \left.\frac{\partial \bar{p}}{\partial \bar{x}}\right|_{\bar{y}=\bar{h}} + \left.\frac{\partial^2 \bar{u}}{\partial \bar{x}^2}\right|_{\bar{y}=\bar{h}}\right)\left(\bar{h}\bar{y} - \frac{\bar{y}^2}{2}\right) + \left(2\left.\frac{\partial \bar{u}}{\partial \bar{x}}\right|_{\bar{y}=\bar{h}} - \bar{p}|_{\bar{y}=\bar{h}}\right)\frac{\partial \bar{h}}{\partial \bar{x}}\bar{y}. \tag{4.40}$$

We found that the distribution of $(\partial \bar{u}/\partial \bar{x})|_{\bar{y}=\bar{h}}$, except for the zone very close to the horizontal liquid surface, is apparently similar to the distribution of the film thickness (Figure 4.10). Therefore, we shall assume $(\partial \bar{u}/\partial \bar{x})|_{\bar{y}=\bar{h}} = b(\bar{h}-\bar{h}_0)$. Taking the derivative of this equation with respect to $\bar{x}$ yields $(\partial^2 \bar{u}/\partial \bar{x}^2)|_{\bar{y}=\bar{h}} = b(\partial \bar{h}/\partial \bar{x})$. Treating the pressure profiles in the same manner, that is $\bar{p}|_{\bar{y}=\bar{h}} = c(\bar{h}-\bar{h}_0)$ and $(\partial \bar{p}/\partial \bar{x})|_{\bar{y}=\bar{h}} = c(\partial \bar{h}/\partial \bar{x})$. Therefore, the velocity profile is determined as:

$$\bar{u} = 1 - \left[1 + (b+c)\frac{\partial \bar{h}}{\partial \bar{x}}\right]\left(\bar{h}\bar{y} - \frac{\bar{y}^2}{2}\right) + (2b-c)\left(\bar{h}-\bar{h}_0\right)\frac{\partial \bar{h}}{\partial \bar{x}}\bar{y}. \tag{4.41}$$

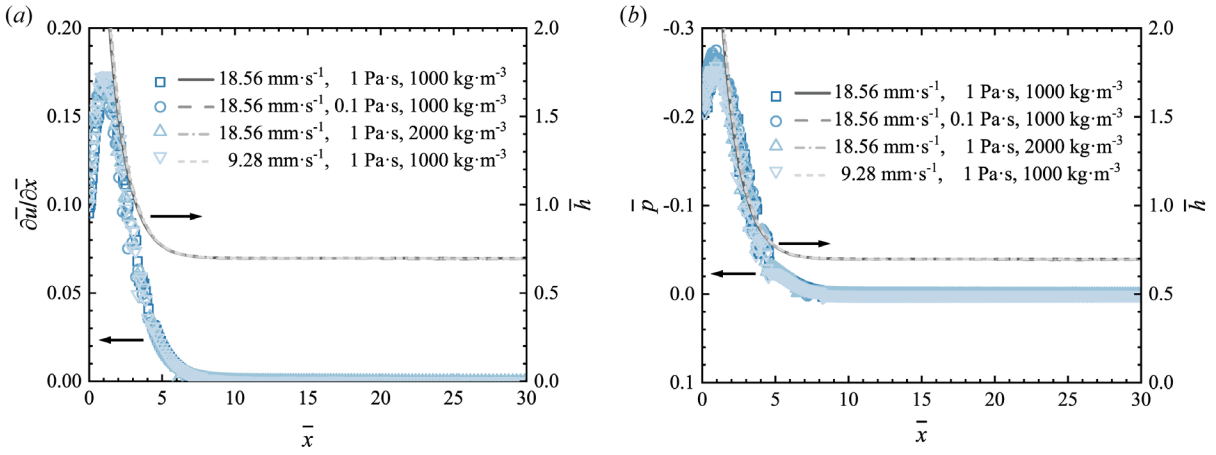

Figure 4.10. Distributions of $\partial\overline{u}/\partial\overline{x}$ (a) and $\overline{p}$ (b) at the liquid-air interface together with that of the film thickness $\overline{h}$ along $\overline{x}$ in the steady meniscus.

Integrating the velocity profile (4.41) with respect to $\overline{y}$ from 0 to $\overline{h}$ yields the flow rate:

$$\overline{q} = \overline{h} - \left[1+(b+c)\frac{\partial\overline{h}}{\partial\overline{x}}\right]\frac{\overline{h}^3}{3} + (2b-c)\left(\overline{h}-\overline{h}_0\right)\frac{\partial\overline{h}}{\partial\overline{x}}\frac{\overline{h}^2}{2}. \tag{4.42}$$

For long withdrawal times, we shall have the following boundary conditions:

$$\overline{h} \to \overline{h}_0 \text{ for } \overline{x} \to +\infty, \tag{4.43}$$

$$\overline{h} \to +\infty \text{ for } \overline{x} \to 0. \tag{4.44}$$

Taking the limit $\overline{x} \to +\infty$ in equation (4.42) and taking into account equation (4.43), we obtain:

$$\overline{q} = \overline{h}_0 - \frac{\overline{h}_0^3}{3}. \tag{4.45}$$

The boundary-value problem (4.42-4.45) can be solved, but the solution exists only for $\overline{h}_0 \geq 1$, the similar scenario was also found in past study.[13] In addition, in the part of the layer of thickness tending to $\overline{h}_0$ ($\overline{h} \to \overline{h}_0$), the velocity distribution can be expressed as $\overline{u} = 1-\overline{h}_0\overline{y}+\overline{y}^2/2$ according to equation (4.41). For $\overline{h}_0 > \sqrt{2}$, the velocity at $\overline{y} = \overline{h}_0$ calculated by $\overline{u} = 1-\overline{h}_0\overline{y}+\overline{y}^2/2$ is negative, which indicates that the liquid at the liquid-air surface flows back to the container. This is contrary to the physical fact that the entire layer, except for the part directly connected to the horizontal liquid surface,

flows towards the withdrawal direction (cf. Figure 4.5*d*). Therefore, the range of the asymptotic thickness should be $1 \le \overline{h}_0 \le \sqrt{2}$ to obtain physically meaningful solution. However, $\overline{h}_0 = 0.698$ in this work, is beyond the aforementioned scope. To keep equations (4.42-4.45) in use, the boundary-value problem is first solved numerically by shooting method within the scope of $1 \le \overline{h}_0 \le \sqrt{2}$. The numerical solution is then modified to fulfil the condition $\overline{h}_0 = 0.698$ by multiplying the numerical solution by $0.698/\overline{h}_0$, where $\overline{h}_0$ is the asymptotic thickness used for numerically solving equations (4.42-4.45). Figure 4.11 shows that the modified numerical solutions (MNS) for $\overline{h}_0 = 1$ and $\overline{h}_0 = \sqrt{2}$ agree well with the dimensionless thickness profile of the steady meniscus obtained from the simulation. In this work, the MNS for $\overline{h}_0 = \sqrt{2}$ will be adopted for subsequent modelling.

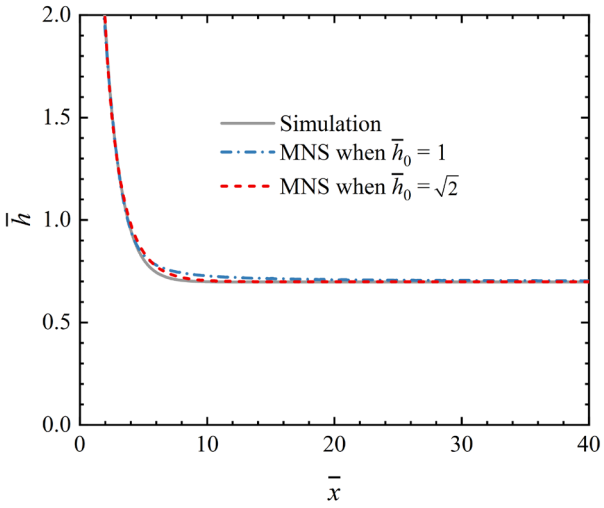

Figure 4.11. Dimensionless thickness profile of the steady meniscus after a sufficiently long withdrawal time. The solid curve is calculated using the simulated results under the condition of viscosity η_L = 1 Pa·s; withdrawal velocity u_0 = 1.86 mm·s^{-1}; density ρ_L = 1000 kg·m^{-3}, time t = 65 s. The dashed-dotted curve and dashed curve represent the modified numerical solutions (MNS) of equations (4.42-4.45) for $\overline{h}_0 = 1$ and $\overline{h}_0 = \sqrt{2}$, respectively.

4.3.4.3 Modelling of the entire layer

The combination the model of unsteady part (equation 4.33) and the model of steady meniscus (MNS of equations 4.42-4.45) leads to a composite model that applies to the entire layer. Specifically,

the thickness calculated from the unsteady part model is added to that calculated from the steady meniscus model, and the value of the overlapping part is then subtracted (i.e., the limit of equation 4.33 at $\bar{x} \to 0$). In this study, the value of the overlapping part is 0.698. Therefore, the composite model can be obtained as:

$$\bar{h}(\bar{x}, \bar{t}) = \bar{h}_u(\bar{x}, \bar{t}) + \bar{h}_s(\bar{x}) - 0.698, \tag{4.46}$$

where $\bar{h}(\bar{x}, \bar{t})$ is the expression of the entire layer thickness, $\bar{h}_u(\bar{x}, \bar{t})$ describes the unsteady part, $\bar{h}_s(\bar{x})$ represents the steady meniscus, and 0.698 is the value of the overlapping part of $\bar{h}_u(\bar{x}, \bar{t})$ and $\bar{h}_s(\bar{x})$.

4.3.5 Validity of the model

Figure 4.12(*a*) compares the thickness profile obtained from the entire layer model (equation 4.46, solid curve) to the thickness profile of the entire layer (open symbol) obtained from experiments. The agreement between the model and the experiments is good, validating the model. At the beginning of the withdrawal (say $\bar{t} = 6.1$), the model predicts a larger layer thickness than the experimental result. This is attributed to the fact that our model is developed assuming a steady meniscus, while the meniscus deforms in time in the beginning. Due to experimental limitations, it was only possible to obtain experimentally the thickness profiles for $\bar{t} \leq 55.5$. Therefore, the model at larger $\bar{t}$ is validated by simulations for $\bar{t} > 55.5$ and $Re = 8.0 \times 10^{-4}$. For $55.5 < \bar{t} < 100$, Figure 4.12(*b*) shows that the dimensionless thickness profiles of the entire layer calculated from the model and the simulations are indistinguishable, which validates again the model. For $\bar{t} > 100$, we emphasize that the head part of the layer is outside the computational domain ($\bar{x} > 100$). The simulation, therefore, only captures the part of the layer within the domain ($\bar{x} < 100$). The comparison between the model and the part of the layer captured by the simulation validates the model for long withdrawal times. For $\bar{t} = 274$, the simulation can only capture the steady part of the layer, while the unsteady part is quite beyond the computational domain. Further increasing the simulation time will give the same layer profile, i.e. the

steady part of the layer. That is to say that simulations with a longer computational domain are needed to verify more rigorously the applicability of the model for very long withdrawal times, which could be an interesting content in our future work.

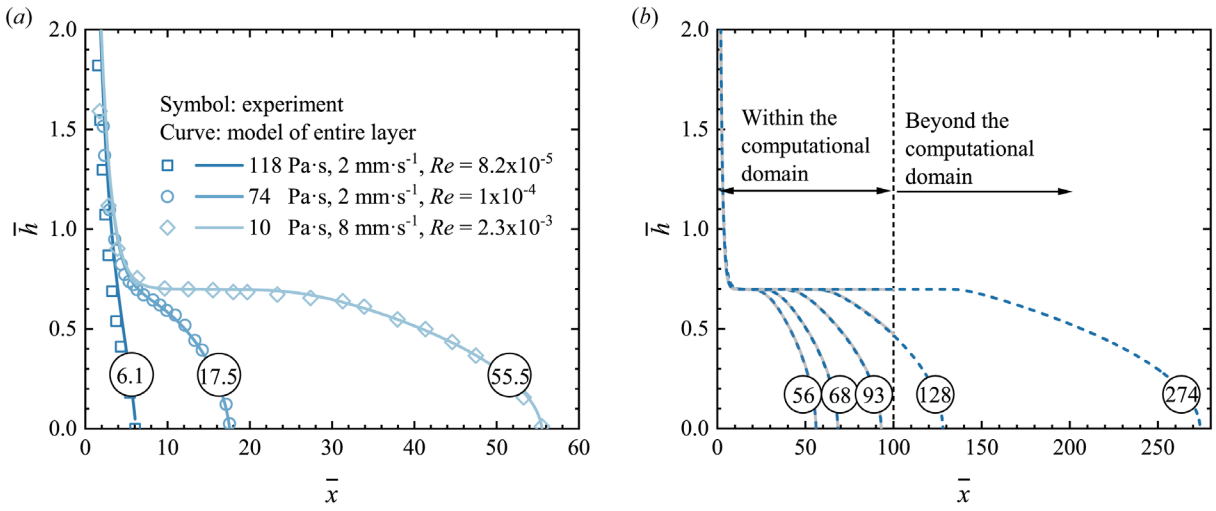

Figure 4.12. Validity of the model of the entire layer. The curves are labelled with the corresponding dimensionless time $\bar{t}$. (*a*) Comparison between the dimensionless thickness profile of the entire layer calculated from the model (solid curve) and the experiments (open symbol); (*b*) comparison between the dimensionless thickness profile of the layer calculated from the model (dashed curve) and the simulations (solid curve). Viscosity η_L: 1 Pa·s; withdrawal velocity u_0: 1.86 mm·s^{-1}; Reynolds number Re: 8.0×10^{-4}.

The layer thickness exhibits intricate spatial-temporal dynamics, indicating that the model would provide different predictive accuracies for different parts of the layer at different dimensionless times. The layer thickness thins monotonically along the withdrawal direction. Therefore, the different thickness values correspond uniquely to different parts of the layer. The parts with larger thickness are closer to the horizontal liquid surface. We consider here that a 10% discrepancy between the model and the experiments is acceptable. Figure 4.13 shows that the discrepancy is larger than 10% for most portions of the layer for $\bar{t} < 16$. When $\bar{t}$ is larger than 16, however, the absolute value of the

discrepancy is smaller than 10% for the part of the layer with the thickness $\bar{h}$ thinner than 3.7, while for the parts with $\bar{h}$ larger than 3.7, the discrepancy is lower than -10%, indicating that the model predicts a much thinner thickness profile than the experiments. Therefore, this model can provide an accurate prediction of the layer thickness in the zone with $\bar{h}$ thinner than 3.7 (this part occupies more than 90% of the entire layer) for $\bar{t} > 16$.

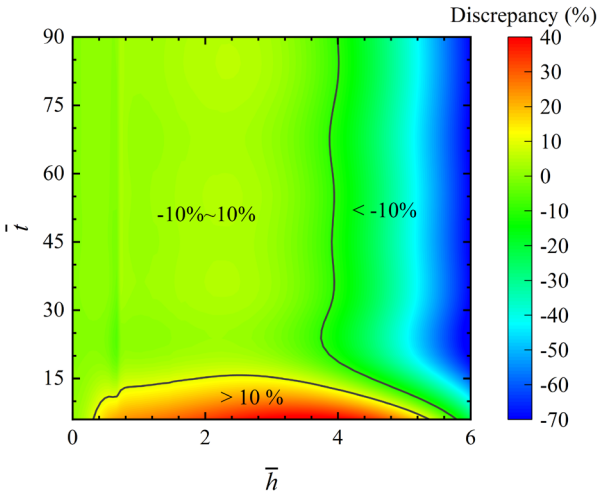

Figure 4.13. Discrepancy between the layer thickness calculated by the model and that calculated by the experimental result for different parts of the layer at different times. Withdrawal velocity u_0 = 2 mm·s^{-1}; viscosity η_L = 74 Pa·s; Reynolds number Re = 1×10^{-4}.

The effect of inertial force will probably become noticeable as the Reynolds number increases, and the layer thickness profile will deviate from our model. To investigate the upper limit of Reynolds number, extra simulations were carried out under the condition of $8.9\times10^{-3} < Re < 8.9$, that is to say beyond the experimental Reynolds range ($8.2\times10^{-5} < Re < 2.3\times10^{-3}$), at a withdrawal time $\bar{t} = 50$. In order to intuitively show the proportion of the valid part to the length of entire layer, we plotted $\bar{x}$ versus Re instead of $\bar{h}$ versus Re. The valid part (blank zone in Figure 4.14*a*) and under-predicted part (the blue zone) of the model and their demarcation (red circles) evolve with Re. For $Re < 1.1$, Figure 4.14(*a*) shows that the model is valid for the part $\bar{x} > 1.1$ and under-predicted (discrepancy <

-10%) for the part $\bar{x} < 1.1$. The effect of inertial force on the layer thickness profile is negligible for the range of $Re < 1.1$; otherwise, the demarcation between valid and under-predicted parts rises with Re. For $Re > 1.1$, the inertial force drags more liquid and increases the thickness of the meniscus, causing the demarcation rises with Re. In addition, when Re is larger than 6.4 (say $Re = 8.9$), besides the under-predicted part, there is an extra over-predicted part (the zone between the red stars). The layer thickness profiles at $Re = 8.9$ predicted by the model and obtained from the simulation are compared in Figure 4.14(b). Therefore, we suggest to use this model within the scope of $Re < 1.1$.

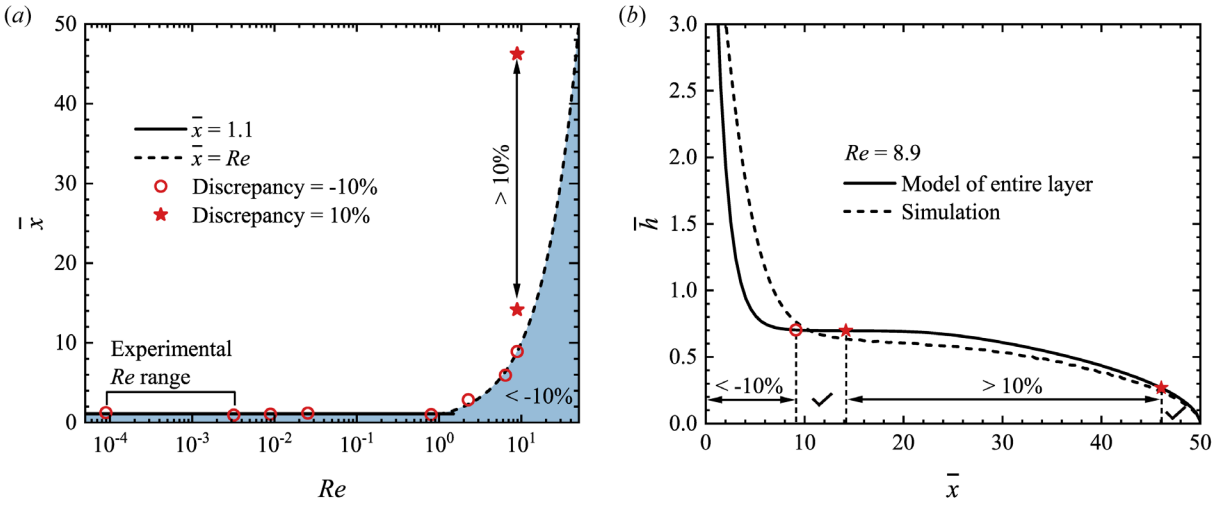

Figure 4.14. Evaluation of the validity of the model. (a) Evolution of valid part, invalid part and demarcation between the two parts over a wide range of Reynolds numbers Re: $8.2\times10^{-5} < Re < 8.9$; ($b$) comparison between the model of the entire layer and simulated result at $Re = 8.9$ with the validity of the model for different parts of the layer.

Overall, the results confirm that the present model is valid under the conditions of $Ca > 0.94$ and $Re < 1.1$. For practical use, the applicable range of this model is specified in the parameter plane (u_0, η_L). For common liquids, the density is about 1000 kg·m^{-3} and the surface tension lies within 20-70 mN·m^{-1}. Therefore, $Ca > 0.94$ and $Re < 1.1$ are reformulated into their dimensional forms $u_0 > 0.94\sigma/\eta_L$ and $u_0 < \left(0.011\eta_L\right)^{1/3}$, respectively, which leads to the blue valid area in Figure 4.15.

When surface tension is 20 mN·m^{-1}, the lower limit of viscosity for which the model is valid is 0.16 Pa·s. With the increasing surface tension, the range of valid interval reduces and the lower limit of viscosity increases (0.39 Pa·s for σ = 70 mN·m^{-1}).

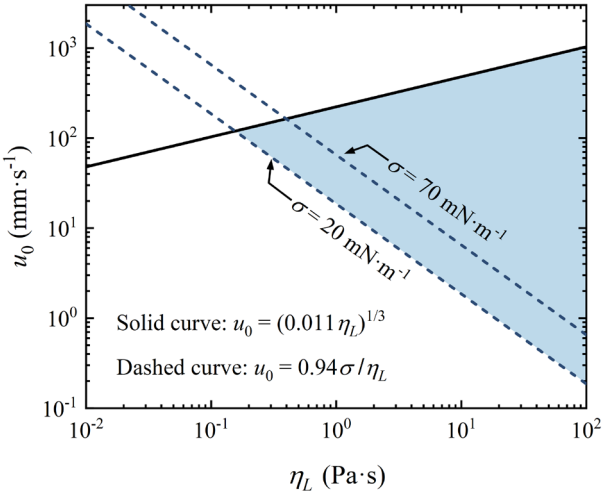

Figure 4.15. Valid interval (blue area) of the present model in the parameter plane (u_0, η_L) for common liquids (density ρ_L: 1000 kg·m^{-3}, surface tension σ: 20-70 mN·m^{-1}).

4.4 Conclusion

In this chapter, the evolution of the Newtonian liquid layer during dip coating with vertical withdrawal subject to viscous force and gravity was studied, using direct numerical simulations. The simulations reveal that the entire layer thins along the withdrawal direction under the effect of gravity. The viscous force increases the layer thickness, whereas gravity opposes the viscous force. The spatial-temporal evolution of the entire layer thickness exhibits self-similarity in the visco-gravity regime. Indeed, the dimensionless layer thickness $\bar{h}$ can be expressed as a function of the dimensionless height $\bar{x}$ and time $\bar{t}$ for $\bar{t} > 16$. The unsteady part and steady meniscus were modelled separately. The Navier-Stokes equations are simplified into a one-dimensional form for the unsteady part and solved analytically, while a two-dimensional form is adopted for the steady meniscus, with a dominating velocity derivative of $\partial\bar{u}/\partial\bar{y}$, and solved numerically. The model of unsteady part and the model of steady meniscus are then combined into one composite model that applies to the entire layer. By

comparing the composite model to the experimental and simulated results, it is demonstrated that the model is valid for dimensionless times larger than 16 over a wide range of Reynolds numbers: $0 < Re < 1.1$. Despite the model assumptions, this composite model effectively depicts the key mechanisms of layer formation. Considering that the one-dimensional flow in the unsteady part is more likely to form for smaller withdrawal angles, we suggest that the current modelling approach can be safely expanded to withdrawals with varying angles.

Reference

1. Rio E, Boulogne F. Withdrawing a solid from a bath: How much liquid is coated? *Adv. Colloid Interface Sci.* Sep 2017;247:100-114.
2. Landau L, Levich B. Dragging of a liquid by a moving plate. *Acta Physicochim. URSS.* 1942;17(2):42-54.
3. Maleki M, Reyssat M, Restagno F, Quere D, Clanet C. Landau-Levich menisci. *J. Colloid Interface Sci.* Feb 1 2011;354(1):359-363.
4. White DA, Tallmadge JA. A gravity corrected theory for cylinder withdrawal. *AIChE J.* 1967;13(4):745-750.
5. Wilson SDR. The drag-out problem in film coating theory. *J. Eng. Math.* 1982;16(3):209-221.
6. Baikov VI, Chorny AD. Withdrawing a Bingham viscoplastic fluid. *J. Rheol.* 2019;63(6):927-938.
7. Spiers RP, Subbaraman CV, Wilkinson WL. Free coating of a Newtonian liquid onto a vertical surface. *Chem. Eng. Sci.* 1974;29(2):389-396.
8. Derjaguin B. On the thickness of the liquid film adhering to the walls of a vessel after emptying. *Acta Physicochim. URSS.* 1943;20:349-352.
9. Zhang H-K, Yin Y-R, Hu G-H, Zhang X-M. Temporal evolution of demarcations between the unsteady and steady regions and between the film and meniscus during dip coating with vertical withdrawal of Newtonian fluids. *Chem. Eng. Sci.* 2024;293:120052.
10. De Ryck A, Quéré D. Fluid Coating from a Polymer Solution. *Langmuir.* 1998;14(7):1911-1914.
11. Peralta JM, Meza BE, Zorrilla SE. Mathematical modeling of a dip-coating process using a generalized Newtonian fluid.1. model development. *Ind. Eng. Chem. Res.* 2014;53(15):6521-6532.
12. Peralta JM, Meza BE, Zorrilla SE. Mathematical modeling of a dip-coating process using a generalized Newtonian fluid. 2. model validation and sensitivity analysis. *Ind. Eng. Chem. Res.* 2014;53(15):6533-6543.
13. Benilov ES, Zubkov VS. On the drag-out problem in liquid film theory. *J. Fluid Mech.* 2008;617:283-299.
14. Polyanin AD, Zaitsev VF, Moussiaux A. *Handbook of First-Order Partial Differential Equations*. London, New York: Taylor & Francis; 2002.
15. Gutfinger C, Tallmadge JA. Films of non-Newtonian fluids adhering to flat plates. *AIChE J.* 1965;11(3):403-413.

5 Film deposition of Newtonian fluids on a partially wetting cylinder upon dip coating

The wetting and deposition of partially wetting Newtonian fluids on a cylinder in dip coating have been studied by direct numerical simulation and lubrication theory. The results show that the capillary number and the cylinder radius change qualitatively the interfacial morphology, not only influence the film thickness. For a radius larger than 2, as the capillary number increases, there are four successive scenarios of interfacial morphology: (I) a stationary meniscus, (II) a capillary number-independent thick film connecting to the container through a stationary dimple, (III) a capillary number-independent thick film connecting to a classical Landau-Levich (LL) film through a travelling capillary ridge, and (IV) a film with thickness decreasing along the withdrawal direction. For a radius smaller than 2, scenario (II) disappears. The further decrease in radius triggers the appearance of wavy film scenarios. The waves on the two films (LL film and thick film) are independent and do not transfer to each other. The waving state of LL film is controlled by the capillary number and the cylinder radius; while the thick film becomes wavy at radii less than the critical radius (0.255). Except for wavy films, the film profile and transition between different scenarios are analysed through the lubrication theory, which aligns well with the direct numerical simulations. The criteria for assessing the waving state of the films are derived by the combination of the lubrication theory and the absolute-and-convective instability theory.

5.1 Introduction

As mentioned in section 2.3.1, the dynamics of dip coating on a partially wetting plate has been wildly studied and promising results have been obtained. However, when it comes to the dip coating of cylinders, the liquid-air interface is subject to the radial capillary pressure which is affected by the cylinder radius r_0.[1] Accordingly, besides the capillary number, the radius r_0 also influences the interfacial morphology.[1,2] This indicates that the related analysis for plate cannot be extended to the dip coating of cylinder. Based on the lubrication theory in the axisymmetric reference system, Chan *et al*. (2012) derived the analytical equation of the critical capillary number $Ca_{c,1}$ beyond which the

cylinder would be wetted by using the matched asymptotic expansion, for small ($r_0 << l_c$) and large radii ($r_0 >> l_c$).[3] Moreover, they also determined the $Ca_{c,1}$ for all radii ($r_0 << l_c$, $r_0 \sim l_c$, and $r_0 >> l_c$) by solving numerically the complete lubrication equation. When $Ca > Ca_{c,1}$, the cylinder is wetted by the liquid and a liquid film is deposited on the cylinder surface. Strikingly, few studies have addressed the morphology of the deposited film. Although there are some studies for similar contexts like the forced wetting of the interior wall of a capillary tube[4] and the droplet spreading on a conical fiber,[5-7] the knowledge about the dynamical film deposition on a partially wetting cylinder in the situation of dip coating is still limited.

Firstly, due to the axisymmetry of the cylinder, the contact line is no longer inclined and instead remains horizontal. Therefore, the film is axisymmetric and we can focus on the film morphology in the withdrawal direction. Secondly, for large radius ($r_0 >> l_c$), the cylinder can be treated as a plate since that the pressure in radial direction is negligible. Accordingly, the scenario of film deposition for the cylinder with large radius is the same as the plate. Yet, it remains unclear how film deposition evolves from small to large radii, and how the radius and the capillary number influence the transitions between different scenarios.

We employ direct numerical simulation (DNS) and lubrication theory (LT) to investigate the dip coating of Newtonian fluids on a partially wetting cylinder, specifically examining the film formation and transition after wetting, which have not been previously studied for cylinder substrate. In the DNS, the volume of fluid (VOF) method is utilized to capture the possible scenarios of interfacial morphology within the scope of $0.2l_c < r_0 < 100l_c$ and $0 < Ca < 0.2$. The different interfacial morphologies and the boundary between different scenarios are analysed based on the LT, which exhibits a good agreement with the DNS. In addition, the waves on the film are described and the critical conditions for their appearance are predicted, by combining the LT with the absolute-and-convective instability theory of Duprat *et al*. (2007)[8]. We ultimately obtain a map showing full complete scenarios of interfacial morphology in the (r_0, Ca) parameter plane.

5.2 Method

5.2.1 Simulation settings

Given the axisymmetric nature of the system, as shown in Figure 5.1, we performed two-dimensional axisymmetric simulations, which are based on simpler equations and require less computation times than three-dimensional simulations. The relative pressure at the red boundaries is zero. On the left, bottom and right black boundaries, which correspond respectively to the cylinder surface, the bottom of the container and the wall of the container, the no-slip condition is imposed. The cylinder radius r_0 is set by adjusting the distance between the cylinder surface and the axis of symmetry (z-axis). The length of the cylinder is $30l_c$, except for the simulations with $r_0 < 0.5l_c$ (cylinder length = $95l_c$), which is long enough to compute the complete interfacial morphology. The height of the container wall is $11l_c$. The distance between the cylinder surface and the container wall is $5l_c$ such that the container wall plays a negligible role in the interfacial morphology.[9,10] Initially, the liquid-air interface is flat and $10l_c$ above the bottom of the container. The contact angle at the container wall is 90 degrees to ensure that the liquid-air interface connects to the container horizontally. The contact angle θ_e at the cylinder surface is artificially set at 51.5 degrees to make the cylinder partially wetted by the liquid. Besides the cylinder, we also performed simulations for the plate by switching the axisymmetric simulation to a planar one and keeping other settings unchanged. The viscosity and density of the liquid phase are 0.175 Pa·s and 1000 kg·m^{-3}, respectively. The surface tension is 0.05 N·m^{-1}, which is within the range of common liquids: 0.02-0.08 N·m^{-1}. The capillary number was adjusted by changing the velocity of the substrate (the cylinder or the plate).

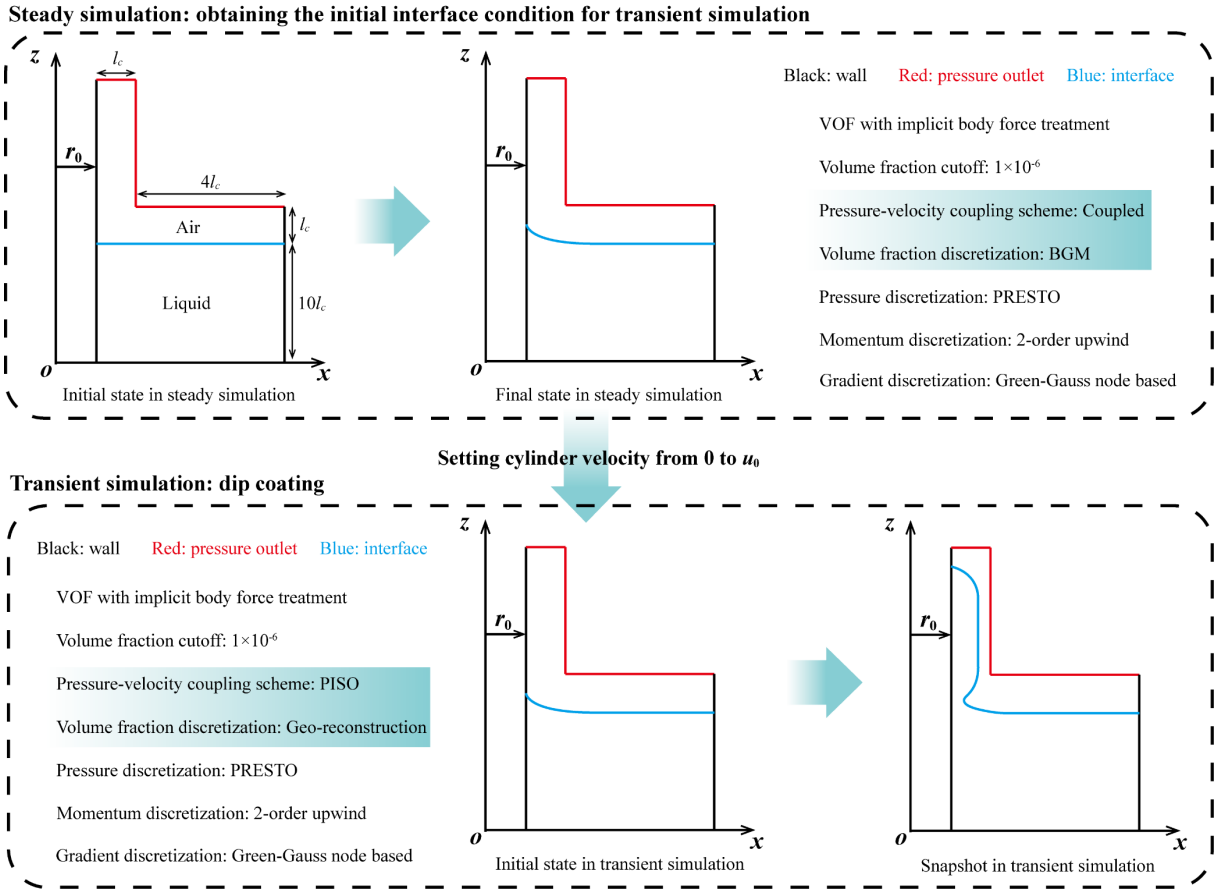

Figure 5.1. Sketch of the simulation scheme and computational domain with the boundary and initial conditions.

It is noteworthy that the DNS in this chapter incorporates both steady simulation and transient simulation. As illustrated in Figure 5.1, a steady simulation was first performed to obtain a physical initial liquid-air interface for the transient simulation of dip coating. In the steady simulation, the horizontally flat liquid-air interface evolves to an equilibrium interface under the influence of surface tension and gravity, even though the substrate is stationary. The equilibrium liquid-air interface then serves as the initial interface for all transient simulations with the same cylinder radius. In the steady simulation, the volume fraction discretization was realized through Boundedness-preserving Gradient Method (BGM). The pressure and velocity were computed with fully coupled scheme. Once the equilibrium liquid-air interface was formed, we switched the steady simulation to transient and set the

substrate velocity to u_0. The pressure-velocity coupling scheme was changed from fully coupled to the Pressure-Implicit with Splitting of Operators (PISO) algorithm. The geo-reconstruction scheme (a piecewise-linear interface approach) was utilized to discretize the volume fraction.

The computational domain was discretized by structured rectangular mesh cells with the global cell size of $l_c/60$. The mesh cells near the initial liquid-air interface and the substrate were refined with the size of $l_c/120$. Such a mesh refinement was shown to ensure spatial resolution.

5.2.2 Lubrication theory

The lubrication theory is a powerful tool to solve free surface flows.[11] Following the derivation routine of classical lubrication theory, we derived the lubrication theory for cylindrical surface. In dip coating, the dominant flow direction is axial (z-direction) so that the non-vanishing component of velocity is axial velocity, that is $|u_r| \ll |u_z|$. Therefore, the film flow is governed by the following equation:

$$0 = -\rho g - \frac{\partial p}{\partial z} + \eta_L \frac{1}{r}\frac{\partial}{\partial r}\left(r\frac{\partial u_z}{\partial r}\right). \tag{5.1}$$

The relative standard atmospheric pressure follows the Young-Laplace equation:

$$p = -\sigma k, \tag{5.2}$$

where the curvature of the air-liquid interface k is given by the following equation:

$$k = \frac{\partial^2 h/\partial z^2}{[1+(\partial h/\partial z)^2]^{3/2}} - \frac{1}{(r_0+h)[1+(\partial h/\partial z)^2]^{1/2}}. \tag{5.3}$$

At the cylinder surface, the velocity fulfils the non-permeable and Navier slip boundary conditions:

$$u_r(r = r_0) = 0, \tag{5.4}$$

$$u_z(r = r_0) = u_0 + \lambda \left.\frac{\partial u_z}{\partial r}\right|_{r = r_0}. \tag{5.5}$$

Observing stress continuity across the interface, the shear stress is vanishing at the air-liquid interface, leading to:

$$\left.\frac{\partial u_z}{\partial r}\right|_{r=r_0+h} = 0. \tag{5.6}$$

By rescaling the length variables by l_c, the velocities by σ/η_L, and the flow rate by $l_c^2\sigma/\eta_L$, the above equations (5.1-5.6) are expressed in the following dimensionless form:

$$0 = -1+\frac{\partial \bar{k}}{\partial \bar{z}}+\frac{1}{\bar{r}}\frac{\partial}{\partial \bar{r}}\left(\bar{r}\frac{\partial \bar{u}_z}{\partial \bar{r}}\right), \tag{5.7}$$

$$\bar{k} = \frac{\partial^2 \bar{h}/\partial \bar{z}^2}{\left[1+\left(\partial \bar{h}/\partial \bar{z}\right)^2\right]^{3/2}}-\frac{1}{\left(\bar{r}_0+\bar{h}\right)\left[1+\left(\partial \bar{h}/\partial \bar{z}\right)^2\right]^{1/2}}, \tag{5.8}$$

with the boundary conditions:

$$\bar{u}_r(\bar{r}=\bar{r}_0) = 0, \tag{5.9}$$

$$\bar{u}_z(\bar{r}=\bar{r}_0) = Ca+\bar{\lambda}\left.\frac{\partial \bar{u}_z}{\partial \bar{r}}\right|_{\bar{r}=\bar{r}_0}. \tag{5.10}$$

$$\left.\frac{\partial \bar{u}_z}{\partial \bar{r}}\right|_{\bar{r}=\bar{r}_0+\bar{h}} = 0. \tag{5.11}$$

Integrating equation (5.7) with respect to $\bar{r}$ twice and taking into account the boundary conditions (5.9-5.11), one obtains the axial velocity profile:

$$\bar{u}_z = Ca-\frac{1}{2}\left(\frac{\partial \bar{k}}{\partial \bar{z}}-1\right)\left[\frac{\bar{r}^2-\bar{r}_0^2}{2}-\left(\bar{r}_0+\bar{h}\right)^2\ln\left(\frac{\bar{r}}{\bar{r}_0}\right)-\bar{\lambda}\left(2\bar{h}+\frac{\bar{h}^2}{\bar{r}_0}\right)\right]. \tag{5.12}$$

The flow rate $\bar{q}$ is obtained by the following integrating:

$$2\pi\int_{\bar{r}_0}^{\bar{r}_0+\bar{h}}\bar{u}_z\bar{r}\,\mathrm{d}\bar{r} = \bar{q}. \tag{5.13}$$

By substituting equation (5.12) into (5.13), the lubrication equation is hence derived as:

$$\frac{\partial \bar{k}}{\partial \bar{z}}-1+\frac{3f(\bar{d})}{\bar{h}\left[\bar{h}+3\bar{\lambda}\left(1+\bar{d}/2\right)f(\bar{d})\right]}\left[Ca-\frac{\bar{Q}}{\bar{h}\left(1+\bar{d}/2\right)}\right] = 0, \tag{5.14}$$

where $\bar{Q} = \bar{q}/(2\pi\bar{r}_0)$, $\bar{d} = \bar{h}/\bar{r}_0$ and $f(\bar{d})$ is a function which reads:

$$f(\bar{d}) = \frac{8\bar{d}^3(2+\bar{d})}{3\left[4(1+\bar{d})^4 \ln(1+\bar{d}) - \bar{d}(2+\bar{d})\left(2+6\bar{d}+3\bar{d}^2\right)\right]}. \tag{5.15}$$

For large radius ($\bar{r}_0 >> 1$), we have $\bar{d} \to 0$ and $f(\bar{d}) \to 1$, the lubrication equation (5.14) hence takes the following asymptotic form:

$$\frac{\partial \bar{k}}{\partial \bar{z}} - 1 + \frac{3}{\bar{h}(\bar{h}+3\lambda)}\left(Ca - \frac{\bar{Q}}{\bar{h}}\right) = 0, \tag{5.16}$$

which is consistent with the lubrication equation for a plate.[10,12]

5.3 Overview of the interfacial morphology

As the dip coating progresses, after a transient evolution, the interfacial morphology reaches a stable state which structure does not change with time. The DNS shows that depending on the values of Ca and $\bar{r}_0$, there are five different interfacial morphologies designated as scenarios I to V, as depicted in Figure 5.2. Scenario I refers to the stationary meniscus. In scenario II, a thick film, which connects to the liquid surface through a stationary dimple, is deposited on the cylinder. Unlike the classical LL film, the thickness $\bar{h}_T$ measured in the uniform region of the thick film is independent of Ca and larger than that of LL film ($\bar{h}_L$). The local minimum thickness $\bar{h}_D$ of dimple decreases with Ca. The length of the thick film increases with time due to the upward propagation of the contact line; its thickness instead is time-independent. In scenario III, a thick film (of thickness $\bar{h}_T$) coexists with a LL film and the two films are connected through a travelling capillary ridge. The thickness of the LL film ($\bar{h}_L$) increases with Ca and $\bar{r}_0$. The travelling capillary ridge and the contact line move upward with time. Scenario IV is a film of monotonic thickness where $\bar{h}_L > \bar{h}_T$ and the capillary ridge hence disappears. The thick film is connected to the LL film through a monotonic transition. In addition, there are three types of wavy film, that is WTFL (wavy thick film and flat LL film), WTWL (wavy thick film and wavy LL film), and FTWL (flat thick film and wavy LL film).

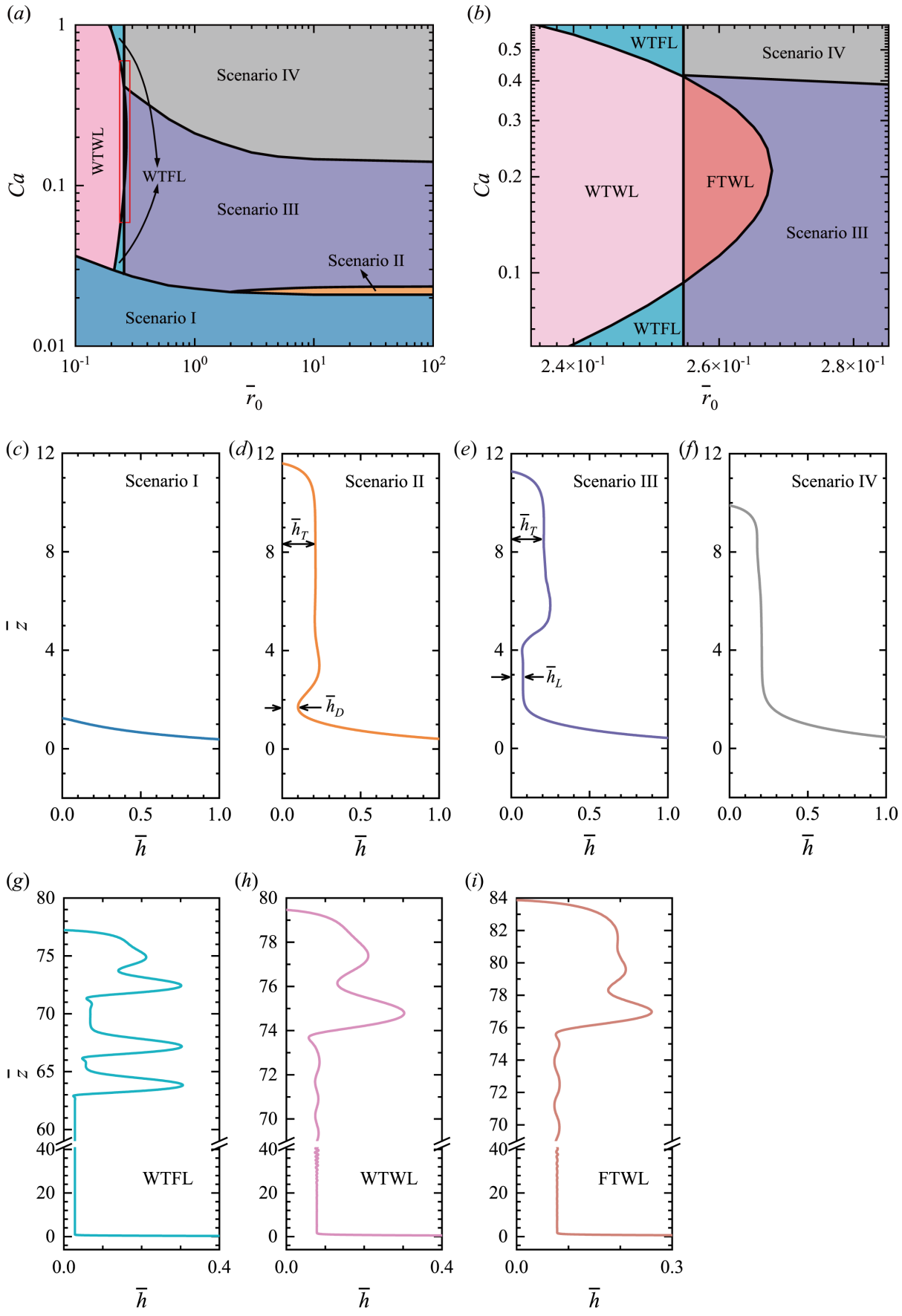
(a)
Ca
$\bar{r}_0$
WTWL
WTFL
Scenario IV
Scenario III
Scenario II
Scenario I
(b)
WTFL
Scenario IV
WTWL
FTWL
Scenario III
WTFL
(c)
Scenario I
(d)
Scenario II
$\bar{h}_T$
$\bar{h}_D$
(e)
Scenario III
$\bar{h}_T$
$\bar{h}_L$
(f)
Scenario IV
$\bar{z}$
$\bar{h}$
(g)
WTFL
(h)
WTWL
(i)
FTWL

Figure 5.2. Influence of Ca and r_0 on the interfacial morphology. (*a*) Map of interfacial morphology obtained from the lubrication theory in the parameter plane ($\bar{r}_0$, Ca). (*b*) Magnified view of the region enclosed by the red box in figure (*a*). (*c-i*) Interfacial morphologies for typical values of Ca and $\bar{r}_0$. (*c*) Scenario I: Ca = 0.02, $\bar{r}_0$ = 100, stationary meniscus. (*d*) Scenario II: Ca = 0.022, $\bar{r}_0$ = 10, coexistence of a thick film and a stationary dimple. (*e*) Scenario III: Ca = 0.025, $\bar{r}_0$ = 10, coexistence of a thick film and a LL film, connected through a travelling capillary ridge. (*f*) Scenario IV: Ca = 0.2, $\bar{r}_0$ = 1, film of monotonic thickness. (*g*) Scenario WTFL: Ca = 0.033, $\bar{r}_0$ = 0.2, coexistence of a wavy thick film and a flat LL film. (*h*) Scenario WTWL: Ca = 0.13, $\bar{r}_0$ = 0.2, coexistence of a wavy thick film and a wavy LL film. (*i*) Scenario FTWL: Ca = 0.1, $\bar{r}_0$ = 0.275, coexistence of a flat thick film and a wavy LL film. The interfacial morphologies shown in (*d-i*) are the snapshots of times $\bar{t}$ = 527, 451, 50, 5315, 709, and 1012, respectively, where the time is scaled by $\eta_L l_c/\sigma$.

For a given cylinder radius, the transition between different scenarios can be achieved by adjusting Ca (cf. Figure 5.2*a*, *b*). When Ca is small, the liquid surface takes the shape of a stationary meniscus and cannot wet the cylinder, i.e., scenario I. The occurrence of wetting and the deposition of film is only possible when Ca exceeds the first critical value ($Ca > Ca_{c,1}$). For large cylinder radii (approximately $\bar{r}_0 > 2$), the film exhibits scenario II for $Ca > Ca_{c,1}$. If Ca is larger than a second critical value ($Ca > Ca_{c,2}$), the film shifts to scenario III. The further increase of Ca ($Ca > Ca_{c,3}$) triggers the transition of film from scenario III into scenario IV. For small radii (approximately $0.23 < \bar{r}_0 < 1$), the morphology transition is similar to large radii, but the scenario II disappears, the interface enters scenario III directly from scenario I. For even smaller radii (approximately $\bar{r}_0 < 0.23$), the film is wavy when $Ca > Ca_{c,1}$, with scenarios WTFL, WTWL or FTWL depending on the exact value of Ca.

5.4 Stationary meniscus before wetting

The DNS captures the establishment of the meniscus in scenario I, as plotted in Figure 5.3. When the cylinder is at rest ($\bar{t} = 0$), the interface is a stationary meniscus under the driving of capillary force, the initial vertical position of the contact line ($\bar{z}_{cl}$) is thus non-zero. As the cylinder moves upward, the liquid is entrained under the viscous force and the contact lines hence rises, while the capillary force hinders the rise of the contact line. Once the contact line rises to a certain vertical position, the interface keeps unchanged with time and forms a new stationary meniscus under the equilibrium between viscous, capillary forces and gravity.

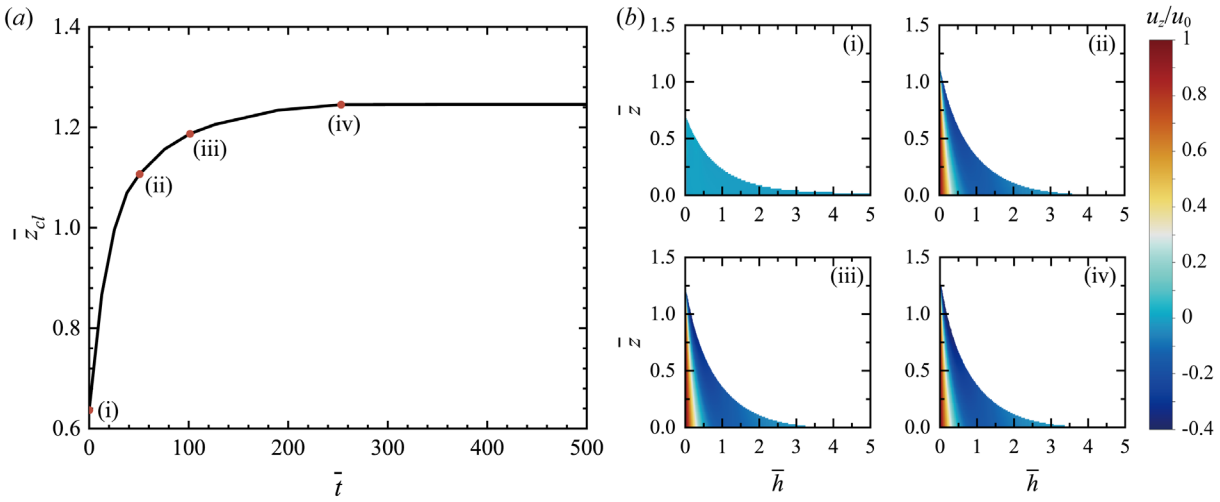

Figure 5.3. Dynamic process of scenario I: $Ca = 0.02$ and $\bar{r}_0 = 100$. (*a*) Evolution of $\bar{z}_{cl}$ (the vertical position of the contact line) with time. (*b*) Contours of normalized axial velocity (u_z/u_0) in the liquid phase at the times labelled in figure (*a*), i: $\bar{t} = 0$, ii: $\bar{t} = 50$, iii: $\bar{t} = 100$, and iv: $\bar{t} = 253$.

At the long-time limit, since the cylinder is not wetted, $\bar{Q}$ is zero and the lubrication equation reduces to:

$$\frac{\partial \bar{k}}{\partial \bar{z}} - 1 + \frac{3Caf(\bar{d})}{\bar{h}\left[\bar{h} + 3\bar{\lambda}(1+\bar{d}/2)f(\bar{d})\right]} = 0. \tag{5.17}$$

Equation (5.17) has been solved numerically by Chan *et al.* (2011)[3] with the boundary conditions at the contact line ($\bar{z} = \bar{z}_{cl}$):

$$\bar{h} = 0, \tag{5.18}$$

$$\frac{\partial \bar{h}}{\partial \bar{z}} = -\tan(\theta_e), \tag{5.19}$$

and at the free surface in the container ($\bar{z} \to 0$):

$$\frac{\partial \bar{h}}{\partial \bar{z}} = -\infty, \tag{5.20}$$

$$\bar{k} = 0. \tag{5.21}$$

Equations (5.20) and (5.21) constraint the liquid surface connecting to the container to be flat. By ignoring the viscous force, Snoeijer *et al.* (2007) obtained the more accurate boundary condition at $z = 0$ for a plate substrate: $\bar{h} = \ln(c/\bar{z})$, where c is a free parameter.[13] Following the derivation of Snoeijer *et al.* (2007), the viscous term (the third term containing Ca) in equation (5.17) is ignored to obtain the following equation:

$$\frac{\partial \bar{k}}{\partial \bar{z}} = 1, \text{ with } \bar{k} = \frac{\partial^2 \bar{h}/\partial \bar{z}^2}{\left[1+\left(\partial \bar{h}/\partial \bar{z}\right)^2\right]^{3/2}} - \frac{1}{\bar{r}\left[1+\left(\partial \bar{h}/\partial \bar{z}\right)^2\right]^{1/2}}. \tag{5.22}$$

Taking into account $\left(\partial \bar{h}/\partial \bar{z}\right)^2 \gg 1$ at $\bar{r} \to +\infty$, the asymptotic solution of equation (5.22) as $\bar{r} \to +\infty$ is thus solved as:

$$\bar{z} = c\sqrt{\frac{\pi}{2(\bar{r}_0+\bar{h})}}\, e^{-(\bar{r}_0+\bar{h})}; \tag{5.23}$$

or equivalently, $\bar{h}$ as a function of $\bar{z}$:

$$\bar{h} = \frac{1}{2} W\left(\frac{c^2\pi}{\bar{z}^2}\right) - \bar{r}_0, \tag{5.24}$$

where $W(\bar{z})$ is the Lambert W function, defined implicitly by the relation $W(\bar{z})e^{W(\bar{z})} = \bar{z}$.

Differently from the study by Chan *et al.* (2011), equation (5.17) is solved numerically in the present study through a shooting method with the boundary conditions (5.18, 5.19 and 5.24) instead of the boundary conditions (5.18-5.21). The present numerical solutions are compared with those of

Chan *et al*. (2011) under the conditions of $\bar{r}_0 = 0.1$, $\bar{\lambda} = 10^{-5}$ and $\theta_e = 0.05$. Figure 5.4(*a*) shows that the evolution of $\bar{z}_{cl}$ with *Ca* obtained by the present theory agrees well with that of Chan *et al.* (2011). Above a critical capillary number $Ca_{c,1} = 9.6\times10^{-6}$, the stationary meniscus solution cannot be found. The solution can be divided into a lower branch and an upper branch. In the lower branch, $\bar{z}_{cl}$ increases with *Ca*. After reaching $Ca_{c,1}$, the curve turns back toward the upper branch solution. The curve further undergoes a series of bifurcations with *Ca* oscillating around a characteristic capillary number $Ca^* = 3.1\times10^{-6}$. Figure 5.4(*b*) compares the interfacial profile solved by the present lubrication theory and by Chan *et al.* (2011) at $Ca = Ca^*$ and $\bar{z}_{cl} = +\infty$, showing a very good agreement between both.

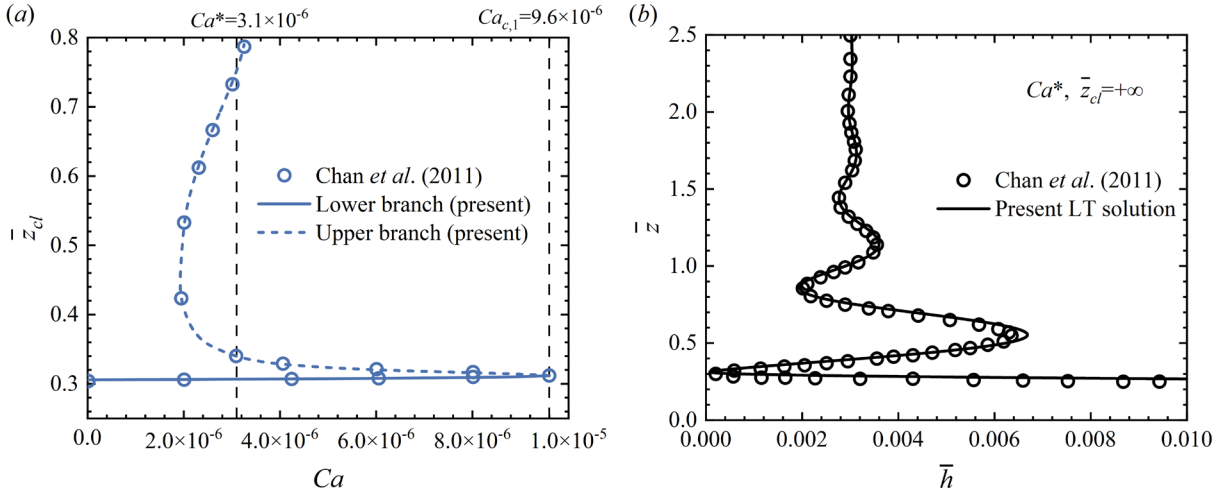

Figure 5.4. Comparison between present lubrication theory and Chan *et al.* (2011)'s under the conditions of $\bar{r}_0 = 0.1$, $\bar{\lambda} = 10^{-5}$ and $\theta_e = 0.05$. (*a*) Evolution of $\bar{z}_{cl}$ with *Ca*. (*b*) Interfacial morphology at $Ca = Ca^*$ and $\bar{z}_{cl} = +\infty$.

From the DNS may only be obtained the lower branch solution and is unable to solve the upper branch one (cf. Figure 5.5). This phenomenon was also found in the study by Gao *et al*. (2016), where the diffuse-interface method was utilized to simulate the dip coating process of Newtonian fluids on a partially wetting plate.[10] The inability of DNS to yield the upper branch solution is not due to any incorrect boundary conditions or inappropriate algorithm used in DNS. Recall that the interface

evolves from a horizontal surface, thus the interface cannot reach the upper branch solution without passing through the lower branch one. The lower branch solution, however, is a stable state and once it reaches, the interface stops evolving. Put it differently, if the liquid is initially at rest and the interface is unperturbed, the upper branch solution cannot be computed in the DNS, nor can it be observed experimentally.

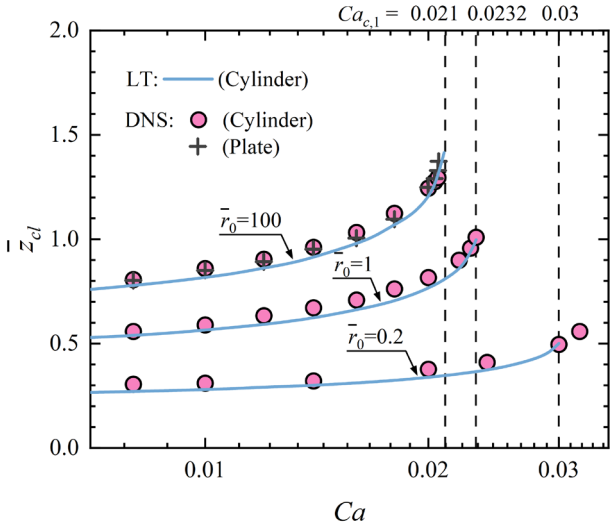

Figure 5.5. Evolution of $\bar{z}_{cl}$ with Ca for the plate and the cylinders with different radii $\bar{r}_0$ = 0.2, 1 and 100 and the slip length $\bar{\lambda}$ = 1×10^{-3}. The symbols correspond to the direct numerical simulation (DNS), and the curves denote the lower branch of the lubrication theory (LT).

As shown in Figure 5.5 for a slip length $\bar{\lambda}$ = 1×10^{-3}, the lower branch solution agrees well with the DNS. As $\bar{r}_0$ increases, the wetting resistance by capillary forces decreases, leading to a reduction in $Ca_{c,1}$ and a corresponding increase in $\bar{z}_{cl}$. In particular, the critical capillary numbers $Ca_{c,1}$ calculated from LT for radii $\bar{r}_0$ = 0.2, 1 and 100 are 0.03, 0.0232 and 0.021, coinciding with the value of DNS: 0.032, 0.0232 and 0.0207. The absolute discrepancy between LT and DNS reaches a maximum of 0.02 at $\bar{r}_0$ = 0.2, with a relative discrepancy of 6%. Additionally, the agreement between the DNS calculations for a plate and the DNS and LT calculations for a cylinder with $\bar{r}_0$ = 100 is very

good. This evidences that the plate can be considered as an asymptotic case of the cylinder with a sufficiently large radius r_0, a characteristic also captured by the lubrication theory.

A more quantitative description of the dependence of $Ca_{c,1}$ on $\bar{r}_0$ is displayed in Figure 5.6, showing once again a good agreement between the DNS and LT. At very small radii (say $\bar{r}_0 < 0.2$), $Ca_{c,1}$ decreases logarithmically with $\bar{r}_0$. It keeps decreasing until it reaches the asymptotic value of 0.21 and then ceases to evolve with $\bar{r}_0$ at very large radii (say $\bar{r}_0 > 10$). Chan *et al.* (2011) derived $Ca_{c,1}$ for small ($\bar{r}_0 << 1$) and large radii ($\bar{r}_0 >> 1$) by using asymptotic matching (AM). The AM is qualitatively consistent with the LT, showing a logarithmic decrease at small radius and an unchanged value at large radius, but exhibits slightly lower values than LT. The reason is that the AM is developed under the assumption that $\theta_e << 1$ which is obviously violated in the present study, since $\theta_e = 51.5°$ or equivalently $\theta_e = 0.899$ in radian unit.

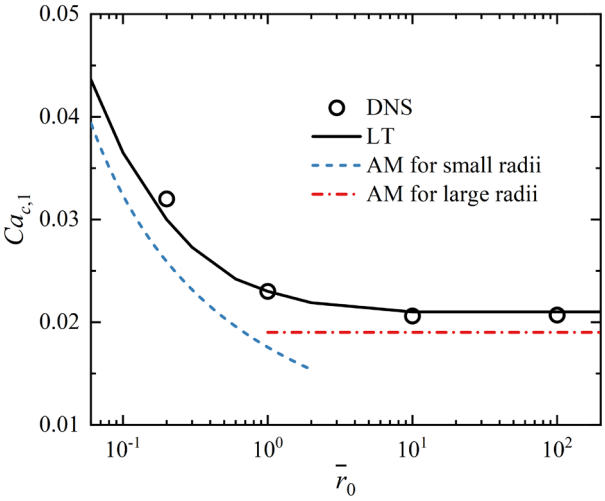

Figure 5.6. Critical capillary number $Ca_{c,1}$ versus cylinder radius r_0. Symbol, continuous black curve, blue dashed curve and red dash dotted curve represent the direct numerical simulation (DNS), lubrication theory (LT), and the asymptotic matching (AM) for small and large radii ($\bar{r}_0 << 1$ and $\bar{r}_0 >> 1$), respectively. The slip length used for LT and AM is $\bar{\lambda} = 1\times10^{-3}$.

5.5 Film deposition after wetting

5.5.1 Scenario II

As shown in Figure 5.7(*a*), the contact line altitude $\bar{z}_{cl}$ in scenario II first increases with time in a non-linear manner and then linearly. This indicates that, except for the early stage of the dip coating, the contact line moves upward at a constant velocity. Figure 5.7(*b*) depicts the film morphology and its vertical velocity contours at different times. Initially, the moving contact line yields a bump at the tip of the film, and a dimple below. As the withdrawal progresses, the bump evolves into a thick film which extends into a long uniform region. The dimple develops to a stable shape, connecting the thick film and the liquid in the container. In addition, the downward velocity at the surface of the thick film, especially the part near the dimple, indicates gravitational drainage.

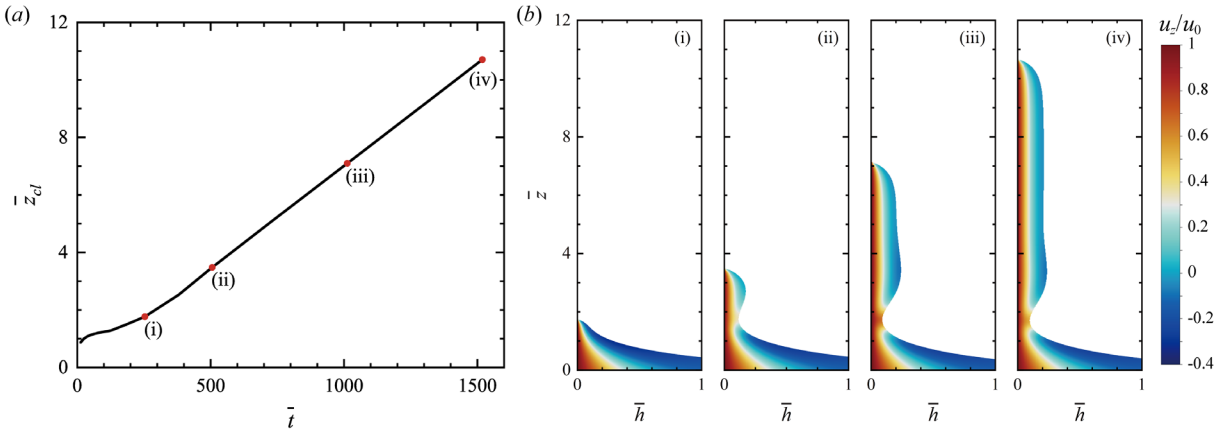

Figure 5.7. Dynamic process of scenario II for Ca = 0.022 and $\bar{r}_0$ = 10. (*a*) Evolution in time of $\bar{z}_{cl}$ (the vertical position of the contact line). (*b*) Contours of normalized axial velocity (u_z/u_0) in the liquid phase at the times labelled in figure (*a*), i: $\bar{t}$ = 253, ii: $\bar{t}$ = 506, iii: $\bar{t}$ = 1012, and iv: $\bar{t}$ = 1518.

For convenience, following the past studies on the film deposition on a partially wetting plate,[12,14] the thick film is analysed in the frame of reference moving with the contact line. It is worth highlighting that, in view of the occurrence of the thick film both in scenarios II and III, the following lubrication analysis for the thick film is valid not only for scenario II but also for scenario III. At long times, the

shape of the thick film reaches a steady state and the flow rate $\overline{Q}$ across the film cross-section is zero. Therefore, the lubrication equation reduces to:

$$\frac{\partial \overline{k}}{\partial \overline{z}} - 1 + \frac{3f(\overline{d})\Delta Ca_{cl}}{\overline{h}\left[\overline{h} + 3\overline{\lambda}\left(1 + \overline{d}/2\right)f(\overline{d})\right]} = 0, \tag{5.25}$$

where ΔCa_{cl} is the cylinder velocity relative to the contact line. The boundary conditions are

$$\frac{\partial \overline{h}}{\partial \overline{z}} = -\tan(\theta_e) \tag{5.26}$$

at the contact line ($\overline{z} = 0$) and

$$\overline{h} = \overline{h}_T \tag{5.27}$$

in the uniform region of the thick film ($\overline{z} \to -\infty$).

In the uniform region of the thick film ($\overline{z} \to -\infty$), the curvature $\partial \overline{k}/\partial \overline{z}$ is zero, and for $\overline{\lambda} \ll 1$ equation (5.25) simplifies into

$$3f(\overline{d}_T)\Delta Ca_{cl} = \overline{h}_T^2, \tag{5.28}$$

where $\overline{d}_T = \overline{h}_T/\overline{r}_0$.

The lubrication equation (5.25) is solved numerically together with equation (5.28) to obtain the interfacial morphology of the thick film, by shooting from the uniform region of the thick film ($\overline{z} \to -\infty$) to the contact line ($\overline{z} = 0$). Taking $\overline{r}_0 = 10$ as an example, Figure 5.8(*a*) shows an excellent agreement between the interfacial morphology calculated by the DNS and the LT. The thickness $\overline{h}_T$, as shown in Figure 5.8(*b*), increases with $\overline{r}_0$. The dependence of $\overline{h}_T$ on $\overline{r}_0$ decreases with $\overline{r}_0$ and is almost negligible for $\overline{r}_0 > 10$. As expected, the thickness calculated by DNS for a cylinder of large radius (say $\overline{r}_0 > 100$) is equal to that obtained for a plate.

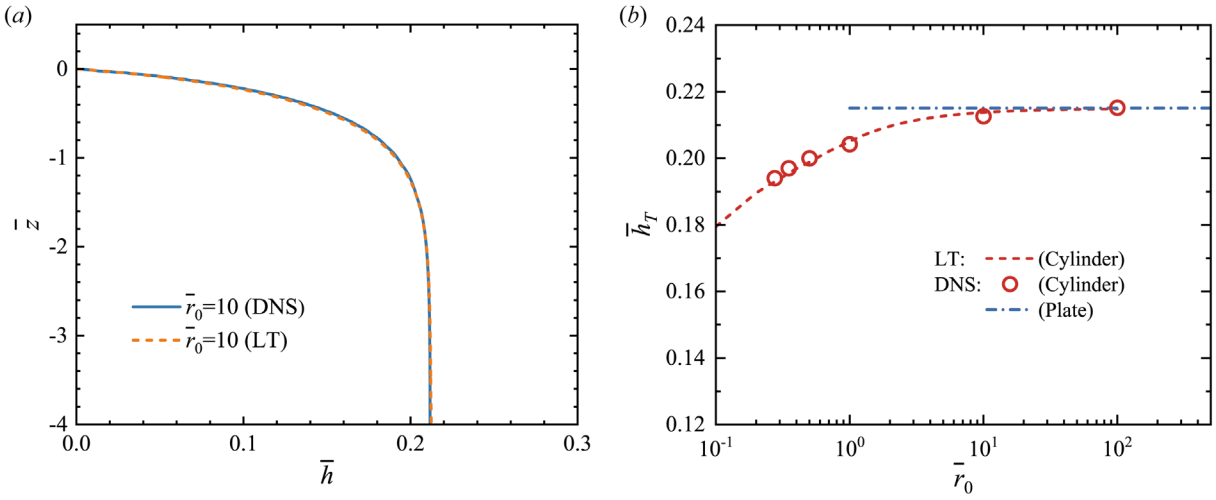

Figure 5.8. (*a*) Comparison of the interfacial morphology of the thick film calculated by the DNS (solid curve) and the LT (dashed curve) at $\bar{r}_0 = 10$. (*b*) Evolution of the thickness $\bar{h}_T$ with radius $\bar{r}_0$: the symbols and red dashed curve denote the DNS and the LT respectively. The blue dash dotted curve represents the $\bar{h}_T$ of plate calculated by the DNS.

For the dimple region, also at long times, the shape ceases to evolve with time. Due to the absence of contact line in this region, the slip length $\bar{\lambda}$ is omitted. The lubrication equation (5.14), in the laboratory reference frame, thus reduces to:

$$\frac{\partial \bar{k}}{\partial \bar{z}} - 1 + \frac{3f(\bar{d})}{\bar{h}^2}\left[Ca - \frac{\bar{Q}}{\bar{h}(1+\bar{d}/2)}\right] = 0. \tag{5.29}$$

The dimple as well as its adjacent regions (the uniform region of the thick film and the region connecting to the container) are treated as a whole. In the uniform region of the thick film ($\bar{z} \to +\infty$), $\bar{h} = \bar{h}_T$ and $\partial \bar{k}/\partial \bar{z} = 0$, the following expression is thus obtained from equation (5.29):

$$\bar{Q} = \bar{h}_T\left(1+\frac{\bar{d}_T}{2}\right)\left(Ca - \frac{\bar{h}_T^2}{3f(\bar{d}_T)}\right). \tag{5.30}$$

From equation (5.28), we know that $\bar{h}_T^2/[3f(\bar{d}_T)] = \Delta Ca_{cl}$. Therefore, the term $Ca - \bar{h}_T^2/[3f(\bar{d}_T)]$ in equation (5.30) represents the velocity of contact line and is positive. Equation (5.30) also indicates

that, although the moving contact line has a negative velocity relative to the cylinder, the parameter $\overline{Q}$ (or equivalently, the flow rate $\overline{q}$) is positive and increases with *Ca*.

The lubrication equation (5.29) is solved numerically together with equation (5.30) through a shooting method with the boundary condition at the free surface in the container ($\bar{z} \to 0$):

$$\overline{h}(\bar{z}) = \frac{1}{2} W\left(\frac{c^2\pi}{\bar{z}^2}\right) - \bar{r}_0, \tag{5.31}$$

and the boundary condition at the contact line ($\bar{z} \to +\infty$):

$$\overline{h} = \overline{h}_T. \tag{5.32}$$

The boundary condition as $\bar{z} \to 0$ is the same as equation (5.24), representing the asymptotic solution of lubrication equation. The local minimum thickness of the dimple $\overline{h}_D$ and the corresponding height $\bar{z}_D$ for different *Ca* are plotted in Figure 5.9(*a*, *b*). The bifurcation behaviour, similar to that in scenario I as well as in the dip coating on a partially wetting plate, is observed as *Ca* evolves. The solution consists of two branches. More specifically, in the first branch, $\overline{h}_D$ decreases while $\bar{z}_D$ increases with *Ca*. There exists a second critical capillary number $Ca_{c,2}$, beyond which no numerical solution can be found and the dip coating transitions from scenario II to III. For $\bar{r}_0 = 10$, the second critical capillary number $Ca_{c,2}$ is 0.0232 which is close to the value from DNS 0.022. After reaching $Ca_{c,2}$, the curves in Figure 5.9(*a*, *b*) turn back towards the second branch where the dimple is located higher and is thinner. The curves further undergo a series of bifurcations with *Ca* oscillating around the characteristic capillary number *Ca***.

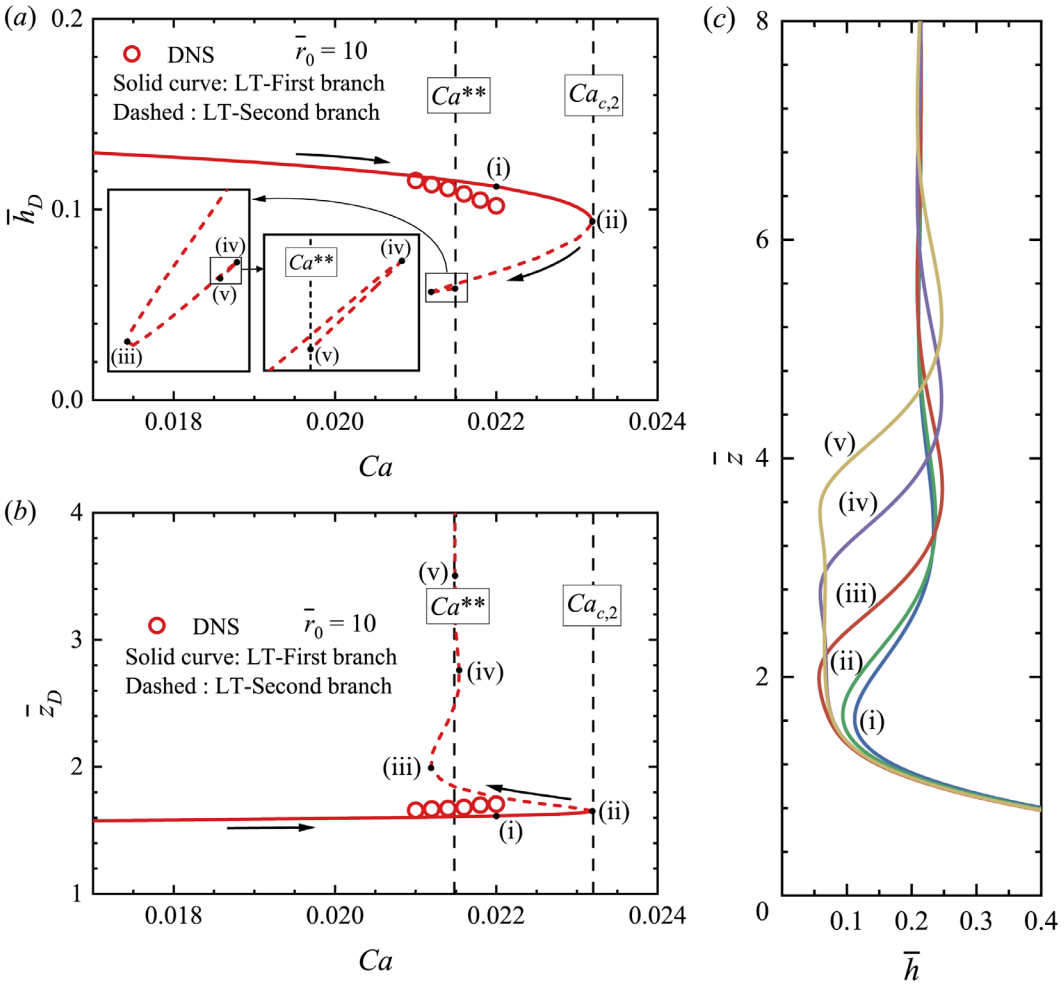

Figure 5.9. Bifurcation curve of the dimple thickness $\bar{h}_D$ (*a*) and its corresponding location $\bar{z}_D$ (*b*) for $\bar{r}_0 = 10$. The circle symbols and the curves denote the DNS and the LT, respectively. (*c*) Interfacial morphologies at the configurations labelled in figure (*a*, *b*).

As shown in Figure 5.9(*c*), the interfacial morphologies for different situations labelled as (i-v) show that, from situation (i) to situation (v), the dimple becomes flatter and eventually evolves to a thin film (identified as a LL film). The LL film connects upward to the thick film through a capillary ridge and downward to the container through a meniscus. This morphology may look similar to that in scenario III, but they are different. Indeed, in scenario II, the capillary ridge is stationary, while in scenario III, the capillary ridge is propagating upward as the cylinder moves. Moreover, the thickness of LLD film in scenario II is independent of *Ca*, since the LLD film only occurs at *Ca* = *Ca***. In

scenario III, however, the thickness of LLD film increases with Ca. Owing to the same reason elaborated in scenario I, with present initial conditions, the upper branch solution and hence the stationary capillary ridge cannot be achieved by the DNS nor the experiment.

The evolution of the critical capillary numbers $Ca_{c,1}$ and $Ca_{c,2}$ as a function of r_0 is shown in Figure 5.10. The blue area below the $Ca_{c,1}$ curve represents scenario I, the orange area sandwiched by the $Ca_{c,1}$ curve and $Ca_{c,2}$ curve denotes scenario II. $Ca_{c,2}$ increases with $\bar{r}_0$ and tends to a constant at large $\bar{r}_0$, indicating that smaller $\bar{r}_0$ favour the transition from scenario II to scenario III. Moreover, the intersection of $Ca_{c,1}$ curve and $Ca_{c,2}$ at $\bar{r}_0 = 2.3$ indicates that scenario II only occurs for $\bar{r}_0 > 2.3$. For $\bar{r}_0 < 2.3$, however, the dip coating transitions from scenario I directly to scenario III or to wavy films, skipping scenario II.

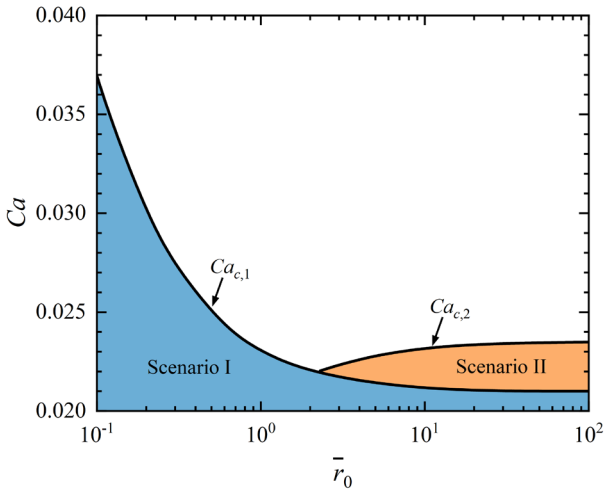

Figure 5.10. Critical capillary numbers $Ca_{c,1}$ and $Ca_{c,2}$ from the LT versus the cylinder radius $\bar{r}_0$.

5.5.2 Scenario III

As shown in Figure 5.11(a), the evolution of contact line in scenario III with time is qualitatively the same as in scenario II. Except for the early stage, the contact line propagates upward linearly with time, indicating a constant velocity. Following the method in *Gao et al.* (2016), the vertical position of the capillary ridge is measured at the location where the thickness equals $(\bar{h}_T+\bar{h}_L)/2$.[10] Figure 5.11(a) illustrates that the capillary ridge also moves upward linearly with time, thus at a constant velocity. The evolution of film morphology in scenario III is also like that in scenario II. The rise of the contact

line leads to the formation of a bump, below which appears a dimple (cf. Figure 5.11*b*). The bump eventually evolves into a thick film as the cylinder moves upward. Differently from scenario II, the dimple in scenario III then evolves to a LL film. The LL film connects to the thick film upward through a moving capillary ridge, and to the container downward in a smoother monotonic manner.

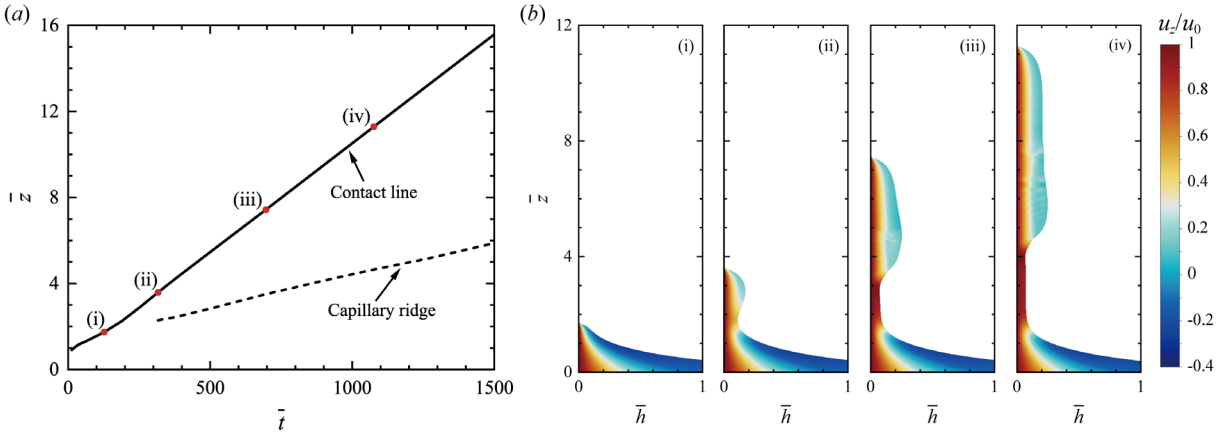

Figure 5.11. Dynamic process of scenario III for Ca = 0.025 and $\bar{r}_0$ = 10. (*a*) Temporal evolution of the vertical positions of the contact line and capillary ridge. (*b*) Contours normalized axial velocity (u_z/u_0) in the liquid phase at the times labelled in figure (*a*), i: $\bar{t}$ = 126, ii: $\bar{t}$ = 316, iii: $\bar{t}$ = 696, and iv: $\bar{t}$ = 1076.

The thick film is described with the same equations as those derived for scenario II. We shall describe here the LL film and the capillary ridge. The LL film is widely present on a well wetting surface and has been studied in depth. For large radius ($\bar{r}_0$ >> 1), the cylinder reduces to a plate and the film thickness is independent of $\bar{r}_0$. After the pioneering studies by Landau and Levich (LL) (1942)[15], Wilson improved the LL theory by including gravitational drainage[16]:

$$\bar{h}_L = 0.946Ca^{2/3} - 0.107Ca. \tag{5.33}$$

For small radius ($\bar{r}_0$ << 1) and radius close to unity ($\bar{r}_0$ ~ 1), the radius has a great effect on the film thickness. White and Tallmadge (WT) (1966) proposed a theory for predicting the film thickness for a thin film ($\bar{h}_L$ << $\bar{r}_0$) and small radius ($\bar{r}_0$ << 1):[2]

$$\frac{\overline{h}_L}{\overline{r}_0} = \frac{1.33Ca^{2/3}}{1\text{-}1.33Ca^{2/3}}. \tag{5.34}$$

Recently, Zhang *et al.* (2022) developed a lubrication theory under the assumption of thin film ($\overline{h}_L << \overline{r}_0$):[1]

$$\frac{\partial \overline{k}}{\partial \overline{z}} + \frac{3Ca}{\overline{h}^2}\left(1\text{-}\frac{\overline{h}_L}{\overline{h}}\right)\text{-}1+\frac{\overline{h}_L^3}{\overline{h}^3} = 0, \tag{5.35}$$

with the boundary conditions at the free surface in the container ($\overline{z} \to 0$):

$$\frac{\partial \overline{h}}{\partial \overline{z}} \to \text{-}\infty, \overline{k} = 0, \tag{5.36}$$

and at the uniform region of the LL film ($\overline{z} \to +\infty$):

$$\overline{h} = \overline{h}_L. \tag{5.37}$$

Thanks to maintaining the full nonlinear capillary pressure term in the modelling, the film thickness calculated numerically from Zhang theory (2022) (equations 5.35-5.37) is valid within a wide range of radius (from $\overline{r}_0 << 1$ to $\overline{r}_0 >> 1$).

Within the present framework of lubrication theory, the interfacial morphology of LL film is governed by equations (5.29) and (5.30) by replacing $\overline{h}_T$ with $\overline{h}_L$ in equations. The lubrication equation for LL film is solved numerically by a shooting method with the boundary conditions (5.36 and 5.37). As shown in Figure 5.12, the film thickness $\overline{h}_L$ calculated by the present theory exhibits a good agreement with the experiments of Zhang *et al.* (2022)[1]. As expected, Wilson theory (1982) (equation 5.33), over-predicts the film thickness, with a discrepancy decreasing for increasing $\overline{r}_0$. WT theory (1966) (equation 5.34) gives an acceptable prediction only for $Ca < 10^{-2}$ and $\overline{r}_0 = 0.11$, due to the assumptions of small radius and thin film adopted. The prediction of Zhang theory (2022) (equations 5.35-5.37) is almost identical to the present theory. Zhang theory (2022), however, did not consider the gravitational drainage (due to the thin-film assumption), thus yielding an over-prediction

when $\bar{h}_L$ and $\bar{r}_0$ are comparable (see the region $Ca > 10^{-1}$ in Figure 5.12a). All in all, the present theory predicts $\bar{h}_L$ better than past theories.

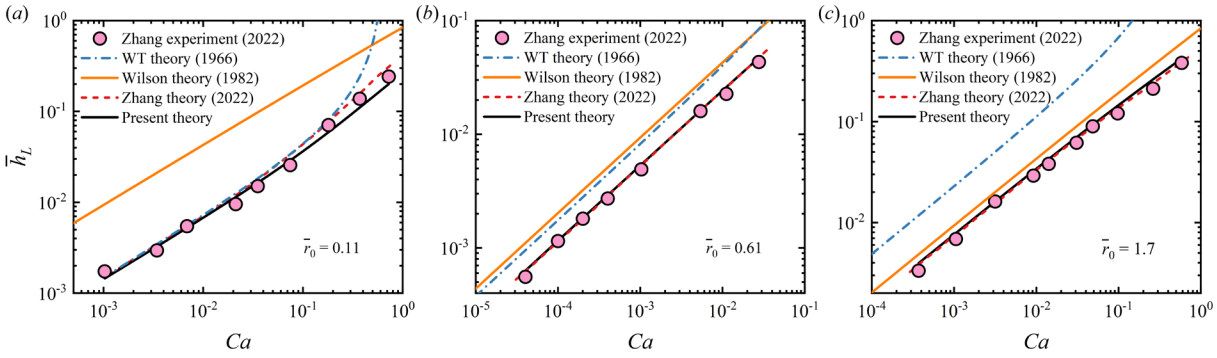

Figure 5.12. Comparison of the LL film thickness $\bar{h}_L$ calculated by the present theory with the experiment of Zhang [Zhang experiment (2022)], the theory of White and Tallmadge [WT theory (1966)], the theory of Wilson [Wilson theory (1982)], and the theory of Zhang [Zhang theory (2022)].

Given that the LL film not only occurs in scenario III but also in scenarios IV and WTFL, the lubrication theory for LL film is compared with the DNS for all three scenarios. Figure 5.13(a) illustrates the typical interfacial morphology of LL film for $\bar{r}_0 = 1$ and $Ca = 0.025$. The interfacial morphology calculated from the LT agree well with the DNS, not only for the uniform region of the LL film, but also for the meniscus region. A quantitative description of the thickness $\bar{h}_L$ for different Ca and $\bar{r}_0$ is given in Figure 5.13(b), once again, showing an excellent agreement between the LT and the DNS. On a logarithmic scale, the thickness $\bar{h}_L$ increases linearly with Ca. Similarly to the thick film thickness $\bar{h}_T$, the LL film thickness $\bar{h}_L$ increases with the radius $\bar{r}_0$. However, for large $\bar{r}_0$ (say $\bar{r}_0 = 100$), the cylinder reduces to a plate and the thickness $\bar{h}_L$ thus becomes independent of $\bar{r}_0$.

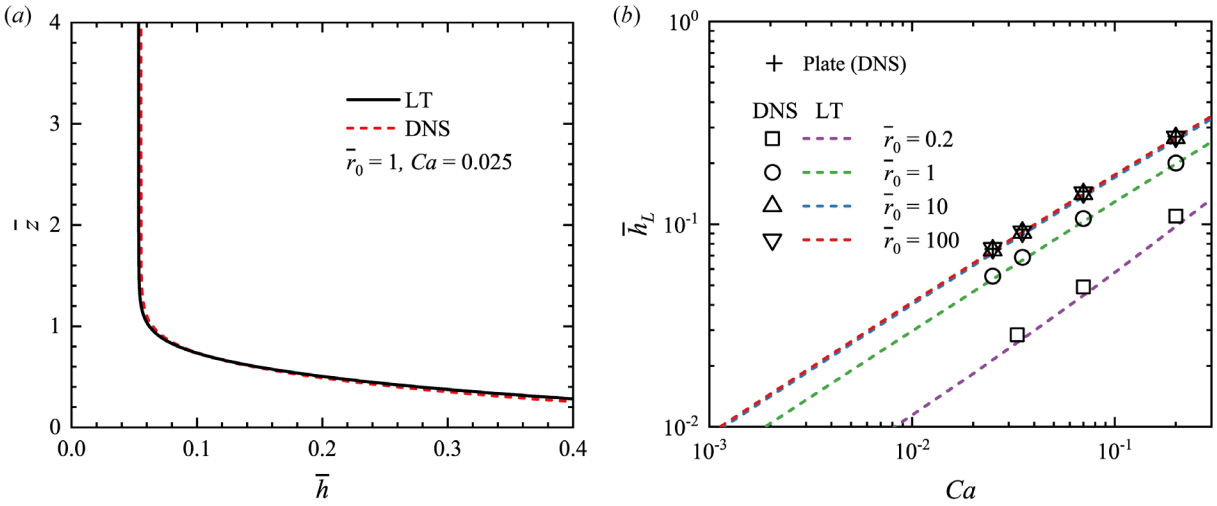

Figure 5.13. (*a*) Comparison of the interfacial morphology of the LL film calculated by the LT (solid curve) and the DNS (dashed curve) for $\bar{r}_0 = 1$ and $Ca = 0.025$. (*b*) Evolution of the thickness $\bar{h}_L$ with Ca at different $\bar{r}_0$: the symbol and the dashed curve denote the DNS and the LT respectively.

Another structure of the film in scenario III is the travelling capillary ridge that connects the thick film and the LL film. In the reference frame moving with the capillary ridge, Ca is replaced by ΔCa_{cr} that represents the cylinder velocity with respect to the capillary ridge. Therefore, the lubrication equation becomes

$$\frac{\partial \bar{k}}{\partial \bar{z}} - 1 + \frac{3f(\bar{d})}{\bar{h}^2}\left[\Delta Ca_{cr} - \frac{\bar{Q}}{\bar{h}(1+\bar{d}/2)}\right] = 0, \tag{5.38}$$

with the boundary conditions

$$\bar{h} = \begin{cases} \bar{h}_T & \text{as } \bar{z} \to +\infty \\ \bar{h}_L & \text{as } \bar{z} \to -\infty \end{cases}. \tag{5.39}$$

In the uniform region of thick film (or thin film) ($\bar{z} \to +\infty$ or $\bar{z} \to -\infty$), we shall have $\partial \bar{k}/\partial \bar{z} = 0$, equation (5.38) hence gives the following relationship:

$$\bar{Q} = \bar{h}_T\left(1+\frac{\bar{d}_T}{2}\right)\left[\Delta Ca_{cr} - \frac{\bar{h}_T^2}{3f(\bar{d}_T)}\right] = \bar{h}_L\left(1+\frac{\bar{d}_L}{2}\right)\left[\Delta Ca_{cr} - \frac{\bar{h}_L^2}{3f(\bar{d}_L)}\right]. \tag{5.40}$$

From equation (5.40) we can further derive the cylinder velocity with respect to the capillary ridge ΔCa_{cr}:

$$\Delta Ca_{cr} = \frac{f(\bar{d}_L)(1+\bar{d}_T/2)\bar{h}_T^3 - f(\bar{d}_T)(1+\bar{d}_L/2)\bar{h}_L^3}{3f(\bar{d}_L)f(\bar{d}_T)\left[(1+\bar{d}_T/2)\bar{h}_T - (1+\bar{d}_L/2)\bar{h}_L\right]}. \tag{5.41}$$

The boundary value problem (5.38-5.41) is solved numerically with a shooting method. Note that the corresponding thicknesses $\bar{h}_T$ and $\bar{h}_L$ have been solved in the analysis of thick film and LL film. A typical morphology of capillary ridge calculated from present LT and DNS for $\bar{r}_0$ = 10 and Ca = 0.03 is shown in Figure 5.14(a). The LT matches closely the DNS, with only small deviations in the waves. From equation (5.41) and the relation $Ca_{cr} = Ca - \Delta Ca_{cr}$, the velocity of capillary ridge in the laboratory reference frame, i.e. Ca_{cr} can be solved. Figure 5.14(b) illustrates that the agreement between Ca_{cr} solved by the LT and that obtained from the DNS is quite good. The capillary ridge velocity Ca_{cr} increases as the cylinder velocity Ca increases. Besides, a smaller radius also favours the upward travel of the capillary ridge.

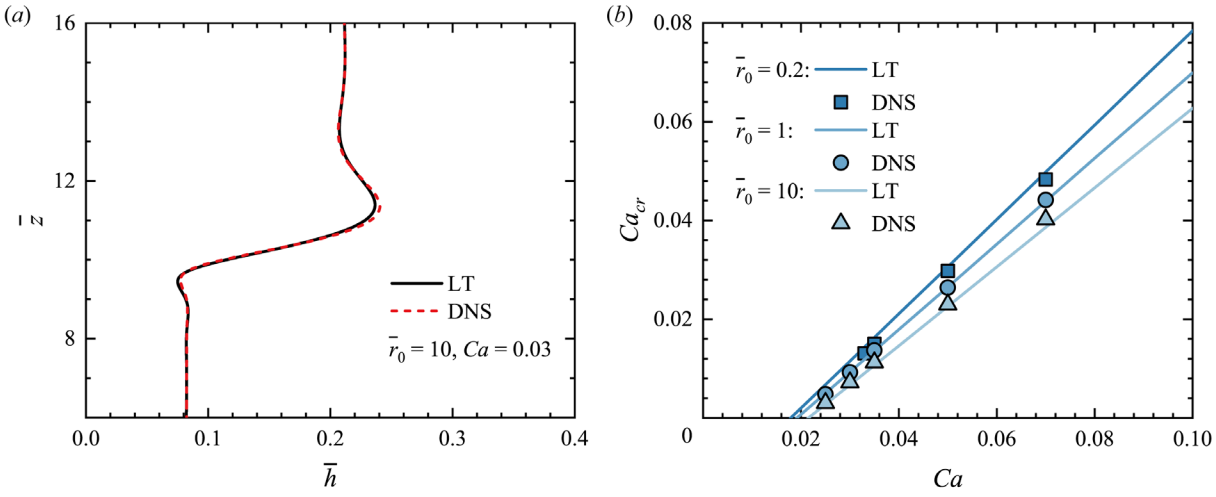

Figure 5.14. (a) Interfacial morphology of the capillary ridge calculated by the LT (solid curve) and the DNS (dashed curve) for $\bar{r}_0$ = 10 and Ca = 0.03. (b) Evolution of the capillary ridge velocity Ca_{cr} with Ca, at different $\bar{r}_0$: the symbol and the dashed curve denote the DNS and the LT respectively.

The travelling capillary ridge occurs only when $Ca > Ca_{c,1}$ or $Ca > Ca_{c,2}$. Therefore, there exists a minimum Ca_{cr} at either the critical capillary number $Ca_{c,1}$ or $Ca_{c,2}$, depending on the value of $\bar{r}_0$. Therefore, there exists a minimum Ca_{cr} at either the critical capillary number $Ca_{c,1}$ or $Ca_{c,2}$, depending on the value of $\bar{r}_0$. Specifically, in the interval $\bar{r}_0 < 2.3$, in which there is no scenario II and the dip coating enters scenario III directly from scenario I, the minimum Ca_{cr} hence occurs at $Ca = Ca_{c,1}$: minimum $Ca_{cr} = Ca_{c,1}$-ΔCa_{cr}. For $\bar{r}_0 > 2.3$, the minimum Ca_{cr} instead occurs at $Ca = Ca_{c,2}$: minimum $Ca_{cr} = Ca_{c,2}$-ΔCa_{cr}. As shown in Figure 5.15(a), the minimum Ca_{cr} decreases with $\bar{r}_0$ for small $\bar{r}_0$. Beyond the threshold radius ($\bar{r}_0 > 2.3$), the minimum Ca_{cr} converges to a constant value of $Ca_{cr} = 0.0013$, becoming independent of further increases in $\bar{r}_0$, as evidenced by the asymptotic behaviour in Figure 5.15(a). The minimum Ca_{cr} is always larger than zero, indicating that there is no stationary capillary ridge in scenario III. In fact, as analysed in scenario II or discussed in the study by Gao *et al.* (2016)[10] for plate geometry, the stationary capillary ridge only exists theoretically at $Ca = Ca^{**}$ (see Figure 5.9). To verify this, we solved theoretically the Ca_{cr} at $Ca = Ca^{**}$. As illustrated in Figure 5.15(b), the theoretical Ca_{cr} at $Ca = Ca^{**}$ is almost zero, with an order of magnitude of 10^{-5}.

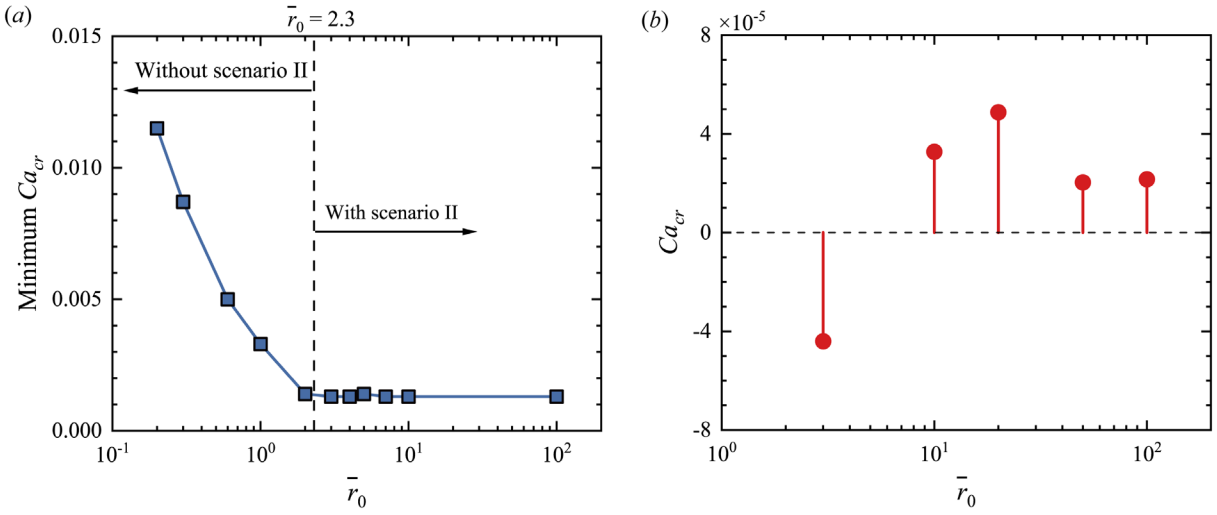

Figure 5.15. (a) Minimum velocity of the capillary ridge (minimum Ca_{cr}) in scenario III and (b) velocity of the capillary ridge (Ca_{cr}) at $Ca = Ca^{**}$, as a function of radius $\bar{r}_0$. All the results are obtained from the lubrication theory.

Our analysis shows that the thickness of the thick film $\bar{h}_T$ is not affected by Ca, while the thickness of the LL film $\bar{h}_L$ increases with Ca. This implies a critical $Ca_{c,3}$ at which the two thicknesses are equal. As demonstrated in Figure 5.16, the $Ca_{c,3}$ decreases with $\bar{r}_0$ and then tends to a constant, indicating that the large $\bar{r}_0$ favours the transition from scenario III to scenario IV. Furthermore, this also suggests that with increasing $\bar{r}_0$, the thickness of the LL film $\bar{h}_L$ increases significantly more than the thickness of the thick film $\bar{h}_T$.

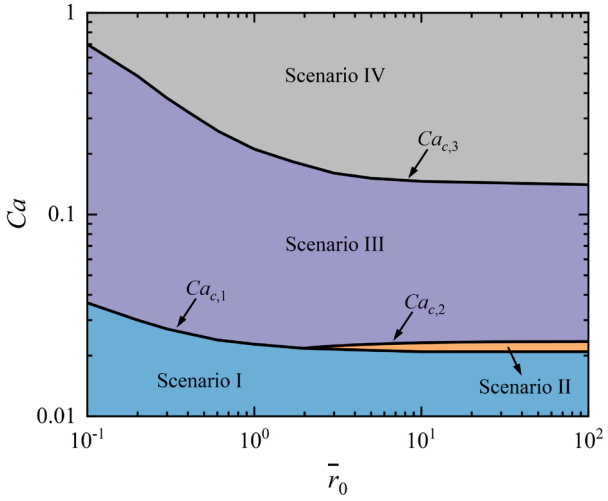

Figure 5.16. Critical capillary numbers $Ca_{c,1}$, $Ca_{c,2}$ and $Ca_{c,3}$ obtained from the LT versus the cylinder radius $\bar{r}_0$.

5.5.3 Scenario IV

Beyond $Ca_{c,3}$, dip coating enters scenario IV. As shown in Figure 5.17(*a*), the contact line moves upward linearly with time at a constant velocity. Unlike scenarios II and III, the film in scenario IV thins monotonically along the z direction, without any bump nor dimple (Figure 5.17*b*). The thickness of the LL film $\bar{h}_L$ is larger than that of the thick film $\bar{h}_T$, the moving capillary ridge thus no longer occurs and the two films connect in a smoother manner. The thicknesses of the two films, i.e. $\bar{h}_T$ and $\bar{h}_L$, can still be solved by the lubrication equations. However, the structure connecting the two films cannot be solved by equations (5.38-5.41) if $\bar{h}_T < \bar{h}_L$.

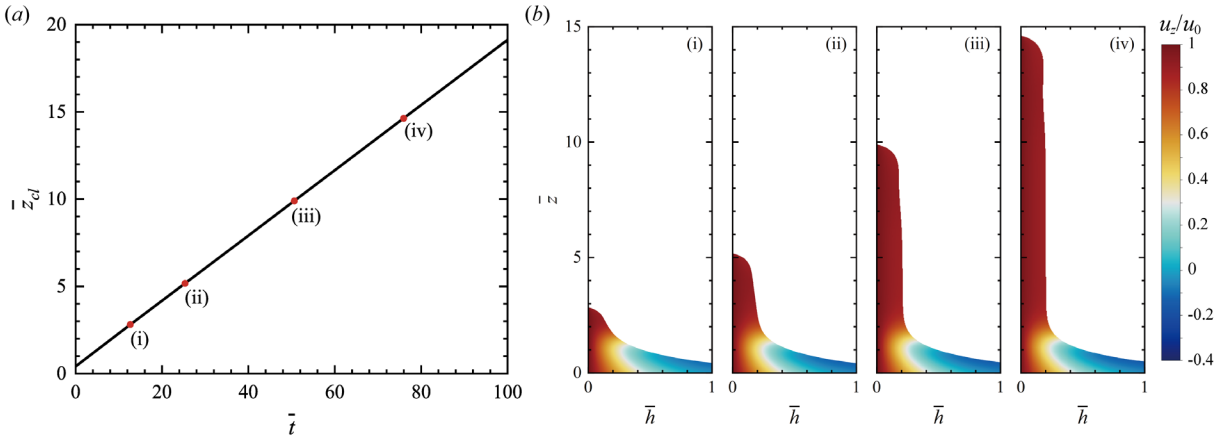

Figure 5.17. Dynamic process of scenario V: Ca = 0.2 and $\bar{r}_0$ = 1. (*a*) Evolution of $\bar{z}_{cl}$ (vertical position of the contact line) with time. (*b*) Normalized contours of axial velocity (u_z/u_0) in the liquid phase at the times labelled in figure (*a*), i: $\bar{t}$ = 13, ii: $\bar{t}$ = 25, iii: $\bar{t}$ = 51, and iv: $\bar{t}$ = 77.

We will prove that equations (5.38-5.41) have no solution for $\bar{h}_T < \bar{h}_L$. Multiply equation (5.38) by $\partial\bar{h}/\partial\bar{z}$ can be written as the following format:

$$\int_{-\infty}^{+\infty} \frac{\partial\bar{k}}{\partial\bar{z}}\frac{\partial\bar{h}}{\partial\bar{z}}\mathrm{d}\bar{z} = \int_{-\infty}^{+\infty} \left\{1-\frac{3f(\bar{d})}{\bar{h}^2}\left[\Delta Ca_{cr}-\frac{\bar{Q}}{\bar{h}(1+\bar{d}/2)}\right]\right\}\frac{\partial\bar{h}}{\partial\bar{z}}\mathrm{d}\bar{z}. \tag{5.42}$$

The integrals of both sides of equation (5.42) are too complex to solve analytically, so that we numerically solve them. The results show that if $\bar{h}_L > \bar{h}_T$, the sign of the left-hand side (l.h.s.) is negative but the sign of the right-hand side (r.h.s.) is positive, which means that equations (5.38-5.41) have no solution in this case. We also present an analytical proving for large cylinder radius. Equation reduces to the following equation at the limit of large radius:

$$\int_{-\infty}^{+\infty} \frac{\partial\bar{k}}{\partial\bar{z}}\frac{\partial\bar{h}}{\partial\bar{z}}\mathrm{d}\bar{z} = \int_{-\infty}^{+\infty} \left[1-\frac{3}{\bar{h}^2}\left(\Delta Ca_{cr}-\frac{\bar{Q}}{\bar{h}}\right)\right]\frac{\partial\bar{h}}{\partial\bar{z}}\mathrm{d}\bar{z}. \tag{5.43}$$

Considering boundary condition (5.39) in equation (5.43) yields:

$$\text{l.h.s. of equation (5.43)} = -\int_{-\infty}^{+\infty} \bar{k}\frac{\partial^2\bar{h}}{\partial\bar{z}^2}\mathrm{d}\bar{z} = -\int_{-\infty}^{+\infty} \frac{\left(\partial^2 h/\partial z^2\right)^2}{[1+(\partial h/\partial z)^2]^{3/2}}\mathrm{d}\bar{z}, \tag{5.44}$$

$$\text{r.h.s. of equation (5.43)} = \bar{h}_T - \bar{h}_L + 3\Delta Ca_{cr}\left(\frac{1}{\bar{h}_T} - \frac{1}{\bar{h}_L}\right) - \frac{3\bar{Q}}{2}\left(\frac{1}{\bar{h}_T^2} - \frac{1}{\bar{h}_L^2}\right). \tag{5.45}$$

Equation (5.44) shows that the sign of l.h.s of (5.43) is negative.

Taking the limit of large radius in equation (5.40) and equation (5.41), and injecting them into equation (5.45), we obtain:

$$\text{r.h.s. of equation (5.43)} = \frac{1}{2}\frac{\left(\bar{h}_L - \bar{h}_T\right)^3}{\bar{h}_T \bar{h}_L}. \tag{5.46}$$

Equation (5.46) shows if $\bar{h}_L > \bar{h}_T$, the sign of r.h.s of (5.43) is positive and opposite to the sign of l.h.s., accordingly, equations (5.38-5.41) have no solution in this case.

5.5.4 Wavy films: WTFL, WTWL and FTWL

Wavy films have been widely observed in the coating of cylinders[8,17,18] and tubes[19]. In this study, the film is wavy when the cylinder radius is very small. The waves on the thick film and the LL film are independent and do not transfer to each other. Correspondingly, there are in total three different wavy film, including WTFL (wavy thick film and flat LL film), WTWL (wavy thick film and wavy LL film) and FTWL (flat thick film and wavy LL film) (see Figure 5.18). More specifically, for Ca = 0.033 and $\bar{r}_0$ = 0.2, the wave just occurs in the thick film and does not enter the LL film through the capillary ridge; for Ca = 0.13, $\bar{r}_0$ = 0.2, both the thick film and the LL film are wavy; for Ca = 0.1, $\bar{r}_0$ = 0.275, the wave just occurs in the LL film and does not enter the thick film through the capillary ridge.

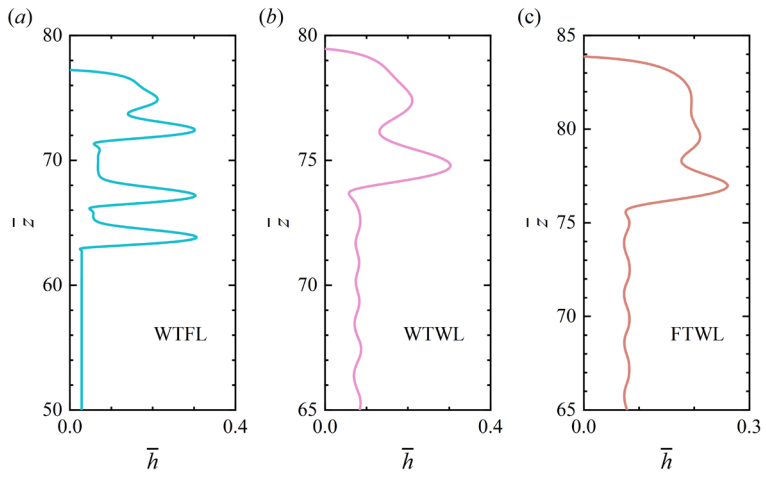

Figure 5.18. Magnified view of the interfacial morphologies from Figure 5.2(*g*-*i*), showing detailed interfacial features. (*a*) WTFL: $Ca = 0.033$, $\bar{r}_0 = 0.2$, coexistence of wavy thick film and flat LL film. (*b*) WTWL: $Ca = 0.13$, $\bar{r}_0 = 0.2$, coexistence of wavy thick film and wavy LL film. (*c*) FTWL: $Ca = 0.1$, $\bar{r}_0 = 0.275$, coexistence of flat thick film and wavy LL film.

Figure 5.19 illustrates the dynamic process of wavy film taking WTFL as a representative case. The waves, as shown in Figure 5.19(*a*), do not affect the contact line that moves upward at a constant velocity except at the early stages. Differently from scenarios II-IV, the bump in this scenario does not evolves to a flat film but instead to a series of waves (Figure 5.19*b*-*g*). Under different wavy scenarios, the thick film and LL film exhibit their respective wave.

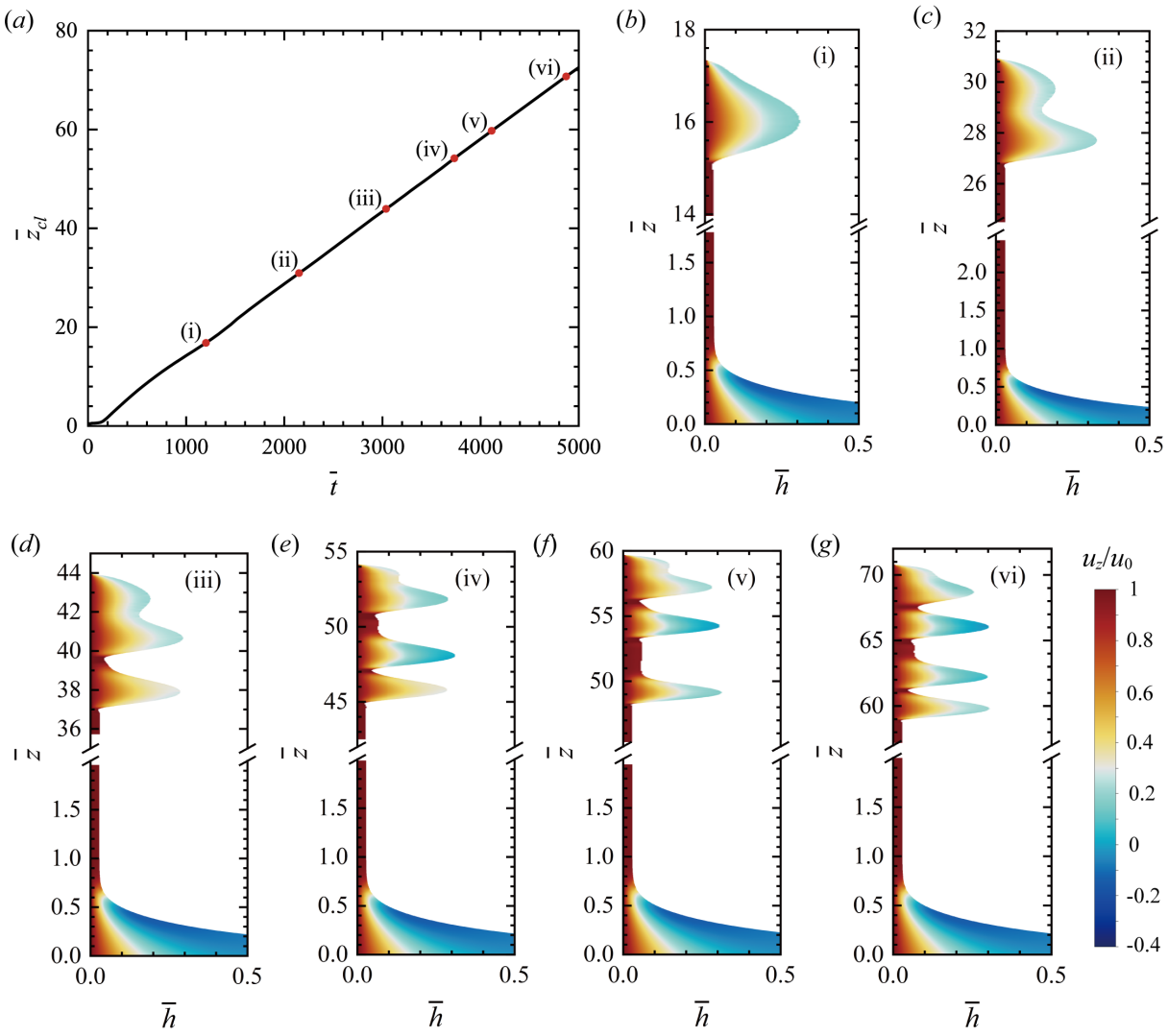

Figure 5.19. A typical dynamic process of scenario WTFL (wavy thick film and flat LL film): Ca = 0.033 and $\bar{r}_0$ = 0.2. (*a*) Temporal evolution of the vertical position of the contact line. (*b*-*g*) Contours of normalized axial velocity (u_z/u_0) in the liquid phase at the times labelled in figure (*a*), (i): $\bar{t}$ = 1240, (ii): $\bar{t}$ = 2151, (iii): $\bar{t}$ = 3037, (iv): $\bar{t}$ = 3733, (v): $\bar{t}$ = 4113, and (vi): $\bar{t}$ = 4872.

A natural inquiry arises regarding the critical conditions between the different wavy film scenarios. Duprat *et al.* (2007) proposed a theory predicting the instability of a film flowing down a vertical cylinder.[8] The present dip coating can be treated as a case of film flowing down in the frame of reference moving with the cylinder. Therefore, their theory can be extended directly to the present dip coating on a partially wetting cylinder. To avoid redundancy, we present only the final model of this

paper, a comprehensive derivation of this theory is available in the study by Duprat *et al.* (2007).[8] Specifically, the film is absolutely unstable (which will eventually cause the waves or drops) once fulfilling the following equation:

$$\frac{\bar{d}_N}{c_k\left(1+\bar{d}_N\right)^4} > \beta_{ca}^{3/2}\bar{r}_0^2, \tag{5.47}$$

where $\bar{d}_N = \bar{h}_N/\bar{r}_0$, h_N represents the uniform thickness of thick film or LL film (i.e. $\bar{h}_N = \bar{h}_T$ or $\bar{h}_L$) and $\beta_{ca} = \left[(9/4)\left(7\sqrt{7}\text{-}17\right)\right]^{1/3} \approx 1.507$. c_k, the speed of the linear kinematic wave as the complex wave number tends to 0, is expressed by the following equation:

$$c_k = \frac{1+\dfrac{\phi'(\bar{d}_N)}{3\phi(\bar{d}_N)}\bar{d}_N}{1+\bar{d}_N}, \tag{5.48}$$

where $\phi'(\bar{d}_N)$ denotes the differential function of $\phi(\bar{d}_N)$ with respect to $\bar{d}_N$, and the geometric factor $\phi(\bar{d}_N)$ has the following form:

$$\phi\left(\bar{d}_N\right) = \frac{12\left(1+\bar{d}_N\right)^4\log\left(1+\bar{d}_N\right) - 3\bar{d}_N\left(2+\bar{d}_N\right)\left(3\bar{d}_N^2+6\bar{d}_N+2\right)}{16\bar{d}_N^3}. \tag{5.49}$$

Equations (5.47-5.49) are plotted as a solid curve in Figure 5.20(*a*) on the parameter plane $\bar{h}_N$ versus $\bar{r}_0$. The region to the left of the curve corresponds to the wavy (absolute unstable) film, while the right side represents the flat (convective unstable) film. To conclude, on the one hand, the wavy state of the film is controlled by both the film thickness $\bar{h}_N$ and the cylinder radius $\bar{r}_0$. On the other hand, the thickness of the thick film is controlled by $\bar{r}_0$, while the thickness of the LL film is controlled by both *Ca* and $\bar{r}_0$. Therefore, the wavy state of the thick film depends on $\bar{r}_0$, while the wavy state of the LL film is controlled by both *Ca* and $\bar{r}_0$.

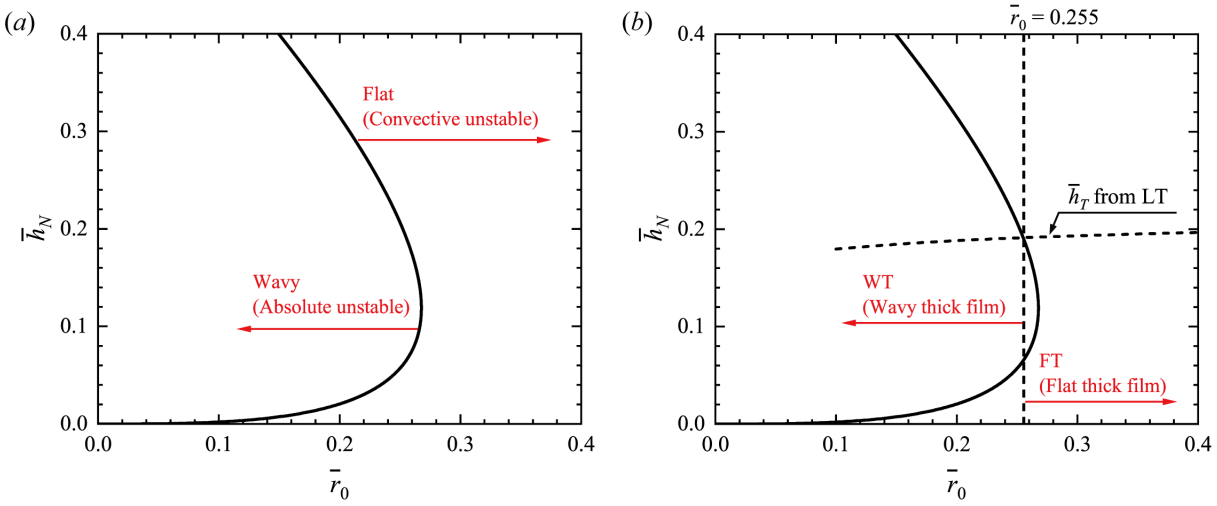

Figure 5.20. (*a*) Critical condition between wavy (absolute unstable) film and flat (convective unstable) film in the parameter plane $\bar{h}_N$ versus $\bar{r}_0$ obtained from equations (5.47-5.49). (*b*) Critical $\bar{r}_0$ between WT (wavy thick film) and FT (flat thick film). The solid curve refers to the solution of equations (5.47-5.49) and the dashed curve refers to the thickness $\bar{h}_T$ of the thick film obtained from the LT (5.25-5.28).

Given the independence of the wave dynamics between the thick film and the LL film, as well as their distinct film-forming mechanisms, we analyse the two films separately by using equations (5.47-5.49). We begin with the thick film, as its thickness remains independent of *Ca*, making it tractable for analysis. The critical condition obtained from equations (5.47-5.49) is replotted in Figure 5.20(*b*) together with the thickness $\bar{h}_T$ of the thick film obtained from the LT (5.25-5.28). The radius $\bar{r}_0$ at the intersection of the two curves is the critical $\bar{r}_0$ demarcating the WT (wavy thick film) and the FT (flat thick film). The critical radius obtained from DNS is 0.26 that is very close to the theoretical one. For a radius $\bar{r}_0$ inferior (resp. superior) to the critical $\bar{r}_0$, the thick film is wavy (resp. flat).

The critical *Ca* separating the WL (wavy LL film) and the FL (flat LL film) scenarios is derived from equations (5.47-5.49) and lubrication theory, expressed as a function of $\bar{r}_0$. As shown in Figure 5.21(*a*), the region to the left (resp. right) of the solid curve corresponds to the WL (resp. FL) scenario.

This critical condition is then combined with the critical $\bar{r}_0$ demarcating the WT and the FT to give the wavy states of the entire film. Accordingly, as depicted in Figure 5.21(*b*), the coating scenario is sub-divided into four scenarios by the two critical conditions, including WTFL (wavy thick film and flat LL film), WTWL (wavy thick film and wavy LL film), FTWL (flat thick film and wavy LL film), and no wave scenarios. Since the theory (5.47-5.49) was developed under the zero-inertia and thin-film assumptions, the boundary between the four scenarios revealed by this theory is quantitatively different from that captured by the DNS. More accurate results could be obtained from the linear stability analysis of the axisymmetric Navier-Stokes equations, which is beyond the scope of present study. However, the boundary obtained from equations (5.47-5.49) is at least topologically similar to DNS.

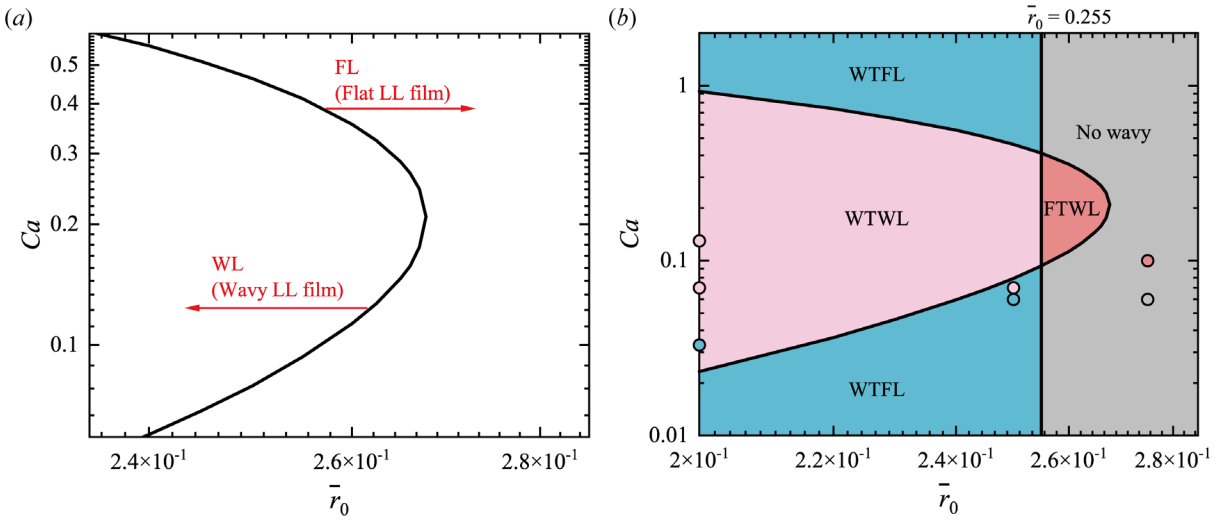

Figure 5.21. (*a*) Critical condition between WL (wavy LL film) and FL (flat LL film) obtained from equations (5.47-5.49) and LT on the parameter plane of (Ca, $\bar{r}_0$). (*b*) WTFL (wavy thick film and flat LL film), WTWL (wavy thick film and wavy LL film), FTWL (flat thick film and wavy LL film) and no waving scenarios on the parameter plane of (Ca, $\bar{r}_0$). The solid curve refers to the critical conditions obtained from theory. The symbol refers to the DNS, coloured in the same manner as the corresponding scenario.

Figure 5.21(*b*) is plotted together with Figure 5.16 to obtain the map encompassing all scenarios. As shown in Figure 5.22, the interfacial morphology depends not only on the capillary number *Ca* but also on the cylinder radius $\bar{r}_0$. For $\bar{r}_0 > 2$, as the capillary number *Ca* increases, dip coating undergoes successively four scenarios: I → II → III → IV. For $0.268 < \bar{r}_0 < 2$, scenario II disappears, there are hence only three scenarios: I → III → IV. For $0.255 < \bar{r}_0 < 0.268$, the LL film exhibits waves for certain *Ca* values, leading to the FTWL scenario: I → III → FTWL → III → IV. When the radius $\bar{r}_0$ is less than 0.255, it is more prone to the formation of waves, while III and IV do not occur. Specifically, for $0.21 < \bar{r}_0 < 0.255$, I → WTFL → WTWL → WTFL; for $\bar{r}_0 < 0.21$, I → WTWL → WTFL.

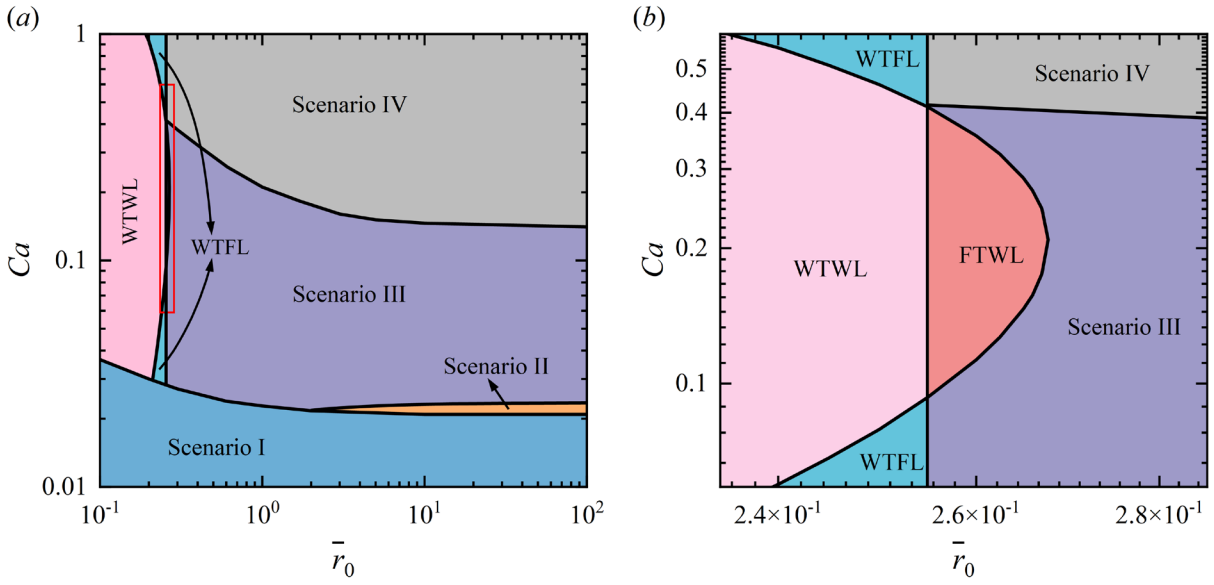

Figure 5.22. (*a*) Different scenarios in the ($\bar{r}_0$, *Ca*) parameter plane. (*b*) A magnified view of the region enclosed by the red box in figure (*a*).

5.6 Conclusion

This study investigates the wetting and deposition of Newtonian fluids on a partially wetting cylindrical substrate during dip coating. Using direct numerical simulation and lubrication theory, we focus primarily on the film formation and the subsequent film transition that occurs after wetting that have hitherto not been addressed in the literature for cylindrical geometries. The results show that the capillary number *Ca* and the cylinder radius $\bar{r}_0$ not only influence quantitatively the film thickness but

also change qualitatively the interfacial morphology. For $\bar{r}_0 > 2.3$, when increasing Ca, there are four successive scenarios of interfacial morphologies. For $Ca < Ca_{c,1}$, the cylinder cannot be wetted by the liquid and the interface is fixed as a stationary meniscus. For $Ca_{c,1} < Ca < Ca_{c,2}$, the cylinder is coated by a thick film whose thickness $\bar{h}_T$ increases with $\bar{r}_0$ and is independent of Ca. The thick film connects to the container through a stationary dimple. For $Ca_{c,2} < Ca < Ca_{c,3}$, the stationary dimple evolves to an LL film with a thickness $\bar{h}_L$ less than the thickness $\bar{h}_T$ of the thick film. The LL film connects with the thick film through a travelling capillary ridge. The thickness $\bar{h}_L$ of the LL film increases both with Ca and $\bar{r}_0$. When the capillary number Ca exceeds the critical $Ca_{c,3}$, the LL becomes thicker than the thick film. Therefore, the capillary ridge disappears and the two films connect in a smoother manner.

As shown by our lubrication theory, also as figured out in the literature for plate substrates,[10,13,20] the wetting transition is associated with the saddle-node bifurcation of the meniscus solution and the transition from the dimple to the LL film corresponds to the saddle-node bifurcation of the dimple solution. More importantly, our lubrication theory reveals that the critical capillary number $Ca_{c,1}$ of wetting transition decreases with $\bar{r}_0$, while the critical capillary number $Ca_{c,2}$ of transition from the dimple to the LL film increases with $\bar{r}_0$. When $\bar{r}_0$ is small enough ($\bar{r}_0 < 2.3$ in this paper), $Ca_{c,1}$ is larger than $Ca_{c,2}$, and the stationary meniscus evolves directly to the film consisting of the thick film and the LL one as Ca increases, without undergoing the dimple scenario.

The further decrease in radius $\bar{r}_0$ triggers waves of the thick film and the LL film. The wavy states of the two films are independent and do not transfer to each other. The thick film becomes wavy when $\bar{r}_0$ is less than 0.255; whether the LL film is wavy is complicated and controlled by Ca and $\bar{r}_0$. For $0.255 < \bar{r}_0 < 0.268$, the LL exhibits waves at certain Ca. For $0.21 < \bar{r}_0 < 0.255$, the LL film undergoes successively flat, wavy and flat states, with Ca increasing. For $\bar{r}_0 < 0.21$, the LL film is wavy and becomes flat only at large Ca.

Reference

1. Zhang Z, Salamatin A, Peng F, Kornev KG. Dip coating of cylinders with Newtonian fluids. *J. Colloid Interface Sci.* Feb 2022;607(Pt 1):502-513.
2. White DA, Tallmadge JA. A theory of withdrawal of cylinders from liquid baths. *AIChE J.* 1966;12(2):333-339.
3. Shing Chan T, Gueudré T, Snoeijer JH. Maximum speed of dewetting on a fiber. *Phys. Fluids.* 2011;23(11):112103.
4. Gao P, Liu A, Feng JJ, Ding H, Lu X-Y. Forced dewetting in a capillary tube. *J. Fluid Mech.* 2018;859:308-320.
5. Chan TS, Pedersen C, Koplik J, Carlson A. Film deposition and dynamics of a self-propelled wetting droplet on a conical fibre. *J. Fluid Mech.* 2021;907:A29.
6. Chan TS, Yang F, Carlson A. Directional spreading of a viscous droplet on a conical fibre. *J. Fluid Mech.* 2020;894:A26.
7. Chan TS, Lee CL, Pedersen C, Dalnoki-Veress K, Carlson A. Film coating by directional droplet spreading on fibers. *Phys. Rev. Fluids.* 2021;6(1):014004.
8. Duprat C, Ruyer-Quil C, Kalliadasis S, Giorgiutti-Dauphine F. Absolute and convective instabilities of a viscous film flowing down a vertical fiber. *Phys Rev Lett.* Jun 15 2007;98(24):244502.
9. de Gennes P-G, Brochard-Wyart F, Quéré D. *Capillarity and Wetting Phenomena*2004.
10. Gao P, Li L, Feng JJ, Ding H, Lu X-Y. Film deposition and transition on a partially wetting plate in dip coating. *J. Fluid Mech.* 2016;791:358-383.
11. Oron A, Davis SH, Bankoff SG. Long-scale evolution of thin liquid films. *Rev. Mod. Phys.* 1997;69(3):931-980.
12. Snoeijer JH, Delon G, Fermigier M, Andreotti B. Avoided critical behavior in dynamically forced wetting. *Phys. Rev. Lett.* May 5 2006;96(17):174504.
13. Snoeijer JH, Andreotti B, Delon G, Fermigier M. Relaxation of a dewetting contact line. Part 1. A full-scale hydrodynamic calculation. *J. Fluid Mech.* 2007;579:63-83.
14. Gao P, Li L, Lu XY. Dewetting films with inclined contact lines. *Phys Rev E Stat Nonlin Soft Matter Phys.* Feb 2015;91(2):023008.
15. Landau L, Levich B. Dragging of a liquid by a moving plate. *Acta Physicochim. URSS.* 1942;17(2):42-54.
16. Wilson SDR. The drag-out problem in film coating theory. *J. Eng. Math.* 1982;16(3):209-221.
17. GonzÁLez AG, Diez JA, Gratton R, Campana DM, Saita FA. Instability of a viscous liquid coating a cylindrical fibre. *J. Fluid Mech.* 2010;651:117-143.
18. Kliakhandler IL, Davis SH, Bankoff SG. Viscous beads on vertical fibre. *J. Fluid Mech.* 2001;429:381-390.
19. Duclaux V, Clanet C, QuÉRÉ D. The effects of gravity on the capillary instability in tubes. *J. Fluid Mech.* 2006;556:217-226.
20. Chan TS, Snoeijer JH, Eggers J. Theory of the forced wetting transition. *Phys. Fluids.* 2012;24(7):072104.

6 Hydrodynamics of viscoplastic fluids upon dip coating of a fully wetting plate

The present chapter simulates the dip coating of a fully wetting plate in viscoplastic fluid using the Volume of Fluid (VOF) method, visualize the flow field, and parametrically investigate the influence of yield stress, consistency factor, flow index, and withdrawal speed on the flow field and resulting film thickness. The yielded-unyielded interfaces as well as the profiles of flow velocity and shear stress were theoretically determined under final steady state. The main flow characteristics of drainage in the meniscus were captured. Under the negligible effect of surface tension on the film coating, a semi-empirical model of film thickness considering drainage effect is proposed with good prediction performance.

6.1 Introduction

Early works on dip coating of yield stress fluids focused on ordinary Bingham fluids.[1-4] Moreover, the Bingham number *Bi* was larger than l. $Bi = \tau_c/K\dot{\gamma}^n$ (In this work, the film thickness h_0 is taken as the characteristic length for calculating $\dot{\gamma}$, unless specified otherwise) is the ratio of the yield stress τ_c to the shear-rate dependent shear stress $K\dot{\gamma}^n$, where K, $\dot{\gamma}$ and n are the consistency factor, shear rate and flow index, respectively. Much less attention was paid to the numerical simulation of dip-coating for low *Bi* number fluids. For dip coatings in the laboratory, such as colloids suspensions[5-7], Carbopol solutions[8], and poly(styrene-butadiene-styrene) paraffin gels[9], the *Bi* number is between 10^{-1} and 10^{1}. Modern dip coating processes, such as magnetic tapes, photographic films and drug patches, require high withdrawal velocities (> 1 m·s^{-1}) to be commercially interesting.[10] The corresponding *Bi* numbers are much lower than 1. Studies on dip coating processes at high withdrawal velocities or low *Bi* numbers are necessary to understand and guide such operations.

Another unsolved issue is related to the hydrodynamics of viscoplastic fluids during the withdrawal stage of the plate in the bath. It can be divided into three regions from the plate to the container wall: inner yielded region, unyielded region and outer yielded region, respectively. Currently, many studies focus only on the hydrodynamics of the inner yielded region. They suggest that the coated

film is formed from the fluid in the inner yielded region[11] and has a thickness proportional to the yielded region thickness[11]. However, it is almost unrealistic to theoretically predict the coating thickness based only on the flow of the inner yielded region without paying attention to the other two regions, which leads to the fact that the coating thickness is generally empirically correlated to the Bingham number.[12,13] Recently, for the dip coating of a rod, the flow characteristics (including the thickness of the inner yielded region) of the three regions have been determined by the velocity continuity and mass conservation.[14] Logically, this method can be extended to determining the flow characteristics of the fluid for the plate geometry.

Besides, the fluid flow in the meniscus region has attracted extensive interest, since it can be directly related to the coating thickness. In particular, the drainage phenomenon (i.e. the fact that part of the fluid in the meniscus region flows back to the container) should be paid attention to when the gravitational force is strong enough, which tends to reduce the film thickness.[15] Currently, researches on the drainage effect mainly focus on Newtonian fluids, and little on the yield stress fluids. To the best of our knowledge, Maillard *et al.* 2016[12] introduced the contribution of the drainage effect to the film thickness model. However, due to the complexity of the flow in the meniscus, the draining fluid was simplified in the model as a layer of Newtonian fluid rather than viscoplastic fluid.

This chapter used the volume of fluid (VOF) method to simulate the dip coating process of a series of simple viscoplastic fluids (without thixotropy) of *Bi* number below 1. More specifically, the hydrodynamics of fluids in the three regions was investigated, with special attention to the downward velocity in the inner yielded region. The flow regime and coating thickness of viscoplastic fluids with different rheological properties (K and τ_c) were investigated at various withdrawal velocities. The profiles of shear stress and flow velocity in each region were determined theoretically with the drainage occurrence, and showed good agreement with the simulated results. The modified capillary number was defined to better consider the effects of the surface tension on the film thickness. The drainage in

the meniscus was simplified as free flow along the plate under gravity. Considering the drainage effect, the film thickness model was proposed and showed good prediction performance.

6.2 Numerical settings

6.2.1 Fluid properties

The viscoplastic fluid is described by the bi-viscous model (3.9) presented in Chapter 3, which distinguishes the liquid and solid regimes by the critical shear rate $\dot{\gamma}_c$. The DNS results exhibit significant dependence on the critical shear rate. Indeed, the variations of this parameter directly affect the film profile. As demonstrated in Figure 6.1, for τ_c = 15 Pa, K = 90.0 Pa·s^n, and n = 0.60 (fluid F4) and u_0 = 10 mm·s^{-1}, the free surface profile gradually converges with the critical shear rate decreasing from 10^{-2} to 10^{-6} s^{-1}. In particular, the film profiles with the critical shear rates of 10^{-5} and 10^{-6} s^{-1} superimpose well. This is why, to ensure the calculation quality and save time, the critical shear rate was set to 10^{-5} s^{-1} for all viscoplastic fluids. Table 6.1 shows the physical and rheological properties of the fluids used in this work.

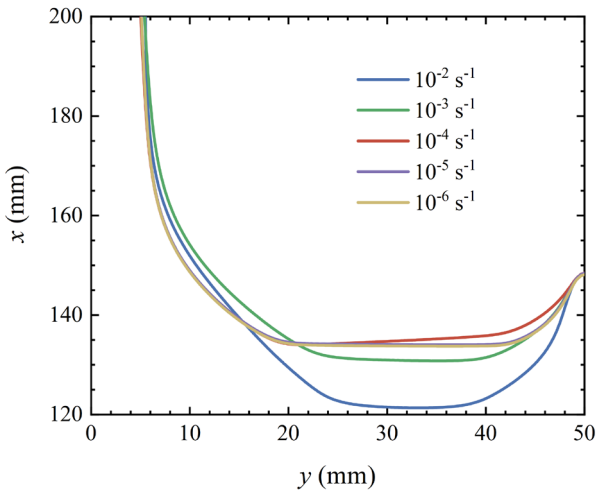

Figure 6.1. Effect of the critical shear rate $\dot{\gamma}_c$ on the simulated free surface profile for fluid F4 at a withdrawal velocity of u_0 = 10 mm·s^{-1}.

Table 6.1 Physical and rheological properties of the coating fluids

Fluid	Density ρ ($kg \cdot m^{-3}$)	Surface tension σ ($N \cdot m^{-1}$)	Consistency factor K ($Pa \cdot s^n$)	Flow index n	Yield stress τ_c (Pa)	Critical shear rate $\dot{\gamma}_c$ (s^{-1})
Fa	1000	0.072	10.7	0.35	27	1×10^{-5}
Fb	1000	0.072	40.7	0.35	82	1×10^{-5}
F1	1020	0.072	90.0	0.80	15	1×10^{-5}
F2	1020	0.072	90.0	0.80	35	1×10^{-5}
F3	1020	0.072	45.0	0.80	15	1×10^{-5}
F4	1020	0.072	90.0	0.60	15	1×10^{-5}

Fa and Fb are viscoplastic fluids used in the literature[11].

6.2.2 Computational domain and meshing

The computational domain under investigation is a rectangular region of total height $H = 200$ mm and of width $W = 50$ mm, as illustrated in Figure 6.2. The initial depth of the liquid (the distance between the initial liquid-air interface and the bottom) is 150 mm. The bottom and the wall of the container (black lines) are defined as static wall. The standard atmospheric pressure is imposed on the upper outlet (green line). The plate (red line) is defined as a wall moving vertically upward at a constant velocity u_0. The contact angles at the plate and the container wall are 90 degrees to ensure the liquid-air interface to connect to the container horizontally.

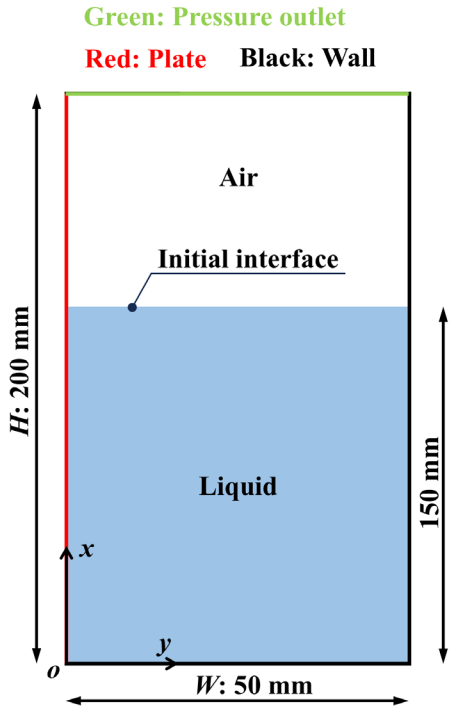

Figure 6.2. Schematic of the computational domain with the initial and boundary conditions.

As shown in Figure 6.3, the computational domain is discretized by structured quad mesh cells with refinement near the plate and the liquid-air interface. The mesh cell size may have an effect on the accuracy of simulations. It should be small at low withdrawal velocity because the film thickness is thinner. Four different cell numbers (M1 = 59501, M2 = 74451, M3 = 89401 and M4 = 104351 cells) are used to evaluate the effects of the mesh refinement on the film profile of F1 for u_0 = 1 mm·s^{-1} (the lowest withdrawal velocity tested in this chapter). As the cell number increases or the mesh cell size decreases from M1 to M4, the film profile gradually converges, Figure 6.4. The gap between the film profiles obtained with M3 and M4 is less than 1%. Therefore, mesh M3 is used for the subsequent simulations.

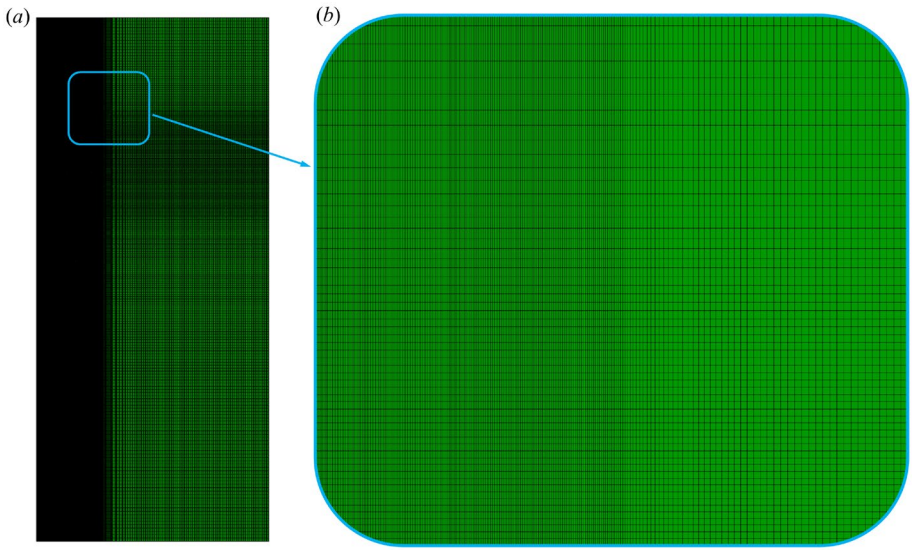

Figure 6.3. Computational domain and mesh details. (*a*) Global mesh structure. (*b*) Refined mesh near the plate and liquid-air interface.

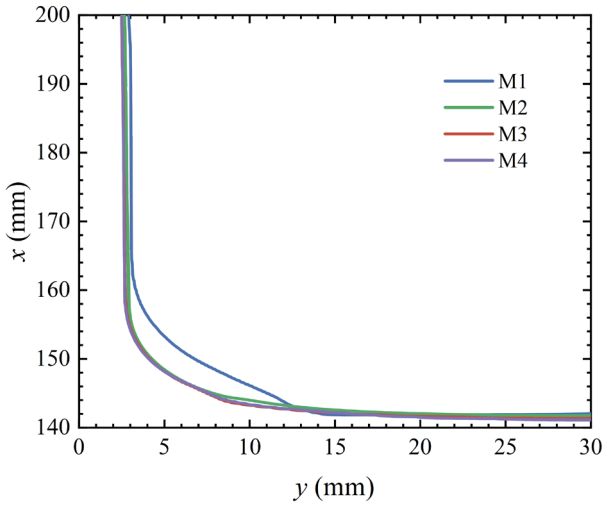

Figure 6.4. Liquid-air interface profiles obtained from simulations with different mesh cell sizes. Fluid: F1; withdrawal velocity u_0: 1 mm·s^{-1}.

6.3 Results and discussions

6.3.1 Model validation

The simulation covers the entire withdrawal process, from the beginning to the steady state (Figure 6.5). At the very beginning of the withdrawal, there exists a visible local flow near the plate at the bottom of the container, which disappears after some time (see Figure 6.5*a*). The coating film forms at a distance x = 180 ~ 200 mm from container bottom. The thickness is zero at the beginning, until the tip of the coating film reaches the height of 180 mm and then film thickness gradually increases over time (Figure 6.5*b*). After a sufficiently long time, the film thickness reaches a plateau ($h = h_0$) and the coating reaches steady state. The rest of the study will focus on the steady state.

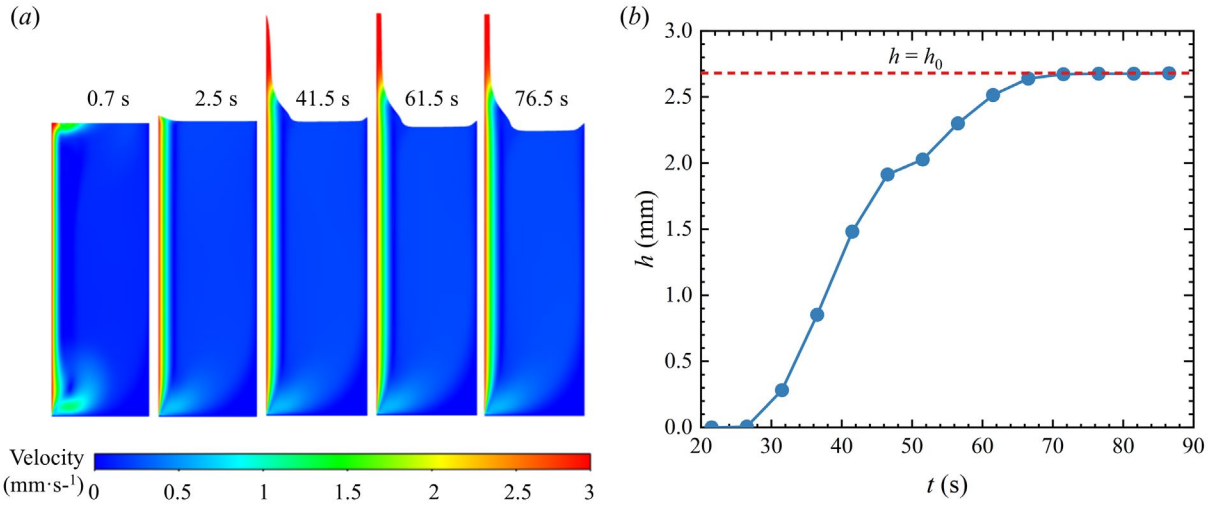

Figure 6.5. Velocity contours (*a*) and film thickness (*b*) of fluid F1 during the coating process at u_0 = 3 mm·s^{-1}.

In order to verify the accuracy of the simulation, additional simulations were performed in a W = 75 mm wide container. The simulated film thicknesses were compared with the experimental ones reported in the literature[11]. The measurement was done by weighing the film over a given height in the x-direction. Thus, the experimental film thickness is an average value. The values of the simulated film thickness agree with the experimental ones with most deviations less than 15% (Figure 6.6). Such relative deviations are acceptable considering the complex rheological properties of viscoplastic fluids and possible experimental errors.

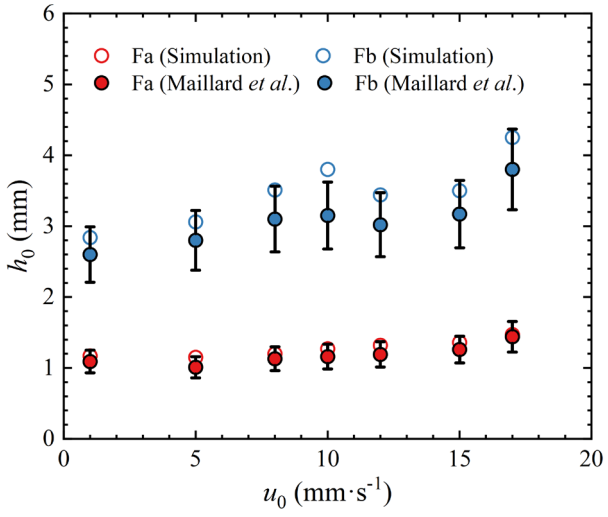

Figure 6.6. Film thickness h_0 as a function of the withdrawal velocity u_0. Comparison between simulations and experiments[11].

6.3.2 Flow regime

The logarithmic distribution of strain rate of F1 at u_0 = 3 mm·s^{-1} is plotted in Figure 6.7(*a*). The fluid in the bath can be divided into two yielded regions ($\dot{\gamma} \geq \dot{\gamma}_c$) and an unyielded region ($\dot{\gamma} \leq \dot{\gamma}_c$).[16,17] Based on the distribution of velocity and strain rate, the flow during the dip coating is simplified as shown in Figure 6.7(*b*). The yielded and unyielded regions are demarcated by δ_1 and δ_2 on axis y, respectively. Due to the no-slip condition, the velocity of fluid at the plate equals the withdrawal velocity u_0. The velocity in the inner yielded region decreases along axis y, become negative at δ_0, and reaches the maximum downward velocity u_d at δ_1. In the unyielded region, the fluid moves downward as a whole, at the uniform velocity u_d. In the outer yielded region, the velocity gradually increases from the negative value u_d and reaches zero at the container wall.

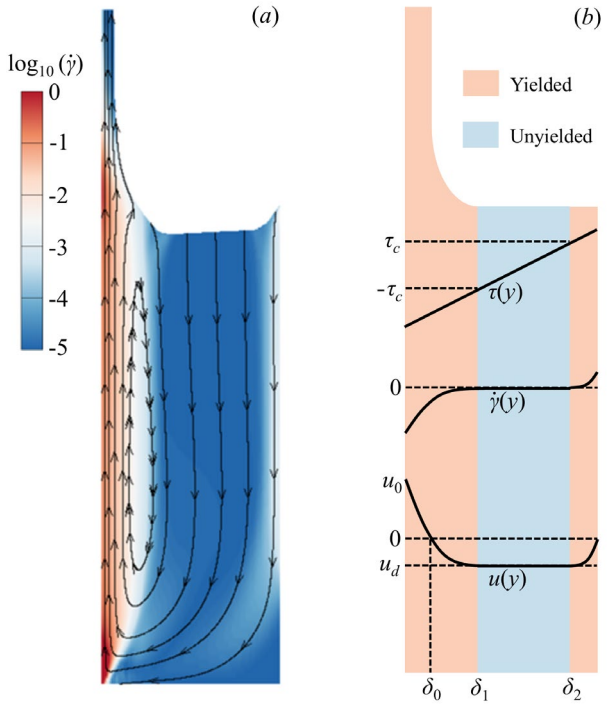

Figure 6.7. Typical distribution of $\log_{10}(\dot{\gamma})$ of F1 at u_0 = 3 mm·s^{-1} (*a*) and flow velocity schematic (*b*) during the dip coating.

Figure 6.8 shows the velocity contours in the container for various withdrawal velocities. As the plate is moving upward, the fluid near the plate is dragged up. In the meniscus there is obvious drainage: the dragged-up fluid is no more confined and partly flows back to the container. Meanwhile, under the actions of pressure and gravity, the surrounding fluid on the right flows down, in order to compensate for the fluid that is dragged up. As the withdrawal velocity increases, the shear stress increases, so that the yielded region broadens while the unyielded region narrow accordingly. The upward velocity and the downward one both increase.

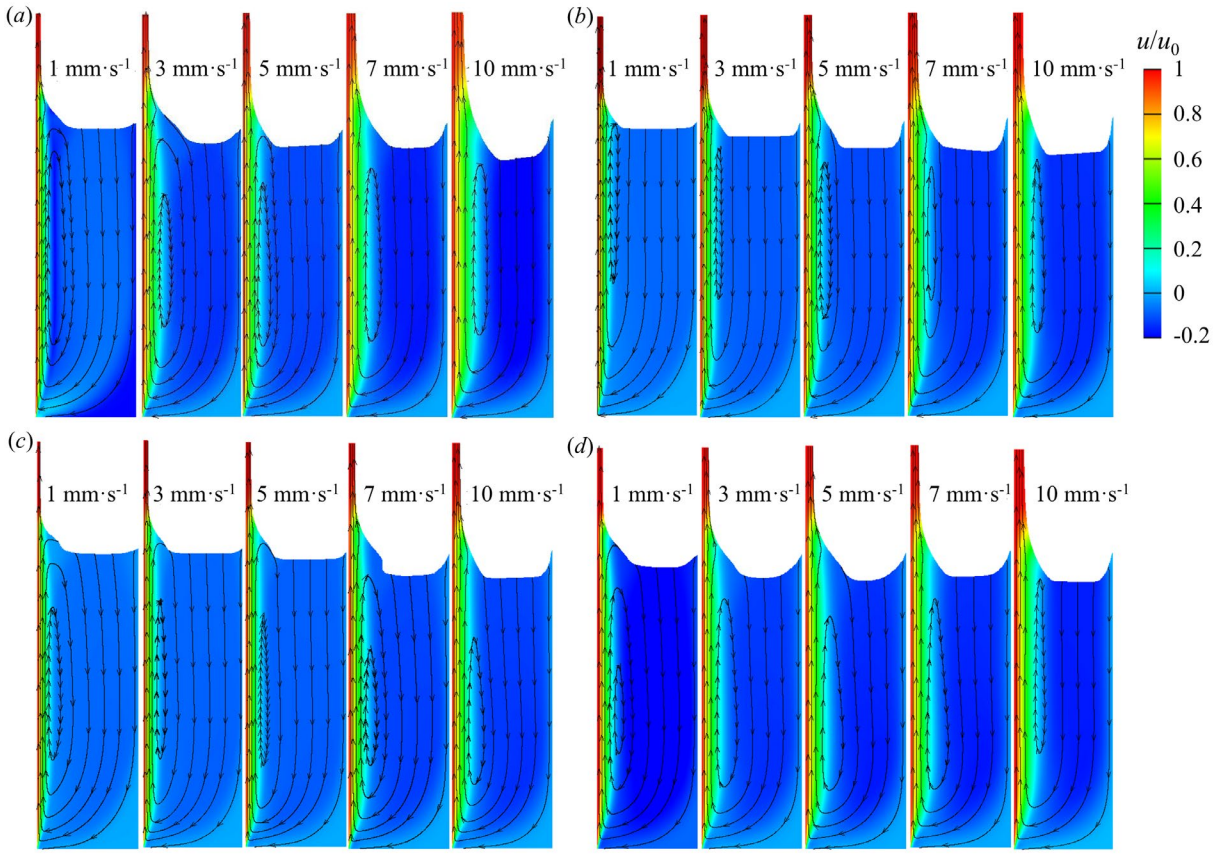

Figure 6.8. Contours of normalized vertical velocity and streamlines of F1 (*a*), F2 (*b*), F3 (*c*) and F4 (*d*) at different withdrawal velocities.

6.3.3 Shear stress and velocity profiles

For a given viscoplastic fluid, a higher withdrawal velocity creates a more significant downward flow of the fluid in the inner yielded region (as discussed in section 6.3.2), resulting in a higher downward velocity, a higher velocity gradient (Figure 6.9*a*) and therefore a higher shear rate as well

as a higher shear stress gradient (Figure 6.9*b*). The outer yielded region follows a trend similar to the inner one, which is in agreement with the literature[14]. Therefore, the unyielded region narrows. Since the critical stress at the boundary between the yielded and unyielded regions remains unchanged (equal to τ_c), the shear stress gradient in the unyielded region increases.

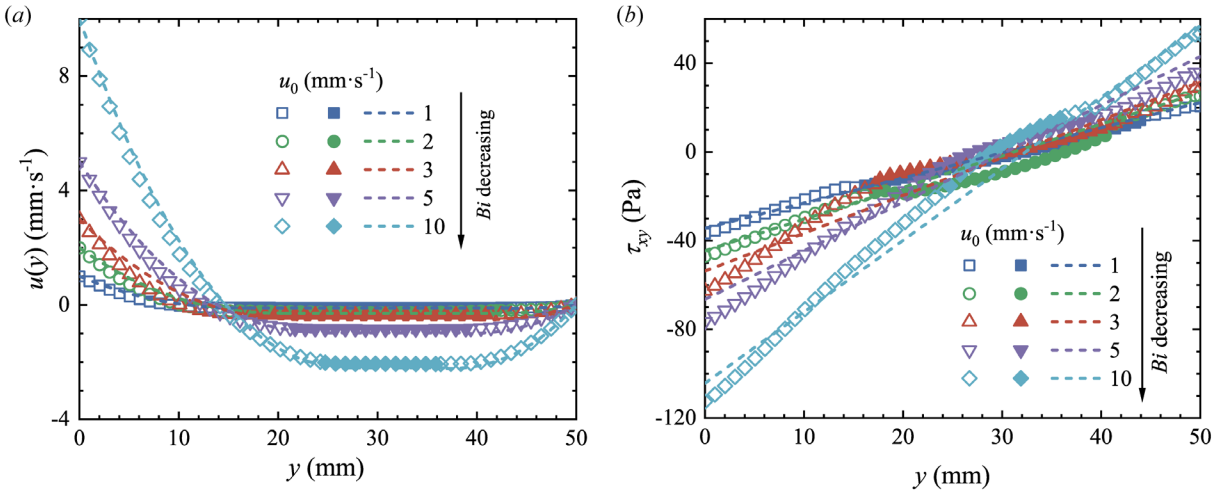

Figure 6.9. Profiles of velocity (*a*) and shear stress component τ_{xy} (*b*) in the container at x = 120 mm for viscoplastic fluid F1 at different withdrawal velocities. The open and solid symbols represent the yielded and unyielded regions obtained from DNS, respectively. The dashed curves are the calculated values from equations (6.5) and (6.9).

For a given withdrawal velocity, a fluid with lower τ_c is easier to yield. As a result, the inner and outer yielded regions expand and correspondingly the unyielded region narrows (Figure 6.10*a*, *b*). The velocity gradient in the yielded regions decreases as the yield stress τ_c decreases from 35 Pa to 15 Pa. Similarly, the shear stress and its gradient decrease with decreasing τ_c. As for the unyielded region, its width narrows and its downward velocity increases while its shear stress and shear stress gradient decrease with decreasing τ_c. The influences of K on the velocity profile and the width of yielded and unyielded regions are opposite to the influence of τ_c on them. A lower K leads to a decrease in shear stress ($\tau = (\tau_c/|\dot{\gamma}|+K|\dot{\gamma}|^{n-1})\dot{\gamma}$) in the yielded regions as well as its gradient. As for the unyielded region,

since its width expands and τ_c remains unchanged, the shear stress gradient of the fluid with lower K is decreased (see Figure 6.10*c* and *d*).

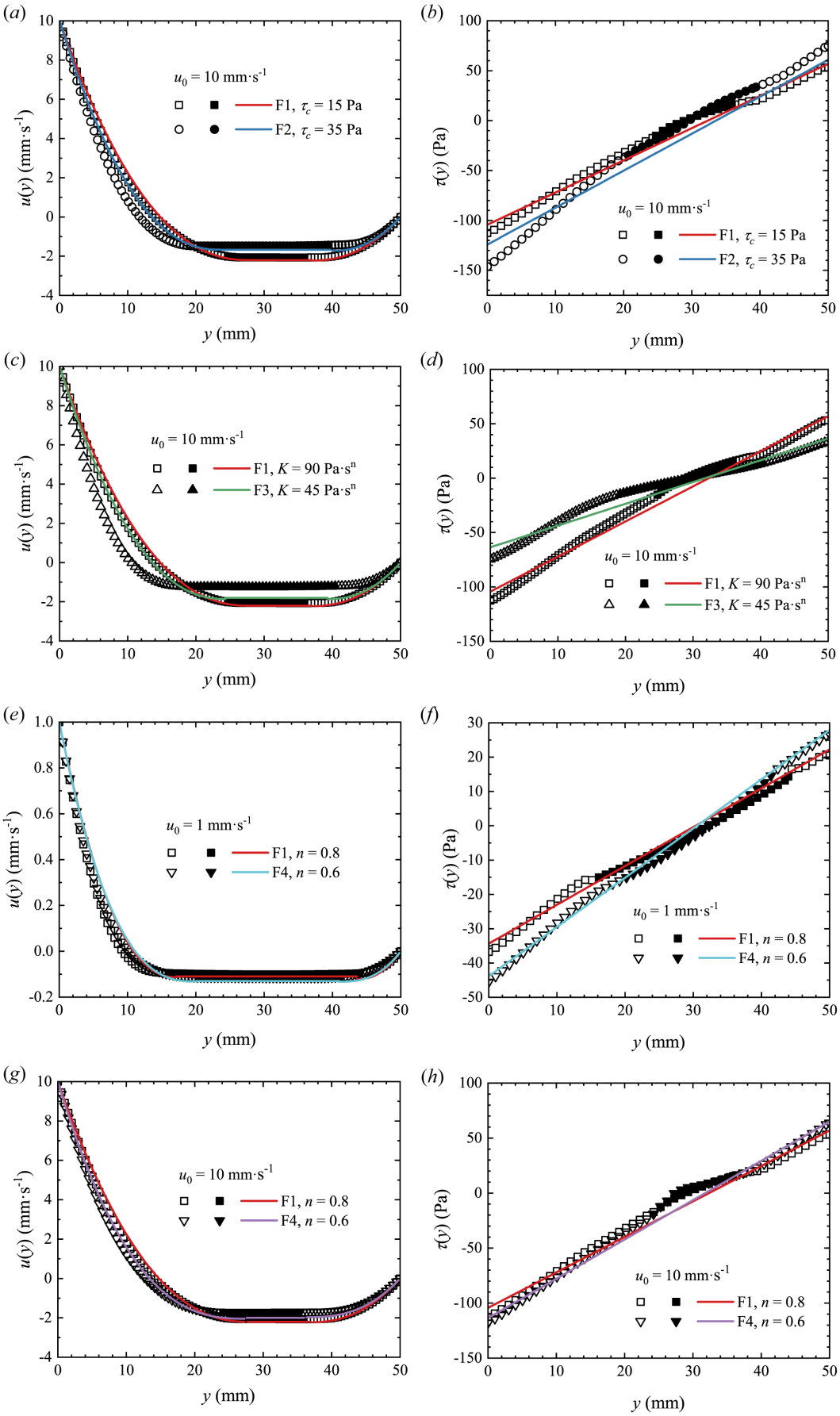
(a)
u(y) (mm·s-1)
y (mm)
u0 = 10 mm·s-1
F1, τc = 15 Pa
F2, τc = 35 Pa
(b)
τ(y) (Pa)
y (mm)
u0 = 10 mm·s-1
F1, τc = 15 Pa
F2, τc = 35 Pa
(c)
u(y) (mm·s-1)
y (mm)
u0 = 10 mm·s-1
F1, K = 90 Pa·sn
F3, K = 45 Pa·sn
(d)
τ(y) (Pa)
y (mm)
u0 = 10 mm·s-1
F1, K = 90 Pa·sn
F3, K = 45 Pa·sn
(e)
u(y) (mm·s-1)
y (mm)
u0 = 1 mm·s-1
F1, n = 0.8
F4, n = 0.6
(f)
τ(y) (Pa)
y (mm)
u0 = 1 mm·s-1
F1, n = 0.8
F4, n = 0.6
(g)
u(y) (mm·s-1)
y (mm)
u0 = 10 mm·s-1
F1, n = 0.8
F4, n = 0.6
(h)
τ(y) (Pa)
y (mm)
u0 = 10 mm·s-1
F1, n = 0.8
F4, n = 0.6

Figure 6.10. Profiles of velocity and shear stress in the container at x = 120 mm for viscoplastic fluids with different yield stress τ_c (*a*, *b*), consistency factor K (*c*, *d*), and flow index n (*e*-*h*). The open and solid symbols represent the yielded and unyielded regions, respectively. The dashed curves are the calculated values from equations (6.5) and (6.9).

The flow index has a minor effect on the velocity profiles. As demonstrated in Figure 6.10(*e*, *g*), the velocity profiles of F1 and F4 almost superimpose with each other. The effect of flow index on the shear stress depends on the withdrawal velocity. For the viscoplastic fluid demonstrating shear-thinning behaviour post-yield (i.e., when the shear stress exceeds yield stress), there is a threshold of shear rate (= 1 s^{-1}). When the shear rate is less than 1 s^{-1}, the shear stress decreases monotonically with increasing n; and otherwise, an inverse trend is observed that the shear stress increases with increasing n. At low withdrawal velocity (which corresponds to a shear rate lower than 1 s^{-1}), the higher shear stress and stress gradient of F4 (n = 0.6) than those of F1 (n = 0.8) expand the yielded regions and narrows the unyielded region (see Figure 6.10*f*). At high withdrawal velocity (corresponding to a shear rate close to 1 s^{-1}), the shear stress profiles of F1 and F4 superimpose well (see Figure 6.10*h*). As the withdrawal velocity is further increased, the stress and stress gradient of F4 may be lower than those of F1 if the shear rate is much greater than 1 s^{-1}.

In what follows, the velocity and shear stress profiles as well as the relationship between them are developed theoretically based on the simulated results obtained above. It is assumed that the flow between the meniscus zone and the container bottom is one-dimensional. Therefore, the only non-zero stress and velocity are $\tau_{xy} = \tau(y)$ and $u = u(y)$, respectively. In the fully developed flow region between the free surface and the container bottom, far from both boundaries, the momentum conservation equation is thus expressed by the following equations:

$$-\frac{\partial p}{\partial x}+\frac{\partial \tau_{xy}}{\partial y}-\rho_L g = 0, \tag{6.1}$$

where p is the pressure. By integrating with respect to y, the general solution of equation (6.1) is obtained:

$$\tau_{xy} = (\frac{\partial p}{\partial x}+\rho_L g)y+c, \tag{6.2}$$

where c is an underdetermined integration parameter. The demarcations (δ_1 and δ_2) between the unyielded and yielded regions can be given by the boundary conditions $\tau(\delta_1) = -\tau_c$ and $\tau(\delta_2) = \tau_c$. Substituting the boundary conditions into equation (6.2) yields:

$$\frac{\partial p}{\partial x}+\rho_L g = \frac{2\delta_2}{\delta_2-\delta_1}, \tag{6.3}$$

$$c = -\frac{\tau_c(\delta_2+\delta_1)}{\delta_2-\delta_1}, \tag{6.4}$$

Therefore, by substituting equations (6.3) and (6.4) back into equation (6.2) the shear stress profile is obtained:

$$\tau_{xy} = \frac{\tau_c(2y-\delta_1-\delta_2)}{\delta_2-\delta_1}. \tag{6.5}$$

The velocity continuity and mass conservation yield the following equations, respectively:

$$u(\delta_1) = u(\delta_2), \tag{6.6}$$

$$\int_0^W u(y)\mathrm{d}y = 0. \tag{6.7}$$

In the fully developed flow region, the dominant velocity is u and the dominant velocity derivative is $\partial u/\partial y$. Therefore, we can obtain from equation (2.10) $\dot{\gamma} = \partial u/\partial y$. To obtain the velocity, we first substitute the shear stress (6.5) into the Herschel-Bulkley model (2.14) to get the shear rate:

$$\frac{\partial u}{\partial y} = \begin{cases} -\left(\frac{2\tau_c}{K}\right)^{1/n}\left(\frac{\delta_1-y}{\delta_2-\delta_1}\right)^{1/n} & 0 \le y \le \delta_1 \\ 0 & \delta_1 < y < \delta_2 \\ \left(\frac{2\tau_c}{K}\right)^{1/n}\left(\frac{y-\delta_2}{\delta_2-\delta_1}\right)^{1/n} & \delta_2 \le y \le W \end{cases}. \tag{6.8}$$

By integrating equation (6.8) with the no-slip boundary conditions $u(0) = u_0$ and $u(W) = 0$, the velocity can be expressed as:

$$u(y)=\begin{cases} u_0+\dfrac{n}{n+1}\left[\dfrac{2\tau_c}{K(\delta_2-\delta_1)}\right]^{1/n}\left[(\delta_1-y)^{\frac{n+1}{n}}-\delta_1^{\frac{n+1}{n}}\right] & 0\le y\le\delta_1 \\ u_0-\dfrac{n}{n+1}\left[\dfrac{2\tau_c}{K(\delta_2-\delta_1)}\right]^{1/n}\delta_1^{\frac{n+1}{n}} & \delta_1<y<\delta_2 \\ \dfrac{n}{n+1}\left[\dfrac{2\tau_c}{K(\delta_2-\delta_1)}\right]^{1/n}\left[(y-\delta_2)^{\frac{n+1}{n}}-(W-\delta_2)^{\frac{n+1}{n}}\right] & \delta_2\le y\le W \end{cases}. \tag{6.9}$$

Introducing equation (6.9) into equations (6.6) and (6.7) leads to the following analytical expressions:

$$u_0=\frac{n}{n+1}\left[\frac{2\tau_c}{K(\delta_2-\delta_1)}\right]^{1/n}\left[\delta_1^{\frac{n+1}{n}}-(W-\delta_2)^{\frac{n+1}{n}}\right], \tag{6.10}$$

$$(W-\delta_2)^{\frac{n+1}{n}}(n\delta_2+nW+W)-n\delta_1^{\frac{2n+1}{n}}=0. \tag{6.11}$$

While the direct numerical simulation (DNS) captures the gravitational drainage in the meniscus, our model does not account for it. Nevertheless, the calculated shear stress (6.5) and velocity (6.9) in the container are plotted in Figure 6.9 and Figure 6.10 and are in good agreement with the DNS results. This indicates that the drainage has little effect on the flow in the container.

6.3.4 Film thickness

The above analysis has shown the significant effects of Bi number ($Bi = \tau_c/K\dot{\gamma}^n$) on the hydrodynamics (flow region boundaries, shear stress and velocity profiles) of the fluid in the container, which inevitably affects the final film thickness h_0. Figure 6.11 shows that the film thickness h_0 increases with increasing withdrawal velocity u_0 for all viscoplastic fluids studied in this chapter. Nevertheless, while the film thickness h_0 increases significantly for fluids F1 to F4, the rise is much more gradual for fluids Fa and Fb. In the case of Fa and Fb, the viscous stress component $K\dot{\gamma}^n$ contributes only to a small extent to the total shear stress τ ($\tau = \tau_c+K\dot{\gamma}^n$), as the Bingham number Bi ranges between 1.04 and 2.91. For fluids F1-F4, since both K and $\dot{\gamma}$ are high, the viscous stress $K\dot{\gamma}^n$ becomes relatively significant compared to the yield stress τ_c, with $0.11 < Bi < 0.95$. Therefore, the effect of withdrawal velocity on the film thickness becomes significant. The Bi number also explains

the difference in the evolution of the film thickness of fluids F1-F4 with the withdrawal velocity. Taking F1 as a reference, only one rheological parameter was changed with different fluids to understand the causality (see Table 6.1). An increment of yield stress increases significantly the film thickness at low withdrawal velocity u_0, while insignificantly at high u_0 (see F1 and F2 in Figure 6.11). The larger consistency factor of F1 compared to F3 results in a larger film thickness and a rapider increase in film thickness with increasing u_0. The influence of the flow index on the film thickness depends on u_0 (see F1 and F4). For u_0 less than 3 mm·s^{-1}, the shear rate is lower than 1 s^{-1}, and the films made of F4 ($n = 0.6$) are thicker than those of F1 ($n = 0.8$). Once u_0 exceeds 3 mm·s^{-1}, the trend is opposite. The film thickness exhibits a positive correlation with the stress magnitude. Specifically, factors that enhance the stress in the inner yielded region, including yield stress, consistency factor, flow index and withdrawal velocity, also contribute to an increase in the film thickness.

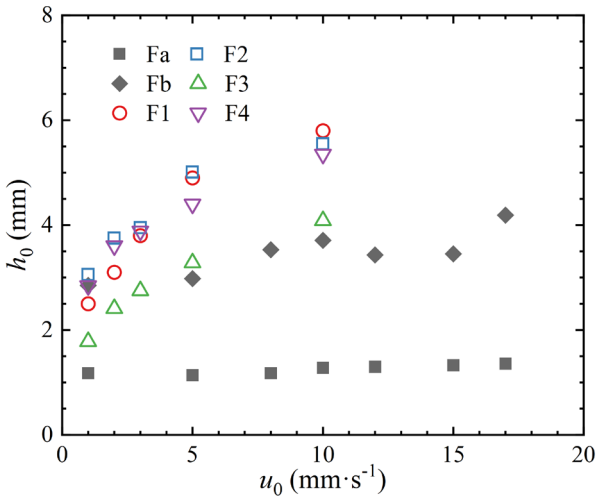

Figure 6.11. Evolution of film thickness h_0 with the withdrawal velocity u_0 for the different viscoplastic fluids described in Table 6.1.

Another factor which may influence the film thickness is the capillary pressure. A comparative analysis of capillary pressure and shear stress is conducted to evaluate the relative significance of capillary effects on film thickness. The magnitude of capillary pressure scales as $\sigma k \sim \sigma/h_0$ (where k

is the curvature of the liquid-air interface), while the shear stress is of the order of $\tau_c+K(u_0/h_0)^n$. The capillary number *Ca* here is thus defined by the following equation:

$$Ca = \frac{\text{Shear stress}}{\text{Capillary pressure}} = \frac{\tau_c+K(u_0/h_0)^n}{\sigma/h_0} = \frac{\tau_c h_0}{\sigma}+\frac{Ku_0^n h_0^{1-n}}{\sigma}. \tag{6.12}$$

The first term on the right-hand side, $\tau_c h_0/\sigma$, represents the ratio of yield stress to capillary pressure, while the second term, $Ku_0^n h_0^{1-n}/\sigma$, corresponds to the ratio of viscous stress to capillary pressure. In this chapter, the capillary number *Ca* is relatively large, ranging from 1 to 14. Consequently, the capillary effect is expected to have negligible influence on the film thickness h_0, which is further examined by the DNS. Figure 6.12 presents the variation of dimensionless thickness ($T_0 = \sqrt{\rho_L g h_0/[\tau_c+K(u_0/h_0)^n]}$), calculated by using the film thickness h_0 from the DNS, as a function of capillary number *Ca*. It appears that, for u_0 between 1 and 10 mm·s^{-1} for fluids F1-F4, *Ca* has little effect on T_0, and $T_0 \approx 0.64$. Therefore, the film thickness h_0 is proportional to $\sqrt{\rho_L g h_0/[\tau_c+K(u_0/h_0)^n]}$, indicating that it is controlled by the square root of the ratio between the viscous force and gravity. For smaller *Ca* numbers, the influence of physical parameters of fluids on the film thickness is investigated the literature.[2,18,19] In the limit of $Ca \ll 1$, the film thickness does not depend on consistency factor, flow index or withdrawal velocity, but relates primarily to a balance between yield stress and capillary pressure.

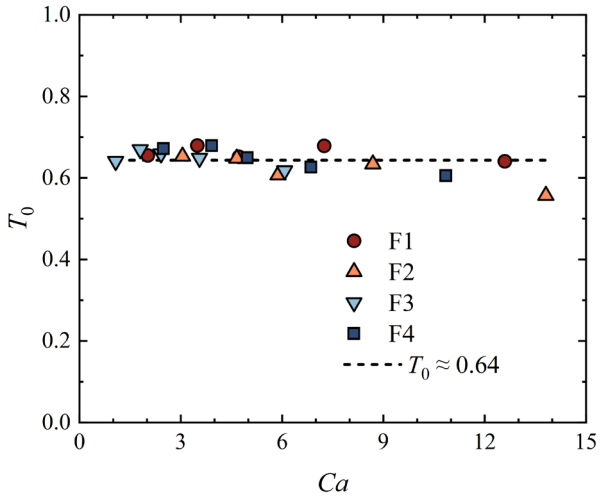

Figure 6.12. Variations of the dimensionless film thickness T_0 with Ca for F1-F4. Ca is changed via the withdrawal velocity from 1 to 10 mm·s^{-1} (see equation 6.12).

Many studies have revealed that the fluid in the coated film comes from the fluid in the inner yielded region.[11,12,14,15,20] Maillard *et al.* (2014)[20] developed a simple model of film thickness according to the observation that the coated film has a thickness proportional to that of the inner yielded region, i.e., $h_0 = a\delta_1$ where a is a free parameter. They first considered that in the inner yielded region the gravity work per unit time is balanced by the viscous dissipation per length and width of the plate: $\rho_L g\delta_1 u_0/2 = \tau\dot{\gamma}\delta_1$, where τ is the shear stress and where the shear rate is defined based on the thickness of inner yielded region. A general expression for the film thickness was then deduced by using the foregoing observation:

$$T = 2a\left(1+a^n Bi^{-1}\right), \tag{6.13}$$

where the dimensionless film thickness $T = \rho_L g h_0/\tau_c$ and $Bi = \tau_c/[K(u_0/h_0)^n]$. Through data regression, a is determined as 0.34, for the conditions of the present chapter. As illustrated in Figure 6.13, a good agreement between the DNS and theory (6.13) is obtained for fluids F1-F4.

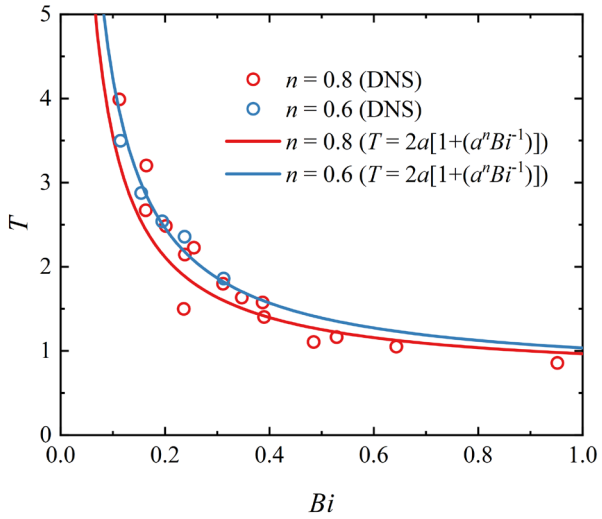

Figure 6.13. Variation of the dimensionless film thickness T with the Bi number for fluids F1-F4.

Recently, a more mathematically rigorous correlation between the thickness of the film and the inner yielded region has been developed.[12,15] Specifically, if all the fluid of the inner yielded region is coated to the plate, the film thickness is expressed by:

$$h_{\max} = \frac{n\delta_1}{1+2n}, \tag{6.14}$$

where the thickness of inner yielded region δ_1 can be determined empirically[12] or theoretically by equations (6.10 and 6.11). Model (6.14), however, fails to predict our film thickness obtained from the DNS, and results in a large positive deviation, as shown in Figure 6.14. The reason is that this model is developed for the case without gravitational drainage where the fluids in inner yielded region are all coated to the plate; while the drainage in the meniscus does exist in all our DNS (see Figure 6.8). To be exact, this model is the upper limit of film thickness. Previously, Maillard *et al.* (2016) contributed the effect of the drainage to the model:[12]

$$h_0 = h_{\max} - c\frac{\rho_L g \lambda_f^2}{3\tau}, \tag{6.15}$$

where the shear stress τ writes $\tau_c + K(u_0/W)^n$. This model is based on mass conservation, where the flow rate in the film equals the flow rate in the inner yielded region minus the drainage flow rate. The drainage is simplified as a freely flowing Newtonian fluid layer of thickness λ_f (λ_f equals $2h_{\max}$) along the plate under gravity. The fitting parameter c characterizes the deviation between actual and hypothetical drainage flow rates. By modelling the drainage as a freely flowing viscoplastic layer (of thickness λ_f) under gravity, the film thickness can be deduced through the following derivations. The momentum conservation equation for the hypothetical drainage is

$$\frac{\partial \tau_{xy}}{\partial y} + \rho_L g = 0, \tag{6.16}$$

with the boundary condition on the plate surface ($y = 0$)

$$u = 0 \tag{6.17}$$

and the boundary condition at the liquid-air interface ($y = \lambda_f$)

$$\tau_{xy} = 0. \tag{6.18}$$

Combining constitutive equation (2.14) and momentum conservation equation (6.16), and integrating with the boundary conditions (6.17) and (6.18), the drainage flow rate fluid per unit width of the plate is derived as follows:

$$\begin{aligned} Q_{drain} &= \int_0^{\lambda} u(y)\mathrm{d}y \\ &= \frac{nK}{(1+n)\rho_L g}\left\{\lambda_f\left(\frac{\rho_L g\lambda_f - \tau_c}{K}\right)^{1+\frac{1}{n}} - \frac{nK}{(1+2n)\rho_L g}\left[\left(\frac{\rho_L g\lambda_f - \tau_c}{K}\right)^{2+\frac{1}{n}} - \left(\frac{\tau_c}{K}\right)^{2+\frac{1}{n}}\right]\right\}. \end{aligned} \tag{6.19}$$

Considering the difference between actual and hypothetical drainage flow rates, the actual drainage flow rate should be given by equation (6.19) times a factor c. The mass conservation in the film and meniscus yields $h_0(u_0-u_d) = h_{\max}(u_0-u_d) - cQ_{drain}$, deducing the film thickness as following:

$$h_0 = h_{\max} - \frac{cQ_{drain}}{u_0-u_d}. \tag{6.20}$$

The present model (6.20) only includes one empirical parameter c, while other parameters can be theoretically obtained through equations (6.9-6.11), (6.14), and (6.19). As illustrated in Figure 6.14, compared to model (6.14) without drainage, model (6.15) with drainage and the present model (6.20) obtain a better agreement with the experimental film thickness in the literature[11] with deviations less than 20% by taking $c = 0.5$ for model (6.15) and $c = 0.15$ for the present model (6.20).

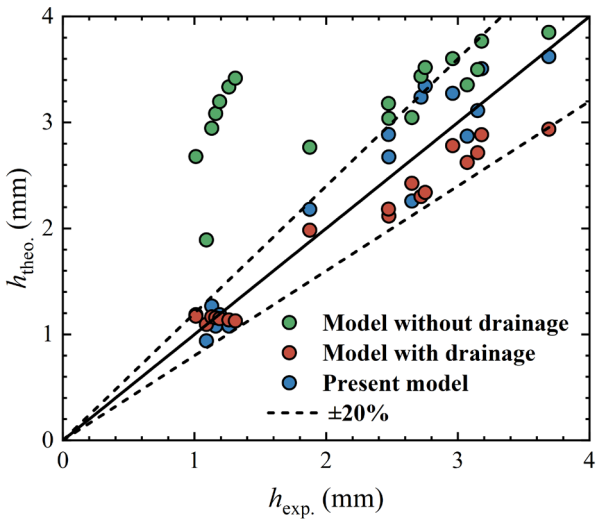

Figure 6.14. Comparison of film thickness predicted with different theoretical models with experimental values.

6.4 Conclusion

A two-dimensional numerical model was conducted to study the dip coating of a fully wetting plate with viscoplastic fluids, with a special attention to the hydrodynamics in the container feeding the plate. This study focuses on configurations with Bingham numbers *Bi* less than 1 with a series of withdrawal velocities and yield stress fluids. The fluid in the container can be divided into three regions, namely, inner yielded (in contact with the plate), unyielded and outer yielded (in contact with the container wall) regions. The film thickness is positively related to the magnitude of stress in the inner yielded region. Larger withdrawal velocity, yield stress or consistency factor increase the stress and its gradient, resulting in a thicker film. The effects of flow index on stress and film thickness depend on the shear rate. As the shear rate is less than 1 s^{-1}, a larger flow index can decrease the stress and film thickness; above 1 s^{-1}, it is the opposite. These phenomena are inconsistent with the literature focusing on high *Bi* numbers (> 1), where the film thickness is mainly determined by the yield stress and almost unaffected by withdrawal velocity. The drainage phenomenon was found to occur in the meniscus. The drainage flow hardly affects the theoretical predictions of the shear stress and flow velocity in each region under the assumption of one-dimensional flow in the container, which agree well with the DNS, but it reduces the film thickness. After determining the negligible role of surface tension in coating, a semi-empirical model of film thickness considering the influence of drainage flow was proposed with good prediction performance. Indeed, the thicknesses predicted by the model were validated with data from the literature. This work gives insight into the film forming mechanism of viscoplastic fluids and guides the design and optimization of dip coating for practical applications.

Reference

1. Ashmore J, Shen AQ, Kavehpour HP, Stone HA, McKinley GH. Coating flows of non-Newtonian fluids: weakly and strongly elastic limits. *J Eng Math.* 2007;60(1):17-41.

2. Baikov VI, Chorny AD. Withdrawing a Bingham viscoplastic fluid. *J. Rheol.* 2019;63(6):927-938.

3. Filali A, Khezzar L, Mitsoulis E. Some experiences with the numerical simulation of Newtonian and Bingham fluids in dip coating. *Comput. Fluids.* 2013;82:110-121.

4. Hurez P, Tanguy PA. Finite element analysis of dip coating with bingham fluids. *Polym. Eng. Sci.* 1990;30(18):1125-1132.

5. Berteloot G, Daerr A, Lequeux F, Limat L. Dip coating with colloids and evaporation. *Chem. Eng. Process.* 2013;68:69-73.

6. Gans A, Dressaire E, Colnet B, Saingier G, Bazant MZ, Sauret A. Dip-coating of suspensions. *Soft Matter.* Jan 2 2019;15(2):252-261.

7. Peev G, Kyrsheva M. Thickness of a film obtained by the vertical withdrawal of a plate from a suspension described by the shvedov-bingham model. *J. Eng. Phys.* 1988;55(6):1355-1358.

8. Trottet B MM, Keddie J. Mastering the coating thickness obtained using liquids with a yield-stress. *Chem. Eng. Trans.* 2017;57:1897-1902.

9. Kajiya T, Brunet P, Royon L, Daerr A, Receveur M, Limat L. A liquid contact line receding on a soft gel surface: dip-coating geometry investigation. *Soft Matter.* Nov 28 2014;10(44):8888-8895.

10. Benkreira H. The effect of substrate roughness on air entrainment in dip coating. *Chem. Eng. Sci.* 2004;59(13):2745-2751.

11. Maillard M, Boujlel J, Coussot P. Flow characteristics around a plate withdrawn from a bath of yield stress fluid. *J Non-Newton Fluid.* 2015;220:33-43.

12. Maillard M, Bleyer J, Andrieux AL, Boujlel J, Coussot P. Dip-coating of yield stress fluids. *Phys. Fluids.* 2016;28(5):31-49.

13. Boujlel J, Maillard M, Lindner A, Ovarlez G, Chateau X, Coussot P. Boundary layer in pastes—Displacement of a long object through a yield stress fluid. *Journal of Rheology.* 2012;56(5):1083-1108.

14. Smit WJ, Kusina C, Joanny JF, Colin A. Stress field inside the bath determines dip coating with yield-stress fluids in cylindrical geometry. *Phys. Rev. Lett.* Oct 4 2019;123(14):148002.

15. Smit WJ, Kusina C, Colin A, Joanny J-F. Withdrawal and dip coating of an object from a yield-stress reservoir. *Phys. Rev. Fluids.* 2021;6(6):063302.

16. Hewitt DR, Balmforth NJ. Viscoplastic slender-body theory. *J. Fluid Mech.* 2018;856:870-897.

17. Jalaal M, Stoeber B, Balmforth NJ. Spreading of viscoplastic droplets. *J. Fluid Mech.* Mar 5 2021;914:A21.

18. Jalaal M, Balmforth NJ. Long bubbles in tubes filled with viscoplastic fluid. *J Non-Newton Fluid.* 2016;238:100-106.

19. Laborie B, Rouyer F, Angelescu DE, Lorenceau E. Yield-stress fluid deposition in circular channels. *J. Fluid Mech.* 2017;818:838-851.

20. Maillard M, Boujlel J, Coussot P. Solid-solid transition in Landau-Levich flow with soft-jammed systems. *Phys. Rev. Lett.* Feb 14 2014;112(6):068304.

7 Hydrodynamics and rheological characterization upon the immersion process of a slotted plate into viscoplastic fluids

Many industrial processes involve the motion of objects in viscoplastic fluids such as coating, drilling, and mixing. The understanding of the flow and the rheological behaviour is beneficial for optimization of these processes. However, viscoplastic fluids often demonstrate wall slip, presenting a challenge for flow analysis and rheological characterization. This study pays attention to the immersion process of a slotted plate into viscoplastic fluids. The forces on the plate and the flow in the container are investigated by experiment and computational fluid dynamics and are modelled analytically. The shear stress at the fluid-fluid interface at different immersion velocities is correlated with the pseudo-Herschel-Bulkley model to determine the yield stress. The flow index and the consistency factor are calculated by the analytical model of flow. The immersion method is validated by comparing the flow curves obtained from this method with those from the parallel disk method and from the literature.

7.1 Introduction

Many industrial processes, everyday life and natural disasters involve viscoplastic fluids such as concrete, toothpaste, and landslides. The prevalent existence and growing attention towards viscoplastic fluids promoted the development of various test methods, for example, capillary[1], parallel disk[2], cone-and-plane[3], and Couette-type rheometers[4]. Nevertheless, viscoplastic fluids, like many other complex fluids, demonstrate wall slip.[5-11] When multiphasic viscoplastic fluids flow along a wall, the dispersed phase moves away from the wall, leading a low-viscosity pure continuous phase layer on the wall.[12] This low-viscosity layer of fluid flows more readily than other parts of the fluid, resulting in a higher measured shear rate for a given shear stress and therefore an underestimation of yield stress and viscosity.[9-11] In many cases, we need to characterize the wall slip and analyse the flow under wall slip rather than eliminate it, since wall slip is also present in material processing such as screw extrusion and injection moulding.[13-15] A classical quantification method of wall slip proposed by

Mooney *et al.* (1931)[16] has been extended and used in many studies[17-19]. Nowadays, the flow visualization has become a powerful method to characterize the wall slip, including particle image velocimetry (PIV)[20], magnetic resonance imaging (MRI)[21], and ultrasonic velocimetry (USV)[22]. These methods are capable to capture the velocity directly and thus evaluate the wall slip. The flow visualization methods are expensive and some of them are hampered by the transparency of the fluids and the nature of the rheometer walls. For example, transparent fluids and transparent rheometer walls are required for PIV, whereas non-metallic walls are necessary for MRI.

Sometimes we attempt to relate the interactions between microstructures to the bulk rheological properties (such as flow curves, which are defined as shear stress-shear rate curves), on which the wall slip produces a detrimental effect. There are two approaches to measure the flow curves under wall slip. One is the foregoing flow visualization method. The other approach involves extending the constitutive equations by wall slip analysis. However, few studies have examined the validity of this latter approach[19,23], particularly from the perspective of fluid dynamics. Numerous studies attempt to eliminate the wall slip by roughening the surface of the rheometer walls.[20,24,25] Despite the fact that this method leads in some cases to the fracture of the sample[26], it has been successfully used in many tests[27-29] by roughening the wall or gluing a sand paper on the wall to provide a roughness being of the order of the microstructure size of the samples.

Immersion test, as a widely used method to determine the hardness and strength of the materials[30], has been developed to measure the yield stress of the viscoplastic fluids[31-33]. Zhu and De Kee *et al.* (2001, 2002 and 2007)[34-36] measured the forces on the slotted plate as it moves vertically in viscoplastic fluids (TiO_2 suspensions and bentonite suspensions) in the fully immersed state. Based on this, they proposed a potentially effective slotted plate immersion method. As displayed in Figure 7.1, they hypothesized that the fluid in the slots remains static relative to the plate and move together with the plate. To strengthen this hypothesis, the ratio of the slot height (S) to the plate thickness (E) was made smaller than 3. The shear stress, τ, was obtained by dividing the total shear force applied on the plate

by the area of the plate. This shear stress includes contributions from the stress at the fluid-fluid interface, τ_f, and the stress on the slipping plate surface, τ_w, that is $\tau = \tau_f\beta+\tau_w(1-\beta)$ with β the slot ratio (the ratio of the slot area to the plate area). For all suspensions and plates used, it was observed that the value of τ was constant for a given fluid when the immersion velocity, u_0, was lower than 0.1 mm/min and when the slot ratio was larger than 50%. They believed this constant shear stress to be the yield stress, namely $\tau_c = \tau_f\beta+\tau_w(1-\beta)$ for $u_0 < 0.1$ mm/min and $\beta > 50\%$. Obviously, this measured yield stress results from the contributions of both τ_f and τ_w unless β approaches 100% which is impossible for a slotted plate. In addition, their slotted plate method is limited to measuring the yield stress and cannot determine other rheological parameters such as viscosity-related parameters: flow index and consistency factor. Boujlel and Coussot 2012[37] analysed the evolution of forces on the roughen plate and cylinder during immersion process from the first contact to the fully immersed state. They also proposed another method to measure the yield stress and flow index, that is correlating the pseudo-Herschel-Bulkley model with the variation of shear stress on the rough non-slotted plate's surface versus immersion velocity. However, the consistency factor K from Herschel-Bulkley model could not be obtained due to the lack of analysis about the flow in the container. There are a variety of methods for dealing with wall slip, and they have unique characteristics and also limitations.

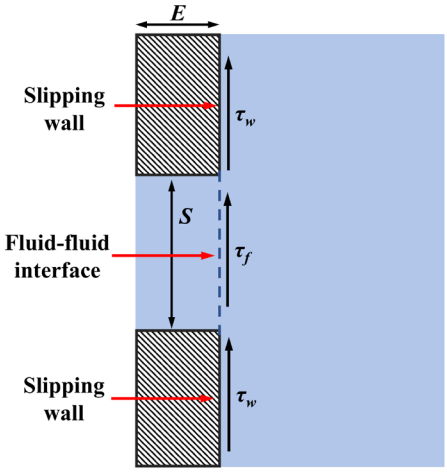

Figure 7.1. Schematic of the shear stresses on the slipping wall and at the fluid-fluid interface.

This chapter focuses on the immersion process of a slotted plate into viscoplastic fluids in different regimes. The dynamics of this process including the force acting on the plate and the flow field are investigated by immersion experiments, computational fluid dynamics simulations, and analytical modelling. Inspired by the characteristics of force and flow, we proposed a new immersion method to measure the bulk Herschel-Bulkley parameters of the viscoplastic fluids including the yield stress, flow index, and consistency factor. The new immersion method is applicable to a slotted plate with or without wall slip on the plate surface, and a rough non-slotted plate where the wall slip is weak enough to be negligible. We stress here that we do not attempt to dismiss or replace other methods, but rather provide a new possibility to measure the flow curve of viscoplastic fluids under wall slip. This paper presents the theoretical principle of this method as well as the detailed steps taking the slotted plate as an example. Firstly, the τ_f and τ_w are obtained by analysing the evolution of forces exerted on the plate with immersion depth. By comparing the magnitudes of τ_f and τ_w, the wall slip on the plate surface could be evaluated. Secondly, the obtained τ_f at different immersion velocities are fitted with the pseudo-Herschel-Bulkley model to determine the yield stress. Thirdly, the consistency factor and flow index are solved using the analytical model of the flow in the container, combined with the a priori known operating parameters and the determined yield stress. It is worth emphasizing that this method also allows the obtain of the stress on the surface of a rough non-slotted plate and thus the Herschel-Bulkley parameters through the aforementioned three steps. This new immersion method is validated by comparing the Herschel-Bulkley parameters determined by this method with those obtained from the parallel disk method in bulk flow and from a previously published article[37]. This chapter also provides insight into the flow behaviour in the container when a slotted plate penetrates the viscoplastic fluids.

7.2 Force and flow characteristics

7.2.1 Regime identification

A typical curve of force versus immersion depth is displayed in Figure 7.2. The immersion test can be divided into four regimes: before the effective immersion (I), the plate surfaces and the slots alternately penetrate the gels (II), the slots are all penetrated in the gels (III), and the plate tip is close to the container bottom (IV).

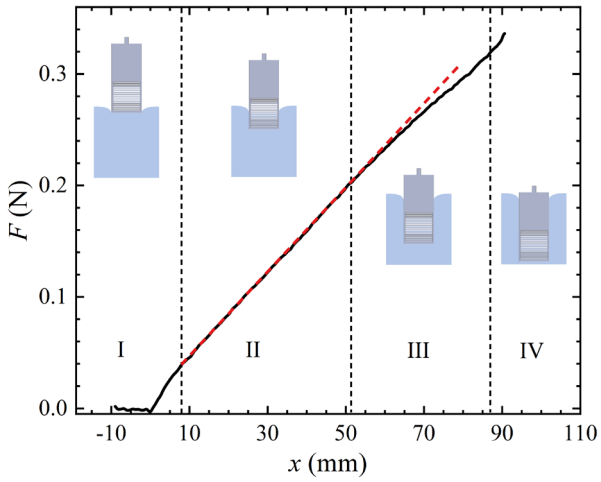

Figure 7.2. Force (black solid curve) applied on the plate versus immersion depth during the immersion test. Gel: 0.25 wt% Carbopol; plate: P1S2N17; immersion velocity: 2 mm·s^{-1}. The red dashed line serves as a visual guide highlighting the difference in force slope between regime II and regime III.

7.2.1.1 Regime I

For this regime, we review the analysis of Boujlel and Coussot 2012[37] and give complementary new interpretations. As demonstrated in Figure 7.3(a), the measured force is zero with slight fluctuations before first contact. When the plate contacts the gel surface, it does not immediately penetrate the gels, but capillary effect first occurs. The interfacial tension between the air and gel phases, σ, is directed to the interior of the gels with the apparent contact angle between the gels and the plate, θ_{ap}, less than 90 degrees. Therefore, the effective capillary force, $F_c = -2(W_p+E)\sigma\cos\theta_{ap}$, is negative, as shown by the sudden drop of the measured force in Figure 7.3(a). As the plate is lowered further, the contact angle increases, leading to an increasing effective capillary force. Meanwhile, the

downward elastic deformation of the gels increases, resulting in an increase in resistance at the plate tip, F_e. Therefore, the measured force increases after the aforementioned sudden drop.

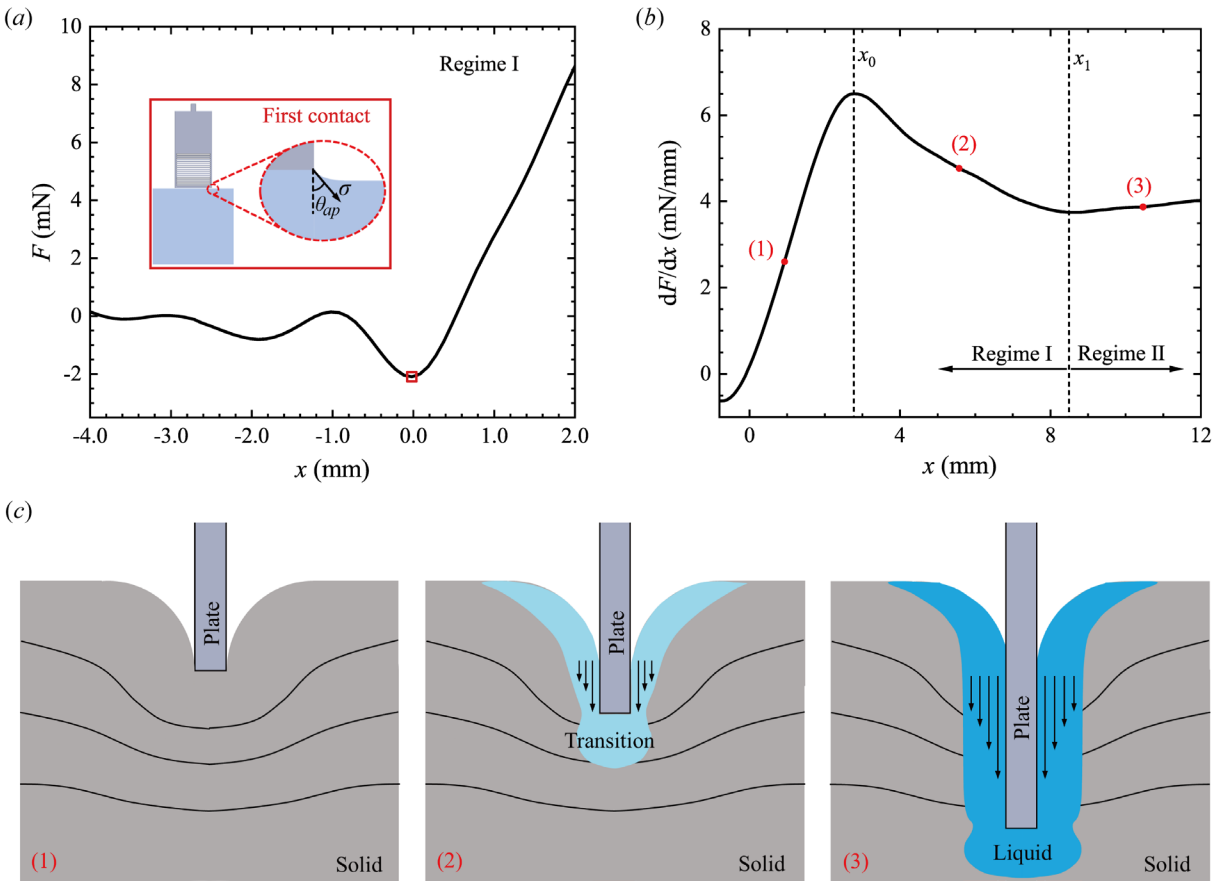

Figure 7.3. Force variation (*a*) and derivative of force to immersion depth (*b*) as a function of immersion depth; (*c*) schematic of deformation and flow fields around the plate at the points labelled in Figure 7.3(*b*). Gel: 0.25 wt% Carbopol; plate: P1S2N17; immersion velocity: 2 mm·s^{-1}.

The derivative of the force with respect to the immersion depth shown in Figure 7.3(*b*), i.e., d*F*/d*x*, gives further insight into the force increment required for the plate displacement. In the beginning, the derivative monotonically increases. The gels are in a solid state exhibiting Hookean elastic deformation (as in Figure 7.3*c*1). The archetypal characteristic of the Hookean elastic deformation is a force proportional to the displacement, leading to a constant value of d*F*/d*x*. This is inconsistent with the results obtained from the immersion tests (see Figure 7.3*b*). It is probably the rapid increase in contact angle leading to the rapid increase in the effective capillary force, that leads to an increasing derivative.

When the gels reach the critical deformation (at $x = x_0$), the surface of the gels does not deform further, the elastic force and the effective surface tension reach their maximum value, F_c^{max} and F_e^{max}, respectively. At this critical position $x = x_0$, the total force on the plate is hence given by the following equation:

$$F_0 = F(x = x_0) = F_c^{max} + F_e^{max}. \tag{7.1}$$

After this regime, the elastic force and the effective surface tension remain unchanged, whose sum is F_0. Please keep this in mind, because it will be used together with the force evolution in regime III to determine the shear stress on the plate.

After the critical position $x = x_0$, the plate begins to penetrate the gels. The capillary force (F_c) and the resistance at the plate tip (F_e) no longer contribute to the slope of force curve (dF/dx). If the flow around the plate is stable, the force on the plate would be roughly proportional to the immersion depth and the slope of force curve would hence be constant. This deviates from the slope of observed force curve (cf. Figure 7.3*b*), which exhibits a significant slope decrease in the interval between x_0 and x_1. The slope decrease indicates a flow transition caused by the plate immersion is occurring in this interval. The shear rate is increasing, but its rate of increase slows down as the immersion proceeds. Additionally, past studies have shown that the Carbopol gels do not go directly from a solid to a liquid state, but enter a solid-to-liquid transition where the rheological behaviour of the gels is neither that of a Hookean solid nor that of a viscous fluid (as in Figure 7.3*c*2).[38] The gels in our immersion test are experiencing a such solid-to-liquid transition in the interval between x_0 and x_1. As the immersion progresses, the gels around the plate enter the liquid state and the flow is stable (Figure 7.3*c*3). More direct conclusions may require the aid of PIV method to be drawn, which is worth the more in-depth study in the future but indeed beyond the scope of present work. However, anyway, the slope of force curve will remain unchanged with the displacement when both transitions (flow transition and solid-to-liquid transition) complete (at $x = x_1$). Thereafter, the immersion comes into regime II.

7.2.1.2 Regime II

Figure 7.4 depicts that the plate surfaces and the gels in the slots alternately penetrate the gels. The further immersion increases the buoyancy on the plate, F_b, and the shear force along the plate, F_v. By treating the plate and the gels in the slots as a whole, the increased buoyancy can be expressed as $F_b = \rho_L g W_p E x_e$ with the effective immersion depth $x_e = x\text{-}x_0$. The increased viscous force is relatively complex and discussed below.

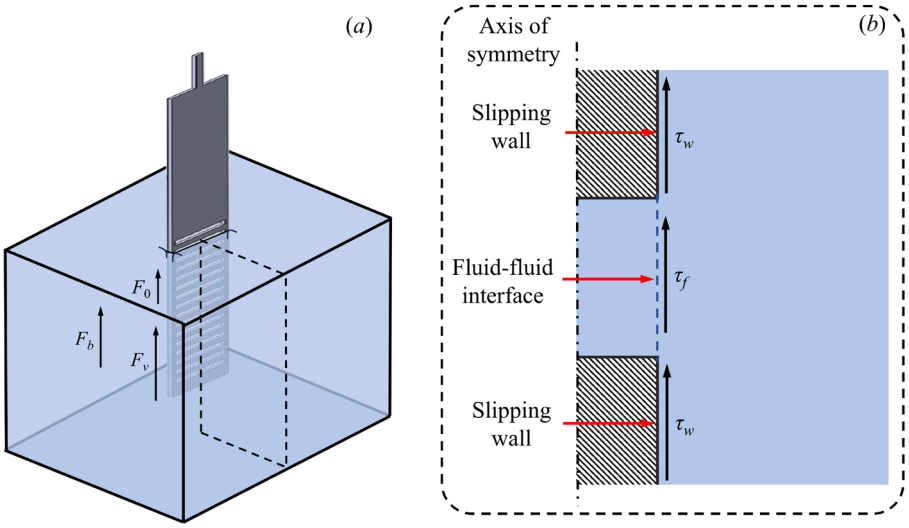

Figure 7.4. Schematic of forces applied on the plate in regime II (a) and force distribution near one slot in Figure 7.4(a) including shear stresses on the slipping wall, τ_w, and at the fluid-fluid interface, τ_f (b).

It is assumed that the gels in the slots remain static relative to the plate, without secondary flow and with the shearing occurring at the fluid-fluid interface, as displayed in Figure 7.4(b). This assumption is invalid for fluids without yield stress, also invalid in scenarios involving high immersion velocities and high ratios of slot height over plate thickness. The applicability of this assumption and immersion method will be discussed subsequently under conditions of different immersion velocities and plate geometries (section 7.3.1). The shear stress on the plate surface, τ_w, is lower than the shear stress at the fluid-fluid interface, τ_f, due to wall slip. The viscous force will be discussed in different

cases. For the case where the i-th plate surface is partially penetrating the gel surface (referred to as case 1), the viscous forces applied at the fluid-fluid interface and on the plate surface of both sides of the plate are $2W_sS(i\text{-}1)\tau_f$ and $2\left[W_px_e\text{-}W_sS(i\text{-}1)\right]\tau_w$, respectively. When the i-th slot is partially penetrating the gel surface (referred to as case 2), the viscous forces applied at the fluid-fluid interface and on the plate surface are $2W_s(x_e\text{-}Pi)\tau_f$ and $2\left[(W_p\text{-}W_s)x_e+W_sPi\right]\tau_w$, respectively. Thereby, the total viscous force can be calculated as:

$$F_v=\begin{cases}2W_sS(i\text{-}1)\tau_f+2\left[W_px_e\text{-}W_sS(i\text{-}1)\right]\tau_w, \text{ for case 1}\\ 2W_s(x_e\text{-}Pi)\tau_f+2\left[(W_p\text{-}W_s)x_e+W_sPi\right]\tau_w, \text{ for case 2}\end{cases} \tag{7.2}$$

Therefore, the total force, F, can be expressed as:

$$F=F_0+F_b+F_v=\begin{cases}F_0+\rho_LgW_pEx_e+2W_sS(i\text{-}1)\tau_f+2\left[W_px_e\text{-}W_sS(i\text{-}1)\right]\tau_w, \text{ for case 1}\\ F_0+\rho_LgW_pEx_e+2W_s(x_e\text{-}Pi)\tau_f+2\left[(W_p\text{-}W_s)x_e+W_sPi\right]\tau_w, \text{ for case 2}\end{cases} \tag{7.3}$$

The above equations can be equivalently simplified as:

$$F=\begin{cases}W_p\left(\rho_LgE+2\tau_w\right)x_e+2W_sS\left(\tau_f\text{-}\tau_w\right)(i\text{-}1)+F_0, \text{ for case 1}\\ \left(\rho_LgW_pE+2W_s\tau_f+2W_p\tau_w\text{-}2W_s\tau_w\right)x_e+2W_sP(\tau_w\text{-}\tau_f)i+F_0, \text{ for case 2}\end{cases} \tag{7.4}$$

From equation (7.4), it is concluded that the total force is a continuous piecewise function of effective immersion depth x_e, with the slopes $W_p\left(\rho_LgE+2\tau_w\right)$ and $\left(\rho_LgW_pE+2W_s\tau_f+2W_p\tau_w\text{-}2W_s\tau_w\right)$ for case 1 and case 2, respectively. The immersion test shown in Figure 7.5 confirms the piecewise evolution of the force curve with the effective immersion depth. Furthermore, the slope of the force curve of case 2 (the slot penetrates the gel surface) is significantly larger than that of case 1 (the plate surface penetrates the gel surface). This illustrates that the shear stress at the fluid-fluid interface is larger than that on the plate surface, i.e., $\tau_f > \tau_w$, demonstrating the wall slip on the plate surface; otherwise, τ_f should equal τ_w. However, the change in the slope of the force curve is not exactly synchronized with the alternate immersion of the slot and plate surface. This is probably attributed to the fact that the rheological behaviour and flow state of the gels do not respond instantaneously to the alternate immersion. A more in-depth study on this phenomenon would be carried out in our future

work, while not performed in present work since our new slotted immersion method does not rely on the force in this regime (regime II).

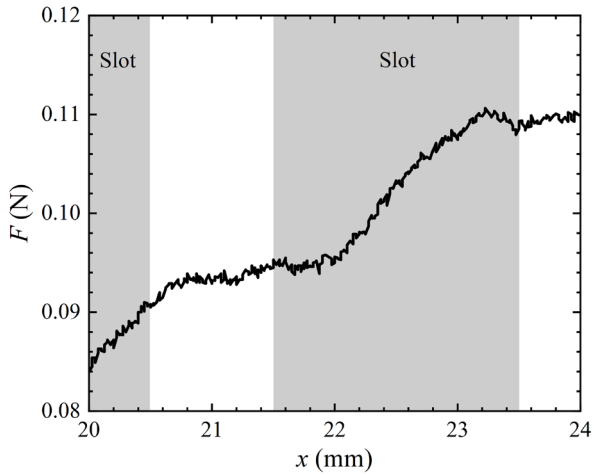

Figure 7.5. Evolution of the force exerted on the plate with the immersion depth in regime II. The grey and white areas refer to the case when the slot and the plate surface is penetrating the gel surface, respectively. Gel: 0.25 wt% Carbopol; plate: P1S2N17; immersion velocity: 2 mm·s^{-1}.

7.2.1.3 Regime III

When all slots are penetrated in the gels, the immersion test enters regime III. As displayed in Figure 7.6, the continuous plate surfaces penetrate the gel surface. Since all slots are already immersed in the gels, the viscous force at the fluid-fluid interface is $2NW_sS\tau_f$. The viscous forces applied on the plate surface is $2\left(W_px_e\text{-}NW_sS\right)\tau_w$. Therefore, the total force is derived as:

$$F = F_0+F_b+F_v = F_0+\rho_L gW_pEx_e+2NW_sS\tau_f+2(W_px_e\text{-}NW_sS)\tau_w,$$

or equivalently, in a more concise form:

$$F = W_p\left(\rho_L gE+2\tau_w\right)x_e+2NW_sS\left(\tau_f\text{-}\tau_w\right)+F_0. \quad (7.5)$$

Equation (7.5) indicates that the total force increases linearly with the effective immersion depth x_e (or the immersion depth, x), which is consistent with the force curve depicted in Figure 7.2. We remark again that equation (7.5) will be used together with equation (7.1) to determine the shear stress τ_f and τ_w on the plate.

For a non-slotted plate, $S = 0$, equation (7.5) thus reduces to $F = W_p(\rho_L gE+2\tau_f)x_e+F_0$. One can also consider $N = 0$ or $\tau_f = \tau_w$. By differential, the shear stress is hence given by $\tau_f = 0.5(\mathrm{d}F/\mathrm{d}x-\rho_L gW_pE)/W_p$. This is the same as the expression proposed in the literature[37], which somewhat corroborates the relevance of our analysis.

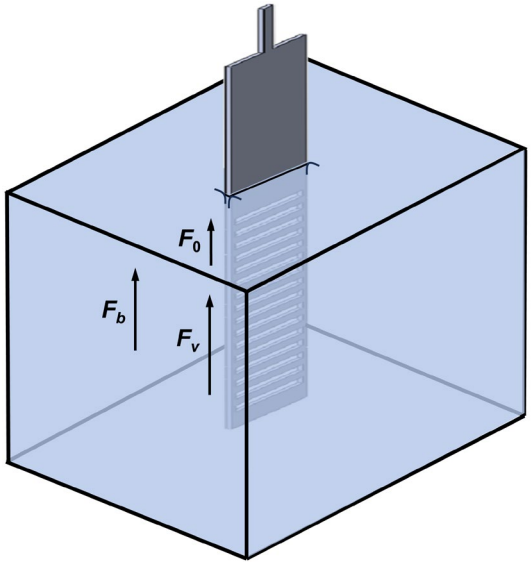

Figure 7.6. Schematic of forces applied on the plate in regime III.

7.2.1.4 Regime IV

As the distance between the plate tip and the bottom of the container becomes closer, the effect of the bottom on the flow especially the flow around the plate tip becomes bigger, thus the resistance at the plate tip increases with immersion depth. Therefore, as depicted in Figure 7.7, $\mathrm{d}F/\mathrm{d}x$ is not constant but instead increases rapidly.

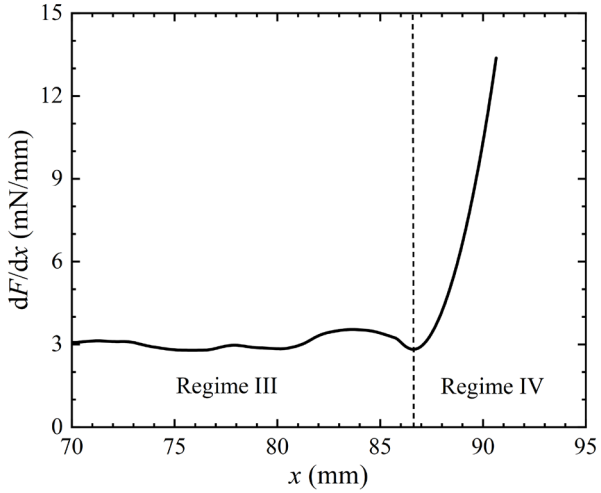

Figure 7.7. Derivative of force with respect to immersion depth, dF/dx, as a function of immersion depth. Gel: 0.25 wt% Carbopol; plate: P1S2N17; immersion velocity: 2 mm·s^{-1}.

7.2.2 Flow characteristics

The flow in the container is rather complicated due to the alternate distribution of slots and plate surfaces. As depicted in Figure 7.8(*a*), the flow is simplified as follows: the flow in the region between the plate surface and the wall (region A) and that in the region between the fluid-fluid interface and the wall (region B) are independent of each other. Our previous study[39] and other studies[40,41] about withdrawing a non-slotted plate from the viscoplastic fluid suggest that the fluid is sheared and yielded only near the moving plate and the container wall, while the other portion of fluids is unyielded in a solid regime. This conclusion can be safely extended to region B upon the immersion process of a slotted plate. As illustrated in Figure 7.8(*b*), the fluid can be subdivided into three regions: inner yielded region, unyielded region and outer yielded region. The interfaces between yielded and unyielded regions are located in $y = \delta_1$ and δ_2. The flow is simplified as vertical, so that the only nonvanishing stress and velocity components are τ_{xy} and u, respectively.[39]

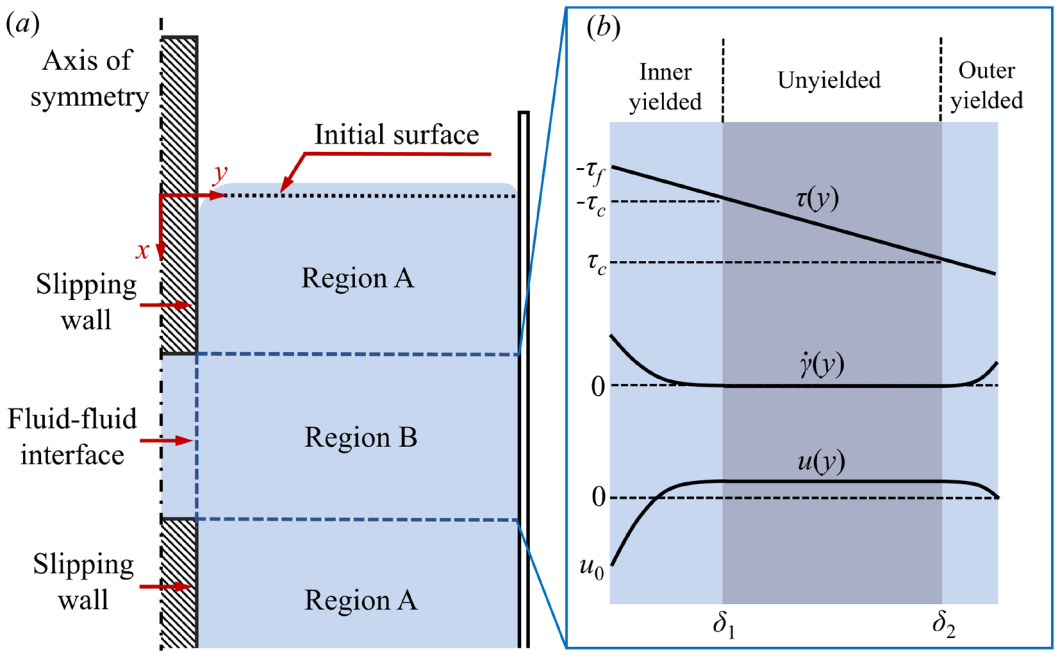

Figure 7.8. Schematic of the simplified flow regions in container (*a*) and the flow profiles between the fluid-fluid interface and the container wall (*b*).

Therefore, the flow in the container is governed by the following momentum conservation equation:

$$-\frac{\partial p}{\partial x}+\frac{\partial \tau_{xy}}{\partial y}+\rho_L g=0, \tag{7.6}$$

Following the routine of derivation in section 6.3.3, one obtains the shear stress profile

$$\tau_{xy}=\frac{\tau_c(2y-\delta_1-\delta_2)}{\delta_2-\delta_1}, \tag{7.7}$$

And the shear rate profile

$$\frac{\partial u}{\partial y}=\begin{cases}-\left(\dfrac{2\tau_c}{K}\right)^{1/n}\left(\dfrac{\delta_1-y}{\delta_2-\delta_1}\right)^{1/n} & 0\le y\le\delta_1\\ 0 & \delta_1<y<\delta_2\\ \left(\dfrac{2\tau_c}{K}\right)^{1/n}\left(\dfrac{y-\delta_2}{\delta_2-\delta_1}\right)^{1/n} & \delta_2\le y\le W\end{cases}. \tag{7.8}$$

and the velocity profile

$$u(y)=\begin{cases} u_0+\dfrac{n}{n+1}\left[\dfrac{2\sigma_y}{K(\delta_2-\delta_1)}\right]^{\frac{1}{n}}\left[(\delta_1-y)^{\frac{n+1}{n}}-\delta_1^{\frac{n+1}{n}}\right] & 0\le y\le\delta_1 \\ u_0-\dfrac{n}{n+1}\left[\dfrac{2\sigma_y}{K(\delta_2-\delta_1)}\right]^{\frac{1}{n}}\delta_1^{\frac{n+1}{n}} & \delta_1<y<\delta_2 \\ \dfrac{n}{n+1}\left[\dfrac{2\sigma_y}{K(\delta_2-\delta_1)}\right]^{\frac{1}{n}}\left[(y-\delta_2)^{\frac{n+1}{n}}-(W_c-\delta_2)^{\frac{n+1}{n}}\right] & \delta_2\le y\le W_c \end{cases}. \tag{7.9}$$

Injecting boundary condition $\tau(0)=-\tau_f$ into equation (7.7), one obtains the shear stress at the fluid-fluid interface:

$$\tau_f=\frac{\tau_c(\delta_1+\delta_2)}{\delta_2-\delta_1}. \tag{7.10}$$

The profiles of shear stress (7.7) and velocity (7.9) upon immersion have the same form as those (equations 6.5 and 6.9) upon withdrawal. The locations δ_1 and δ_2 are determined through velocity continuity and mass conservation:

$$u(\delta_1)=u(\delta_2), \tag{7.11}$$

$$\int_0^W u(y)\mathrm{d}y=-\frac{E}{2}u_0. \tag{7.12}$$

By substituting the velocity profile (7.9) into equations (7.11) and (7.12), we obtain the following analytical equality:

$$u_0=\frac{n}{n+1}\left[\frac{2\tau_c}{K(\delta_2-\delta_1)}\right]^{1/n}\left[\delta_1^{\frac{n+1}{n}}-(W-\delta_2)^{\frac{n+1}{n}}\right], \tag{7.13}$$

$$(W-\delta_2)^{\frac{n+1}{n}}(n\delta_2+nW+W)-n\delta_1^{\frac{2n+1}{n}}=\frac{E}{2}(1+2n)\left[\delta_1^{\frac{n+1}{n}}-(W-\delta_2)^{\frac{n+1}{n}}\right]. \tag{7.14}$$

If the plate thickness E is ignored, equation (7.12) reduces to equation (6.6), and equation (7.14) correspondingly reduces to equation (6.4).

7.3 Rheological measurement by immersion method

7.3.1 Determination of shear stress

Based on the aforementioned force analysis, it is surprising to find that the shear stress at the fluid-fluid interface, τ_f, can be derived from the force variation in regime III:

$$F = W_p(\rho_L g E+2\tau_w)(x-x_0)+2NW_sS(\tau_f-\tau_w)+F_0, \tag{7.15}$$

where, x_e has been equivalently replaced by x-x_0. The geometric parameters of the plate, W_p, E, N, W_s and S, as well as the gravitational acceleration, g, are a priori known. It should be noted that x_0 and F_0 can be obtained from the force evolution curve in regime I. In particular, the critical immersion depth, x_0, where the plate begins to penetrate the gels can be determined according to the variation of dF/dx. The depth corresponding to the maximum value of the derivative dF/dx is exactly x_0. Then, the value of F_0 is calculated with equation (7.1): $F_0 = F(x = x_0)$. By fitting equation (7.15) with the force variation detected during regime III, τ_f and τ_w can be easily determined.

7.3.1.1 Impact of geometric parameter

We first consider the impact of the geometric parameters of the plate on the force from a theoretical perspective based on analysis (7.15) for forces in regime III. The increment of the width W_p and thickness E of the plate increases the slope of the force. In addition, the plates with larger W_p and E have larger section perimeter and section area and thus are subjected to larger F_0, and accordingly, larger total forces. The increase in the slot width, W_s, slot height, S, and slot number, N, increases the area of the fluid-fluid interface, thus increasing the total forces. The slot pitch, P, has no effect on the force in regime III, but does affect the duration of this regime. Specifically, the increment in P decreases the duration of regime III and increases that of regime II.

From the perspective of the experiment, the immersion tests for plates with different slot pitch P, slot height S, and slot number N at a velocity of 0.5 mm·s^{-1} are performed, and the results are shown in Figure 7.9. Note that in order to exclude interference from the container bottom, the force curves

after the distance between the plate tip and the container bottom is less than 10 mm are discarded and not analysed here. Figure 7.9(*a*) shows that the slopes of force curves are the same since the width W_p and thickness E of the plate are both changeless. The magnitude of the force is not affected by P, say the forces of plates P1S2N17 and P2S2N17 are almost the same, while it increases with the increasing of the product of S and N. The agreement between the experimental force curves and the theoretical analysis indicates that the force evolution mechanism is correctly revealed at least from a qualitative perspective. Figure 7.9(*b*) further depicted the shear stress measured by plates with different geometric parameters. The shear stresses of plates P1S2N17, P2S2N11 and P2S2N17 are approximately equal, 39.2, 39.3 and 38.7 Pa, respectively. This indicates that the parameters P and N do not affect the measurement of shear stress. When S exceeds 2 mm, or more specifically, the ratio of S over E exceeds 2, the measured shear stress is significantly larger (cf. P2S3N14 and P2S4N11 in Figure 7.9*b*). The excessive ratio of S over E hinders the flow from satisfying the assumption that the gels in the slots move together with the plate without secondary flow. The secondary flow causes additional force applied on the plate and thus leads to an increase in the measured shear stress. Moreover, with the increase in the ratio S/E, the extent of the secondary flow and accordingly the measured shear stress increase. Zhu *et al.* 2001 suggested to keep ratio S/E smaller than 3 to avoid secondary flow, but without experimental or theoretical proof.[34] The immersion experiment in our study for slotted plates with different geometric parameters indicates that the ratio of S over E should be smaller than 2.

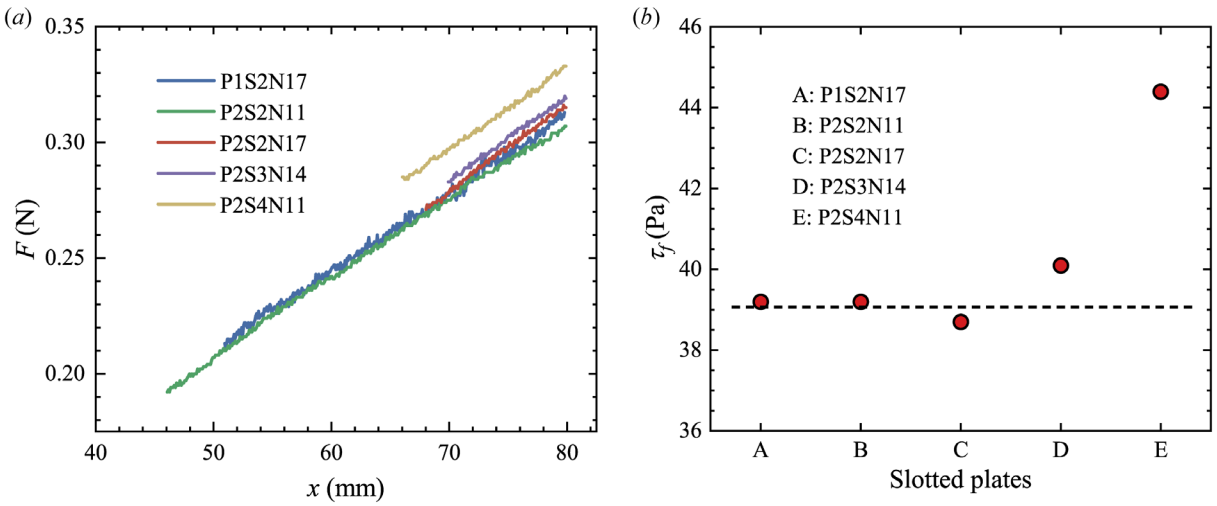

Figure 7.9. Curves of force versus immersion depth in regime III (*a*) and measured shear stress at the fluid-fluid interface (*b*) for slotted plates with different geometric parameters. Gel: 0.40 wt% Carbopol; immersion velocity: 0.5 mm·s^{-1}.

7.3.1.2 Impact of immersion velocity

The impact of immersion velocity on the force and shear stress at the fluid-fluid interface was studied over a range of velocities from 0.1 to 8.0 mm·s^{-1}. Figure 7.10(*a*) depicts the force curve for plate P1S2N17 penetrating 0.40 wt% Carbopol gels at different velocities. Similar results are obtained with other plates and other gels. The increment in immersion velocity enhances the shear effect in the container and thus the total force applied on the plate becomes larger. Moreover, according to the analysis (7.15), the slope of the force curve becomes larger because of the larger shear stress at the fluid-fluid interface. Correlating the force curve and the theoretical analysis yields the shear stresses at the fluid-fluid interface τ_f and the plate surface τ_w in Figure 7.10(*b*). The τ_f is larger than τ_w at the same velocity, evidencing again the occurrence of wall slip on the plate surface. As expected, both τ_f and τ_w increase with the velocity, and the shape of the τ_f versus u_0 curve is extremely similar to the flow curve (shear stress-shear rate curve) obtained from a conventional parallel disk method in bulk flow (as shown in Figure 3.4). It can be concluded that we now have a robust method for measuring the shear stress at the fluid-fluid interface when a slotted plate penetrates a viscoplastic fluid.

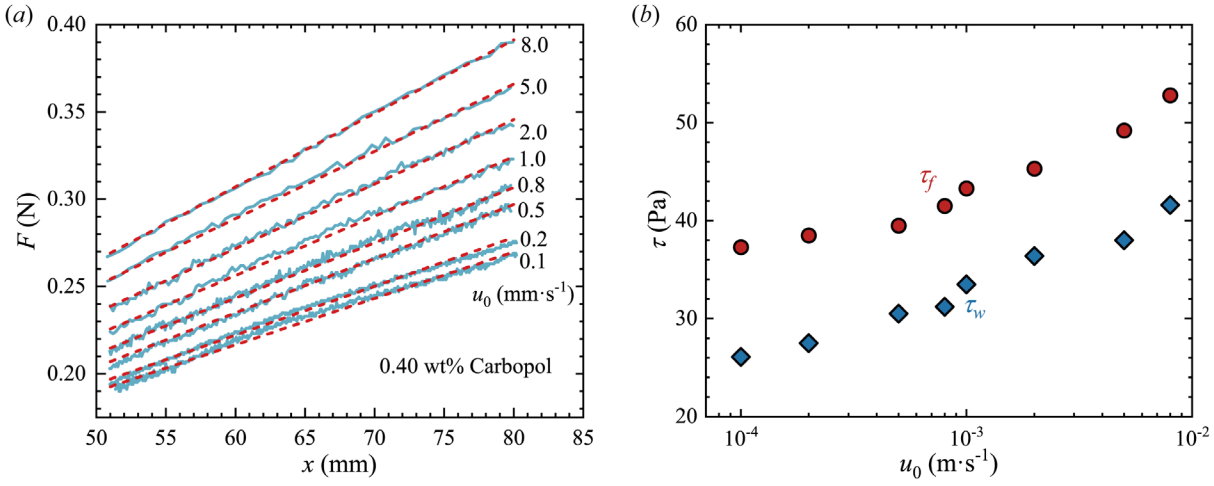

Figure 7.10. Force curve (*a*) and shear stresses at the fluid-fluid interface τ_f and on the plate surface τ_w (*b*) at different immersion velocities. Gel: 0.40 wt% Carbopol; plate: P1S2N17. The solid curve is the force evolution obtained from the immersion test, and the dotted curve is the best fit of equation (7.15).

7.3.2 Measuring rheological parameters

7.3.2.1 Yield stress

According to the variation of shear stress versus immersion velocity (as in Figure 7.10*b*), the yield stress is determined in this section. In the immersion test, the shear rate is dependent on the rheological properties which are a priori unknown. What we have is the variation of shear stress with the immersion velocity, which cannot be directly correlated with Herschel-Bulkley model to obtain the three characteristic parameters.

It is reasonable to use the pseudo-Herschel-Bulkley model, $\tau = \tau_c + Au_0^B$ for $\tau > \tau_c$, to obtain the yield stress. Figure 7.11 shows that the pseudo-Herschel-Bulkley model fits very well with the experimental shear stress as a function of velocity for both gels. The yield stresses are determined as τ_c = 12.18 Pa and τ_c = 34.31 Pa for 0.25 wt% and 0.40 wt% Carbopol gels, respectively. In addition, A = 104.25 Pa·s^B·m^{-B} and B = 0.41 for 0.25 wt% Carbopol gels and A = 135.60 Pa·s^B·m^{-B} and B = 0.41 for 0.40 wt% Carbopol gels. Although the value of parameter B is close to the flow index, they are theoretically different. By combining equations (7.8) and (7.13) and considering y = 0, one obtains the shear rate at the fluid-fluid interface:

$$|\dot{\gamma}(y=0)| = \frac{(n+1)\delta_1^{\frac{1}{n}} u_0}{n\left[\delta_1^{\frac{1}{n}+1} - (W-\delta_2)^{\frac{1}{n}+1}\right]}. \tag{7.16}$$

Inserting equation (7.16) into the Herschel-Bulkley model (2.14) yields:

$$\tau_f = \tau_c + K\left\{\frac{n+1}{n\left[\delta_1^{\frac{1}{n}+1} - (W-\delta_2)^{\frac{1}{n}+1}\right]}\right\}^n \delta_1 u_0^n. \tag{7.17}$$

Although equation (7.17) explicitly contains u_0^n, the demarcation positions (δ_1 and δ_2) are also functions of the velocity u_0, the real exponent of u_0 is hence not equal to n, i.e., $B \neq n$. A more rigorous method will be used to determine the flow index as well as the consistency factor.

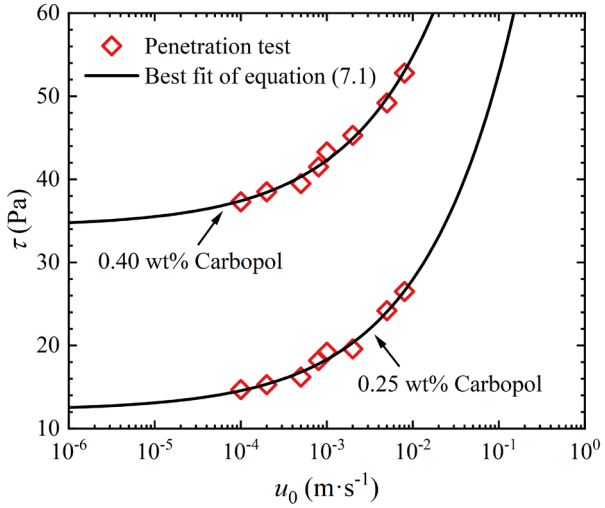

Figure 7.11. Shear stress obtained from immersion test (diamonds) as a function of immersion velocity. The solid curves are the best fit of pseudo-Herschel-Bulkley model (3.12) with the parameters τ_c = 12.18 Pa, A = 104.25 Pa·s^B·m^{-B} and B = 0.41 for 0.25 wt% Carbopol gels and τ_c = 34.31 Pa, A = 135.60 Pa·s^B·m^{-B} and B = 0.41 for 0.40 wt% Carbopol gels.

7.3.2.2 Consistency factor and flow index

Knowing the yield stress allows the calculation of the consistency factor and the non-Newtonian exponent by using equations (7.10), (7.14) and (7.17). The geometric parameters of the container (W) and plate (E) and the operating condition (u_0) are known a priori. The shear stress at the fluid-fluid interface τ_f is determined in section 7.3.1.2. The yield stress τ_c is determined in section 7.3.2.1. Therefore, only four parameters remain unknown: the consistency factor K, the flow index n and the demarcations between the yielded and unyielded regions δ_1 and δ_2. In equation (7.17), δ_1 can be

replaced by $\delta_1=\delta_2\left(\tau_f-\tau_c\right)/\left(\tau_f+\tau_c\right)$ which is obtained from equation (7.10). Herein, only three parameters (K, n and δ_2) are undetermined. We then introduce equation $\delta_1=\delta_2\left(\tau_f-\tau_c\right)/\left(\tau_f+\tau_c\right)$ into equation (7.14), obtaining:

$$(W-\delta_2)^{\frac{n+1}{n}}(n\delta_2+nW+W)-n\left[\frac{\delta_2(\tau_f-\tau_c)}{\tau_f+\tau_c}\right]^{\frac{2n+1}{n}}=\frac{E}{2}(1+2n)\left\{\left[\frac{\delta_2(\tau_f-\tau_c)}{\tau_f+\tau_c}\right]^{\frac{n+1}{n}}-(W-\delta_2)^{\frac{n+1}{n}}\right\}. \tag{7.18}$$

δ_2 in equation (7.17) can be implicitly represented by equation (7.18) without introducing any additional variables. Therefore, equation (7.17) contains two underdetermined parameters (K and n), which are exactly of interest. Substituting two sets of u_0 and τ_f into equation (7.17) is enough to solve for K and n. In the previous section, a series of τ_f under different u_0 were obtained. Substituting different sets of u_0 and τ_f into equation (7.17) probably yields different K and n. As displayed in Figure 7.12, we adopt the averages (dashed curves) as the eventual results. The values of K and n are 10.98 Pa·s^n and 0.40 for 0.25 wt% Carbopol gels, and 12.21 Pa·s^n and 0.39 for 0.4wt% Carbopol gels. Moreover, the discrepancy between the results obtained from different sets of u_0 and τ_f is very small and acceptable.

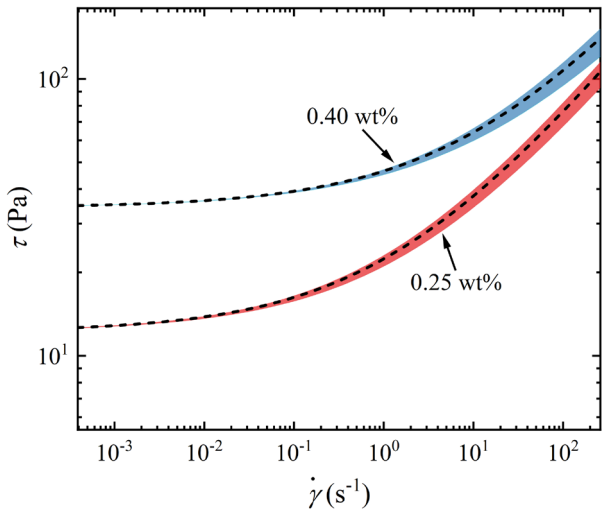

Figure 7.12. Flow curves obtained from the slotted plate immersion method. The dashed curves are the averages and the colour blocks represent the error range.

Overall, the aforementioned study indicates that a new method for determining the parameters (τ_c, K, and n) of the Herschel-Bulkley model has been developed. This method includes three steps: Firstly, by correlating the experimental force curve with the theoretical one, the shear stress free of wall slip, namely the shear stress at the fluid-fluid interface, is determined. Secondly, fitting the variation of shear stress versus immersion velocity with the pseudo-Herschel-Bulkley model determines τ_c. Thirdly, based on the determined τ_c, parameters K and n are calculated from the analysis of the flow field in the container.

7.3.3 Validation of immersion method

7.3.3.1 Comparison of flow curves obtained from different methods

The comparison of flow curves obtained from different methods is shown in Figure 7.13. Since the conventional parallel disk method at three gaps suffers the wall slip, it generates flow curves that are significantly different from the ones obtained from the slotted plate immersion method. Specifically, the flow curves obtained from the two methods agree well at high shear rates, while at low shear rates, the parallel disk method yields much lower shear stress than the slotted plate immersion method. On the other hand, the agreement between the flow curves generated by the Herschel-Bulkley model fitted to the data obtained from the parallel disk method in bulk flow and the ones fitted to the data from the slotted plate immersion method is excellent in a wide range of shear rates. This validates the slotted plate immersion method in measuring the Herschel-Bulkley parameters of viscoplastic fluids.

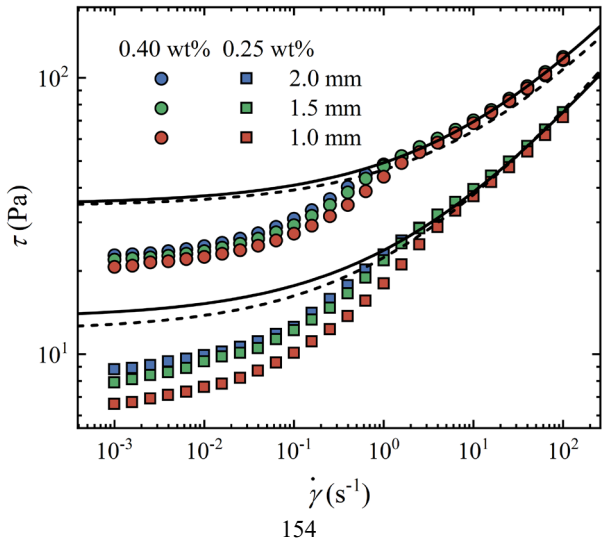

Figure 7.13. Comparison of flow curves obtained from different methods. Symbols and continuous lines represent the same data as in Figure 3.4 and are replotted here: symbols, flow curves obtained from the conventional parallel disk method; continuous lines, the Herschel-Bulkley model fitted with the data obtained from the conventional parallel disk method in bulk flow. The dashed lines correspond to flow curves obtained from the slotted plate immersion method.

We also calculated the values of K and n for the viscoplastic fluids used in the study of Boujlel and Coussot 2012[37], where the roughened plate penetrates various viscoplastic fluids: Carbopol gel, emulsion, soft cheese and foam. The Herschel-Bulkley parameters of one of the fluids (denoted as C5 in their study) are: τ_c = 81 Pa, K = 31.0 Pa·s^n and n = 0.38. Based on the shear stress- immersion velocity data of fluid C5 from their immersion experiments the values of K and n are calculated using our analytical model (7.10, 7.17, and 7.18) and compared with the reference values in Figure 7.14. The calculated values at different W (distance between the plate and the container wall, cf. Figure 3.5) are in acceptable agreement with the reference values, validating our calculation. In particular, the calculated values of n (for W = 0.04 m, n = 0.39; for W = 0.06 m, n = 0.38) are almost the same as the reference one (n = 0.38). The discrepancy concerns mainly K: K = 34 Pa·s^n for W = 0.04 m and K = 29 Pa·s^n for W = 0.06 m, while the reference K is 31 Pa·s^n.

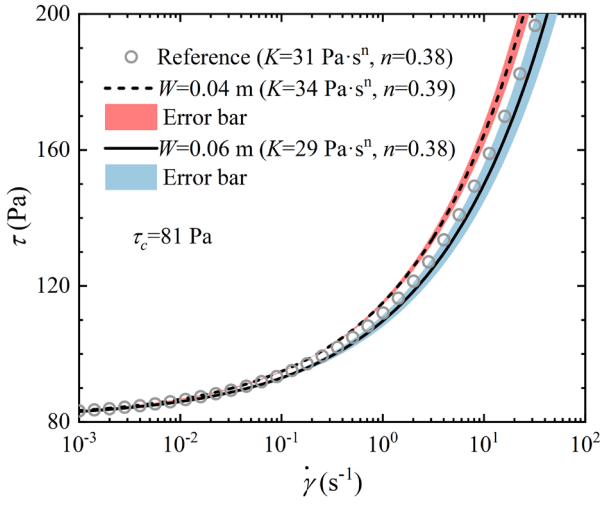

Figure 7.14. Flow curves with different values of K and n: reference value from the study of Boujlel and Coussot 2012[37] (symbols) and the calculated values (curves) using our analytical model (7.10), (7.17), and (7.18) at different W.

7.3.3.2 Comparison of analytical and simulated velocity profiles

The determination of the consistency factor and flow index by immersion method involves the calculation of the flow in the container. An additional rigorous validation of this method is performed by comparing the analytical and simulated velocity profiles obtained with the same slipping condition as in the immersion test (see details of the simulation in Appendix B). To clarify, the vertical component of velocity field was normalized by the immersion velocity and the corresponding results for Carbopol gels with different concentrations and at different velocities are depicted in Figure 7.15(*a-d*). Figure 7.15(*a-c*) illustrate that the shear effect increases with increasing velocity, thus more fluid is sheared along the plate and the thickness of the liquid layer increases. Figure 7.15(*b*, *d*) show that fluids with smaller yield stress are more likely to yield and therefore have thicker liquid layers. The comparison of the velocity profiles in the liquid layer adjacent to the plate calculated using equation (7.9) and obtained from simulations are displayed in Figure 7.15(*e*) for different velocities and in Figure 7.15(*f*) for different concentrations. The results show that the analytical predictions agree well with the simulated results for different velocities and different concentrations, and the agreement becomes better at lower velocities. At higher velocities (say 5 $mm \cdot s^{-1}$), as shown in Figure 7.15(*e*), the gels in the slots deviate from the assumption of moving with the plate and move slower than the plate. This leads to the velocity of the gels in the yielded region lower than the analytical prediction.

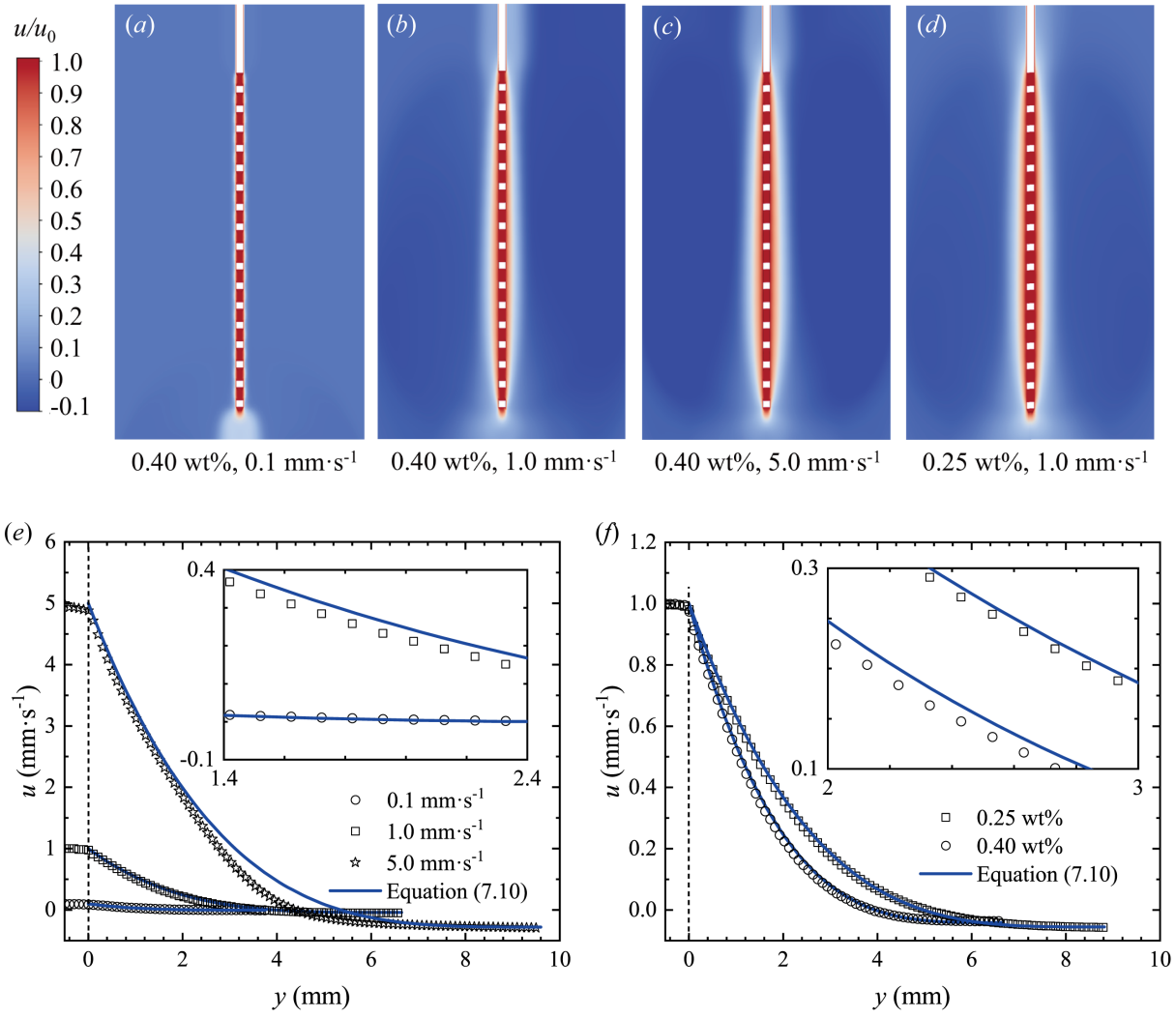

Figure 7.15. Contours of normalized vertical component of velocity around the plate for 0.40 wt% Carbopol gels at 0.1 mm·s^{-1} (*a*), 1.0 mm·s^{-1} (*b*), 5.0 mm·s^{-1} (*c*), and 0.25 wt% Carbopol gels at 1.0 mm·s^{-1} (*d*). Comparison of the velocity profiles calculated using equation (7.9) and obtained from simulations for different immersion velocities (*e*) and Carbopol gels with different concentrations (*f*).

The secondary flow is then evaluated in terms of the normalized transversal velocity (v/u_0) around the slot under different immersion velocities (u_0) and different ratios of slot height over plate thickness (S/E). The extent and intensity of secondary flow almost remain unchanged as the immersion increases from 1 mm·s^{-1} to 5 mm·s^{-1}, since the contours of normalized transversal velocity at two velocities are almost the same (cf. Figure 7.16*a*, *b*). This also indicates that the increase in immersion velocity

increases the absolute transversal velocity. In terms of slot height-plate thickness ratio (*S*/*E*), Figs 18a and 18c show that an excessively large *S*/*E* (say 3) enhances significantly the secondary flow. Therefore, the velocity and the force on the plate will deviate from our models, which aligns with the experimental results in section 7.3.1.1 Impact of geometric parameter.

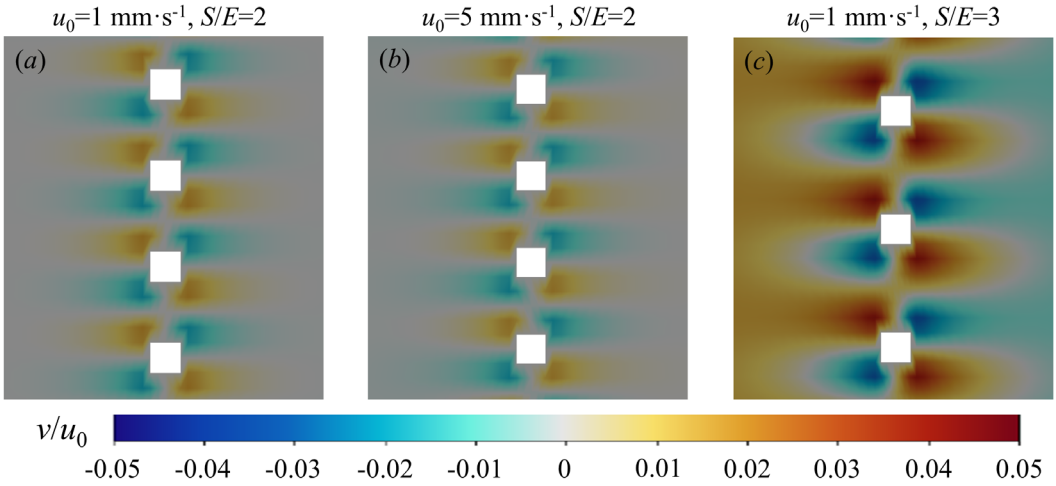

Figure 7.16. Contours of normalized transversal velocity component around the slots for 0.40 wt% Carbopol gels under different immersion velocities (u_0) and different slot height to plate thickness ratios (*S*/*E*): (*a*) u_0 = 1 mm·s^{-1}, *S*/*E* = 2, (*b*) u_0 = 5 mm·s^{-1}, *S*/*E* = 2, (*c*) u_0 = 1 mm·s^{-1}, *S*/*E* = 3.

7.3.4 Applicability of immersion method

The immersion method applies to simple viscoplastic fluids, but not to fluids without yield stress nor to viscoplastic fluids with thixotropic. The immersion test is performed in the coating model of MCR 301 rheometer (Anton Paar), which is highly automated and easy to operate. As confirmed by our investigation, this method is applicable to both slotted and non-slotted plates. We recommend using slotted plates as the default option, but non-slotted plates should be prioritized under certain circumstances. Specifically, non-slotted plates are more suitable when the fluid cannot fill the slots well, such as liquid foam and suspensions with large particles. Additionally, due to the shorter test time associated with non-slotted plates, non-slotted plates are preferable for fluids with high volatility or significant sedimentation.

We then propose suggestions on the choice of the geometry of container and plate and the immersion velocity based on the present work. Additional works are needed to give a more exact range of applicability of this immersion method. In terms of the geometry of container and plate, a wide distance between the plate and the container wall is recommended, to minimize the impact of wall-slip at the container wall on the flow around the plate. The present work confirms that 40 mm is sufficient. For slotted plates, an additional requirement is that the ratio of slot height over plate thickness should be less than 2. Regarding immersion velocity, the reliability of the velocity model (7.9) as well as the immersion method decreases at higher velocities (say 5 $mm \cdot s^{-1}$) for slotted plates. The upper limit of velocity depends on the yield stress of fluids. Fluids with higher yield stress is easier to fulfil the co-motion assumption of the plate and the fluid in slots, the upper limit of velocity hence can be higher. For non-slotted plates, the upper limit of velocity is less restrictive, provided the laminar flow is maintained and inertial effects remain negligible. In addition, to mitigate evaporation, we suggest that the duration of each test should not exceed 1 hour.

The unresolved aspect of this method is that it requires a much larger sample volume (480 mL in present work) than rotating rheometers (several to dozen mL), as well as the temperature control issue resulting from the large sample volume. It is difficult to accurately control the temperature of such a large volume of liquid when the test temperature deviates significantly from the ambient temperature.

7.4 Conclusion

The forces and flow characteristics of the viscoplastic fluids, i.e., the Carbopol gels, during the immersion of the slotted plate were investigated through both immersion experiments and computational fluid dynamics. The fluid in the slots remained static relative to the plate and sheared at the fluid-fluid interface. Moreover, the wall slip did not affect the flow between the fluid-fluid interface and the container wall. Based on the above information, a new slotted plate immersion method was proposed to successfully obtain the shear stress (which is free of wall slip) at the fluid-fluid interface. The impacts of geometric parameters of the slotted plate and immersion velocity on the measured shear

stress were studied, which showed that the ratio of the slot height to the plate thickness had to be less than 2 to avoid possible secondary flow. By fitting the shear stress- immersion velocity data to the pseudo-Herschel-Bulkley model, the yield stress was determined. Knowing the yield stress allows us to calculate the consistency factor and the flow index, based on the analytical model of the flow in the container. The proposed method was validated by comparing it successfully with the conventional parallel disk method in bulk flow. In addition, there is a good agreement between the calculated K and n by using stress-velocity data of a rough non-slotted plate and the reference K and n. This proves that our method is not only applicable to slotted plates but also to rough non-slotted plates. The additional rigorous comparison of the predicted and simulated velocity profiles in the container also validates our new immersion method.

Reference

1. Laun HM. Capillary rheometry for polymer melts revisited. *Rheol. Acta.* 2004;43(5):509-528.
2. Chen M, Zheng M, Zhang L, Xu Y, Zhang X, Chen W. Correlation between structural evolution and rheological properties for polycarbonate in the molten state. *J. Appl. Polym. Sci.* 2022;140(5S):e53418.
3. Paul AS, Freed BAD, Benjamin CCC. Application of the Gram-Schmidt factorization of the deformation gradient to a cone and plate rheometer. *Phys. Fluids.* 2021;33(1):017113
4. Estellé P, Lanos C, Perrot A. Processing the Couette viscometry data using a Bingham approximation in shear rate calculation. *J Non-Newton Fluid.* 2008;154(1):31-38.
5. Cloitre M, Bonnecaze RT. A review on wall slip in high solid dispersions. *Rheol. Acta.* 2017;56(3):283-305.
6. Abbasi Moud A, Piette J, Danesh M, Georgiou GC, Hatzikiriakos SG. Apparent slip in colloidal suspensions. *J. Rheol.* 2022;66(1):79-90.
7. Bertola V, Bertrand F, Tabuteau H, Bonn D, Coussot P. Wall slip and yielding in pasty materials. *J. Rheol.* 2003;47(5):1211-1226.
8. Quan L, Kalyon DM. Parallel-disk viscometry of a viscoplastic hydrogel: yield stress and other parameters of shear viscosity and wall slip. *Gels.* Apr 7 2022;8(4):230.
9. Marinho TO, Marchesini FH, de Oliveira MCK, Nele M. Apparent wall slip effects on rheometric measurements of waxy gels. *J. Rheol.* 2021;65(2):257-272.
10. He J, Lee SS, Kalyon DM. Shear viscosity and wall slip behavior of dense suspensions of polydisperse particles. *J. Rheol.* 2019;63(1):19-32.
11. Datta A, Tanmay VS, Tan GX, Reynolds GW, Jamadagni SN, Larson RG. Characterizing the rheology, slip, and velocity profiles of lamellar gel networks. *J. Rheol.* 2020;64(4):851-862.
12. Barnes HA. A review of the slip (wall depletion) of polymer solutions, emulsions and particle suspensions in viscometers: its cause, character, and cure. *J Non-Newton Fluid.* 1995;56(3):221-251.
13. Lawal A, Kalyon DM. Single screw extrusion of viscoplastic fluids subject to different slip coefficients at screw and barrel surfaces. *Polym. Eng. Sci.* 1994;34(19):1471-1479.

14. Kalyon DM, Lawal A, Yazici R, Yaras P, Railkar S. Mathematical modeling and experimental studies of twin-screw extrusion of filled polymers. *Polym. Eng. Sci.* 1999;39(6):1139-1151.

15. Sorgato M, Masato D, Lucchetta G, Orazi L. Effect of different laser-induced periodic surface structures on polymer slip in PET injection moulding. *CIRP Ann.* 2018;67(1):575-578.

16. Mooney M. Explicit Formulas for Slip and Fluidity. *J. Rheol.* 1931;2(2):210-222.

17. Aktas S, Kalyon DM, Marín-Santibáñez BM, Pérez-González J. Shear viscosity and wall slip behavior of a viscoplastic hydrogel. *J. Rheol.* 2014;58(2):513-535.

18. Kalyon DM. Apparent slip and viscoplasticity of concentrated suspensions. *J. Rheol.* 2005;49(3):621-640.

19. Medina-Bañuelos EF, Marín-Santibáñez BM, Pérez-González J, Malik M, Kalyon DM. Tangential annular (Couette) flow of a viscoplastic microgel with wall slip. *J. Rheol.* 2017;61(5):1007-1022.

20. García-Blanco YJ, Urazaki VY, Rivera ÁDJ, Quitian LH, Germer EM, Franco AT. Rheological characterization of viscoplastic fluid flow in a pipe with wall slip using in situ particle image velocimetry. *Rheol. Acta.* 2022;62(2-3):93-110.

21. Bonn D, Rodts S, Groenink M, Rafaï S, Shahidzadeh-Bonn N, Coussot P. Some applications of magnetic resonance imaging in fluid mechanics: complex flows and complex fluids. *Annu. Rev. Fluid Mech.* 2008;40(1):209-233.

22. Divoux T, Barentin C, Manneville S. Stress overshoot in a simple yield stress fluid: An extensive study combining rheology and velocimetry. *Soft Matter.* 2011;7(19):9335.

23. Ortega-Avila JF, Pérez-González J, Marín-Santibáñez BM, et al. Axial annular flow of a viscoplastic microgel with wall slip. *J. Rheol.* 2016;60(3):503-515.

24. Dimitriou CJ, McKinley GH, Venkatesan R. Rheo-PIV analysis of the yielding and flow of model waxy crude oils. *Energy Fuels.* 2011;25(7):3040-3052.

25. Zhang X, Lorenceau E, Bourouina T, et al. Wall slip mechanisms in direct and inverse emulsions. *J. Rheol.* 2018;62(6):1495-1513.

26. Aral BK, Kalyon DM. Effects of temperature and surface roughness on time-dependent development of wall slip in steady torsional flow of concentrated suspensions. *J. Rheol.* 1994;38(4):957-972.

27. Geffrault A, Bessaies-Bey H, Roussel N, Coussot P. Instant yield stress measurement from falling drop size: The “syringe test”. *J. Rheol.* 2023;67(2):305-314.

28. Meeker SP, Bonnecaze RT, Cloitre M. Slip and flow in soft particle pastes. *Phys Rev Lett.* May 14 2004;92(19):198302.

29. Maillard M, Boujlel J, Coussot P. Flow characteristics around a plate withdrawn from a bath of yield stress fluid. *J Non-Newton Fluid.* 2015;220:33-43.

30. Lootens D, Jousset P, Martinie L, Roussel N, Flatt RJ. Yield stress during setting of cement pastes from penetration tests. *Cem. Concr. Res.* 2009;39(5):401-408.

31. Pott U, Stephan D. Penetration test as a fast method to determine yield stress and structural build-up for 3D printing of cementitious materials. *Cem. Concr. Compos.* 2021;121:104066.

32. De Kee D, Turcotte G, Fildey K, Harrison B. New method for the determination of yield stress. *J. Texture Stud.* 2007;10(3):281-288.

33. Samaniuk JR, Shay TW, Root TW, Klingenberg DJ, Scott CT. A novel rheometer design for yield stress fluids. *AIChE J.* 2014;60(4):1523-1528.

34. Zhu L, Sun N, Papadopoulos K, De Kee D. A slotted plate device for measuring static yield stress. *J. Rheol.* 2001;45(5):1105-1122.

35. Zhu L, De Kee D. Slotted-plate device to measure the yield stress of suspensions: finite element analysis. *Ind. Eng. Chem. Res.* 2002;41(25):6375-6382.

36. De Kee D, Dae Kim Y, Dzuy Nguyen Q. Measuring rheological properties using a slotted plate device. *Korea-Aust Rheol J.* 2007;19(2):75-80.

37. Boujlel J, Coussot P. Measuring yield stress: a new, practical, and precise technique derived from detailed penetrometry analysis. *Rheol. Acta.* 2012;51(10):867-882.
38. Putz AMV, Burghelea TI. The solid-fluid transition in a yield stress shear thinning physical gel. *Rheol. Acta.* 2009;48(6):673-689.
39. Zhang H-K, Yin Y-R, Zhang X-M, Chen S-C, Chen W-X, Hu GH. Numerical simulation of the hydrodynamics of yield stress fluids during dip coating. *J Non-Newton Fluid.* 2021;298:104675.
40. Maillard M, Boujlel J, Coussot P. Solid-solid transition in Landau-Levich flow with soft-jammed systems. *Phys. Rev. Lett.* Feb 14 2014;112(6):068304.
41. Smit WJ, Kusina C, Joanny JF, Colin A. Stress field inside the bath determines dip coating with yield-stress fluids in cylindrical geometry. *Phys. Rev. Lett.* Oct 4 2019;123(14):148002.

8 Summary and perspectives

8.1 Summary

1. Spatial-temporal evolution of a Newtonian liquid layer on a fully wetting plate during dip coating: Gravity drives thinning along the withdrawal direction, while viscous forces counteract this effect, increasing the layer thickness. Spatial-temporal evolution of the layer thickness exhibits self-similarity in the visco-gravity regime. The flows in the unsteady part and the steady meniscus are one dimensional and two dimensional with the dominant velocity derivative of $\partial\overline{u}/\partial\overline{y}$, respectively. The two regions were modelled separately first and were then integrated into a unified composite model applicable to the entire liquid layer. Validation against experimental and simulated data confirms the model's accuracy for dimensionless times $\bar{t} > 16$ in the Reynolds number range $0 < Re < 1.1$.

2. The wetting and deposition dynamics of Newtonian fluids on a partially wetting cylinder during dip coating: Both the capillary number (Ca) and the dimensionless cylinder radius ($\overline{r}_0$) not only quantitatively influence the deposited film thickness but also qualitatively alter the interfacial morphology. For sufficiently large cylinder radius ($\overline{r}_0 > 2.3$), four distinct interfacial regimes emerge as Ca increases: (I) a stationary meniscus, (II) a capillary number-independent thick film connecting to the container through a stationary dimple, (III) a capillary number-independent thick film connecting to a classical Landau-Levich (LL) film through a travelling capillary ridge, and (IV) a film with thickness decreasing along the withdrawal direction. For radius smaller than 2.3, scenario (II) disappears. Further reducing $\overline{r}_0$ induces wave instabilities in both films. The thick film becomes wavy when $\overline{r}_0 < 0.255$, while the LL film exhibits a more complex wavy behaviour, dependent on both Ca and $\overline{r}_0$. Notably, the waves in the two films remain independent, with no observable transfer between them.

3. Hydrodynamics of viscoplastic fluids upon dip coating of a fully wetting plate: Focusing on Bingham numbers $Bi < 1$, the analysis revealed three regions in the container: inner yielded, unyielded, and outer yielded. Film thickness correlated positively with stress in the inner yielded

region, increasing with higher withdrawal velocity, yield stress, and consistency factor. The effect of the flow index depended on shear rate: for shear rates < 1 s^{-1}, larger flow indices reduced stress and film thickness; the opposite occurred at higher rates. These findings contrast with studies focusing on higher *Bi* numbers (> 1), where yield stress dominates and withdrawal velocity has negligible impact. Drainage flow in the meniscus reduced film thickness without significantly altering shear stress or velocity profiles in the container, enabling a semi-empirical model that integrates drainage effects. This work elucidates viscoplastic film formation mechanisms, offering practical insights for optimization of dip coating.

4. Hydrodynamics and rheological characterization upon the immersion process of a slotted plate into viscoplastic fluids: A novel immersion method was developed to accurately measure the rheological properties of plastic fluids, which was applicable for both slotted and rough non-slotted plates. Yield stress was determined by fitting shear stress to the so-called pseudo-Herschel-Bulkley model, enabling subsequent calculation of consistency factor *K* and flow index *n* through the analytical model of the flow in the container. Method validation showed excellent agreement with conventional parallel disk measurements and reference values in the literature. Additional verification came from excellent agreement between predicted and simulated velocity profiles in the container, establishing the reliability of this new rheometric method for viscoplastic fluids.

8.2 Perspectives

1. The model of film thickness profile in Chapter 4 is developed under vertical withdrawal angle. It would be valuable and interesting to extend this model to various withdrawal angle. The film thickness profiles, as well as the asymptotic film thicknesses, are distinct under different withdrawal angles. Predictably, the flow in the unsteady film is also one-dimensional under withdrawal angle below 90°. Therefore, our modelling strategy is expectantly to be applicable for small withdrawal angles but requires further examination.

2. The film deposition of Newtonian fluids on a partially wetting cylinder was studied in Chapter 5. The complex rheological properties like the yield stress will significantly affect the dynamics of the contact line, accordingly affecting the wetting and film transition. Our ongoing work shows that the combination of direct numerical simulation and lubrication theory is feasible for solving the dynamics of viscoplastic fluids on a partially wetting plate, and has led to some preliminary results.

3. We studied in Chapter 6 the hydrodynamics of viscoplastic fluids upon dip coating and modelled the film thickness. As discussed in Chapter 2 (literature review and state of the art), the film thickness of the viscoplastic fluid is determined in some cases by the meniscus, while in other cases it is determined by the flow in container. The next step should delve into figuring out the critical conditions between the two cases or even other cases.

4. The pseudo-Herschel-Bulkley model used in Chapter 7 is a useful model which describes the relationship between shear stress and velocity. We have verified its applicability for plate immersion process, but its applicability to other geometries, such as cone-and-plate and concentric cylinders, remains to be examined.

Appendix A

The accuracy and reproducibility of the dip coating experiment in Chapter 4 were examined. An additional three-dimensional simulation was conducted to evaluate the extent of the edge dead phenomenon or edge thickening on both sides of the plate.

A.1 Accuracy and reproducibility of the dip coating experiment

The withdrawal velocity of the plate is a key operating parameter of dip coating and needs to be accurately controlled. Figure A1(*a*) compares the withdrawal velocity of the plate set by the rheometer (set u_0) with that measured by the camera (measured u_0). Three repeated measurements are conducted for each of the three withdrawal velocities set by the rheometer. Both the set and measured velocities agree well with each other in the range of 2 to 8 mm·s^{-1}, with a maximum absolute error of 0.03 mm·s^{-1} and a maximum relative error of 1.5%. Figure A1(*b*) compares the layer thickness profiles (height x versus thickness h of the layer) of three repeated experiments at u_0 = 6 mm·s^{-1}. They all superimpose well, showing that the coating experiments are reproducible. Note that the origin of the coordinate is the intersection between the initial horizontal surface of the liquid and the vertical line of the middle of the substrate. The x-axis is directed in the withdrawal direction, the y-axis is perpendicular to the plate surface, and the z-axis is perpendicular to x-y plane. This coordinate system is used for subsequent discussions in Appendix A.

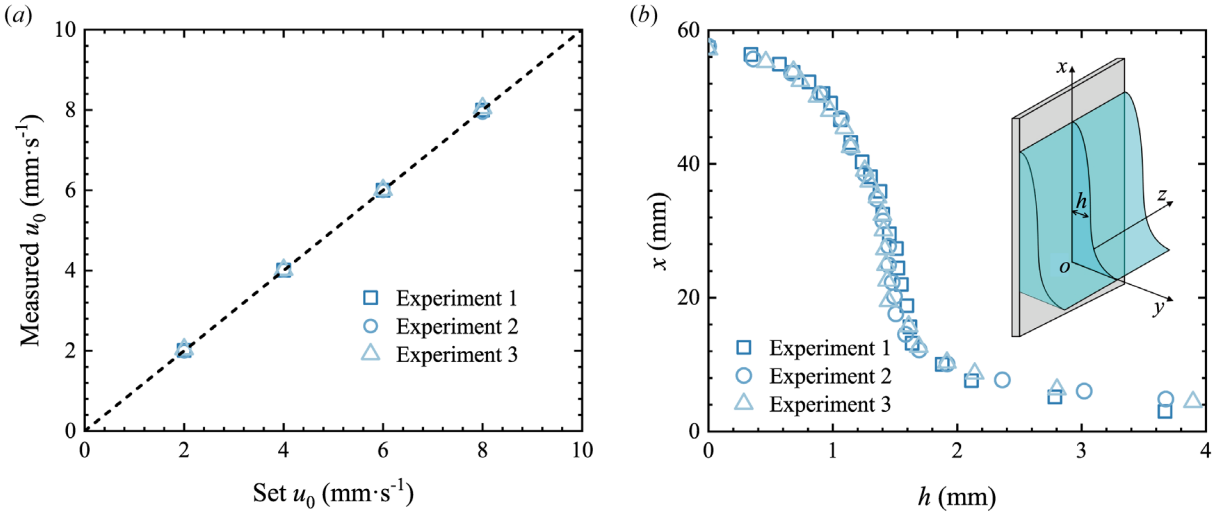

Figure A1. Accuracy and reproducibility of the coating experiments. (*a*) Comparison between the set velocities from 2 to 8 mm·s^{-1} and the measured ones; (*b*) layer thickness profiles *h* of three repeated experiments. Viscosity: 10 Pa·s (silicone S1); withdrawal velocity: 6 mm·s^{-1}; and withdrawal time: 9.5 s.

A.2 Additional three-dimensional simulation

Figure A2 shows the computational domain with initial and boundary conditions. It is made of a cylindrical container (radius: 50 mm; height: 220 mm) and a plate (height: 100 mm; width: 50 mm, and thickness: 1 mm). Initially, the container is filled with a liquid height of 100 mm, and the plate is immersed vertically in the fluid with its bottom place 20 mm above the bottom of the container. The plate is withdrawn upward at a constant velocity. The numerical simulations impose a no-slip condition on the container walls and the plate surfaces. Furthermore, the contact angle on the plate is fixed at 50 degrees, while the angle on the container's wall is set to 90 degrees. This configuration ensures a horizontally flat liquid-gas interface, distant from the plate. It is important to note that these values are hypothetical and are not the experimental ones for the plate/silicone oil systems. However, as revealed in Chapter 4, the layer thickness profile remains unaffected by surface tension and contact angle for $Ca > 0.94$, which aligns with the experimental conditions in this work.

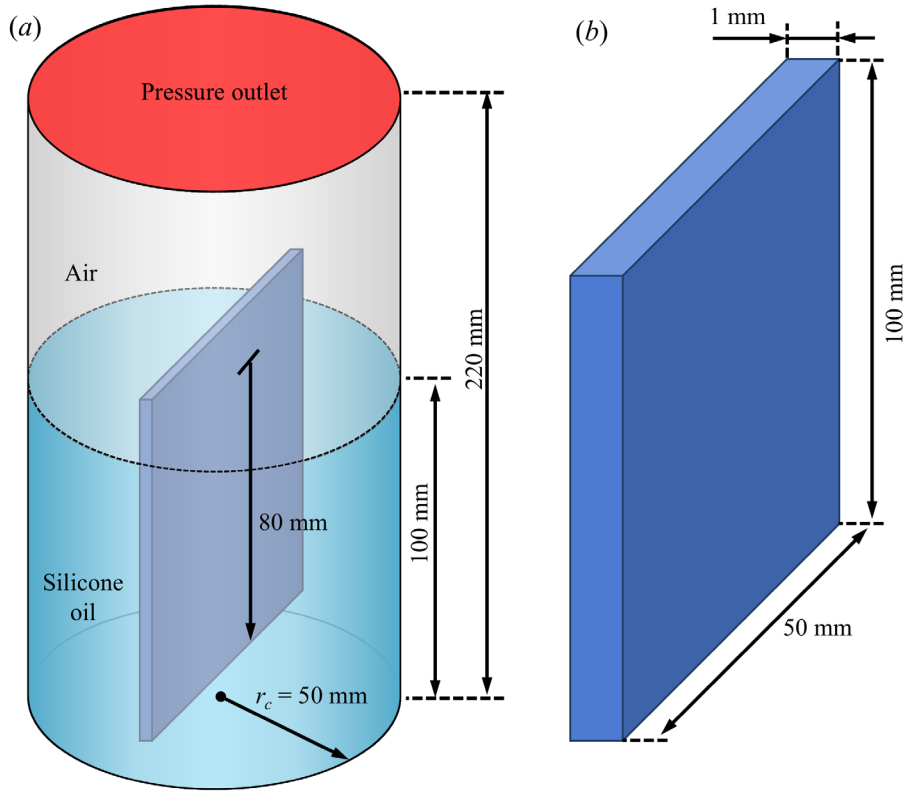

Figure A2. (*a*) Schematic of the computational domain with the boundary and initial conditions, and (*b*) geometrical parameters of the plate.

The withdrawal velocity of the plate is imposed by compiling a user-defined function (UDF). The movement of the plate compresses the cells which height might become negative, and stretches those beneath it, making the simulation divergent. Therefore, the layering method, one of the dynamic mesh methods, is used to merge smaller cells before negative dimensions appear and split larger cells to ensure convergence. It is particularly suitable for a unidirectional rigid body motion with a large displacement, like the withdrawal process in this work.

Figure A3 shows seven separated computational domains: left, right, back, front, top, bottom and central. They are spatially discretized with structured hexahedral cells. The cells in the central domain (120×20×70 mm around the plate) are refined with non-uniform hexahedral ones. The seven domains are merged to form a single computational domain. The data transfer among the seven domains is done by the interfaces between the adjacent domains. The central domain moves upward together with the

plate it encloses. The size of the cells in all domains, except for the central one, is 2×2 mm. A mesh independent evaluation is performed by comparing four different mesh refinements of the central domain for the liquid-air interface at $z = 0$ plane (η_L = 10 Pa·s, u_0 = 2 mm·s^{-1}, withdrawal time t = 27.5 s): M1 = 124736, M2 = 282026, M3 = 446956, and M4 = 698136. When the mesh size increases from M1 to M4, the liquid-gas interface profiles gradually converge and the liquid-air interfaces of M3 and M4 superimpose well with each other (Figure A4). M3 is thus adopted for subsequent simulations to ensure a good compromise between the accuracy and computational cost.

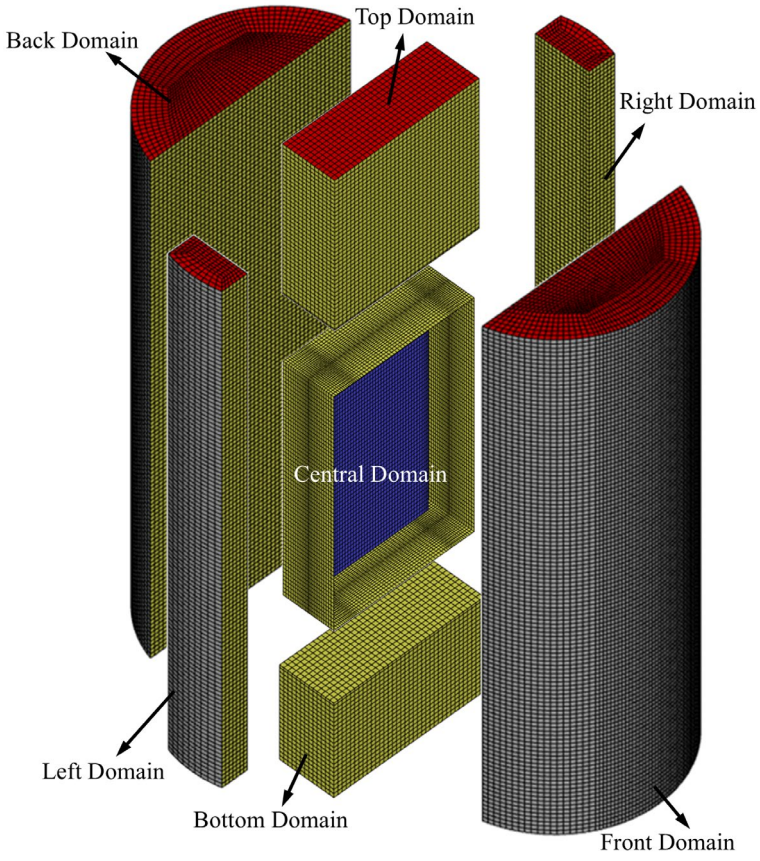

Figure A3. Meshes of the seven separated computational domains (red: pressure outlet; black: walls; yellow: interfaces; and blue: moving plate). The front interface in the central domain is not displayed in order to show the plate in it.

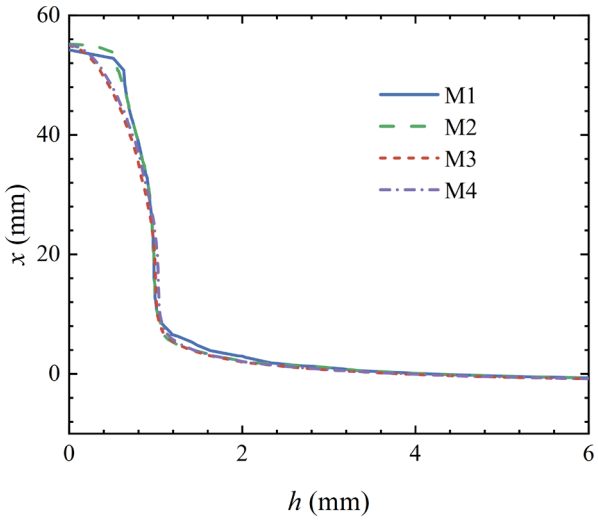

Figure A4. Liquid-air interfaces at z = 0 plane obtained from simulations for four different mesh refinements of the central domain (M1 to M4). Viscosity: 10 Pa·s; withdrawal velocity: 2 mm·s^{-1}; withdrawal height: 55 mm.

Figure A5 compares the simulations and experiments in terms of the evolution of the layer thickness profile in the withdrawal direction on plane z = 0 as a function of the withdrawal time, showing good agreements between the simulations and experiments.

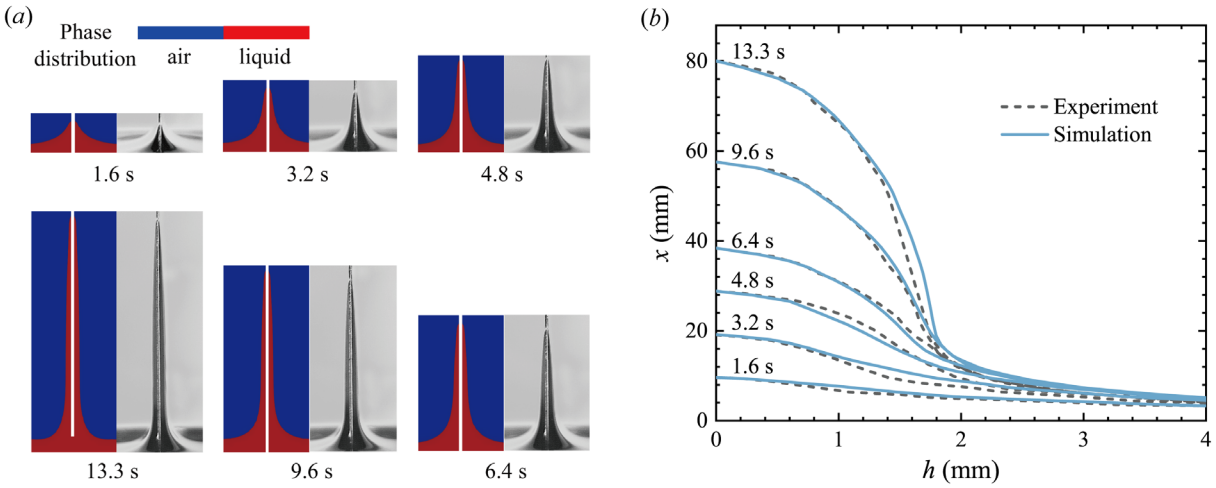

Figure A5. (*a*) Comparison between the simulations (red and blue images on the left) and experiments (black and grey images taken by the camera on the right) in terms of the evolution of the liquid-gas interface during the withdrawal process; (*b*) comparison between the simulations (solid curves) and

experiments (dashed curves) in terms of the evolution of the layer thickness profile. Viscosity: 10 Pa·s; withdrawal velocity: 6 mm·s^{-1}.

A.3 Evaluation of the extent of edge bead phenomenon

Due to the flow symmetry, the edge bead phenomenon is the same on both the left ($y < 0$) and right ($y > 0$) sides of the plate. Figure A6(a) and Figure A6(b) show the layer thickness profile on the right side of the plate for varying liquid viscosities and withdrawal velocities at x = 30 mm when the withdrawal height is 60 mm. To quantify the edge bead phenomenon, the layer thickness at z = 0 mm is defined as the central layer thickness (h_z), the maximum layer thickness at the plate's edge is defined as the edge layer thickness (h_e), and the extent of thickening (ET) is calculated as $ET = (h_e\text{-}h_z)/h_z \times 100\%$. The values of h_z, h_e, and ET increase with higher withdrawal velocities and liquid viscosities. Moreover, the layer thickness distribution exhibits a relatively uniform pattern in the z direction, with only a slight thickening (ET less than 5%) at the plate's edge. If the container wall had an influence on the layer thickness, the thickness would vary significantly with different z-position, that is, with varying distance between the container wall and the plate. However, this contradicts the experimental observation that the layer thickness remains uniform along the z-direction, except near the edge of the plate. Therefore, the influence of the container wall on layer thickness is negligible.

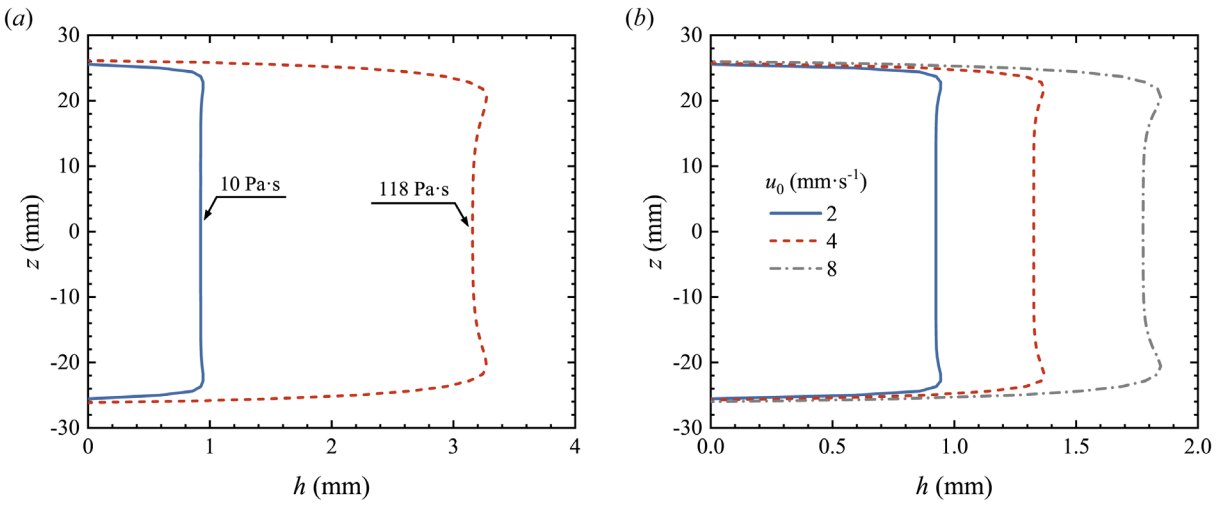

Figure A6. Profiles of layer thickness at x = 30 mm when the withdrawal height is 60 mm. (*a*) Withdrawal velocity: 2 mm·s^{-1}; Viscosity: 10 Pa·s and 118 Pa·s. (*b*) Withdrawal velocity: from 2 to 8 mm·s^{-1}; Viscosity: 10 Pa·s.

Appendix B

To valid the analytical model of the flow in container during penetration process in Chapter 7, the direct numerical simulation (DNS) is performed. A two-dimensional simulation is used on account of its lower computational cost and comparable accuracy compared to a three-dimensional simulation. Given the symmetry of the flow, the left half of the flow domain and the right half of the mesh with boundary and initial conditions are displayed together in Figure B1. The computational domain is an 81 mm wide and 150 mm high rectangle. The left half shows the initial distribution of air phase (blue) and liquid phase (red zone). The mesh domain is divided into five sub-domains, including a central sub-domain (coloured black) around the plate and four outer sub-domains (coloured green). Note that only three mesh outer sub-domains and the central sub-domain are shown in Figure B1, as only the right half of the mesh is displayed. The plum-coloured lines represent the interfaces between different domains. The central domain is 60 mm wide and 130 mm high. The plate, central domain and the upper and bottom interfaces are moved together. The constructed mesh consisting of non-uniform rectangular cells is used. The global cell size is 0.5 mm × 0.5 mm with refinement near the plate.

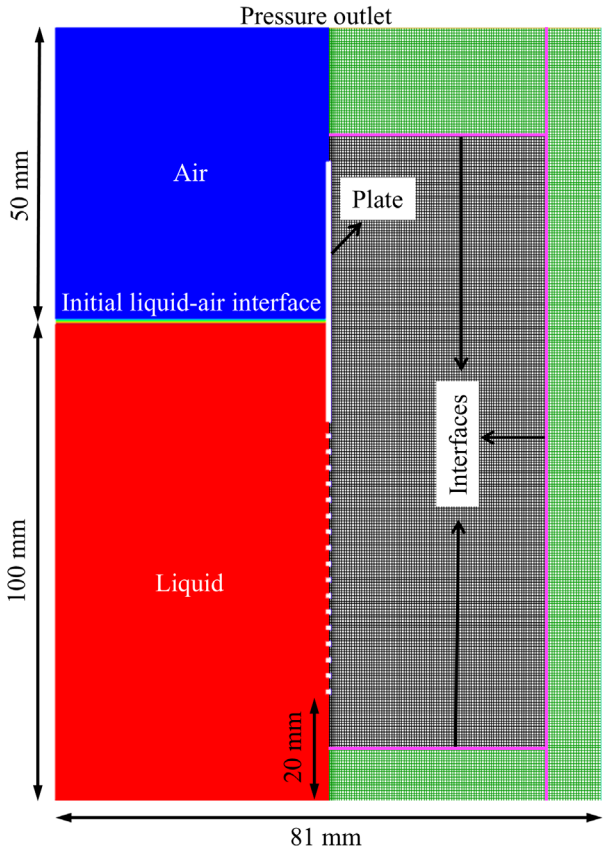

Figure B1. Schematic of the left half of the flow domain and the right half of the mesh with boundary and initial conditions.

The atmospheric pressure boundary condition is imposed at the top outlet. The lateral and bottom walls of the container are set as static walls. The distance between the gel-air interface and the bottom of container is initially 100 mm. The initial immersion depth of the plate is 80 mm. The slot pitch P, slot height S, number of slots N, and plate thickness E are the same as plate P1S2N17. Note that slot height S is increased to 3 to evaluate the secondary flow under S/E = 3. The slipping condition is imposed by setting the same shear stress on the plate surface as in the immersion test. The immersion of the plate is achieved by compiling user-defined functions (UDFs), using the dynamic mesh method with the layering mode.

Nomenclature

A: Pre-factor in pseudo-Herschel-Bulkley model [$Pa \cdot s^B \cdot m^{-B}$]

Ai: Airy function [-]

Ai_{max}: Maximum of Airy function [-]

B: Exponent in pseudo-Herschel-Bulkley model [-]

Cr_{max}: Maximum courant number [-]

E: Plate thickness [m]

F: Total forces applied on the plate [N]

F_0: Forces on the plate at the maximum deformation of gels [N]

F_b: Buoyancy on the plate [N]

F_c: Capillary force on the plate [N]

F_e: Resistance at the plate tip [N]

F_v: Shear force along the plate [N]

$\mathbf{F_{vol}}$: Volume surface tension [$N \cdot m^{-3}$]

g: Gravitational acceleration [$m \cdot s^{-2}$]

h: Film thickness [m]

h_0: Asymptotic film thickness [m]

h_L: Thickness of Landau-Levich (LL) film [m]

h_{max}: Film thickness if liquids entrained from inner yielded region are all coated onto the substrate [m]

h_N: Thickness of thick film or LL film [m]

h_T: Thickness of thick film [m]

k: Curvature [m^{-1}]

K: Consistency factor [$Pa \cdot s^n$]

l: Characteristic length [$l = \sqrt{\eta_L u_0/(\rho_L g)}$] [m]

l_c: Capillary length [m]

L: Plate length [m]

n: Flow index [-]

$\mathbf{n}$: Normal to liquid-air interface [-]

n_m: Number of mesh cells per length of l [m^{-1}]

$\hat{\mathbf{n}}$: Unit normal to liquid-air interface [-]

N: Slot number [-]

p: Pressure [Pa]

P: Slot pitch [m]

q: Flow rate per width of plate in planar dip coating [$m^2 \cdot s^{-1}$] and flow rate in cylindrical dip coating [$m^3 \cdot s^{-1}$]

Q_{drain}: Flow rate due to the gravitational drainage per width of plate [$m^2 \cdot s^{-1}$]

Q_{up}: Flow rate entrained up by the plate per width of plate [$m^2 \cdot s^{-1}$]

r_0: Cylinder radius [m]

r_c: Container radius [m]

s: Carreau-Yasuda parameter [-]

S: Slot height [m]

$\mathbf{S}$: Stress tensor at the liquid-air interface [Pa]

t: Time [s]

Δt: Time step size [s]

u: Vertical velocity [$m \cdot s^{-1}$]

u_0: Withdrawal velocity [$m \cdot s^{-1}$]

u_d: Downward velocity of unyielded region [$m \cdot s^{-1}$]

u_r: Radial velocity [$m \cdot s^{-1}$]

u_z: Axial velocity [$m \cdot s^{-1}$]

v: Transversal velocity [m·s^{-1}]

v: Velocity tensor [m·s^{-1}]

W: Width of container [m]

W_p: Width of plate [m]

W_s: Width of slot [m]

$\Delta x_{\min}$: Minimum mesh cell size [m]

y_{cl}: Vertical height of contact line in planar dip coating [m]

$y_{cl,c}$: Critical vertical height of contact line in planar dip coating [m]

Greek letters

α_A: Volume fraction of air phase [-]

α_L: Volume fraction of liquid phase [-]

$\dot{\gamma}$: Shear rate [s^{-1}]

$\dot{\gamma}_c$: Critical shear rate [s^{-1}]

δ_1: Demarcation between inner yielded region and unyielded region [m]

δ_2: Demarcation between outer yielded region and unyielded region [m]

η: Viscosity [Pa·s]

η_0: Zero-shear viscosity [Pa·s]

η_∞: Infinite-shear viscosity [Pa·s]

η_A: Viscosity of air phase [Pa·s]

η_L: Viscosity of liquid phase [Pa·s]

η_p: Plastic viscosity [Pa·s]

θ: Withdrawal angle [rad or degree]

θ_{ap}: Apparent contact angle [rad or degree]

θ_e: Equilibrium contact angle [rad or degree]

θ_i: Incident angle [rad or degree]

λ: Navier slip length [m]

λ_C: Relaxation time in Carreau model [s]

λ_{CY}: Relaxation time in Carreau-Yasuda model [s]

λ_w: Wavelength of incident laser [m]

ρ_A: Density of air phase [kg·m^{-3}]

ρ_L: Density of liquid phase [kg·m^{-3}]

σ: Surface tension [N·m^{-1}]

τ: Shear stress [Pa]

$\tau_{1/2}$: Shear stress at a viscosity of $\eta_0/2$ [Pa]

τ_c: Yield stress [Pa]

τ_f: Shear stress at fluid-fluid interface [Pa]

τ_w: Shear stress at plate surface [Pa]

χ_1: Number of fringes [-]

χ_2: Refractive index [-]

Dimensionless numbers

Bi: Bingham number [$Bi = \tau_c/K\dot{\gamma}^n$] [$Bi = \tau_c h_0^n/(Ku_0^n)$ in the film region]

Ca: Capillary number [$Ca = \eta_L u_0/\sigma$ for Newtonian fluids, $Ca = Ku_0^n h_0^{1-n}/\sigma$ for power-law fluids, and $Ca = \tau_c h_0/\sigma + Ku_0^n h_0^{1-n}/\sigma$ for Herschel-Bulkley fluids]

$Ca_{c,1}$: First critical capillary number [Rescaling the corresponding velocity by σ/η_L]

$Ca_{c,2}$: Second critical capillary number [Rescaling the corresponding velocity by σ/η_L]

$Ca_{c,3}$: Third critical capillary number [Rescaling the corresponding velocity by σ/η_L]

ΔCa_{cl}: Withdrawal velocity with respect to contact line [Rescaling the corresponding velocity by σ/η_L]

Ca_{cr}: Velocity of capillary ridge [Rescaling the corresponding velocity by σ/η_L]

ΔCa_{cr}: Cylinder velocity with respect to capillary ridge [Rescaling the corresponding velocity by σ/η_L]

Ca^*: Characteristic capillary number which the unstable solution of stationary meniscus oscillates around [-]

Ca^{**}: Characteristic capillary number which the unstable solution of dimple oscillates around [-]

$\bar{d}$: Ration of film thickness to cylinder radius [$\bar{d} = \bar{h}/\bar{r}_0$]

$\bar{d}_N$: Ration of thickness of thick film or LL film to cylinder radius [$\bar{d}_N = \bar{h}_T/\bar{r}_0$ or $\bar{d}_N = \bar{h}_L/\bar{r}_0$]

$\bar{d}_T$: Ration of thickness of thick film to cylinder radius [$\bar{d}_T = \bar{h}_T/\bar{r}_0$]

$\bar{h}$: Dimensionless film thickness [$\bar{h} = h/l$ for planar dip coating and $\bar{h} = h/l_c$ for planar dip coating]

$\bar{h}_0$: Dimensionless asymptotic film thickness [$\bar{h}_0 = h_0/l$]

$\bar{h}_D$: Dimensionless local minimum thickness of dimple [$\bar{h}_D = h_D/l_c$]

$\bar{h}_L$: Dimensionless thickness of Landau-Levich (LL) film [$\bar{h}_L = h_L/l_c$]

$\bar{h}_T$: Dimensionless thickness of thick film [$\bar{h}_T = h_T/l_c$]

$\bar{k}$: Dimensionless curvature [-]

$\bar{p}$: Dimensionless pressure [$\bar{p} = p/\rho_L g l$]

$\bar{q}$: Dimensionless flow rate [$\bar{q} = q/u_0 l$ in planar dip coating and $\bar{q} = q\eta_L/(l_c^2\sigma)$ in cylindrical dip coating]

$\bar{Q}$: Flow rate per unit circumference [$\bar{Q} = \bar{q}/(2\pi\bar{r}_0)$]

$\bar{r}_0$: Dimensionless cylinder radius [$\bar{r}_0/l_c$]

Re: Reynolds number [$Re = \rho_L u_0 l/\eta_L$]

$\bar{t}$: Dimensionless time [$\bar{t} = u_0 t/l$ in planar dip coating and $\bar{t} = t\sigma/(\eta_L l_c)$ in cylindrical dip coating]

T: Dimensionless thickness [$\rho_L g h_0/\tau_c$]

T_0: Dimensionless thickness [$\sqrt{\rho_L g h_0/[\tau_c+K(u_0/h_0)^n]}$]

$\overline{u}$: Dimensionless vertical velocity [$\overline{u} = u/u_0$ in planar dip coating and $\overline{u} = \eta_L u/\sigma$ in cylindrical dip coating]

$\overline{u}_r$: Dimensionless radial velocity [$\overline{u}_r = \eta_L u_r/\sigma$]

$\overline{u}_z$: Dimensionless axial velocity [$\overline{u}_z = \eta_L u_z/\sigma$]

$\overline{v}$: Dimensionless transversal velocity [$\overline{v} = v/u_0$]

$\overline{x}$: Dimensionless height with respect to liquid surface in planar dip coating [$\overline{x} = x/l$]

$\overline{z}$: Dimensionless height with respect to liquid surface in cylindrical dip coating [$\overline{z} = z/l_c$]

$\overline{z}_{cl}$: Dimensional vertical height of contact line in cylindrical dip coating [$\overline{z}_{cl} = z_{cl}/l_c$]

$\overline{z}_D$: Dimensionless height at the location with the thinnest local thickness of dimple [$\overline{z}_D = z_D/l_c$]

$\overline{\lambda}$: Dimensionless Navier slip length [$\overline{\lambda} = \lambda/l_c$]

Publications

(1) **Zhang H-K**, Yin Y-R, Lemaitre C, Zhang X-M, Hu G-H. Spatial-temporal evolution of entire layer thickness during dip coating with vertical withdrawal of Newtonian fluids. *AIChE J*. 2025; 71(10):e70000.

(2) **Zhang H-K**, Yin Y-R, Hu G-H, Zhang X-M. Hydrodynamics and rheological characterization upon the penetration process of a slotted plate into viscoplastic fluids. *Chem. Eng. Sci.* 2025;308:121382.

(3) **Zhang H-K**, Yin Y-R, Hu G-H, Zhang X-M. Temporal evolution of demarcations between the unsteady and steady regions and between the film and meniscus during dip coating with vertical withdrawal of Newtonian fluids. *Chem. Eng. Sci.* 2024;293:120052.

(4) **Zhang H-K**, Yin Y-R, Pan X-Q, Zhang X-M, Chen W-X, Hu G-H. The normal force evolution of the substrate during the withdrawal process. *Polym. Eng. Sci.* 2022;62(10):3241-3253.

(5) **Zhang H-K**, Yin Y-R, Zhang X-M, Chen S-C, Chen W-X, Hu GH. Numerical simulation of the hydrodynamics of yield stress fluids during dip coating. *J Non-Newton Fluid.* 2021;298:104675.

(6) Chen W-Y, Tian X-Y, **Zhang H-K**, Yin Y-R, Zhang X-M, Zhu C-Y, Fu T-T, Ma Y-G. Splitting behavior and breakup mechanism of bubbles in the split-and-recombine microchannel. *AIChE J.* 2024;70(10).